INVESTIGATION OF THE PERFORMANCE AND WATER TRANSPORT OF A POLYMER ELECTROLYTE MEMBRANE (PEM) FUEL CELL

A Dissertation

by

YONG HUN PARK

Submitted to the Office of Graduate Studies of
Texas A&M University
in partial fulfillment of the requirements for the degree of

DOCTOR OF PHILOSOPHY

December 2007

Major Subject: Mechanical Engineering

INVESTIGATION OF THE PERFORMANCE AND WATER TRANSPORT OF A POLYMER ELECTROLYTE MEMBRANE (PEM) FUEL CELL

A Dissertation

by

YONG HUN PARK

Submitted to the Office of Graduate Studies of
Texas A&M University
in partial fulfillment of the requirements for the degree of

DOCTOR OF PHILOSOPHY

Approved by:

Chair of Committee,	Jerald A. Caton
Committee Members,	Thomas R. Lalk
	Prasad Enjeti
	Sai C. Lau
Head of Department,	Dennis L. O'Neal

December 2007

Major Subject: Mechanical Engineering

ABSTRACT

Investigation of the Performance and Water Transport of a Polymer Electrolyte Membrane (PEM) Fuel Cell. (December 2007)

Yong Hun Park, B.S., Kyungpook National University;

M.S., Texas A&M University

Chair of Advisory Committee: Dr. Jerald A. Caton

Fuel cell performance was obtained as functions of the humidity at the anode and cathode sites, back pressure, flow rate, temperature, and channel depth. The fuel cell used in this work included a membrane and electrode assembly (MEA) which possessed an active area of 25, 50, and 100 cm^2 with the Nafion® 117 and 115 membranes.

Higher flow rates of inlet gases increase the performance of a fuel cell by increasing the removal of the water vapor, and decrease the mass transportation loss at high current density. Higher flow rates, however, result in low fuel utilization. An important factor, therefore, is to find the appropriate stoichiometric flow coefficient and starting point of stoichiometric flow rate in terms of fuel cell efficiency. Higher air supply leads to have better performance at the constant stoichiometric ratio at the anode, but not much increase after the stoichiometric ratio of 5.

The effects of the environmental conditions and the channel depth for an air-breathing polymer electrolyte membrane fuel cell were investigated experimentally. Triple serpentine designs for the flow fields with two different flow depths was used. The

shallow flow field deign improves dramatically the performance of the air-breathing fuel cell at low relative humidity, and slightly at high relative humidity.

For proton exchange membrane fuel cells, proper water management is important to obtain maximum performance. Water management includes the humidity levels of the inlet gases as well as the understanding of the water process within the fuel cell. Two important processes associated with this understanding are (1) electro-osmotic drag of water molecules, and (2) back diffusion of the water molecules. There must be a neutral water balance over time to avoid the flooding, or drying the membranes. For these reasons, therefore, an investigation of the role of water transport in a PEM fuel cell is of particular importance.

In this study, through a water balance experiment, the electro-osmotic drag coefficient was quantified and studied. For the cases where the anode was fully hydrated and the cathode suffered from the drying, when the current density was increased, the electro-osmotic drag coefficient decreased.

DEDICATION

I would like to dedicate this thesis to my parents who have been a major influence in my life. They have supported me wholeheartedly in all my endeavors. I also would like to dedicate this dissertation to my wife, Mihwa Lee, who has supported my study more than 7 years and leads me to achieve this goal. Her encouragement has kept me going, throughout my student life.

ACKNOWLEDGEMENTS

I would like to thank my committee chair, Dr. Caton, and my committee members, Dr. Lalk, Dr. Enjeti, and Dr. Lau, for their guidance and support throughout the course of this research.

Thanks also to my friends, colleagues, the department faculty, and staff for making my time at Texas A&M University a great experience.

Finally, special thanks to John Zhang, Antony Parulian and Tim Jiang who have supported and helped me while working at company.

TABLE OF CONTENTS

Page

LIST OF FIGURES

FIGURE Page

FIGURE Page

FIGURE Page

FIGURE Page

FIGURE Page

FIGURE Page

FIGURE Page

FIGURE Page

FIGURE Page

LIST OF TABLES

TABLE Page

1. INTRODUCTION

The principle of a fuel cell was first demonstrated by Grove in 1839 (Larminie and Dicks, 2000). However, it was dismissed since it was not very useful at that time. One of the first applications of the hydrogen fuel cell was for a 1960 NASA mission (Barbir, 2005), which needed a high efficiency power source and no waste products other than water. The fuel could be stored on the spacecraft, and the three products (power, water, and heat) would be useful inside of the spacecraft.

Recently, attention to this technology has been increased due to environmental issues such as global warming and the acknowledgement of the limitation of oil sources. One of the main attractions of the fuel cell relative to the internal combustion (IC) engine (or power sources using any hydrocarbon fuel) is the potential to produce power with minimal or zero emissions.

Hybrid cars are based on a battery and an internal combustion engine together. This may lead to reduced gasoline consumption and less noise at low speed. In the future, the internal combustion engine could be replaced with a fuel cell. However, there are many obstacles for fuel cell cars to be on the market: (1) the infrastructure to refuel a fuel cell car (using hydrogen), (2) the cost to build fuel cell stacks, (3) safety, and (4) the difficulty of integrating a fuel cell system. As fuel cell technology continues to mature, these obstacles will be reduced.

This dissertation follows the style of *International Journal of Green Energy*.

1.1 Principle of the Hydrogen Fuel Cell

A fuel cell is an energy conversion device that converts the chemical energy of a reaction directly into electrical energy without any intermediate thermal or mechanical processes. The basic structure of a fuel cell consists of an electrolyte layer in contact with a porous anode and cathode on each side. The anode is made of substance that easily releases electrons, and the cathode is made of a substance that readily accepts electrons. The basic operation of a fuel cell is such that energy is released whenever the fuel reacts chemically with the oxygen in the air. In contrast, a battery converts chemical energy stored in the chemical bonds of the reactants to electrical work in a closed system. A fuel cell, however, is an energy conversion device that has the capability of producing electrical energy for as long as the fuel and oxidant are supplied to the electrodes as an open system. A gaseous fuel is fed to the anode and an oxidant is fed to the cathode compartment, which leads to the electrochemical reactions taking place at the electrodes to produce an electric current.

The reactions at the anode and cathode are important to understand how the reaction produces an electric current. For this discussion, the fuel will be assumed to be hydrogen. The hydrogen at the anode compartment releases electrons and creates H^+ ions (or protons) as follows:

$$2H_2 \rightarrow 4H^+ + 4e^- \tag{1.1}$$

Oxygen reacts with electrons taken from the electrode and H^+ ion from the electrolyte to form water at the cathode compartment as follows:

$$O_2 + 4e^- + 4H^+ \rightarrow 2H_2O \tag{1.2}$$

H^+ ions must pass through the electrolyte and electrons produced at the anode must pass through an electrical circuit to the cathode. Since certain polymers can be made to contain mobile H^+ ions, these materials are called 'Proton Exchange Membranes (PEM)', as an H^+ ion is also a proton. For the case of a hydrogen/oxygen fuel cell, the overall reaction is

$$H_2 + \frac{1}{2}O_2 \rightarrow H_2O \tag{1.3}$$

The reaction product of this reaction (1.3) is water that is formed at the cathode in the fuel cell with proton conducting membranes. It can be formed at the anode for the case of high temperature fuel cells.

For fuel cells, the 'Gibbs free energy' can be defined as the 'energy available to do external work', neglecting any work done by changes in pressure and/or volume. The product is one mole of H_2O, and the inputs are one mole of H_2 and a half a mole of O_2. Thus the difference between the Gibbs free energy of the products and the Gibbs free energy of the reactants is the released energy:

$$\Delta\overline{g_f} = (\overline{g_f})_{H_2O} - (\overline{g_f})_{H_2O} - \frac{1}{2}(\overline{g_f})_{O_2} \tag{1.4}$$

Table 1-1 shows $\Delta\overline{g_f}$ for the basic hydrogen fuel cell reaction for several temperatures. The values are negative, which means that energy is released. The reversible open circuit voltage of the hydrogen fuel cell (E) can be calculated:

$$E = \frac{-\Delta\overline{g_f}}{2F} \tag{1.5}$$

where F is the Faraday constant (96,485 Coulombs/mol).

Table 1-1 Δg^{O}_{T}, maximum voltage, and efficiency limit for the hydrogen fuel cell at various temperatures.

Enthalpy of Formation	H_2O		O_2		H_2		Δg^{O}_{T} (J/mol)	E (Volts)	Efficiency Limit (%)
H'^{0}_{f} (l)(J/mol)	-285830		0		0				
H'^{0}_{f} (g) (J/mol*K)	-241820								
Temperature (Kelvin)	h'(T) (J/mol)	S'(0)T (J/mol*K)	h'(T) (J/mol)	S'(0)T (J/mol*K)	h'(T) (J/mol)	S'(0)T (J/mol*K)			
298	9,904	69.95	8,682	205.03	8,468	130.57	-237,214	1.229	82.99
320	10,639	69.95	9,325	207.11	9,100	132.62	-232,856	1.207	81.04
380	12,672	196.92	11,109	212.22	10,843	137.61	-224,855	1.165	78.44
400	13,356	198.67	11,711	213.77	11,426	139.11	-223,914	1.160	78.06
600	20,402	212.92	17,929	226.35	17,280	150.97	-214,025	1.109	74.12
800	27,896	223.69	24,523	235.81	23,171	159.44	-203,530	1.055	70.07
1000	35,882	232.6	31,389	243.47	29,154	166.11	-192,629	0.998	65.99
1200	44,380	240.33	38,447	249.91	35,262	171.68	-181,458	0.940	61.93

1.2 Efficiency of a Fuel Cell

For fuel cells, the maximum efficiency may be defined as:

$$\eta_{th,FC} = \frac{Electrical\_energy\_output\_per\_mole\_of\_fuel}{\Delta\overline{h}_f} = \frac{\Delta\overline{g}_f}{\Delta\overline{h}_f} \qquad (1.6)$$

This maximum efficiency limit is called as the thermodynamics efficiency. Table 1-1 gives the values of the efficiency limit, relative to the higher heating value for a hydrogen fuel cell. The theoretical fuel cell voltage decreases for higher operating temperatures. In practice, actual fuel cell voltages are usually higher at higher temperatures (within the operating temperature range), because of voltage losses at low temperature.

1.3 Exergy Analysis

The meaning of exergy, which was first introduced by Gibbs (Gibbs, 1873), is the sum of work (-erg) that is released (ex-). Total exergy (e_{Tot}) consists of physical exergy (thermal exergy and pressure (mechanical) exergy) and chemical exergy (standard chemical exergy and mixing exergy) as follows:

$$e_{Tot} = e_{Ph} + e_{Ch} \tag{1.7}$$

where e_{Ph} is the physical exergy and e_{Ch} is the chemical exergy. The physical exergy deals with temperature and pressure and chemical exergy is responsible for the chemical composition and reactions. In the analysis, gas is treated as an ideal gas. Physical exergy (e_{Ph}) can be obtained as follows:

$$e_{Ph} = (h - h_0) - T_0(s - s_0) \cong c_p T_0 \left(\frac{T}{T_0} - 1 - \ln\left(\frac{T}{T_0}\right) + \ln\left(\frac{p}{p_0}\right)^{\frac{k-1}{k}}\right) \tag{1.8}$$

where h is the enthalpy and s is the entropy. These values may be obtained from curve fits for the thermodynamics properties of gases (Turns, 1996)

$$h = \frac{R_u T}{MW_{hydrogen}} \times \left(a_1 + \frac{a_2}{2}T + \frac{a_3}{3}T^2 + \frac{a_4}{4}T^3 + \frac{a_5}{5}T^4 + \frac{a_6}{6}T^5\right) \tag{1.9}$$

$$s = \frac{R_u}{MW_{hydrogen}} \times \left(a_1 LnT + a_2 T + \frac{a_3}{2}T^2 + \frac{a_4}{3}T^3 + \frac{a_5}{4}T^4 + a_7\right) \tag{1.10}$$

Chemical exergy is the sum of chemical potentials of the component species for both the reactants and products (Bejan, 1996)

$$e_{Ch,i} = -RT_0 \ln \frac{x_i^e p_i}{p_0} \tag{1.11}$$

For example, the chemical exergy of air produced from the reaction should be calculated in terms of the mole fraction of each component in the mixture

$$e_{Ch} = \sum x_n e_{n,Ch} + RT_0 \sum x_n \ln x_n \tag{1.12}$$

where x_n is the mole fraction of the n species

The total exergy of substances are calculated as follows:

$$E_{Total\_Exergy} = \sum_i n_i \varepsilon_i^{\circ} + \overline{R}T_0 \sum_i n_i \ln(\frac{n_i}{\sum_i n_i}) + \sum n_i \overline{c_{p,i}} T_0 (\frac{T}{T_0} - 1 - \ln \frac{T}{T_0}) + \overline{R}T_0 \sum_i n_i \ln \frac{p_i}{p_0} \tag{1.13}$$

The first term is the standard chemical exergy, the second term is the mixing exergy, the third term is the thermal exergy, and the fourth term is the pressure (mechanical) exergy. The first two terms are the chemical exergy and last two terms are the physical exergy. All the terms can be expressed in the form as follows:

$$E_{Total\_Exergy} = (\overline{h} - \overline{h_0}) - T_0 (\overline{s} - \overline{s_0}) \tag{1.14}$$

This is a general expression for the total exergy of substances. The fuel availability is defined as follows:

$$\overline{a}_{fuel} = -\Delta G_{RP}^{\circ} = (\overline{h_R} - \overline{h_P}) - T_0 (\overline{s_R} - \overline{s_P}) \tag{1.15}$$

For the case of hydrogen fuel cell, the reaction between reactants can be written as follows:

$$H_2 + \frac{\lambda}{2}(O_2 + 3.76N_2) + xH_2O \rightarrow (x+1)H_2O + (\frac{\lambda - 1}{2})O_2 + \frac{3.76\lambda}{2} N_2 \tag{1.16}$$

where $\lambda/2$ is the number of mole of air and x is the number of mole of water supplied. The fuel availability of hydrogen is calculated as follows:

$$\bar{a}_{fuel} = [\overline{h_{H_2}} + \frac{\lambda}{2}\overline{h_{O_2}} + \frac{3.76\lambda}{2}\overline{h_{N_2}} + x\overline{h_{H_2O}} - ((x+1)\overline{h_{H_2O}} + \frac{\lambda-1}{2}\overline{h_{o_2}} + \frac{3.76\lambda}{2}\overline{h_{N_2}})]$$

$$-T_0[\overline{s_{H_2}} + \frac{\lambda}{2}\overline{s_{O_2}} + \frac{3.76\lambda}{2}\overline{s_{N_2}} + x\overline{s_{H_2O}} - ((x+1)\overline{s_{H_2O}} + \frac{\lambda-1}{2}\overline{s_{o_2}} + \frac{3.76\lambda}{2}\overline{s_{N_2}})] \quad (1.17)$$

The maximum theoretical work output [kJ/kmol] of the fuel is:

$$\frac{\dot{W}_{\max}}{\dot{N}_{fuel}} = \sum_i (v_i \Delta\bar{g}^0_{f,i})_{reac} - \sum_i (v_i \Delta\bar{g}^0_{f,i})_{prod} \quad (1.18)$$

The maximum theoretical power it can develop [kW] is:

$$\dot{W}_{\max} = \dot{N}_{fuel} * (\sum_i (v_i \Delta\bar{g}^0_{f,i})_{reac} - \sum_i (v_i \Delta\bar{g}^0_{f,i})_{prod}) \quad (1.19)$$

The accompanying rate of heat transfer [kW] is:

$$(\dot{Q}_{cv})_{\min} = (\dot{W}_{cv})_{\max} + \dot{n}_{fuel} (\sum_i (v_i \Delta\bar{h}^0_{f,i})_{prod} - \sum_i (v_i \Delta\bar{h}^0_{f,i})_{reac}) \quad (1.20)$$

Finally, the ideal efficiency [%] is:

$$\eta_i = \frac{\Delta\bar{g}_R}{\Delta\bar{h}_R} \times 100 \quad (1.21)$$

Table 1-2 shows the g_f^o and h_f^o of CO_2, H_2O(l), and hydrocarbon fuels, and Table 1-3 shows the ideal fuel efficiency and voltage for several fuels. The overall reaction for each hydrocarbon fuel is shown in Table 1-4.

Table 1-2 g_f^o and h_f^o of CO_2, H_2O(l), and hydrocarbon fuels.

Substances	CO_2	H_2O(l)	CH_3OH(*l*)	CH_3OH(g)	CH_4	C_3H_8	C_2H_4	C_2H_5OH
g_f^o [kJ/kmol]	-394,380	-237,180	-166,290	-162,140	-50,790	-23,490	60,120	-174,890
h_f^o [kJ/kmol]	-393,520	-285,830	-238,810	-200,890	-74,850	-103,850	52,280	-277,690

Table 1-3 Ideal fuel efficiency and voltage of the several hydrocarbon fuels (298K).

Fuel	Max. Theo. Work	$(W_{cv})_{max}$ =	$(Q_{cv})_{min}$	$\Delta h^0_{R,298}$	Ideal fuel efficiency	Ideal voltage
	[kJ/kmol of fuel]	[kW]	[kW]	[kJ/kmol]	[%]	[V]
Hydrogen	237,180	47.44	-9.73	285,830	82.98	1.229
Methane	817,950	163.59	-14.48	890,330	91.87	1.060
Methyl alcohol (g)	706,600	141.32	-11.54	764,290	92.45	1.221
Methyl alcohol (*l*)	702,450	140.49	-4.78	726,370	96.71	1.213
Propane	2,108,370	421.67	-22.33	2,220,030	94.97	1.214
Ethylene	1,323,240	264.65	-17.55	1,410,980	93.78	1.143
Ethyl alcohol	1,325,410	265.08	-8.29	1,366,840	96.97	1.145

Table 1-4 Overall reactions for each hydrocarbon fuels.

Fuel	Reaction
Hydrogen	$H_2+0.5O_2=H_2O(l)$
Methane	$CH_4+2O_2=CO_2+2H_2O(l)$
Methyl alcohol (g)	$CH_3OH(g)+1.5O_2=CO_2+2H_2O(l)$
Methyl alcohol (*l*)	$CH_3OH(l)+1.5O_2=CO_2+2H_2O(l)$
Propane	$C_3H_8+5O_2=3CO_2+4H_2O(l)$
Ethylene	$C_2H_4+3O_2=2CO_2+2H_2O(l)$
Ethyl alcohol	$C_2H_5OH+3O_2 = 2CO_2+3H_2O$

1.4 Types of Fuel Cells

There are several fuel cells under development and each has its own advantages, handicaps, operating temperature, and potential applications. Fuel cells are mainly classified by the kinds of electrolyte they employ as follows:

- Polymer electrolyte membrane fuel cell (PEMFC)
- Direct-methanol fuel cell (DMFC)

- Alkaline fuel cell (AFC)
- Phosphoric acid fuel cell (PAFC)
- Molten carbonate fuel cell (MCFC)
- Solid-oxide fuel cell (SOFC)

Figure 1-1 shows the several different types of fuel cells with operating temperatures, power ranges, and applications.

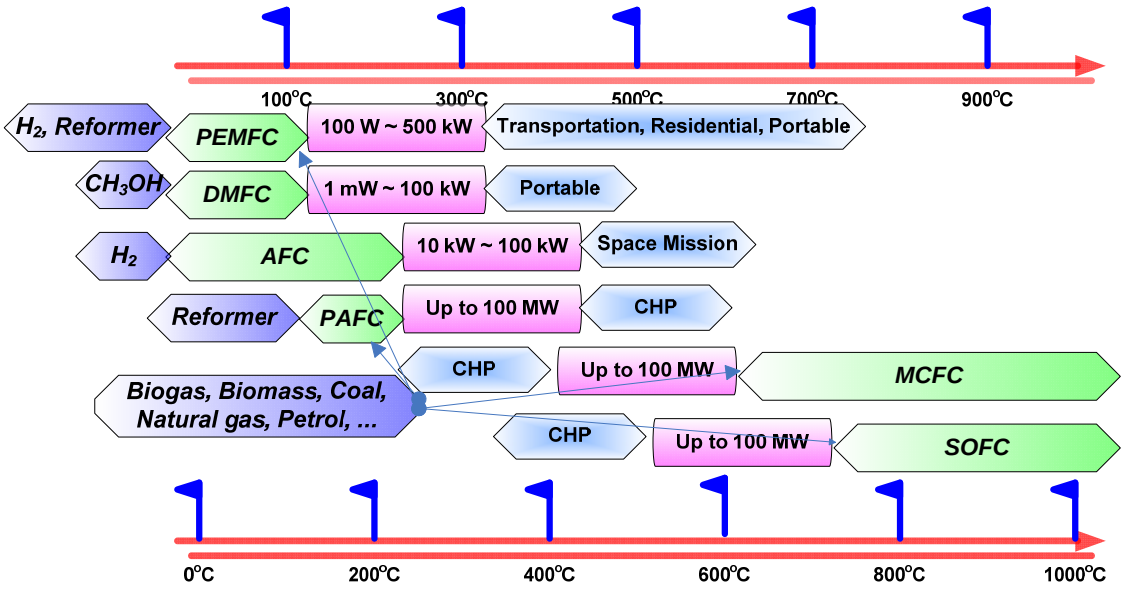

Figure 1-1 The type of the fuel cells showing energy sources, output power ranges, and potential applications.

Polymer electrolyte membrane fuel cells (PEMFC) use a thin solid polymer membrane as an electrolyte. Protons (H^+) are the charge carriers in the electrolyte. The operating temperature range is between about 60°C and 120°C. The advantages of the PEMFC are that it is very simple, has high power density, has good start-stop capabili-

ties, and operates at relatively low temperatures. But, it needs cost reduction since it uses expensive platinum catalyst, and polymer membrane components (O'Hayre et al., 2005)

Direct-methanol fuel cells (DMFC) use the same electrolyte as PEMFCs, but the amount of the catalyst coatings is several times higher than for PEMFCs. The advantages of the DMFCs are that they have high theoretical energy density, can be stored and transported safely because of the use of a liquid fuel, do not require any fuel processing equipment, and can be operated at room temperature. The main problems of the DMFC, however, are that they have low power density, and low fuel utilization due to methanol and water permeation through the membrane (which is called 'crossover').

Alkaline fuel cells (AFC) make use of an aqueous potassium hydroxide electrolyte. They require pure hydrogen and pure oxygen because aqueous alkaline solutions can not tolerate carbon dioxide, which leads to poisoning of the AFC. As one of the advantages, the catalyst for the electrode can be non-precious metal, which are relatively inexpensive.

Phosphoric acid fuel cells (PAFC) employ a liquid (H_3PO_4) electrolyte, which is contained in a thin SiC matrix between two porous graphite electrodes coated with a platinum catalyst. Pure phosphoric acid solidifies at 42^{o}C. Therefore, PAFCs must be operated above this temperature. Optimal performance occurs at temperatures of about 180^{o}C to 210^{o}C. During operation, H_3PO_4 must be continually replenished because it gradually evaporates to the environment (especially during higher temperature operation). It has excellent reliability and long-term performance and the electrolyte is low cost compared

to other types of fuel cells. Disadvantages of the PAFCs include the need for expensive platinum catalysts, and CO poisoning.

Molten carbonate fuel cells (MCFC) use a molten mixture of alkali carbonates as the electrolyte. Because they operate at relatively high operating temperatures, they provide wide fuel flexibility, and high quality waste heat for cogeneration applications. They are, however, only suited for stationary applications and CO_2 needs to be recycled from the anode to the cathode.

Solid oxide fuel cells (SOFC) use a solid ceramic electrolyte. Due to the high operating temperature, they do not need an expensive catalyst, have fuel flexibility, and have high quality waste heat for cogeneration applications. Still, some unresolved issues such as sealing, and relatively expensive components exist.

Table 1-5 shows the types of fuel cells classified by electrolyte, operating temperature, and catalyst used in each fuel cell. Table 1-6 shows the different fuel cell reactions in the anode and the cathode.

Table 1-5 Major types of fuel cells classified by the electrolyte.

Types	AFC	PEMFC	DMFC	PAFC	MCFC	SOFC
Operating Temperature (^{O}C)	100	60-120	60-120	160-220	600-800	500-1000
Charge carrier in the electrolyte	OH^-	H^+	H^+	H^+	CO_3^{2-}	O^{2-}
Catalyst	Pt	Pt	Pt	Pt	Ni	Ce

Table 1-6 Reactions of different fuel cells at the anode and the cathode.

	Anode Reaction	Cathode Reaction
AFC	$H_2 + 2OH^- \rightarrow 2H_2O + 2e^-$	$0.5O_2 + H_2O + 2e^- \rightarrow 2OH^-$
PEMFC	$H_2 \rightarrow 2H^+ + 2e^-$	$0.5O_2 + 2H^+ + 2e^- \rightarrow H_2O$
DMFC	$CH_3OH + H_2O \rightarrow CO_2 + 6H^+ + 6e^-$	$1.5O_2 + 6H^+ + 2e^- \rightarrow 3H_2O$
PAFC	$H_2 \rightarrow 2H^+ + 2e^-$	$0.5O_2 + 2H^+ + 2e^- \rightarrow H_2O$
MCFC	$H_2 + CO_3^{2-} \rightarrow H_2O + CO_2 + 2e^-$	$0.5O_2 + CO_2 + 2e^- \rightarrow CO_3^{2-}$
SOFC	$H_2 + O^{2-} \rightarrow H_2O + 2e^-$	$0.5O_2 + 2e^- \rightarrow O^{2-}$

1.5 Water Management in PEM Fuel Cell

To commercialize fuel cell systems, barriers that need to be overcome include the cost reduction, durability, fuel flexibility, reducing the complexity of an integrated system, and water/thermal management. Among these barriers, water management is the main interest of this work since it is related to the performance and durability of a PEM fuel cell.

1.5.1 Water Transport Process in a PEM Fuel Cell

As explained above, when the hydrogen molecule contacts with the platinum on the catalyst, the molecules are split as shown in equation (1.1). The result is two H^+ ions, and two electrons. At the same time, oxygen gas is supplied through a catalyst on the opposite side of the cell. The oxygen molecules are split after contacting with the catalyst and two separate oxygen atoms result. These atoms have a strong negative charge. This negative charge attracts the two H^+ ions through the membrane. So, protons travel through the membrane. Water is “dragged” from the anode to the cathode by protons

moving through the electrolyte, which is called electroosmotic drag. Typically, the membranes for PEM fuel cells are made of perfluorocarbon-sulfonic acid ionomer (PSA) which has a side chain ending with suophonic acid, HSO_3. The HSO_3 is ionically bonded, and so the end of the side chain is actually an SO_3^- ion. Because of the presence of these SO_3^- and H^+ ions, there is a strong mutual attraction between the + and – ions from each molecule. Within these hydrated regions, the H^+ ions are relatively weakly attracted to the SO_3^- group, and are able to move. In other words, in the presence of water, the proton (H^+) in the pores form hydronium complexes (HSO_3^+) and detach from the sulfonic acid side chains. When sufficient water exists in the pores, the hydronium ions can transport in the aqueous phase. That is the reason why the movement of proton from the anode to the cathode depends on the membrane hydration. In general, the proton conductivity of Nafion increases linearly with increasing water content and exponentially with increasing temperatures. Since water is generated at the cathode and there must be humidified inlet gases, a water concentration gradient exists. This gradient causes back diffusion from the cathode to the anode.

1.5.2 Necessity of the Water Management in a PEM Fuel Cell

As seen in Figure 1-2, there are several water movements. First, water is supplied by an external humidification system to the anode and the cathode. Second, water is generated at the cathode because of the chemical reaction. Third, water is dragged from the anode to the cathode by protons moving through the electrolyte. Fourth, when there is a water concentration gradient because of both water generation at the cathode and

supplied humidified inlet gases, water undergoes back diffusion from the cathode to the anode. Finally, water is removed by circulating hydrogen at the anode and the cathode outlet. All these processes may occur at the same time, which leads to a complex water balance for the fuel cell.

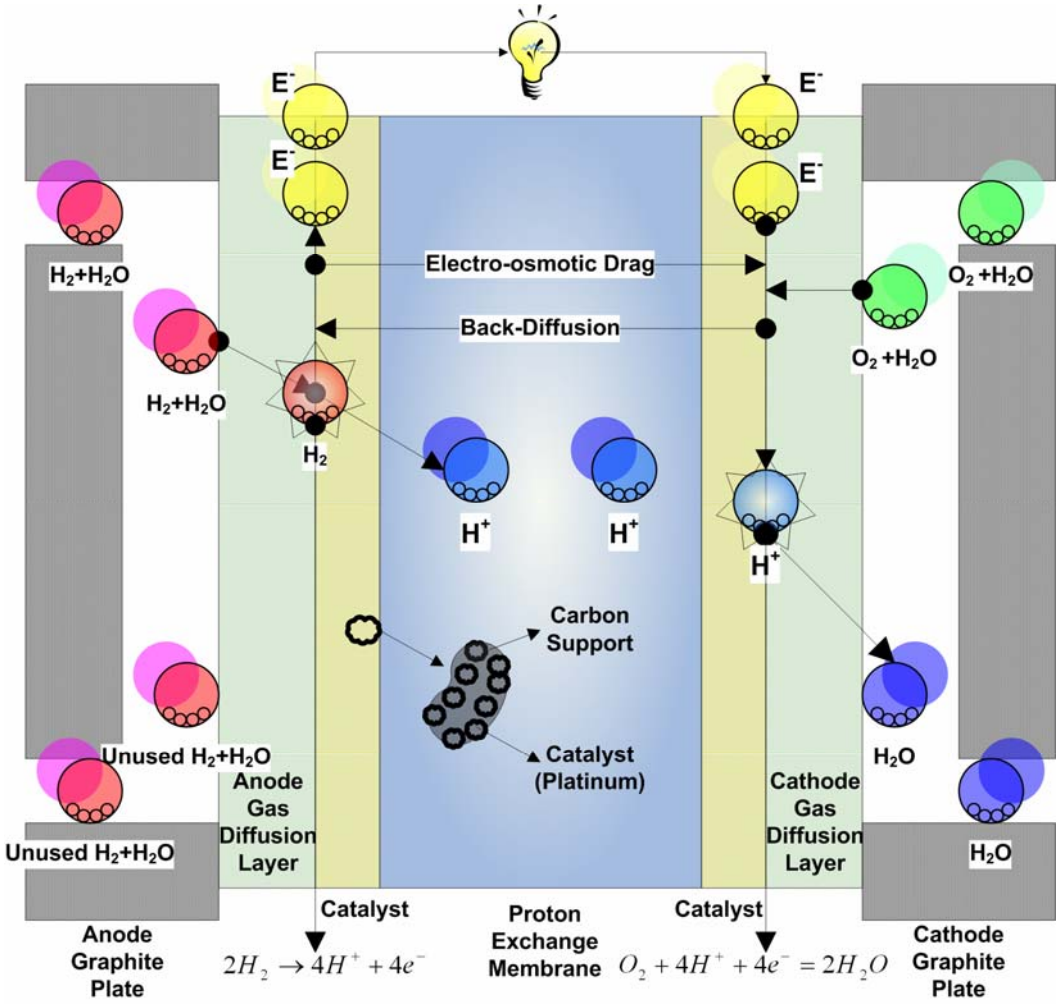

Figure 1-2 The basic principle of operation of a PEM fuel cell.

When insufficient humidified inlet gases are supplied, the water content in the membrane drops. This leads the membrane to start to dry, which increases the ionic re-

sistance, and decreases the proton conductivity as well. Finally, the voltage drops and performance decreases. On the other hand, when excess humidified inlet gases are supplied, the water removal is not efficient. Water is built up at the cathode side, which leads to a "flooding" condition. The excess water blocks porous passages, reduces the electrochemical activity, and reduces the transport rate of the reactant to the catalyst site. As a result of these actions, the excess water decreases the cell performance and reduces reactant diffusion. A sufficient amount of water for the system is a crucial item regarding the performance of the fuel cell.

1.5.3 Sufficient Amount of the Water

The term "sufficient amount" means maintaining the proper amount of water in a PEM fuel cell. Each membrane has its own maximum water uptake capacity. If water content is over the limit of its water uptake, the fuel cell will flood, blocking pores in the electrodes or gas diffusion layer. Vice versa, if water content is less than the water uptake capacity, the conductivity will decrease. Water content in the membrane is defined as follows:

$$\lambda = \frac{N(H_2O)}{N(SO_3H)} \tag{1.22}$$

where $N(H_2O)$ is the number of water molecules, and $N(SO_3H)$ is the number of sulfonic acid groups present in the polymer. Experimental results suggest that λ can vary from almost 0 (for completely dehydrated Nafion) to 22 (for full saturation, under certain conditions) (Barbir, 2005, Zawodzinski et al., 1993a). For example, from experimental

results, a polynomial equation to obtain a relationship between pressure/temperature and water content was introduced as follows (Zawodzinski et al., 1993a):

$$\lambda = 0.043 + 17.13\frac{p}{p_{sat}} - 39.85(\frac{p}{p_{sat}})^2 + 36(\frac{p}{p_{sat}})^3 \tag{1.23}$$

where p is the water partial pressure, and p_{sat} is the saturation pressure at the given temperature. From these two equations ((1.22),(1.23)), the sufficient amount of water can be determined. Equation (1.23) would be different for each membrane, but could be determined from experiments. The rate of water production ($R_{H_2O\_Prod}$) in a fuel cell is derived as follows (Larminie and Dicks, 2000):

$$R_{H_2O\_Prod}[\frac{kg}{s}] = \frac{P_e}{2V_c \bullet F} = 9.34\times10^{-8}\times\frac{P_e}{V_c} \tag{1.24}$$

where P_e is the electrical output power, V_c is the mean voltage of each cell in fuel cell stack, and F is the faraday constant. Depend on the membrane, water molecules are "dragged" for each proton, which is directly proportional to the current. The back diffusion of water from the cathode to the anode depends on the thickness of the electrolyte membrane, and other parameters. If the humidification of the fuel cell is known, the water content in the membrane can be estimated. Humidity is quantified by water vapor activity a_w (essentially relative humidity):

$$a_w = \frac{p_w}{p_{sat}} \tag{1.25}$$

where p_w represents the actual partial pressure of water vapor in the system and p_{sat} represents the saturation water vapor pressure for the system temperature.

Equation (1.23) does not consider the effects of temperature; however, it is reasonably accurate for PEMFCs operating near 80^{o}C (O'Hayre et al., 2005). After calculating the rate of water production and knowing the back diffusion of water, the "sufficient amount" for external humidification of the reactant gases would be known.

1.6 Remaining Sections

As described above, water management of a fuel cell is a complex topic, but is an important topic for improving fuel cell performance. The remaining sections will include (a) literature reviews, (b) research objective, (c) experimental setup, (d) result and discussion for parametric study using a PEM single cell, (e) experimental investigation of water transport in a PEM fuel cell, and (f) conclusions.

2. LITERATURE REVIEW

2.1 Studies Using a Single PEM Fuel Cell

2.1.1 Relative Humidity Effect

Lee et al. (1999) determined that insufficient water lowers the conductivity of the membrane and yields low currents at a fixed voltage, and that excess water leads to low currents at a fixed voltage caused by a decreased reaction area. Nieman (2004) mentioned that humidification is necessary to reduce resistive losses in a cell and to maintain a low ionic resistance throughout the membrane. Decreasing the relative humidity at the cathode has a more detrimental effect on cell performance as compared to a decrease of the humidity at the anode (Yan et al., 2005). The membrane resistance increased as the feed gas relative humidity decreased (Yan et al., 2005). Some studies in the literature have considered dry-reactant conditions (Qi and Kaufman, 2002, Williams et al., 2004, Rajalakshmi et al., 2004, Ahn et al., 2004, Yang et al., 2005, Hogarth and Benziger, 2006). For example, a double-path-type flow field designed by Qi and Kaufman (2002) operated at current densities up to 0.33 amp/cm^2 without drying out. This work demonstrated that the performance of the cell decreased due to insufficient water supply under dry-reactant conditions. Williams et al. (2004) used dry reactant for the cathode while maintaining a fully humidified anode inlet. They found that cell performance decreased 5% at the current density of 400 mA/cm^2. In the case of no humidification, cell performance depended on the cell operating temperature and inlet gas stoichiometric flow rates (Williams et al., 2004). Similar to Williams's group (2004), Rajalakshmi et al. (2004)

showed that various factors like reactant flow field design, area of the electrode, and equilibration time of the electrochemical reactions are important factors for the cell performance with dry gas operation. After supplying dry gases to a fuel cell at room temperature for 48 hours, the voltage dropped abruptly upon applying electric load, due to low proton conductivity of the polymer electrolyte under non-humidified conditions (Ahn et al., 2004). Thin double-layer composite membranes developed by Yang et al. (2005) showed that using dry gases demonstrated 90% performance compared to the humidified reactants. The water generated at the cathode humidifies the cathode side membrane, and self-humidify the anode side membrane by the back-diffusion using double-layer composite. Hogarth and Benziger (2006) examined different fuel cell flow channel designs as a function of pressure, temperature and flow rate with dry feeds. Self-humidifying operation improved at higher pressure and low gas velocities due to enhance back mixing of the product of water with the dry feed.

Most previous studies for reduced humidity operation or dry feed conditions were restricted to short running times or just one polarization curve (Qi and Kaufman, 2002, Williams et al., 2004, Sena et al., 1999). Of the few studies in the literature that consider reduced humidity or dry feed operations for a long time, two of them (Yang et al., 2005, Yoshioka et al., 2005) were presented at fixed current density. Hogarth et al. (2006) conducted experiments with three different voltage ranges (300, 400, and 500 mV).

In summary, these previous studies (Lee et al., 1999, Nieman, 2004, Yan et al., 2005, Qi and Kaufman, 2002, Williams et al., 2004, Rajalakshmi et al., 2004, Ahn et al.,

2004, Yang et al., 2005, Hogarth and Benziger, 2006) have demonstrated where (anode or cathode) humidification is more important, the results of insufficient water level during the cell reaction, and the effect of increasing the self-humidifying to the MEA by different flow field designs. Items which have not been studied in detail include the following. Results are needed for long term operation using dry gases. Fuel cell performance for different humidification levels at the anode and at the cathode, and the relationship between the back pressure and the status of flow field is needed. The current research is aimed to address these items and to demonstrate that proper water management is necessary for maximum fuel cell performance.

2.1.2 Flow Rate Effect

There are three main losses related with the performance of a typical proton exchange membrane fuel cell: the activation loss, the ohmic loss, and the mass transport loss. The activation loss occurs due to the charge transfer rate of the chemical reactions on the surface of the electrodes (Görgün et al., 2006). The ohmic loss is due to the resistance to the flow of ions in the electrolyte, and resistance to the flow of electrons through the fuel cell (Barbir, 2005). The mass transport loss occurs when the reactants at the surface of the electrodes are used up rapidly by the electrochemical reaction (Barbir, 2005). Some techniques to decrease these kinds of losses include increasing the cell temperature, pressure, concentration of reactants, and the roughness of the electrode surface. Further techniques include using more advanced catalysts, and using oxygen instead of air (Barbir, 2005, Ghadamian and Saboohi, 2004, Kazemini, 2001).

Williams et al. (2004) studied optimal cathode stoichiometry with dry operation for PEMFC. They illustrated that the optimum cathode stoichiometries were 3, 2.5, 2, 1.5, and 1.5 for the cell temperature of 60, 65, 70, 75, and 80^{o}C at constant anode stoichiometry (1.3), respectively (Williams et al., 2004). Since these tests were done under dry operation, the optimum region when supplying the humidified inlet gases must be different and needs to be examined.

The relationship between the air flow and the humidity of the membrane affecting the fuel cell performance was explained by Yan et al. (2006). When a low air flow rate was supplied, the humidity at the membrane increased. When a high air flow rate was supplied, the rate of water removal and the availability of oxygen at the cathode membrane increased, and the fuel cell performance improved (Yan et al., 2006).

A pseudo-three-dimensional model developed by Natarjan and Nguyen (2003) explained the effect on the distribution of the gas phase reactant species with stoichiometric flow rate. When the air flow rate increases, the evaporation capacity is increased and the point of saturation is pushed further down the channel and the oxygen concentration along the channel is more uniform and close to the inlet values resulting in better performance (Natarajan and Nguyen, 2003).

As seen from the above literature review, stoichiometric flow rate at the cathode has been studied (Williams et al., 2004, Yan et al., 2006, Natarajan and Nguyen, 2003), but the stoichiometric flow rate variation at the anode is also worthy of studying. The performance associated with the reagent stoichiometric ratio and the desired current (I_0) starting stoichiometric flow rate, the effect of operating temperature, and the relationship

between quantity of air used at the cathode and cell performance are investigated in this study.

2.1.3 Temperature Effect

Like other fuel cells, the polymer electrolyte membrane fuel cell (PEMFC) has an operating temperature range (50~120^{o}C). At the higher temperatures, there are some advantages: better heat rejection, enhanced water management, and increased conductivity. Also, high temperature PEMFC technology can achieve near emission free power for both stationary and mobile applications (Andresen, 2003). Commercially used Nafion-type membranes, however, have some shortcomings: high cost, inadequate properties above 100^{o}C, and the performance of PEMFC degrades rapidly for temperatures above about 100^{o}C (Savinell and Payer, 2001, More, 2004). High operating temperature, high proton conductivity, low gas permeability, high durability with long life cycle and low internal resistance are targets for developing a better material for the MEA. The operating temperature, therefore, is one of the important factors that effect the fuel cell performance.

The reason why temperature is an important issue in fuel cell markets, especially for automobile applications, is that pure hydrogen gas is explosive. Due to the technical difficulty of on-board storage and refueling, hydrogen-rich reformate fuel by several reforming processes is a realistic option for supplying fuel but it contains carbon monoxide as a product, which is detrimental to the MEA. Higher temperature operation significantly alleviated the fuel cell performance loss due to CO poisoning (Jiang et al., 2006).

Fuel cell performance generally increases with increasing operating temperature up to a particular temperature. This temperature effect depends on the characteristics of the fuel cell, owing to more water vapor presence, even though reactants concentration or partial pressure decreased (Qi and Kaufman, 2002b). Another simulation model illustrated that increasing temperature leads to more water removal and this effect is easily achieved at higher current density (Shan and Choe, 2005). Coppo et al. (2006) examined the temperature effect on the three loss regions: activation loss region, ohmic loss region and mass concentration loss region. When temperature increases, it leads to an increase in the kinetic parameters and reduces the concentration term since the oxygen mass fraction decreases and more water is generated in the activation regime (Coppo et al., 2006). Increasing temperature, the cathode activation over-potential decreases, and this results in good efficiency (Coppo et al., 2006). For the ohmic loss region, since membrane conductivity and diffusion coefficient of dissolved water are strong functions of temperature, increasing temperature decreases the high resistance to electro-osmotic drag and water back diffusion (Coppo et al., 2006).

2.1.4 Air-Breathing PEM Fuel Cell

The air-breathing polymer electrolyte membrane fuel cell stack was evaluated under different environmental conditions by Chu and Jiang (1999). They indicated that the proper operating temperatures for the air breathing PEMFC stack would be from 20^{o}C to 40^{o}C, and the appropriate humidity would be 30% relative humidity or higher (Chu and Jiang, 1999). Only one case (at 5^{o}C) below 20^{o}C was studied in their research.

An application as a portable field generator for the dismounted soldier using air breathing proton exchange membrane fuel cells was introduced by Moore et al. (2002). Air breathing proton exchange membrane fuel cells in combination with advanced hydrogen generation technologies and possessing high energy densities have been demonstrated to be viable alternatives for batteries (Moore et al., 2002).

Li et al. (2003) studied the free-convection heat and mass transport for a PEM fuel cell. They found that there was a big drop of power density beyond the maximum point when the free-convection mode was adopted for PEM fuel cells (Li et al., 2003). At low current densities, the fuel cell performance did not show any significant difference between forced air convection and free convection (Li et al., 2003). The orientation of the cathode surface was shown to be important if upward orientation was selected, there was a 10% performance increase (Li et al., 2003).

Natural convection phenomena and the concentration losses were strong factors affecting the performance of air-breathing PEMFC as reported by Ying et al. (2005). At high humidity, the performance of the air-breathing PEM fuel cell increased, but appeared to be unstable (Ying et al., 2005a). In another paper, the channel width effect on the performance of the fuel cell was studied. Among three cases (2 mm, 3 mm, 4 mm), the case having 3 mm width had the best performance using a coupled 3D mathematical model simulation (Ying et al., 2005b).

The use of a thin copper foil with conductive coating for the anode current collector was introduced by Jaouen et al. (2005). Three geometries for the cathode current collector with an active area of 2 cm^2 were evaluated in a complete passive mode except

for the controlled flow of hydrogen. The peak power obtained was around 250 ~ 300 mW/cm^2 with air and pure H_2 (Jaouen et al., 2005).

Jeong et al. (2006a) studied the effects of cathode open area on cell performance. Four different cathode open areas were selected; 52, 64, 77, 92%. When the open area increased, open circuit voltage (OCV) was lowered from 0.9 to 0.84 volts because of a mixed potential at the cathode caused by hydrogen crossover and the low activity of the electrode by low ionic conductivity in the electrode (Jeong et al., 2006a). At low current densities, the greater the cathode open area, the less the cell performance was achieved due to faster water evaporation and higher in-plane electrical resistance (Jeong et al., 2006a). At high current densities, the improved mass transport of oxygen from the atmosphere to the cathode resulted in increased cell performance; whereas, the case with the largest open area (92%) did not show the fast voltage drop at high current densities, but had lower performance due to higher in-plane electrical resistance than other two cases (64% and 77%) (Jeong et al., 2006a). Effects of the relative humidity of the atmosphere were investigated, but only one temperature (at 35^{o}C) was studied (Jeong et al., 2006a).

Their recent paper (Jeong et al., 2006b) shows the effects of the cathode catalyst loading and the GDL (gas diffusion layer) structure on cell performance. When the cathode catalyst loading increased from 0.3 to 1.6 mg/cm^2, the cell performance was improved significantly up to a Pt loading of 0.6 mg/cm^2 and increased slightly because of increase in mass transport resistance (Jeong et al., 2006b). Among the four different GDL thicknesses (100, 190, 280, and 370 μm), the case of 280 μm showed the best per-

formance since water evaporation can be reduced while the mass transport limitation increased (Jeong et al., 2006b).

Fabian et al. (2006) investigated the effect of scan rate: (which is voltage variation (increase/decrease) at the fixed time interval), GDL temperature, the effects of ambient temperature/humidity, and the role of temperature on cell performance. Reverse scan method compared to the forward scan and having more interval time between the scans leads to better performance (Fabian et al., 2006).

A micro fuel cell with an active area of 0.75 cm^2 using air-breathing was evaluated by Min et al. (2006). The maximum power density was only 90 $\mu W/cm^2$ and power density deteriorated gradually as test time passed due to flooding by water generated at the cathode. (Min et al., 2006)

A cathode channel structure consisting of parallel rectangular channels with a vertical orientation was studied for natural convection of the air supply (Mennola, 2004). The current distribution measurement system was used for this research and showed that the flooded region expanded downward in the channel when the relative humidity of air was increased (Mennola, 2004). The effect of the variation of ambient humidity on flooding was small at low over-potential (Mennola, 2004).

In summary, the previous studies (Chu and Jiang, 1999, Moore et al., 2002, Li et al., 2003, Ying et al., 2005a,Ying et al., 2005b, Jaouen et al., 2005, Jeong et al., 2006, Jeong et al., 2006b, Fabian et al., 2006, Min et al., 2006, Mennola, 2004) for air-breathing PEM fuel cell have attempted to determine the proper operating temperature/relative humidity, the performance difference according to the orientation of the fuel

cell, the channel width's effect, the effects of the cathode open area, catalyst loading effect, and GDL thickness' effect. The lowest temperature to operate the air-breathing PEM fuel cell, the effect of the low field depth, and the effect of the relative humidity for various temperatures will be studied (see section 5).

2.2 Studies of PEMFCs Stacks

2.2.1 PEMFC Stack Model

Table 2-1 lists two studies of PEMFC stacks. Modeling was done first by Lee and Lalk (1998). Empirical equations were developed then by Jiang and Chu (2001). Complex numerical modeling is excluded in this review.

Table 2-1 Studies of PEMFC stack models.

	Authors	Year	Cell Numbers	Active Area (cm^2)	Main Topic	Find/Goal
1	Lee and Lalk	1998	4	50	Model developed	Mathematical models developed by authors predicts fuel cell stack behavior correctly
2	Jiang and Chu	2001	42	18	Empirical equations developed	The effect of parameters of the empirical equations were analyzed with various experiments

To study the fundamental thermal-physical behavior of a fuel cell stack for any operating and design configuration, mathematical models using the modeling methodology was introduced by Lee and Lalk (1998). Although this model did not investigate the microscopic electrochemistry of the stack, such a model would be helpful to investigate fuel cell power system. An experimental investigation was conducted to validate the model. A triple serpentine 4 cells with an active area of 50 cm^2 was used for the investi-

gation (Lee and Lalk, 1998). The platinum loading was 0.4 g/cm^2 and 1.4 g/cm^2 for the anode and cathode, respectively, and a Nafion® 112 membrane was used. Two operating points (15 amps and 25 amps) were chosen for verification. The majority of the model for both operating points was within the uncertainty of the variable measured. This modeling would be useful to a design engineer who is interested in optimizing system performance of a fuel cell stack.

Jiang and Chu (2001a) developed several empirical equations to describe the experimental stack temperature-time and the stack voltage-time curves for PEMFC stacks, which had 42 cells in the stack and each cell had active electrode area of 18 cm^2, at constant discharge. The stack voltage for a fuel cell stack can be described as follows (Jiang and Chu, 2001a);

$$E = E_0 - E_{act} - E_{ohmic} - E_{mass} \tag{3.1}$$

$$E = E_0 - b\log(i) - (R + \Delta R)i - E_{mass} \tag{3.2}$$

where, E_0 (V) is the open circuit voltage, E_{act} (V) is the activation loss, E_{ohmic} (V) is the ohmic loss, E_{mass} (V) is the mass concentration loss, b is the sum of Tafel slopes (Tafel, 1905) of all single cells assembled, R is the ohmic resistances, and ΔR is the incremental value of R because of temperature and relative humidity changes. Since all experiments were conducted at constant current discharge, the sum of E_0 (V) and activation over voltage can be considered as a constant, Equation (3.2) can be rewritten as

$$E = E_a - i\Delta R - E_{mass} \tag{3.3}$$

where, E_a (V) is the apparent voltage at a given discharged current and E_{mass}, $i\Delta R$ can be described as

$$i\Delta R = iB\exp[\frac{N(T-T_0)}{T_b-T_0}] \tag{3.4}$$

$$E_{mass} = iA\exp[\frac{1}{T_m-T}] \tag{3.5}$$

where, B (Ω) is a parameter to affect the rate of ohmic resistance change with stack temperature, N is a function parameter for different stack, and A (Ω) is a parameter to affect the rate of stack impedance jump at high temperature because of mass transfer. T (^oC) is the stack temperature at any time, T_0 (^oC) is the ambient temperature, and T_b (^oC) is the stack temperature at a steady state with the ambient. Equation (3.3) can be rewritten as

$$E = E_a - iA\exp[\frac{1}{T_m-T}] \pm iB\exp[\frac{N(T-T_0)}{T_b-T_0}] \tag{3.6}$$

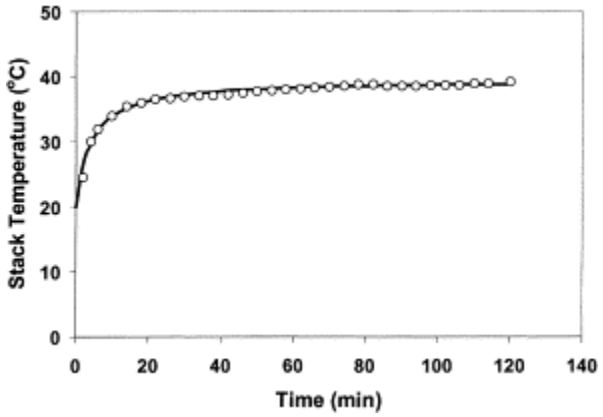

Figure 2-1[*] Variation of stack temperature vs. time for a PEMFC stack at constant current (1.5 A) and ambient temperature of 20°C. The points and line were obtained from experimental and calculated data, respectively. Calculation parameters: T_0=20°C, T_b−T_0=19.5°C and S=4.0 min (Jiang and Chu, 2001a).

* Reprinted with permission from "Voltage-time behavior of a polymer electrolyte membrane fuel cell stack at constant current discharge" by Jiang, R. and Chu, D., 2001. *J. Power Sources*, 92, 193-198, Copyright 2001 by Elsevier Limited.

Figure 2-1 shows the temperature-time curve at constant current discharge (1.5 amps) and at ambient temperature of 20^{o}C by Jiang and Chu (2001a). The stack temperature started increasing rapidly at the beginning (~ 20 minutes), and maintained around 38^{o}C for the rest of the test. Because inlet gases were not heated up to be supplied to this fuel cell stack, this temperature increase came from the generated heat owing to the electrochemical reaction.

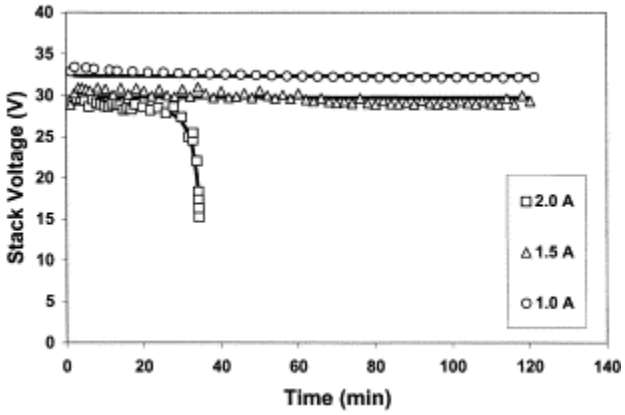

Figure 2-2[*] Constant current discharge performance of a PEMFC stack at ambient temperature of 20°C. The points and lines were obtained from experimental and calculated data, respectively (Jiang and Chu, 2001a).

Figure 2-2 shows voltage-time curves at three different constant discharged currents (1.0 amp, 1.5 amps, and 2.0 amps). When the discharged current was set to 2.0 amps, the voltage dropped rapidly in less than 40 minutes. Even though the stack was humidified with water stream, the voltage dropped for the 2.0 amps case. This may have been due to insufficient water supply, mass concentration loss, or insufficient assembled pressure.

Figure 2-3 shows voltage-time curves at two different constant ambient temperatures (20°C and 30°C). Increasing the ambient temperature leads to an increase of stack temperature. Therefore, proton conductivity must increase and better performance might have been expected. However, this result shows the reverse behavior. In the experimental section, the authors stated that the stack was humidified with a water stream, but the humidification level was not mentioned anywhere in the paper. Because the membrane type, the catalyst coating information about the MEA, and the inlet gas supply temperature were not specified, it was hard to understand all the experimental results, and specifically, the voltage-time behavior at constant discharged current.

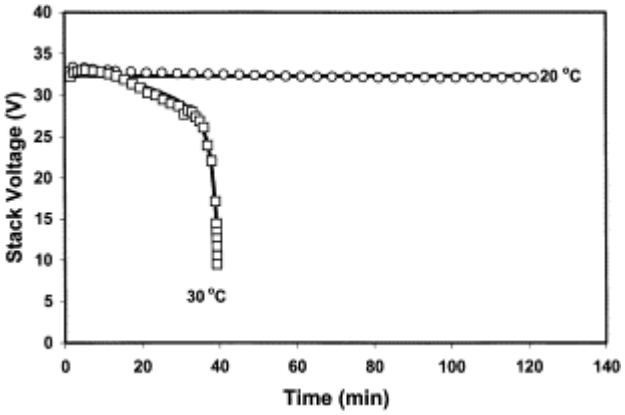

Figure 2-3* Constant current discharge (1.0 A) performance of a PEMFC stack at different ambient temperatures. The points and lines were obtained from experimental and calculated data, respectively (Jiang and Chu, 2001a).

2.2.2 Experiments Testing Membranes for the PEMFC Stack.

Table 2-2 shows a summary of previous studies on testing membranes for PEMFC stacks. Choi et al. (1998) introduced an "internal humidifier" which supplied water and reaction gases flow on opposite side of the membrane. Water permeated

* Reprinted with permission from "Voltage-time behavior of a polymer electrolyte membrane fuel cell stack at constant current discharge" by Jiang, R. and Chu, D., 2001. *J. Power Sources*, 92, 193-198, Copyright 2001 by Elsevier Limited.

through the membrane, and the reaction gases were humidified by passing through the internal humidifier. Using this internal humidifier, selecting a membrane with low cost and good water permeability was studied. Three different membranes, which were Nafion® 115, ultra-filtration membrane, and reverse-osmosis (RO) membrane, were selected and investigated.

Table 2-2 Studies of PEMFC stack for testing membrane.

	Authors	Year	# Cell	Area (cm^2)	Main Topic	Find/Goal
1	Choi et al.	1998	5	50	Membrane tested	Using internal humidifier, gas and water permeability of several membranes were measured. Among them, a low-cost ultra filtration membrane shows better characteristics
2	Chu and Jiang	1999	30	60	Various membranes tested	Different humidifies and temperatures for 30 cell stack and various membranes were evaluated.
3	Bonville et al.	2005	4	300	Higher temperature PEMFC stack	This stack operated at 120^oC at ambient pressure and provided a cell voltage in excess of 0.5 volts at a current density of 400 mA/cm^2
4	Hu et al.	2006	60	100	Catalyst-coated membrane method was used for 10 kW	CCM (catalyst-coated membrane) had a higher Pt utilization compared to the Hydrophobic method

Figure 2-4 shows the polarization curves with external humidifier, UF, RO, and Nafion® 115 membrane. The case using the external humidifier shows the highest performance among them, but not significantly. The RO membrane and Nafion® 115 membrane showed almost the same performance as the UF membrane. However, when it's operated at high current density, the cell voltage dropped sharply since two membranes (RO and Nafion® 115) have a poor water permeation flux having a lower stability than the UF membrane (Choi et al., 1998). Not enough information was presented to fully

understand the performance of the "internal humidifier". Also, the performance change after long time operation and the humidity level change after using the internal humidifier were not provided.

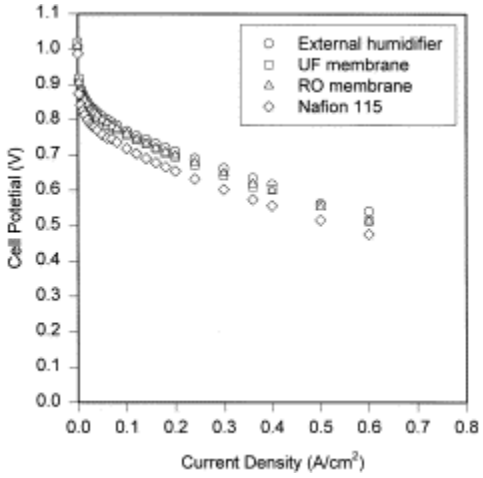

Figure 2-4* Comparison of cell performance for a stack with an external humidifier or with an internal humidifier using Nafion 115, UF, RO membranes at 50°C (Choi et al., 1998).

The self-humidifying PEM stack, which had 30 cells, with an active area of 60 cm^2 was evaluated at different humidities and temperatures by Chu and Jiang (1999b). The air was supplied to the cathode by an electric fan and the environmental temperature and relative humidity were controlled by the environment chamber. The performances of various Nafion membranes (105, 112, 115, and 117) were compared at different temperatures for the single cell. The long-term performance of the stack and the water production were measured. Among them (Nafion membranes (105, 112, 115, and 117)), Nafion 112 provided the best performance.

* Reprinted with permission from "A study of the internal humidification of an integrated PEMFC stack" by Choi, K., Park, D., Rho, Y., Kho, Y., and Lee, T., 1998. *J. Power Sources*, 74, 146-150, Copyright 1998 by Elsevier Limited.

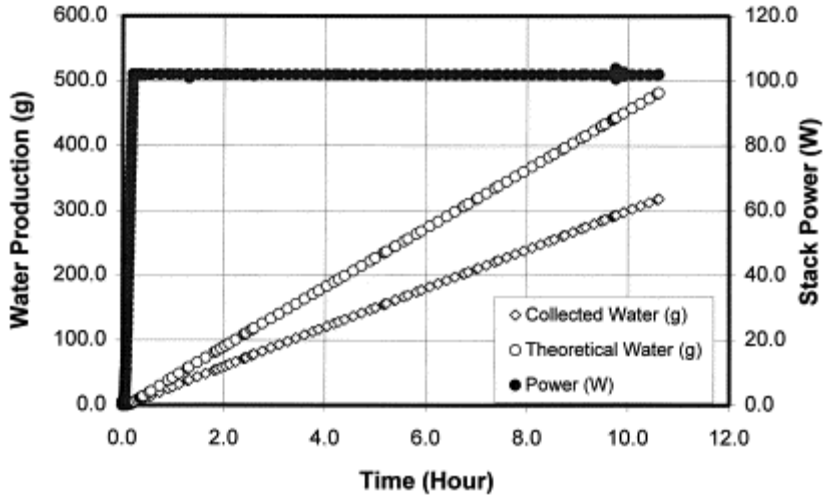

Figure 2-5* Water production during a constant power discharge of the 100 W PEMFC stack. The power was increased gradually at the beginning to 100 W, then kept constant (Chu and Jiang, 1999b).

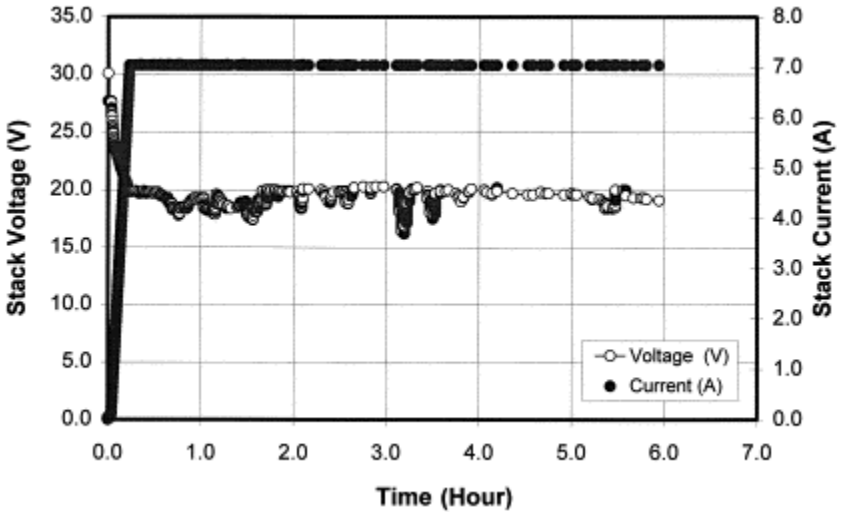

Figure 2-6* Constant current discharge performance of the 100 watt PEMFC stack. The current was increased gradually at the beginning, then kept constant (Chu and Jiang, 1999b).

Figure 2-5 shows the water production during constant power discharge at 100 watts for 10 hours by Chu and Jiang (1999b). Collected water was 34% less than the theoretical water that should have been generated. Since cooling and oxidant fans were

* Reprinted with permission from "Comparative studies of polymer electrolyte membrane fuel cell stack and single cell" by Chu, D. and Jiang, R., 1999, *J. Power Sources*, 80, 226-234, Copyright 1999 by Elsevier Limited.

used, some water was evaporated and blown into the environment, some was in the reaction, and some remained in the flow fields. This was the first experiment to measure the collected water from the fuel cell reaction, experimentally. This method will be used for studying the water transport in a PEM fuel cell (see section 6).

Figure 2-6 shows the plot of voltage versus time of the PEMFC stack at a constant current discharge of 7.0 amps for 6 hours (Chu and Jiang, 1999b). At constant current 7.0 amps, the voltage had some fluctuations for the first 4 hours, and then after this time, the voltage remained more constant at around 20 volts. Electrode activation, self-humidifying, heat-exchange, mass-transfer, and many factors affected the performance of the 30 cell PEMFC stack.

The membrane with a composite of polytetrafluoroethylene (PTFE), Nafion, and phosphotungstic acid was developed to operate at high temperature by Bonville et al. (2005). The procedure for developing the membrane, the catalyst layers, the gas diffusion layers, and the complete stack assembly were illustrated. The stack obtained a performance near 0.6 volts at 400 mA/cm^2 current density at 120^oC and ambient pressure with 35% relative humidity. However, an important factor for high temperature membrane, endurance verification, was not done in this research.

Hu et al. (2006) studied a PEM fuel cell with 60 cells and an active area of 100 cm^2. Before assembling a stack, they found some difficulties: (1) the graphite bipolar plate was very fragile, (2) the Nafion membrane wrinkled easily, (3) the thickness of the gas diffusion electrode should have been uniform, and (4) a problem with the sealing groove. It was not illustrated how they solved these issues, but it looks like that these

issues usually occur when assembling a fuel cell stack. In this study (Hu et al., 2006), a catalyst-coated membrane (CCM) method was used, instead of a hydrophobic method. This method has advantages such as a lower Pt loading with higher utilization efficiency, a closer contact between the membrane and catalyst layer to prevent delamination from flooding. Figure 2-7 shows the performance increase of the CCM method over the hydrophobic method. This performance increase was because the H_2 desorption peak of the CCM method was higher than that of the hydrophobic method due to bigger hydrogen adsorption on the catalyst surface.

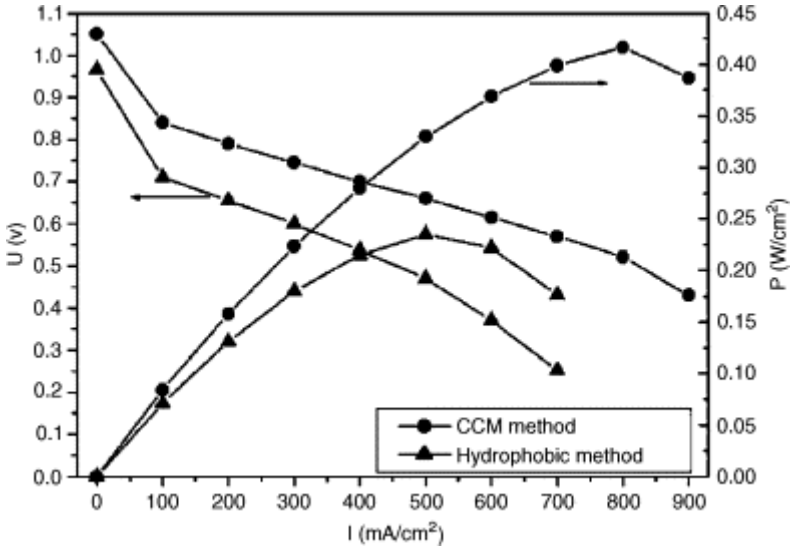

Figure 2-7* Performance of single cells using different methods for the fabrication of the catalyst layer (Hu et al., 2006).

Figure 2-8 shows the power as a function of current at different air utilizations. Air utilization can be calculated by

* Reprinted with permission from "A 10 kW class PEM fuel cell stack based on the catalyst-coated membrane (CCM) method" by Hu, M., Sui, S., Zhu, X., Yu, Q., Cao, G., Hong, X., and Tu, H., 2006. *Int. J. Hydrogen Energy*, 31, 1010-1018, Copyright 2006 by Elsevier Limited.

$$\eta = \frac{V^T}{V^A} \tag{3.7}$$

where V^T, V^A, and η represent the theoretical air consumption, the actual air consumption, and the air utilization, respectively. As shown in Figure 2-8, the performance of 10 kW stack increases with decreasing air utilization, which has a maximum power of 10.9 kW at 325 amps (at 0.3 W/cm^2 power density). Air is a common species, increasing air supply to the fuel cell stack increased cell performance shown in Figure 2-8. There must be a maximum range to increase a fuel cell performance. This is studied in the current work (see section 5).

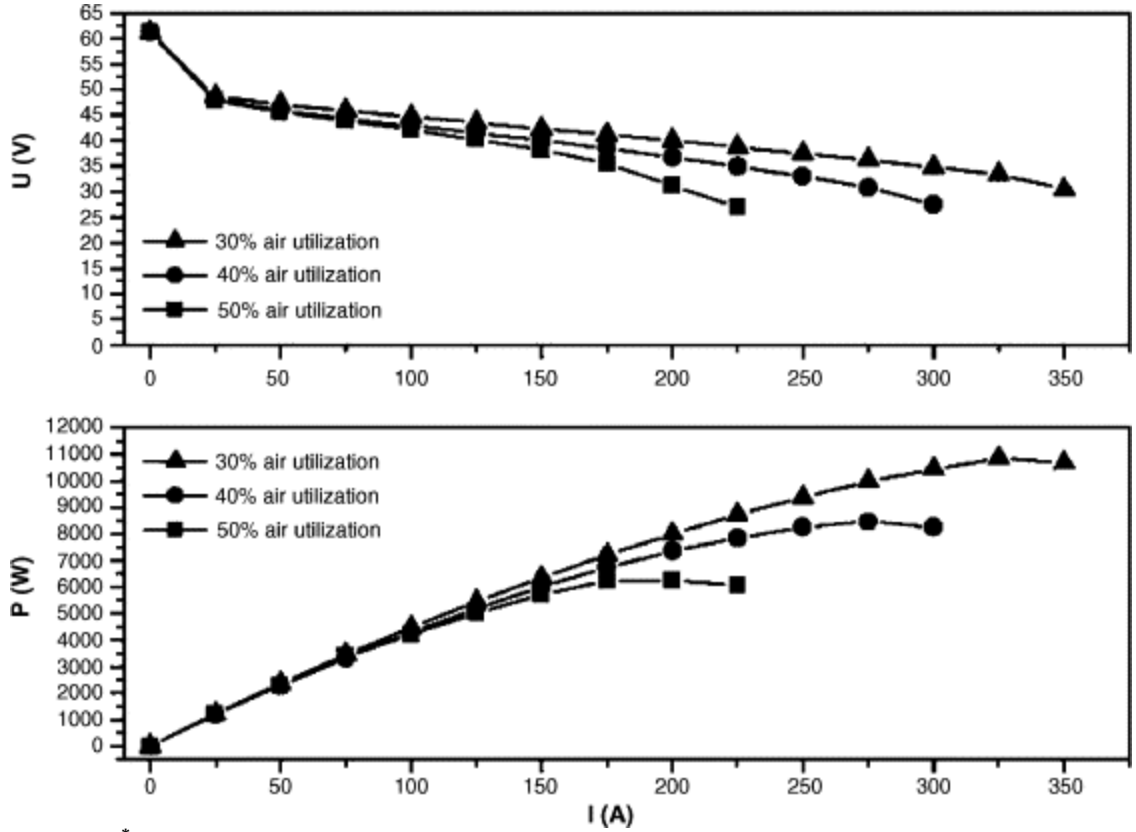

Figure 2-8* Performance of the 10 kW class PEM fuel cell stack at different air utilizations (Hu et al., 2006).

* Reprinted with permission from "A 10 kW class PEM fuel cell stack based on the catalyst-coated membrane (CCM) method" by Hu, M., Sui, S., Zhu, X., Yu, Q., Cao, G., Hong, X., and Tu, H., 2006. *Int. J. Hydrogen Energy*, 31, 1010-1018, Copyright 2006 by Elsevier Limited.

2.2.3 Development of the PEMFC Stack's Plate

Table 2-3 lists studies developing plate material for the PEMFC stack. The graphite plate has been used for PEMFC stack and single cell. The needs of having a light fuel cell stack and low cost motivate different types of plates for the PEMFC stack.

Pressure drop in flow fields and cooling flow fields, flow distribution in a cathode flow field, and fabrication and testing of a fuel cell stack, were studied by Murphy et al. (1998) using 8 cells with an active area of 125 cm^2. To develop low-cost light weight high power density PEM fuel cell stack, they used nickel foam flow field and titanium flow filed. Pressure drop was measured with four different back pressures (0, 12, 16, and 20 psi). The highest pressure drop was found at the lowest operating back pressure (0 psi). Although gas viscosity and gas velocity affected the pressure drop together, the reduction in pressure drop by reduced velocity exceeded the increase produced by the increased gas density (Murphy et al, 1998).

Table 2-3 Studies of developing the plate of PEMFC stack.

	Authors	Year	Cell Numbers	Active Area (cm^2)	Main Topic	Find/Goal
1	Murphy et al.	1998	8	125	Stack fabrication demonstrated	Metal plates, instead of graphite plates, could reduce the size of the stack
2	Cho et al.	2005	12	240	TiN-coated 316 stainless steel bipolar plates	Develop corrosion-resistant and low-cost metallic bipolar plates for PEMFC
3	Yan et al.	2006	16 & 130	270	Development of low cost and low eight bipolar plate	The contact resistance of the bipolar plate was investigated and the electrochemical performance of the fuel cell stacks were tested

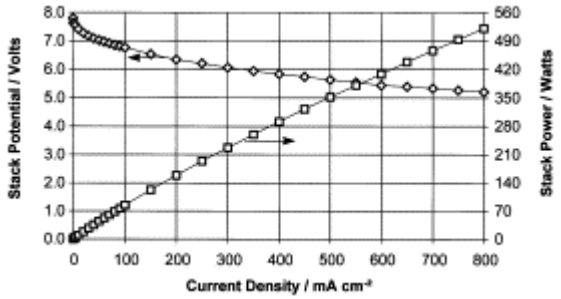

Figure 2-9* Performance of an eight-cell, 125 cm^2 active area stack. The data was collected while operating at an M&E temperature between 62 and 64°C, a reactant gas pressure of 15 psig with both gases humidified to a dew point of 27°C, and air supplied at four-fold stoichiometry. Potential reads to the left axis, and power to the right axis (Murphy et al., 1998).

Figure 2-9 shows the polarization and power curve as functions of current density by Murphy et al. (1998). The operating temperature was between 62°C and 64°C and the reactant gas pressure was 15 psig with both gases humidified to a dew point of 27°C (less than 30% relative humidity). Air was supplied with four stoichiometry. This stack produced 521 watts of power at a current density of 800 mA/cm^2 and a stack voltage of 5.21 volts. Using the metal plates, this fuel cell stack obtained high performance. This could be one of the options to reduce the weight and cost for a fuel cell system.

Cho et al. (2005) researched PEM fuel cell stack with 12 cells with an active area of 240 cm^2. An issue for developing metallic bipolar plates is to prevent degradation of the stack caused by corrosion of bipolar plates. This issues leads to a decrease in electrical conductivity and contamination of MEAs. Therefore, corrosion-resistant alloys should be adopted as bipolar plates of PEMFC. The corrosion-resistant metallic bipolar plate, surface of AISI 316 stainless steel was coated with TiN layer, was introduced by

* Reprinted with permission from "Low-cost light weight high power density PEM fuel cell stack" by Murphy, O., Cisar, A., and Clarke, E., 1998. *Electrochimica Acta*, 43, 3829-3840, Copyright 1998 by Elsevier Limited.

Cho et al. (2005). In their study, the performance using bare 316 stainless steel, graphite plates, and TiN-coated 316 stainless steel bipolar plates were compared.

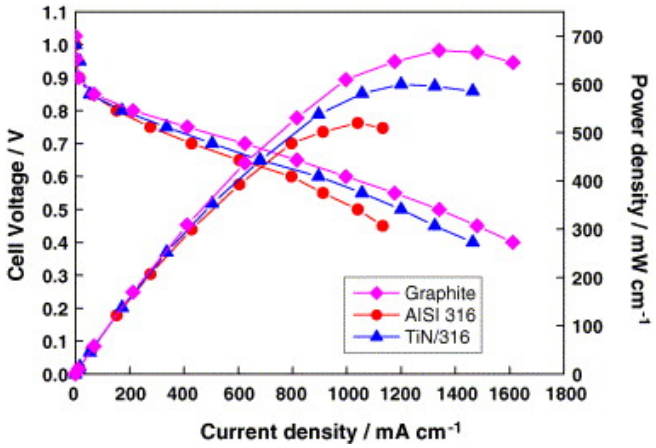

Figure 2-10* I–V curves for the single cells using graphite, AISI 316, and TiN/316 bipolar plates; operating temperature = 80 °C; operating pressure = 1 atm; $\underline{\lambda_{H2}}$ = 1.5 and $\underline{\lambda_{O2}}$ = 3 (Cho et al., 2005).

Figure 2-10 shows the voltage and power density as functions of current density of the single cells. The current density reached 996, 796, and 896 mA/cm^2 at 0.6 volts for graphite, bare 316, and TiN-coated 316 bipolar plates, respectively. Because contact resistance was higher at the metallic bipolar plates than graphite plates, which leads to lower performance.

Figure 2-11 demonstrates the performance degradation of the single cell using graphite, AISI 316, and TiN/316 bipolar plates with long-term operation. The degradation of the graphite bipolar plates was negligible for 1000 hours running. However, current density at 0.6 volts using bare 316 plates and TiN-316 coated plates decreased from 796 mA/cm^2 to 395 mA/cm^2 after 200 hours, from 896 mA/cm^2 to 598 mA/cm^2 after 700 hours, respectively (Cho et al., 2005). The performance of the TiN/316 bipolar plate was

* Reprinted with permission from "Performance of 1 kW-class PEMFC stack using TiN-coated 316 stainless steel bipolar plates" by Cho, E., Jeon, U., Hong, S., Oh, I., and Kang, S., 2005. *J. Power Sources*, 142, 177-183, Copyright 2005 by Elsevier Limited.

significantly improved compared to that of bare 316 plates, but it was still lower than graphite bipolar plates.

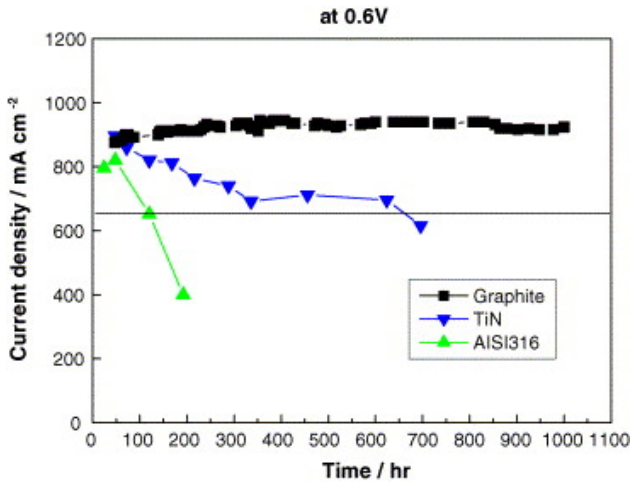

Figure 2-11* Current density measured at a cell voltage of 0.6 V during long-term operation of the single cells using graphite, AISI 316, and TiN/316 bipolar plates; operating temperature = 80°C; operating pressure = 1 atm; H_2 = 1.5 and O_2 = 3 (Cho et al., 2005).

Metal and carbon are commonly used materials for bipolar plates. As discussed by Cho et al. (2005), the advantages of metal plates are that they are less expensive and they are light weight, but they are prone to corrode. The dissolved metal ions results in the poisoning of PEM membrane and lower ionic conductivity. The graphite plate based on carbon material has excellent chemical stability in the fuel cell operating conditions. However, the materials and traditional manufacturing method which is required are expensive. An expanded graphite bipolar plate was developed by Yan et al. (2006) to overcome the handicaps of the graphite bipolar plate. The performance of 1 kW and 10 kW PEMFC stacks were tested, and cost of the expanded graphite bipolar plate was calculated.

* Reprinted with permission from "Performance of 1 kW-class PEMFC stack using TiN-coated 316 stainless steel bipolar plates" by Cho, E., Jeon, U., Hong, S., Oh, I., and Kang, S., 2005. *J. Power Sources*, 142, 177-183, Copyright 2005 by Elsevier Limited.

2.2.4 Design of PEMFC Stacks

Table 2-4 shows a summary of studies related to the design of PEMFC stacks. A stack with 1.7 kW power output using 50 cells having 250 cm^2 active area was assembled and studied by Dhathathreyan et al. (1999). For a fuel cell stack (5 kW) having a single inlet and outlet, the inlet cell had its low voltage reduced to 0.4 volts compared to the average cell voltage of 0.68 volts at 200 mA/cm^2 of current density; whereas, the end cell was overloaded with produced water resulting in flooding in the electrode. To overcome this problem, they designed a 5 kW fuel cell consisted of three modules each having 1.7 kW power output by using a parallel cell configuration at both inlet and outlet cells.

Table 2-4 Studies of designing of PEMFC stack.

	Authors	Year	Cell Numbers	Active Area (cm^2)	Main Topic	Find/Goal
1	Dhathathreyan et al.	1999	9, 24, and 50	100, 200, and 250	Developing a method for electrode preparation	A 5 kW PEMFC stack consisting of three modules each having 1.7 kW power output was demonstrated and found to enhance platinum utilization
2	Jiang and Chu	2001	24	42	Stack design and performance	Three types of stack structure designs were reviewed and evaluated under various humidities and temperatures
3	Giddey et al.	2004	2, 4, 8, and 15	255	Design and assembly of 1 kW PEMFC	PEMFC stack to 1 kW capacity was constructed and operated to investigate the fuel quality issues
4	Scholta et al.	2004	70	250	Development of a 10 kW PEMFC	Stability problems were related with localized water management when operated at 70^oC and above
5	Scholta et al.	2006	50	100	Development of a stack having an optimized flow design	To optimize overall system performance, a fuel cell stack with improved flow field design and performance was developed

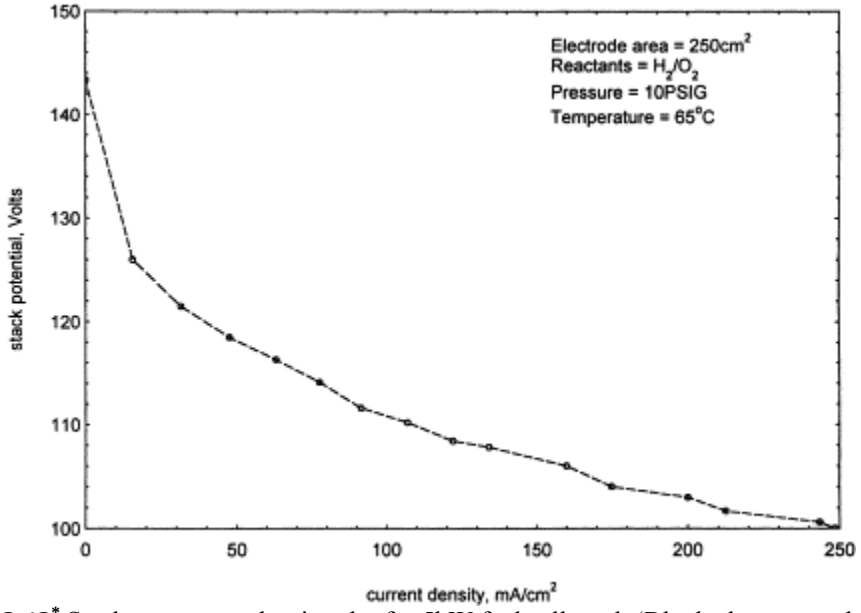

Figure 2-12[*] Stack vs. current density plot for 5kW fuel cell stack (Dhathathreyan et al., 1999).

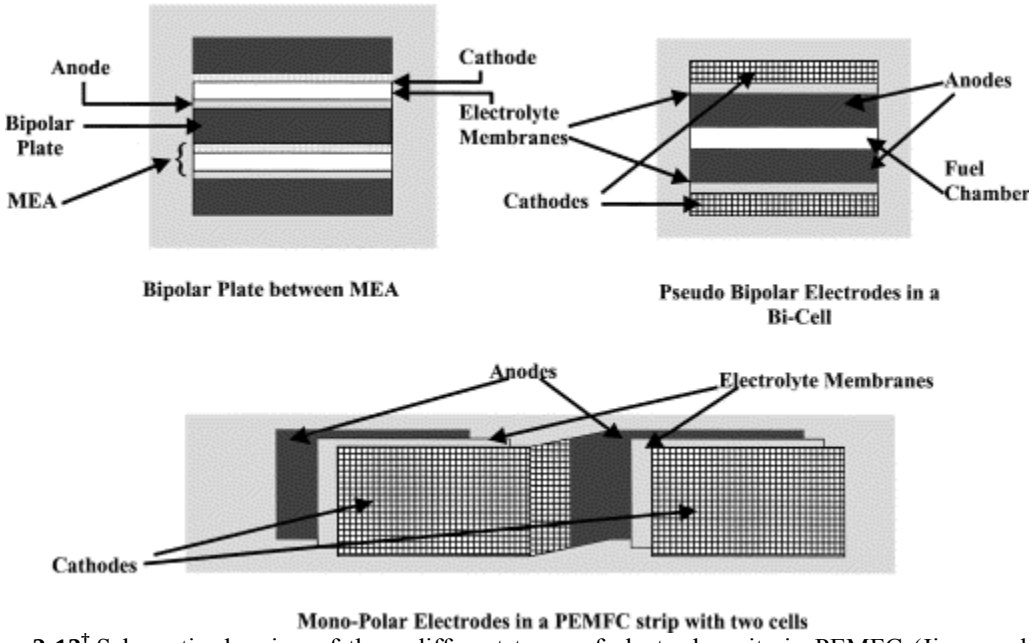

Figure 2-13[†] Schematic drawing of three different types of electrode units in PEMFC (Jiang and Chu, 2001b).

---

* Reprinted with permission from "Development of polymer electrode membrane fuel cell stack" by Dhathathreyan, K., Sridhar, P., Sasujynar, G., Ghosh, K., Velayutham, G., Rajalakshmi, N., Subramaniam, C., Raja, M., and Ramya, K., 1999. *Int. J. Hydrogen Energy*, 24, 1107-1115, Copyright of Elsevier Limited.

† Reprinted with permission from "Stack design and performance of polymer electrolyte membrane fuel cells" by Jiang, R. and Chu, D., 2001. *J. Power Sources*, 93, 25-31, Copyright 2001 of Elsevier Limited.

Figure 2-12 shows the stack voltage as a function of current density using a parallel cell configuration that had three 1.7 kW stacks connected in a series electrically to obtain power output of 5.0 kW. All results displayed only up to 250 mA/cm^2, which was relatively low current density not able to obtain the maximum performance of the fuel cell stack.

Three different stack structure designs, which are bipolar, pseudo bipolar, and mono-polar stacks, were evaluated under various humidities and temperatures by Jiang and Chu (2001b). Figure 2-13 shows the schematic of three different designs. The advantages and disadvantages of the three different stack designs are summarized in Table 2-5.

Table 2-5 Summary of characteristics of three different designs in PEMFC stacks (Jiang and Chu, 2001b).

Type	Advantage	Disadvantage
Bipolar PEMFC	Compact volume	Complex plate design
	Low internal resistance	Heat/Water/Humidity management required
	Able to operate at high pressure	High cost for material and processing
		Compressed/Pumped air is required
Pseudo-bipolar PEMFC	Easy to assembly	Need to fill fuel to each bi-cell unit separately
	Heat management is easy	
	Oxidant (air) can be provided	Need to link each bi-cell unit electrically
	from environment with an auxiliary fan	
	Low cost	
Monopolar PEMFC	Lightweight	High internal resistance
	High voltage of each strip	Unable to achieve high power
	Have largest power density by weight	Fragile
	Low cost	

The bipolar stack design was suitable for high power since it had compact volume and low internal resistance. However, heat/water/humidity management was more necessary to operate this stack design than the other designs. Failure of a single cell can lead to a loss of whole stack power. For the pseudo bipolar plate, the fuel and air should be supplied separately. High internal resistance limited the use of the mono-polar plate design to only low power and high voltage devices (Jiang and Chu, 2001b).

Giddely et al. (2004) constructed a 1 kW_e capacity PEM fuel cell stack to investigate fuel quality issues, start/stop cycling, thermal cycling, and load following capabilities. The stacks were assembled and tested with 2-, 4-, 8- and 15-cell configurations. The polarization curve of a single fuel cell stack can be represented as follows (Giddely et al., 2004)

$$E = E_0 - b\log(i) - R(i) \tag{3.8}$$

where E is the cell voltage under load (mV), E_0 is the open circuit voltage (mV), i is the current density (mA/cm^2), b is the Tafel slope (mV per decade), and R is the ohmic resistance (Ω cm^2) of the cell.

Figure 2-14 shows polarization curves of the 4 different fuel cell stacks, which have maximum power output as 140, 295, 530, and 1011 watts, respectively. The symbols represent the actual testing data recorded and the lines represent the trend line by applying the above model equation (3.8). The maximum power output, power output per cell, open circuit voltage, the Tafel slope, ohmic resistance and correlation coefficients are given in Table 2-6.

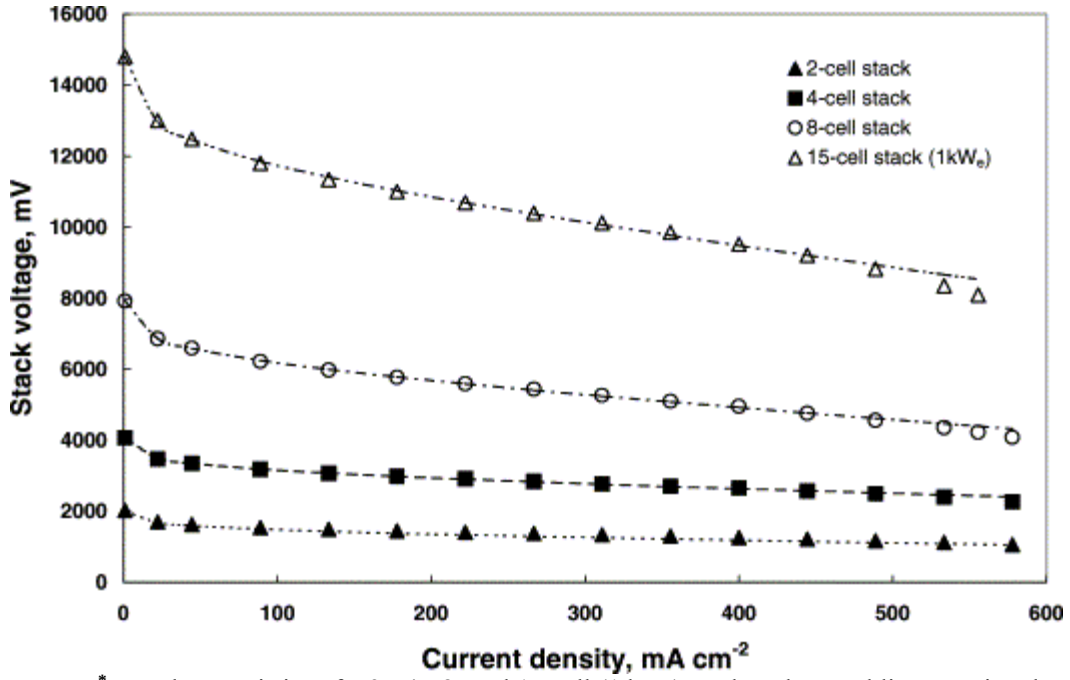

Figure 2-14[*] *V–I* characteristics of a 2-, 4-, 8- and 15-cell (1 kW_e) stacks. The trend lines passing through the data points represent the fitted model (Equation (3.8)) (Giddely et al., 2004).

Table 2-6 Operating and calculated parameters PEM fuel cell stacks of different sizes (Giddely et al., 2004).

Parameter	2 cells stack	4 cells stack	8 cells stack	15 cells stack
Maximum power output (W)	140	295	530	1011
Power output per cell (W)	70	73.7	66.2	67.4
E_o (v)	1.01	1.017	0.99	0.987
b (mV per decade)	122.7	102.7	92.1	85.9
R (Ωcm2)	0.251	0.228	0.338	0.328
Correlation coefficient	0.997	0.999	0.999	0.999

1.6 kW and 10 kW PEM fuel cell stacks were assembled and evaluated by Scholta et al. (2004). Current-voltage performance, pressure drop, gas utilization, uniformity of cell voltages, and endurance were tested.

* Reprinted with permission from "Design, assembly and operation of polymer electrolyte membrane fuel cell stacks to 1 kWe capacity" by Giddey, S., Ciacchi, F., and Badwal, S., 2004. *J.Power Sources*, 125, 155-165, Copyright 2004 of Elsevier Limited.

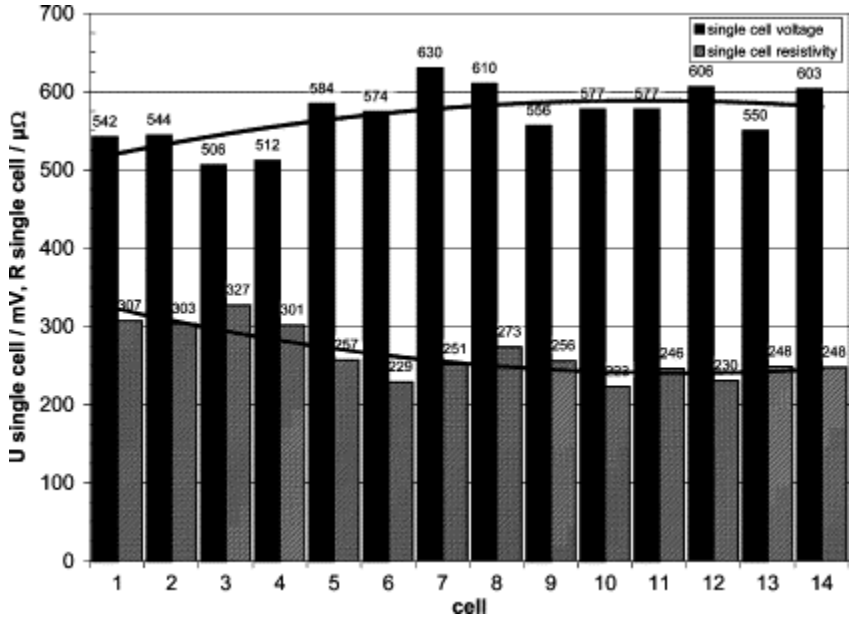

Figure 2-15* Single cell voltages and resistances for stack II at a current density of 0.6 A/cm^2 (Scholta et al., 2004).

Figure 2-15 shows the voltage and resistance distribution of a single cell, of a 14 cell stack, which was at a current density 600 mA/cm^2. Higher internal cell resistance of the first cell from inhomogeneous cell humidification within the stack lead to a small increase in cell voltage. The average cell voltage was 569 mV at a standard deviation of 35 mV.

The current-voltage characteristics of a 3 cell stack are shown in Figure 2-16 before and after 800 hours endurance test (Scholta et al., 2004). The power density of 250 mW/cm^2 was achieved at an averaged single cell voltage of 0.6 volts. After running 800 hours, the power density at 0.6 volts was degraded from 250 mW/cm^2 to 220 mW/cm^2. Stability problems were found because of localized water management

* Reprinted with permission from "Development and performance of a 10 kW PEMFC stack" by Scholta, J., Berg, N., Wilde, P., Jorissen, L., and Garche, J., 2004. *J. Power Sources*, 127, 206-212, Copyright 2004 of Elsevier Limited.

effects when operated 70°C and above. When the stack was operated at a reduced operating temperature, the decay rate was sufficiently low and stable operation was achieved.

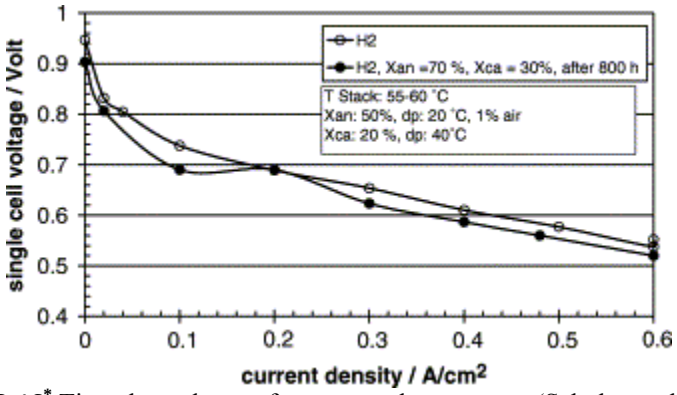

Figure 2-16[*] Time dependence of current–voltage-curves (Scholta et al., 2004).

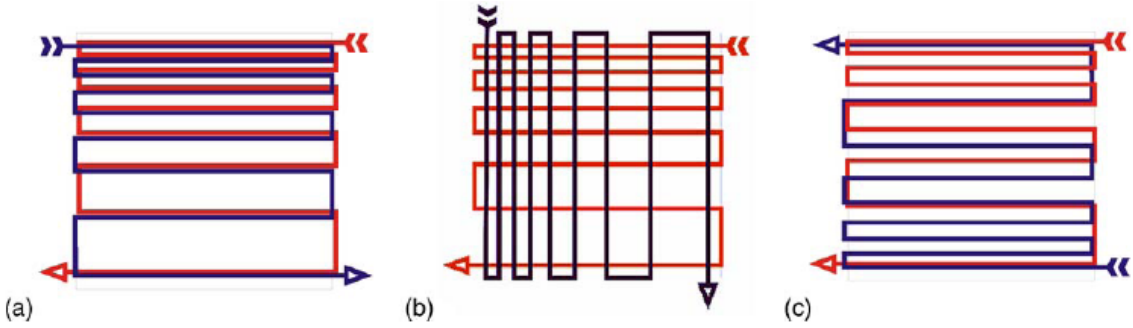

Figure 2-17[†] Flow direction schemes for: (a) co-flow, (b) cross flow and (c) counter flow (Scholta et al., 2006).

The flow field structure is one of the factors to influence the fuel cell performance. It is mainly related to water management because water is generated due to the chemical reaction in the cell. As shown in Figure 2-17, co-flow, cross-flow, and counter flow structures were tested by Scholta et al. (2006).

---

* Reprinted with permission from "Development and performance of a 10 kW PEMFC stack" by Scholta, J., Berg, N., Wilde, P., Jorissen, L., and Garche, J., 2004. *J. Power Sources*, 127, 206-212, Copyright 2004 of Elsevier Limited.

† Reprinted with permission from "Development of a stack having an optimized flow field structure with low cross transport effects" by Scholta, J., Haussler, F., Zhang, W., Kuppers, L., Jorissen, L., and Lehnert, W., 2006. *J. Power Sources*, 155, 60-65, Copyright 2006 of Elsevier Limited.

Figure 2-18 shows the dependence of cell performance on flow directions for co-flow and counter flow. The maximum power density obtained about 0.32 mW/cm^2, 0.42 mW/cm^2 for co-flow design and counter flow design, respectively. The cross flow performance was between co-flow and counter flow.

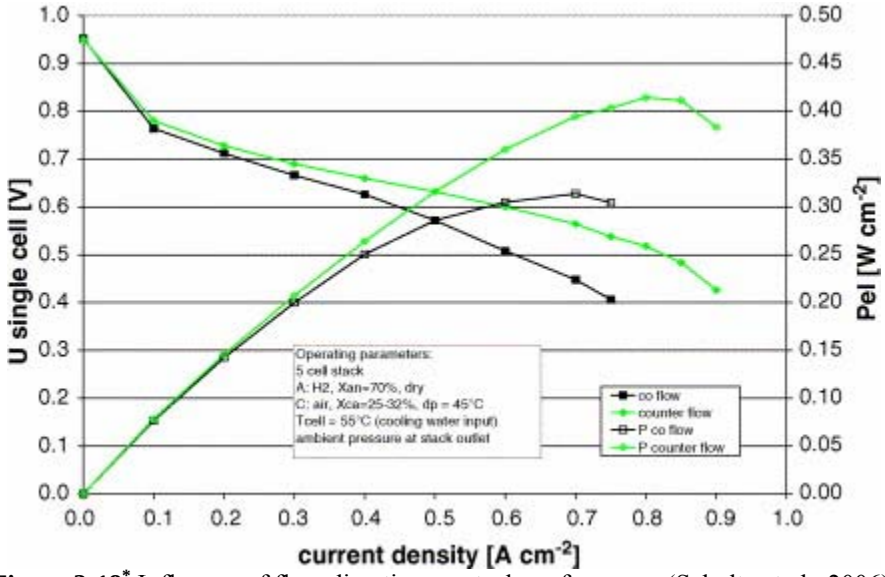

Figure 2-18[*] Influence of flow direction on stack performance (Scholta et al., 2006).

2.2.5 Parametric Studies of PEMFC Stacks

Modeling, material of bipolar plates, design of bipolar plate, and specification of the membrane were reviewed in the above sections. In this section, parametric studies for PEMFC stack will be reviewed. Table 2-7 shows the summary of the parametric studies of PEM fuel cell stacks.

A parametric study of a double-cell stack of PEMFC was studied by Hwang and Hwang (2002), which included the effect of cell operating temperature, effect of dew

* Reprinted with permission from "Development of a stack having an optimized flow field structure with low cross transport effects" by Scholta, J., Haussler, F., Zhang, W., Kuppers, L., Jorissen, L., and Lehnert, W., 2006. *J. Power Sources*, 155, 60-65, Copyright 2006 of Elsevier Limited.

point of reactants, effect of channel flow back-pressure, and effect of flow channel dimensions.

Table 2-7 Summary of parametric studies of PEMFC stacks.

	Authors	Year	#Cell	Area(cm^2)	Main Topic	Find/Goal
1	Hwang and Hwang	2002	2	25	Parametric studies	Empirical correlations were developed to describe the electrode process of the PEMFC under various operating conditions
2	Ahn et al.	2002	40	200	Performance and lifetime analysis	Maximum power of the stack was 2.89 kW and it showed a sharp performance decrease after running 1800 hours
3	Qi and Kaufman	2002	4	27.6	Performance under dry-reactant conditions	A double-path flow design enabled the dry entering gas to become hydrated by acquiring some moisture from the exiting moisture gas
4	Rodatz et al.	2004	100	204	Some critical specifications to operate large stack	Undersupply and negative voltage, leaks in membrane, overheating, and large differential pressure were typical failures when operated large PEMFC stack
5	Knobbe et al.	2004	5	16	Active gas management	After using active gas management, stack power output increased from 38.4 to 50.4 watts
6	Tanaka et al.	2005	40, 50, and 80	80, 200, 225, and 300	Development of a performance test method	To stabilize the PEMFC stack output, to clarify the operating conditions
7	Torchio et al.	2005	30	100	Experimental analysis using a statistical methodology	The cathode flow inlet temperature and the cathode flow stoichiometry shows significant positive effect
8	Philipps et al.	2006	120	Nuvera	Dynamic investigation of PEMFC in interaction with the air supply	Investigations on fuel cell stack and system efficiency in interaction with the air supply
9	Santarelli et al.	2006	20	560	Experimental analysis of cathode flow stoichiometry	Increasing in air stoichiometry caused a significant positive effect (increment) on power

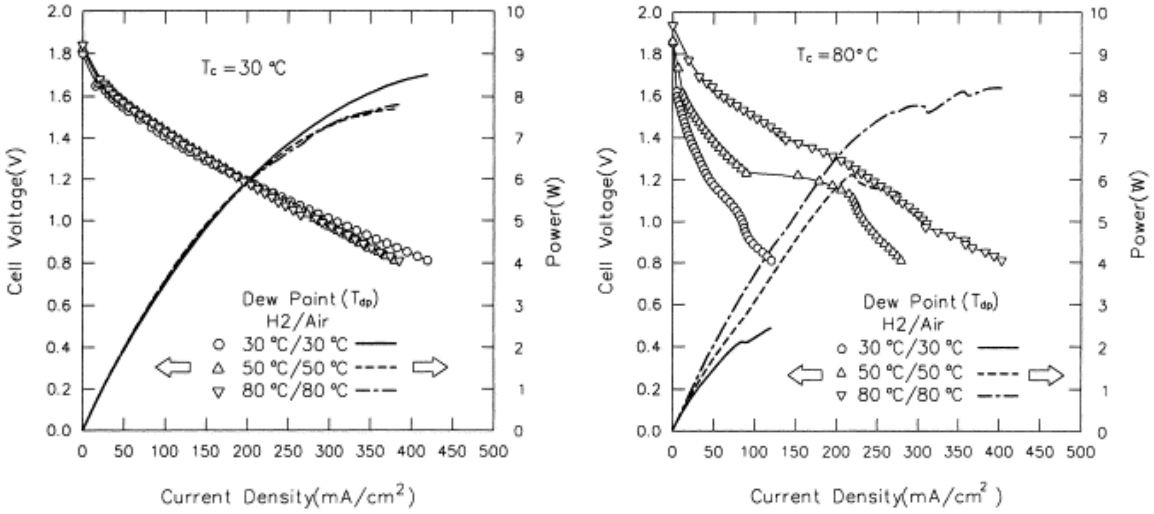

Figure 2-19[*] (a) Left picture: Effect of dew point of reactants on cell performance at cell operating temperature T_c=30 °C. (b) Right picture: Effect of dew point of reactants on cell performance at cell operating temperature of T_c=80 °C (Hwang et al., 2002).

Figure 2-19 shows the effect of dew point of reactants for two different cell temperatures (30^{o}C and 80^{o}C). When the fuel cell operating temperature was 30^{o}C, Figure 2-19 (a), the effect of the dew point of the reactants was insignificant. However, increasing the cell operating temperature to 80^{o}C caused membrane dehydration and decreased cell performance (Hwang et al., 2002).

Figure 2-20 (a) shows the effect of back-pressure of the flow field on cell performance for a cell operating temperature of T_C=80^{o}C. Increase in the back pressure of the fluid flow improved the cell performance since an increase in oxidant pressure increased the reversible cathode potential according to the Nernst equation (Hwang et al., 2002).

* Reprinted with permission from "Parametric studies of a double-cell stack of PEMFC using grafoilTM flow-field plates" by Hwang, J. and Hwang, H., 2002. *J. Power Sources*, 104, 24-32, Copyright 2002 of Elsevier Limited.

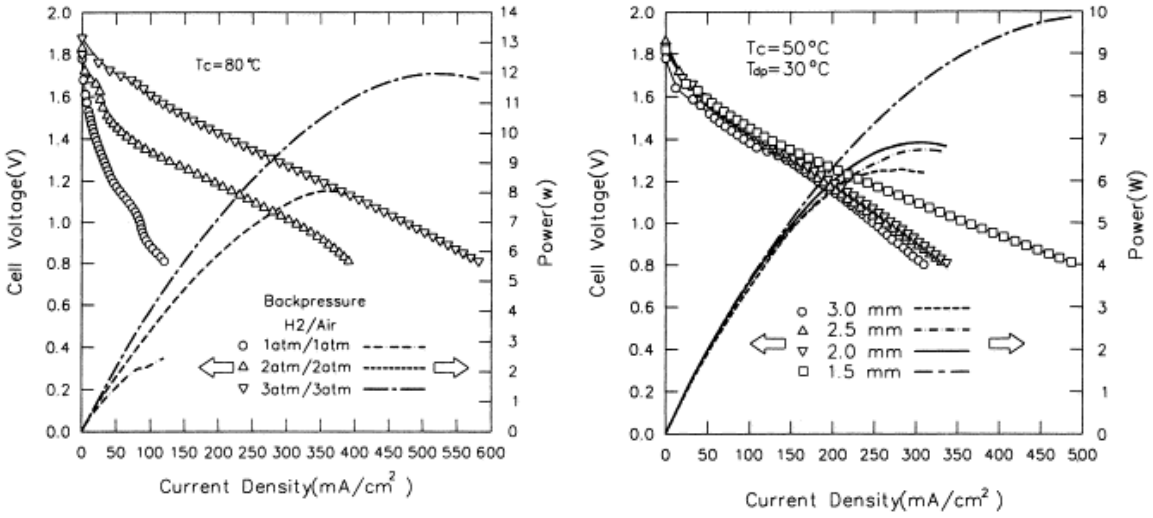

Figure 2-20[*] (a) Left picture: Effect of back-pressure of flow-field on cell performance at T_c=80 °C. (b) Right picture: Effect of channel dimensions on cell performance (Hwang et al., 2002).

Figure 2-20 (b) shows the effect of the channel dimension on cell performance. The widths varied 3.0 mm, 2.5 mm, 2.0 mm, and 1.5 mm. When the narrowest was used, the cell performance increased significantly because it minimized the diffusion pathway (Hwang et al., 2002). The channel depth effect on the performance of a fuel cell is studied in the current work (see section 5).

A counter-flow type 40-cell PEMFC stack with an active area of 200 cm^2 was investigated for its performance and life time by Ahn et al. (2002). As seen in Figure 2-21, the maximum power of the stack was 2.89 kW and 2.3 kW for oxygen and air, respectively. After running 1800 hours, the performance of the stack decreased rapidly because of the degradation of the catalyst and contamination of the polymer electrolyte membrane (Ahn et al., 2002).

---

* Reprinted with permission from "Parametric studies of a double-cell stack of PEMFC using grafoilTM flow-field plates" by Hwang, J. and Hwang, H., 2002. *J. Power Sources*, 104, 24-32, Copyright 2002 of Elsevier Limited.

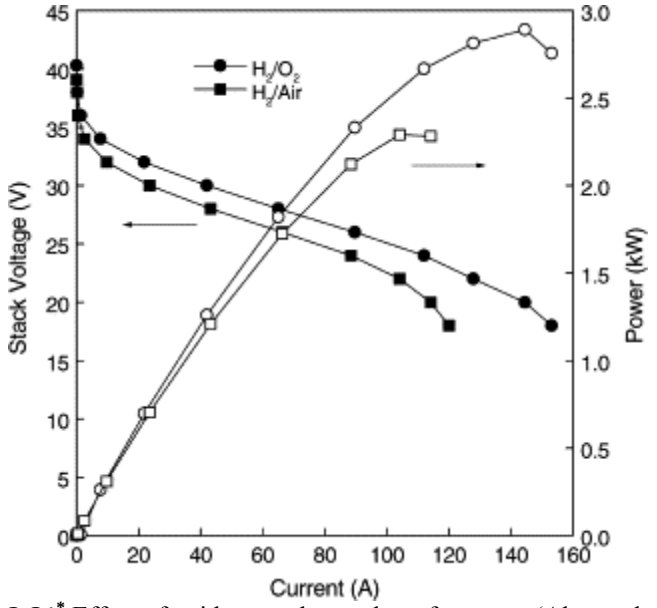

Figure 2-21[*] Effect of oxidant on the stack performance (Ahn et al., 2002).

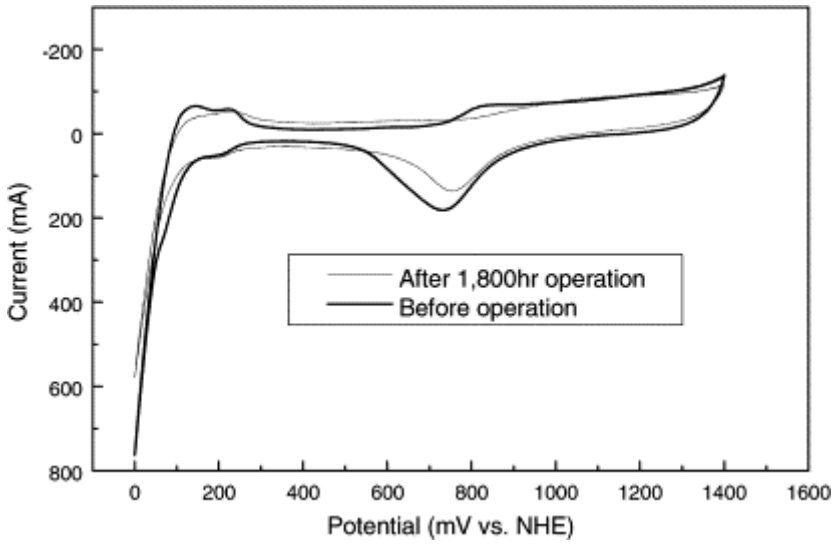

Figure 2-22[*] Cyclic voltammograms before and after 1800 hours operation. Scan rate=50 mV/s, Ca./An.=0.4/0.7 mg Pt/cm^2, Ca./An.=N_2/H_2, T=75 °C and P=1 atm (Ahn et al., 2002).

Figure 2-22 shows the cyclic voltammetry result to compare the activation area of the catalyst in the membrane before and after 1800 hours operation. Hydrogen oxida-

* Reprinted with permission from "Performance and lifetime analysis of the kW-class PEMFC stack" by Ahn, S., Shin, S., Ha, H., Hong, S., Lee, Y., Lim, T., and Oh, I., 2002. *J. Power Sources*,106, 295-303, Copyright 2002 of Elsevier Limited.

tion and hydrogen peak was decreased after operation, which the oxidation peak area was decreased around 23% after operation (Ahn et al., 2002).

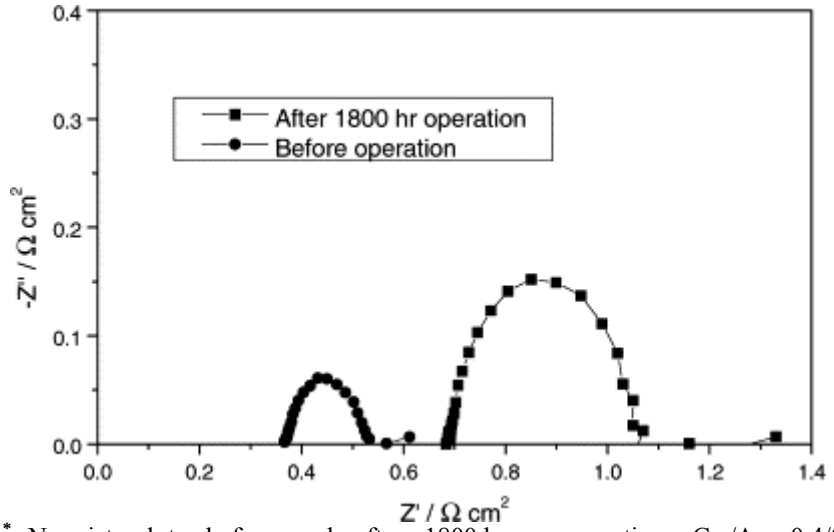

Figure 2-23 * Nyquist plots before and after 1800 hours operation. Ca./An.=0.4/0.7 mg Pt/cm^2, Ca./An.=O_2/H_2, *V*=0.8 V, *T*=75 °C and *P*=1 atm (Ahn et al., 2002).

Figure 2-23 shows the Nyquist plots of before and after 1800 hours operation to compare polarization resistance. The electrolyte resistance and the charge transfer resistance were increased 1.8 and 5.8 times, respectively, which showed that the Nafion membrane was separated with the interface of the electrode (Ahn et al., 2002). After 1800 hours operation, a significant amount of silicon was detected at catalytic layers and oxygen existed at the cathode as platinum oxide using EPMA analysis, and XRF analysis were conducted to examine coolant having various inorganic materials (Ahn et al., 2002). For the durability and life-time cycle test, ac impedance and cyclic voltammetry are useful in-situ techniques to examine the active catalyst area and resistance of the membrane.

* Reprinted with permission from "Performance and lifetime analysis of the kW-class PEMFC stack" by Ahn, S., Shin, S., Ha, H., Hong, S., Lee, Y., Lim, T., and Oh, I., 2002. *J. Power Sources*,106, 295-303, Copyright 2002 of Elsevier Limited.

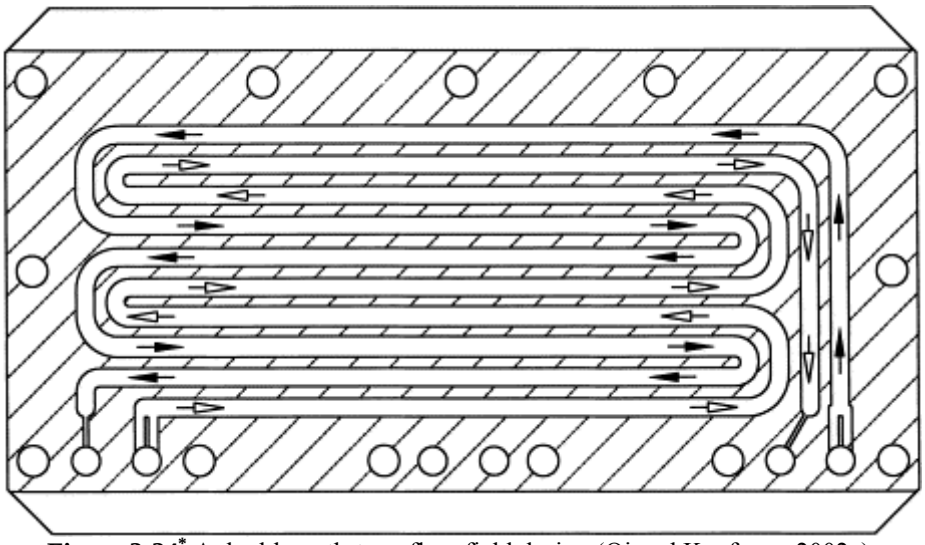

Figure 2-24[*] A double-path-type flow field design (Qi and Kaufman, 2002a).

A double-path-type 4-cell PEMFC stack with an active area of 27.6 cm^2 was investigated for its performance under dry-reactant conditions by Qi and Kaufman (2002a). This stack has two gas inlets and two gas outlets, which were adjacent with reactant flowing in opposite directions as shown in Figure 2-24. Produced water was used to hydrate the membrane and the catalyst layers that the dry entering gas was hydrated by acquiring some moisture from the exiting moist gas (Qi and Kaufman, 2002a).

Figure 2-25 shows the result after 136 hours operation. When the stack generated 6 amps for 2 hours, the stack voltage declined quickly in the beginning and stabilized at 1.7 volts (where the current was less than 1 amp), which was a proof of a drying stack. Since no humidification was added to inlet gases, the produced water was the only source for the electro-osmotic drag, which was insufficient. When no humidified gas was supplied, the current that fuel cell could discharge and maintain was limited at very

* Reprinted with permission from "PEM fuel Cell stacks operated under dry-reactant conditions" by Qi, Z. and Kaufman, A., 2002. *J. Power Sources*, 109, 469-476, Copyright 2002 of Elsevier Limited.

low current density. This design was a good approach for cases not using an external humidifier.

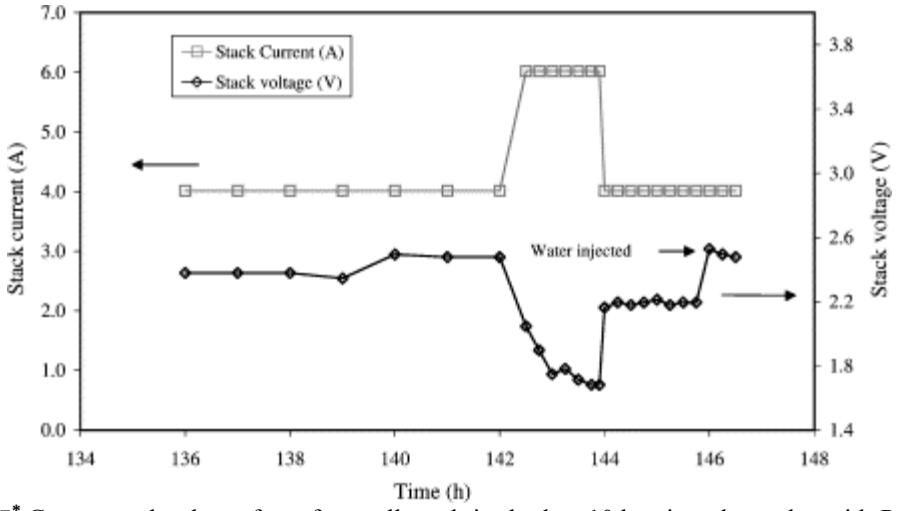

Figure 2-25[*] Current and voltage for a four-cell stack in the last 10 h using electrodes with Pt loading of 0.21 mg/cm^2, Nafion 1135 membrane (Qi and Kaufman, 2002a).

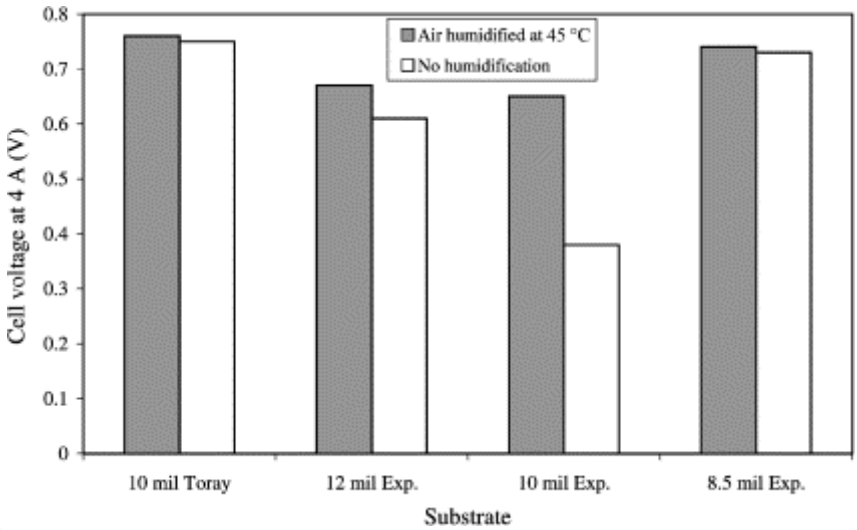

Figure 2-26[*] Effect of air humidification on the performance of MEAs made using different substrates. Pt loading=1.7 mg/cm^2, Nafion 1135 membrane (Qi and Kaufman, 2002a).

* Reprinted with permission from "PEM fuel Cell stacks operated under dry-reactant conditions" by Qi, Z. and Kaufman, A., 2002. *J. Power Sources*, 109, 469-476, Copyright 2002 of Elsevier Limited.

Figure 2-26 shows the effect of air humidification on the performance of MEAs using different substrates. The performance of the stack was affected by the quality of the gas diffusion layer as shown in Figure 2-26. As the authors (Qi and Kaufman, 2002) indicated, even though a double-path-type flow field enabled a fuel cell to run at current densities up to 0.33 A/cm^2 without drying out, the fuel cell suffered from insufficient water supply. This limited the performance of the fuel cell.

Rodatz et al. (2004) investigated some critical aspects of large fuel cell stacks such as the supply system, stack failures, and the voltage stability. Uniform distribution of the reactant gases to the many channels was hard to achieve. When the discharged current change was very fast, compared to the response of the reactants supply system, undersupply and negative voltage may occur. When monitoring the stack voltage, the voltage drop of a single cell was not shown. A solution by Rodatz et al. (2004) was to monitor every cell voltage or at least a small group of cells. Another failure was a leak in the membrane coming from either mechanical stress or hot spots. The generation of large amounts of heat resulted in an increase in the membrane resistance, and hot spots would be formed in the membrane. The way to detect or to solve this issue was not mentioned in this study. The third failure was an overheating of the fuel cell stack, which leads to severe dehydration of the membrane, resulting in a large resistance and a performance loss. To avoid overheating, a sufficient minimum cooling flow should be used at all times. A large pressure difference across the membrane between the reactant gases was one of the reasons for the hot spot in the membrane, which resulted in direct mixing

of hydrogen and air. To prevent this problem, pressure relief valves should be installed and pressure controllers should be used to avoid large pressure differences.

The effects of two variables (reactants' relative humidity and flow rate) on PEMFC stack operation were studied by Torchio et al. (2005). Their results showed that hydrogen inlet temperature and the cathode's relative humidity had no significant effect at every level of current density. Cathode flow inlet temperature showed significant positive effects on the electric power and negative effect on the thermal power recovered from the stack. Considering the water transport and activation loss, the inlet temperature of hydrogen and the cathode's relative humidity should have played a big role in the performance. It will be discussed at section 5.

The behavior of a fuel cell system for an automotive application was studied, especially to examine the air supply and its interaction with the fuel cell stack, by Philipps et al. (2006) using a Nuvera fuel cell stack. Some boundary operating conditions were: (a) 80^{o}C maximum temperature of the stack (air outlet), (b) 75^{o}C operating temperature of the stack (air inlet), (c) 0.4 volts as minimum single cell voltage, and (d) pressure difference between anode and cathode within 0.2 bars. Two operating strategies for the air supply were investigated: (1) the operating pressure and air flow rate is adjusted to the required current, (2) constant operating pressure and air flow rate according to the required current. The pressure at the cathode from a value of 1.2 bars at 40 amps, to a value of 2 bars at 120 amps, respectively. Air flow rate increased in such a way $\lambda = 2$ (λ: ratio of the input oxygen to the oxygen required for the reaction).

Figure 2-27 shows energy demand of the air compressor for a NEDC (New European Drive Cycle) load profile for the operation strategies 1 and 2 by Philipps et al. (2006). Strategy 1 used only 50% of the energy, compare to strategy 2. Strategy 1 leads to a better energy efficiency of the fuel cell system. The operating strategy 1 is suitable for automotive applications. But, operation strategy 2 resulted in a higher efficiency, in particular, for part load due to the modulation of air flow adapted to the current. The stoichiometry of the air supplied to the cathode should be examined and studied with current.

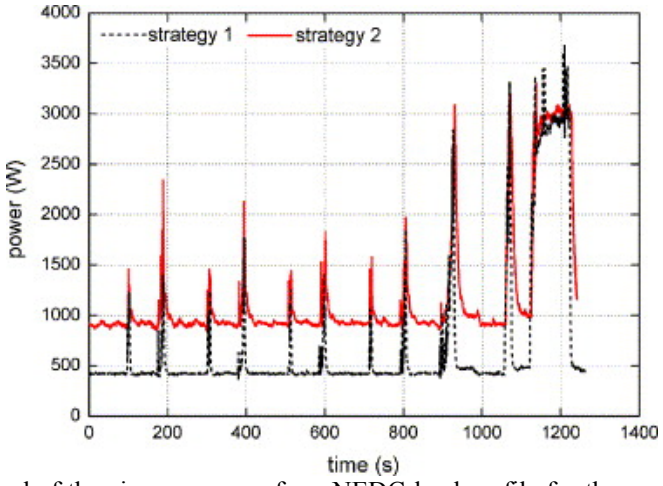

Figure 2-27* Energy demand of the air compressor for a NEDC-load profile for the operation strategies 1 and 2 (Philipps et al., 2006).

Santarelli et al. (2007) investigated the effect of cathode flow stoichiometry on the electrical performance of a PEMFC stack. Increase in air stoichiometry caused a significant positive effect on power at high current density. Figure 2-28 shows polarization curves for different air stoichiometries (1.3, 1.5, 2, 3, and 4.5). Minor performance improvements were observed between 2.0 and 4.5 air stoichiometry. The cell voltage

* Reprinted with permission from "Dynamic investigation of PEFC stacks in interaction with the air supply system" by Philipps, F., Simons, G., and Schiefer, K., 2006. *J. Power Sources*, 154, 412-419, Copyright 2006 of Elsevier Limited.

shown in Figure 2-28, however, was limited up to when the current density was 0.5 A/cm^2. This result was not investigated over the medium current density (> 0.5 A/cm^2), which was important to find the operating range to achieve the maximum performance of a fuel cell. This will be studied and explained in section 5.

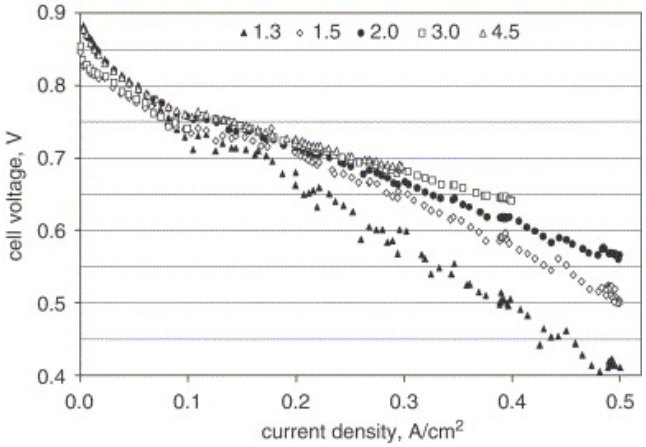

Figure 2-28[*] Polarization curves for different cathode stoichiometries (Santarelli et al., 2007).

2.3 Studies of Water Management

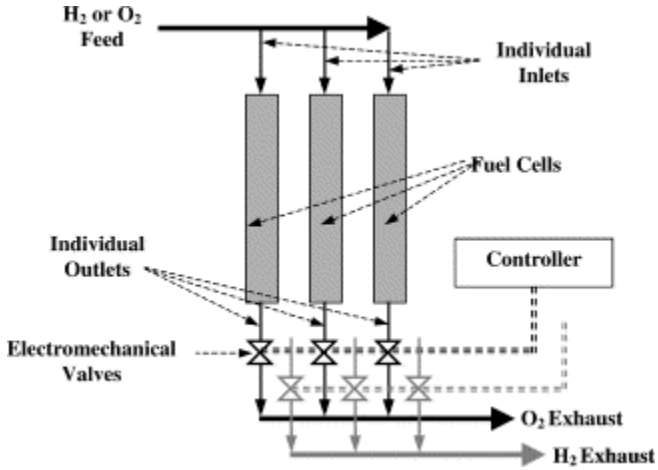

Figure 2-29[**] Fuel cell stack with sequential exhaust system using electromechanical devices (Nguyen et al., 2003).

---

* Reprinted with permission from "Experimental analysis of cathode Flow stoichiometry on the electrical performance of a PEMFC stack" by Santarelli, M., Torchio, M., Cali, M., and Giaretto, V., 2007. *Int. J. Hydrogen Energy*, 32, 710-716, Copyright 2007 of Elsevier Limited.

**Reprinted with permission from "A liquid water management strategy for PEM fuel cell stacks" by Nguyen, V. T. and Knobbe, M. W., 2003. *J. Power Sources*, 114, 70-79, Copyright of 2003 of Elsevier Limited.

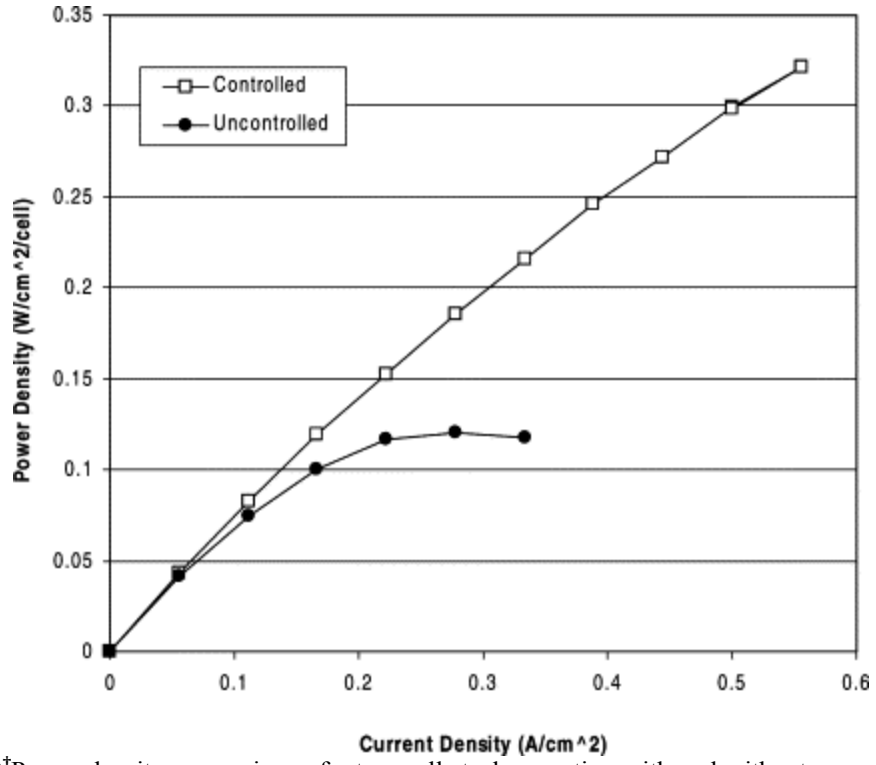

Figure 2-30†Power density comparison of a two-cell stack operating with and without sequential exhaust control. Cell temperature ≈35–40 °C, H_2 flow rate=1.5 A/cm^2 equivalent, O_2 flow rate=2.0 A/cm^2 equivalent (Nguyen et al., 2003).

Nguyen et al. (2003) studied water management with active gas management (AGM) for a PEM fuel cell. As seen in Figure 2-29, electrochemical valves were installed at outlets of each cell. Using a controller, the timing of opening and closing of the electrochemical valves were adjusted. Figure 2-30 shows the power density as a function of the current density for the two cases where active gas management (AGM) was used and not used. When the AGM was used, the power density reached up to 0.33 W/cm^2 at 0.56 A/cm^2 of the current density. Without the AGM, the maximum of the power density only reached up to 0.13 W/cm^2 at 0.28 A/cm^2 of the current density. When the installed

---

† Reprinted with permission from "A liquid water management strategy for PEM fuel cell stacks" by Nguyen, V. T. and Knobbe, M. W., 2003. *J. Power Sources*, 114, 70-79, Copyright of 2003 of Elsevier Limited.

valve closed, the back pressure probably increased which would lead to a decrease of the cathode activation loss and performance increase shown in Figure 2-30.

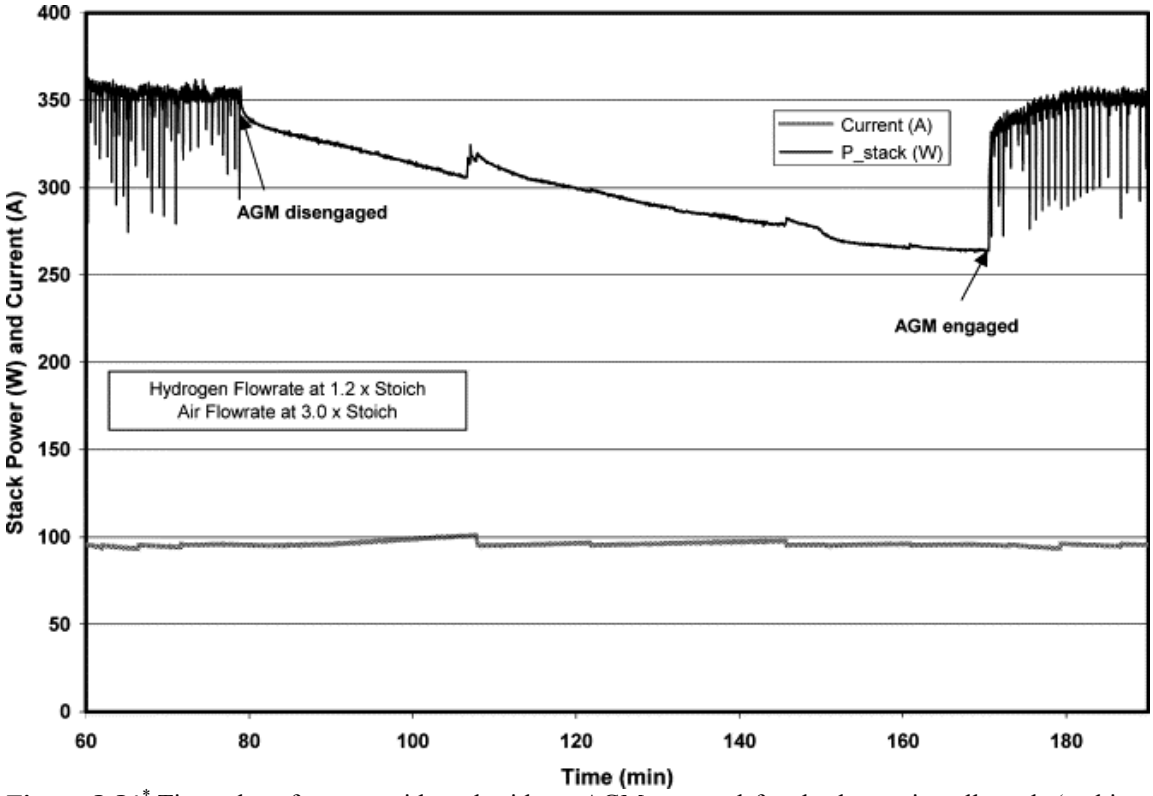

Figure 2-31[*] Time plot of power with and without AGM engaged for the large six-cell stack (ambient pressure, $T = 60$ °C, internal cooling and humidification) (Knobbe et al., 2004).

Figure 2-31 shows the stack power and current as functions of time. When the AGM was disengaged, the power output decreased from 350 watts to 270 watts in one hour. After the AGM was engaged, the stack power output was increased back to 350 watts. This AGM system gave a positive effect on the performance of fuel cell stack. However, while the AGM was engaged, the power output was unstable from 350 watts to 300 watts, changing down and up, repeatedly. This application would not be accept-

* Reprinted with permission from "Active gas management for PEM fuel cell stacks" by Knobbe, M.W., He, W., Chong, P.Y., Nguyen, T.V.Nguyen, V. T., and Knobbe, M. W., 2004. *J. Power Sources*, 138, 94-100, Copyright of 2004 of Elsevier Limited.

able for applications which need stable power output. The decreasing of the performance after the AGM disengaged may result from the insufficient water supply. To maintain performance, sufficient water was needed when inlet gases were supplied. To check whether the AGM was good water management method or not, the performance of the stack should have been stabilized.

Table 2-8 Experimental setup by Eckl et al. (2004).

Number of Cells	20	Pre-conditions	Constant Current	10 amps
Active Area	49cm^2		Operating Temperature	50 ^{o}C (Drying Out), 40^{o}C (Flooding)
Conditions	Self-humidification		Running Time	20 minutes

Eckl et al. (2004) completed an experimental water management study. They studied two scenarios: (1) drying out case and (2) flooding case. Figure 2-32 and Figure 2-33 show the cell voltages as functions of current and testing time. Table 2-8 shows the experimental setup, which included the number of cell, active area, humidification conditions, and pre-conditions for operating. For the scenario of the drying out, when the stack cooling was off, the stack temperature increased. Since the stack has 20 cells, the cells located at the center such as 9, 10, 11 cells had sharp drop of the voltage. This result came from both the local overheating and de-hydration in the cell.

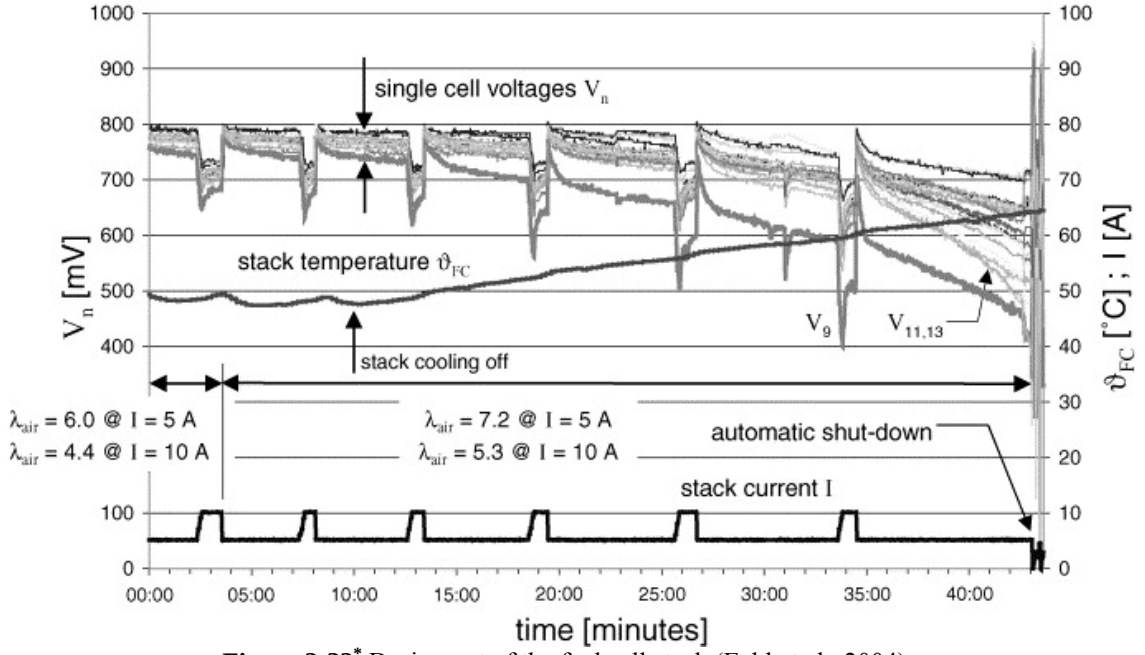

Figure 2-32[*] Drying out of the fuel cell stack (Eckl et al., 2004).

For the scenario of flooding, some of the cell voltages dropped before purging and then increased after purging. In this paper, there are two unusual observations. First, considering the testing conditions (which were a current setting of 10 amps, an operating temperature of 40^{o}C and the self-humidification method), there was no proof that this fuel cell stack suffered from the flooding. Second, the current range was only 10 amps and 15 amps, which was not an appropriate range since the active area of a fuel cell was 49 cm^2. When the air stoichiometries were decreased from 4.4 to 4.0 and 3.6, voltages of some cells in the stack decreased sharply. This performance decrease may result from the concentration loss, instead of flooding at the flow field of the stack.

* Reprinted with permission from "Experimental analysis of water management in a self-humidifying polymer fuel cell stack" by Eckl, R., Zehtner, W., Leu, C., and Wagner, U., 2004. *J. Power Sources*, 138, 137-144, Copyright 2004 of Elsevier Limited.

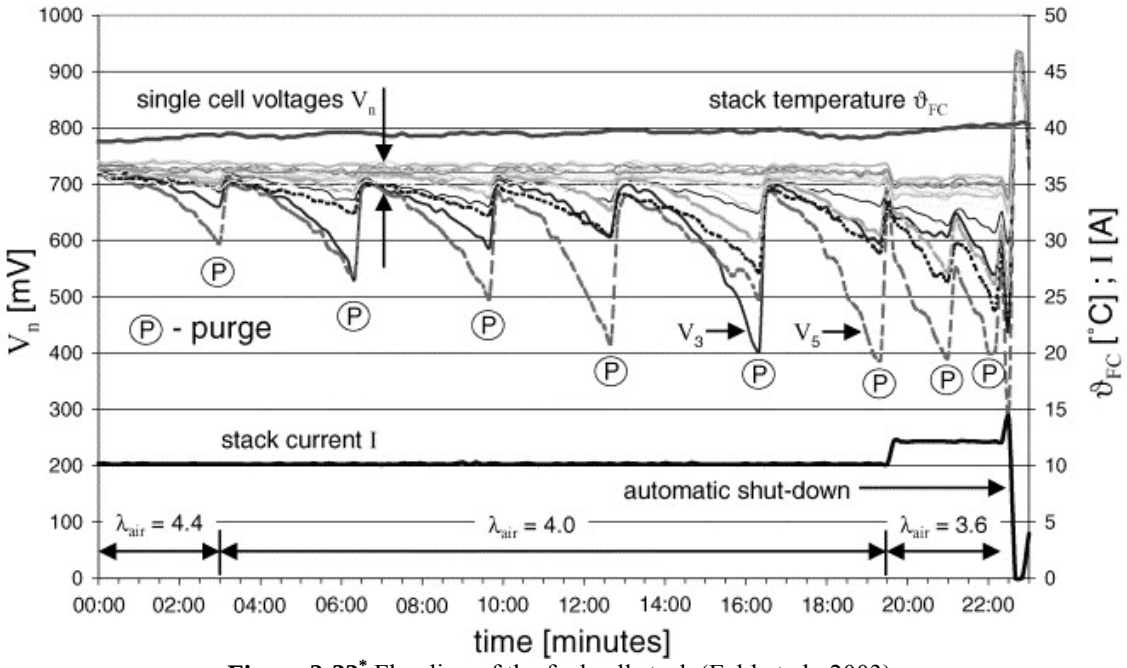

Figure 2-33* Flooding of the fuel cell stack (Eckl et al., 2003).

2.4 Summary of Literature Review

Several approaches to enhance a fuel cell performance have been reviewed in the above sections: (1) parametric studies, (2) modeling of a fuel cell, (3) testing components: membranes and plates, and (4) water management. Generated water will vary with the discharged current, the operating temperature, the flow rate, and the level of inlet humidified gases. These variations will affect the performance of the PEM fuel cell by causing degradation and, eventually, leading to failure of the fuel cell. Detail water transport experimentally has not been studied fully. For these reasons, therefore, an investigation of the role of water transport (water management) in a PEM fuel cell is of particular importance. That is the main focus of this research. The following sections

* Reprinted with permission from "Experimental analysis of water management in a self-humidifying polymer fuel cell stack" by Eckl, R., Zehtner, W., Leu, C., and Wagner, U., 2004. *J. Power Sources*, 138, 137-144, Copyright 2004 of Elsevier Limited.

include research objectives, experimental setup, result/discussion, and summary and conclusions.

3. RESEARCH OBJECTIVES

The ultimate goals of this research are to improve fuel cell performance, and to study the water transport of a PEM fuel cell. To achieve these goals, there are two main research objectives. The first objective of this work was to identify and optimize operating conditions to increase a fuel cell performance by demonstrating how operation parameters affect fuel cell performance. The second objective of this work was to investigate and characterize the water transport (electro-osmotic drag and back diffusion) of a PEM fuel cell through a water balance experiment.

4. EXPERIMENTAL SETUP

4.1 Overview of the Fuel Cell Testing System

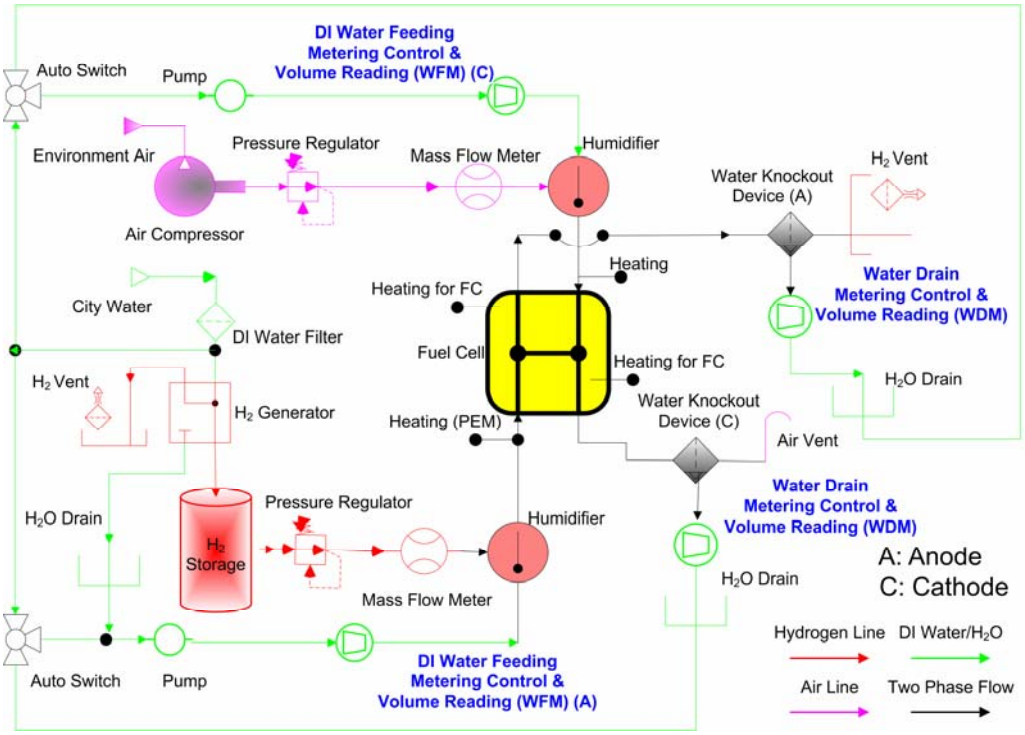

Figure 4-1 Schematic of the fuel cell testing system used in this research.

The next subsections will describe the testing system, MEA preparation, and design of single cell fixtures, air-breathing fuel cell, and PEM fuel cell stack. In this research, a hydrogen generator was used to supply hydrogen to the fuel cell, which led to the elimination of hydrogen cylinders. As shown in Figure 4-1, city water was supplied to the de-ionized (DI) water filtering system. Produced DI water was fed to the hydrogen generator. Chilled water (not shown) was used to control the temperature of the DPH (Dew Point Humidifier). The chilled water is also needed to decrease the temperature of the exhaust gas for water removal. The de-ionized water for the humidification was re-

filled automatically using an automatic level control. The delivery of the gases from the supply to the internal gas line was controlled by a pressure regulator. This pressure regulator reduced the pressure from the inlet pressure to the inline pressure. From the pressure regulator, the delivery of the gases was controlled by electronic MFCs (mass flow controllers), check valves, and solenoid valves. The gas went through the humidifier and heated exit-pipe to the fuel cell. The MFCs were powered and controlled by a flow control board in the computer-controlled module of the testing system. Solenoid valves were all powered by 24 VDC from the local power supply.

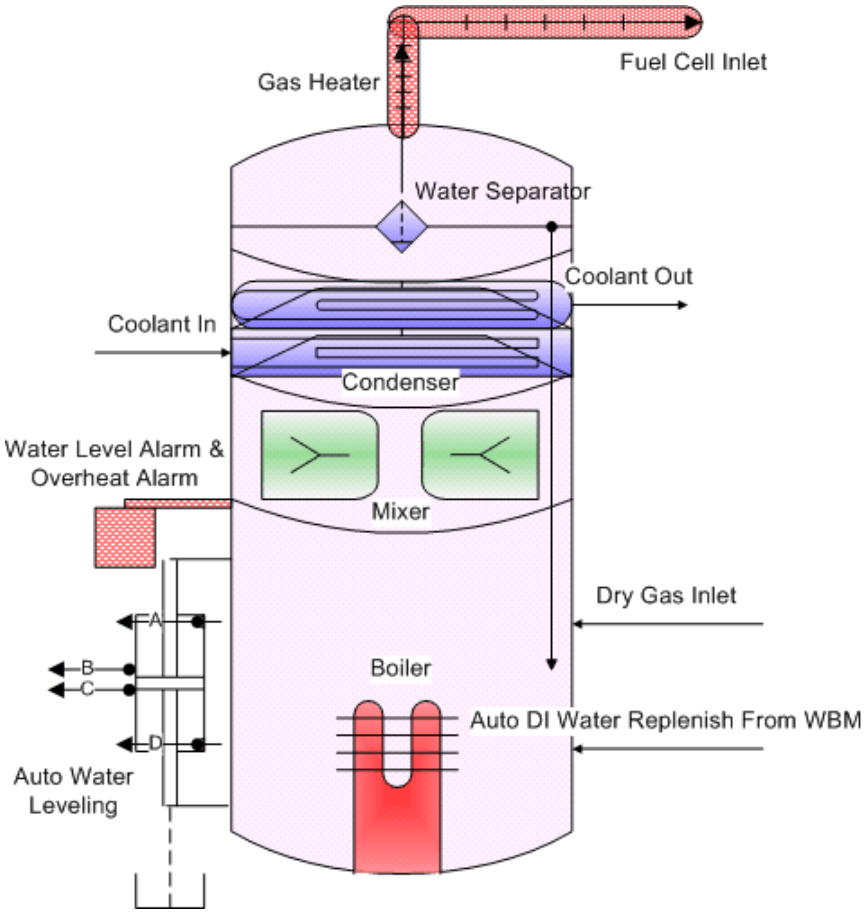

Figure 4-2 Schematic of Arbin patented dew point humidifier (Zhang, 2005).

4.2 Dew Point Humidifier

Humidity control is a key issue in fuel cell operation and testing. The humidifier was able to humidify passing gases to a desired humidity within a specified accuracy within specified ranges of temperature, humidity, flow rate and pressure. The dew point humidifier (DPH), as shown in Figure 4-2, combines several unit processes into one small, but powerful device to achieve precise dew point temperature control for gas humidification (Zhang, 2005). The DPH-GH (with gas heating) adds a gas heater to maintain the temperature and humidity of the gas flowing into the fuel cell and to increase the temperature. Dry reagent gas was pre-humidified by bubbling through de-ionized water in the vessel. The water was maintained at 5°C below the target dew point. A boiler generates steam. The pre-humidified gas was blended with the steam, creating some condensation in the mixture.

Any excess moisture was separated from the gas stream, and the saturated re-agent was delivered to the fuel cell at the desired dew point temperature. The saturated gas stream passed through a heated pipe at a temperature greater than or equal to the dew point temperature to obtain the desired humidity level. The tip of the thermocouple faced upward to avoid accumulation of condensed water and interference of temperature measurement. The exhaust gas from the fuel cell was cooled. Condensed water was separated from the gas and then purged automatically and smoothly without causing pressure interruption to the system.

4.3 Membrane and Electrode Assembly (MEA) Preparation

Table 4-1 Geometric parameters of the fuel cell and specification of MEA.

Active area	*25 cm^2 and 50 cm^2*
Anode channel depth	0.047 cm
Cathode channel depth	0.122 cm
Anode/Cathode channel width	0.122 cm
Average channel length	36.718 cm
Membrane	DuPont Nafion® 117, 115
Gas Diffusion layer	E-TEK ELAT® LT 1200-N
Anode/Cathode catalyst loading	0.57 mg Pt/cm^2

Table 4-1 lists some of the fuel cell and MEA specifications. The active area of the membrane electrode assembly (MEA) was 25 cm^2, with Nafion 117 membrane for experiments in section 5. The MEA with 50 cm^2 of the active area and 115 membrane was used for experiments in section 6. E-TEK ELAT electrodes were used for both the anode and the cathode. The average Pt loading was 0.57 mg/cm^2 on both the cathode and the anode side. As an initial start-up procedure, the MEA was operated at 25^{o}C, with H_2 at 1.2 stoichometric and air at 3 stoichometric flow rates. For this procedure, the fuel cell voltage was constant at 0.2 volts as the cell temperature was raised to 60^{o}C. After reaching this temperature, the cell voltage cycled between 0.2 and 0.6 volts at an interval of 20 minutes, for several hours until the cell performance stabilized.

4.4 Single Cell Design and Fixture

The fuel cell used was equipped with 3 serpentine flow channels for both fuel and oxidant flow fields as shown in Figure 4-3. Standard pure graphite material was used

for the polar plate with flow field. Integrated current collective plates were designed to replace the terminal fixing plate and current collective plate. This leads to simple assembly of cell fixtures, and treated with gold-plated finishing which allowed good chemical resistance, especially small contact resistance between collective plates and flow field plates. The fuel cell had thermocouple wells of outer diameter 1/16” in the flow field plates to monitor the temperature of the flow. Two cartridge heaters were placed at 1/3 and 2/3 positions from the top on both the anode and the cathode end plates to provide uniform heating across the fuel cell. To prevent overheating in the fuel cell fixture, PID (proportional, integral, and derivative) parameters for controlling gas supply heater and humidifier were adjusted and an electrical fan was activated in front of the fuel cell when the cell passed the setting temperature.

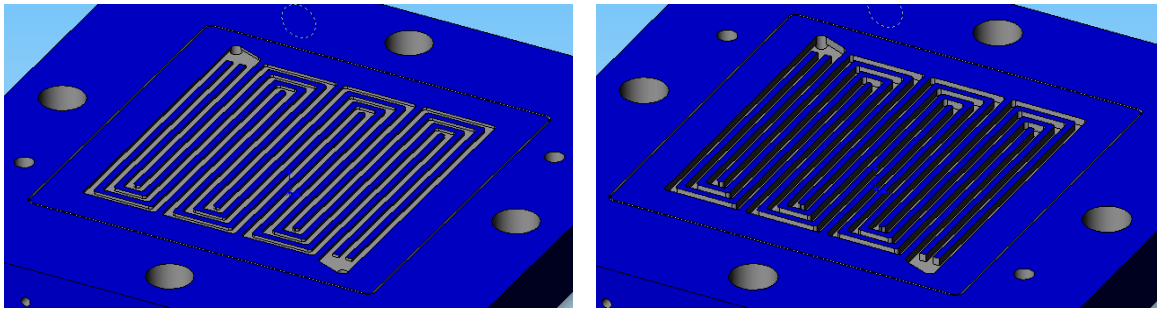

Figure 4-3 Schematic illustrations of two different flow fields: cathode flow field (left), anode flow field (right).

As shown in Table 4-1, the cathode channel had around two and half times more depth than the anode channel, because the oxidation gas was air and for stoichiometric flow rate control, the cathode side gases should be 2 or 3 times higher than the fuel gas at the anode.

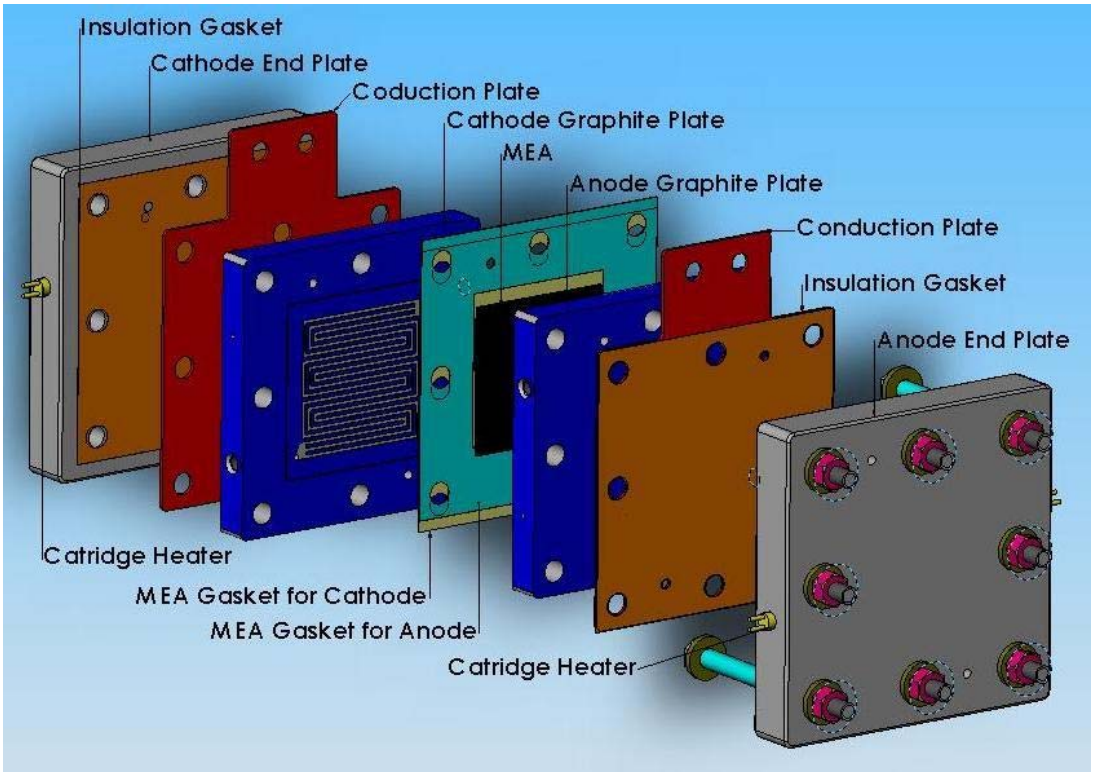

Figure 4-4 Schematic of the single fuel cell showing the essential components.

Figure 4-4 shows a schematic of a proton exchange membrane fuel cell used for this testing. It included two end plates, two conduction plates, anode, cathode graphite flow channels, gaskets, four cartridge heaters, and gas diffusion layers in a membrane electrode assembly.

4.5 Air-Breathing PEM Fuel Cell

The supply of air to the open area of the cathode was by natural convection inside of the temperature/humidity chamber. Figure 4-5 shows the schematic of the experiment setup for the air-breathing fuel cell.

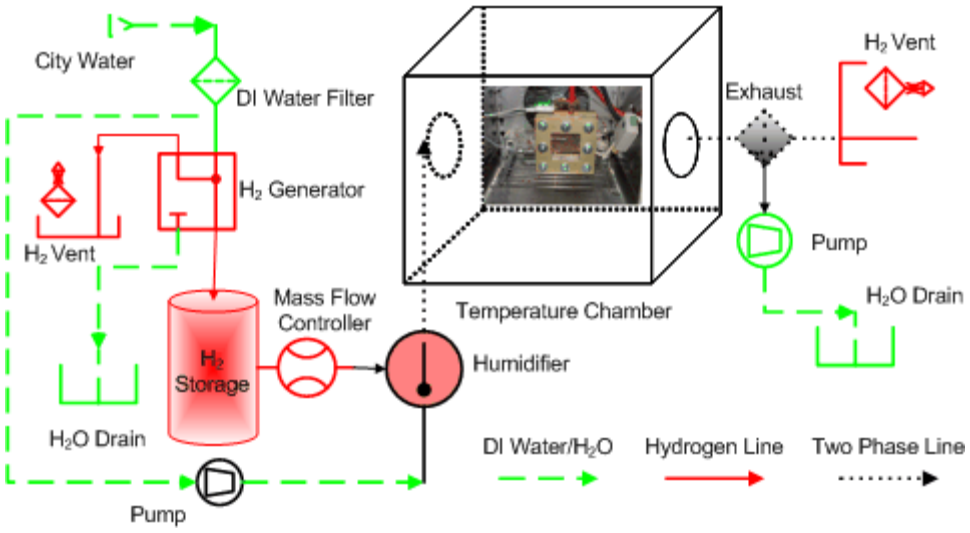

Figure 4-5 Schematic of the experimental setup in passive fuel cell testing system.

The temperature and relative humidity were controlled by an Espec temperature/humidity chamber (model No. SH-221) integrated with the Arbin passive testing system. The principal of the temperature/humidity chamber is illustrated in Figure 4-6 (a). A temperature sensor, around which is wrapped a wet cloth, helps to indicate humidity. Humidity is obtained from the web-bulb temperature and the air temperature (dry-bulb temperature). The chamber balances temperature/humidity to create the desired environmental conditions inside the test area. This is performed by continually controlling a heater and humidifier of low heat load against a constantly running cooler (doubles as dehumidifier) of high heat load. The setting values of the temperature and relative humidity were controlled by Arbin's MitsPro software (Arbin, 2006).

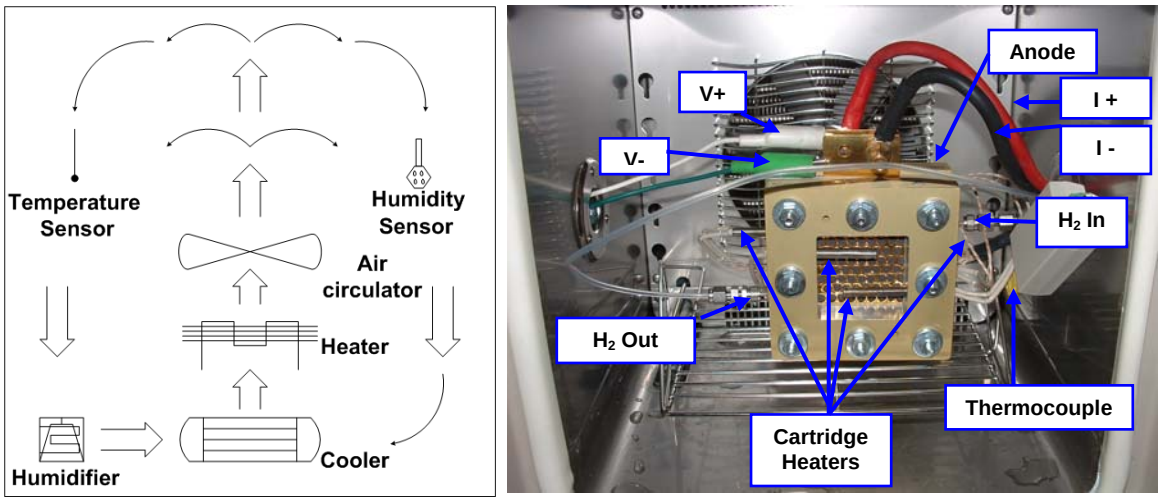

Figure 4-6 (a) The principle of the balanced temperature humidity chamber used in this study. (b) Air-breathing fuel cell's testing setup inside of the temperature humidity chamber.

The temperature of the fuel cell was measured with a thermocouple located in a hole drilled into the anode graphite plate. A cartridge heater was placed at both the anode and cathode end plates to maintain the set temperature of the fuel cell. Figure 4-6 (b) shows the connection with the electronic-load, the hydrogen supply line, the thermocouple location, and the place where the cartridge heaters are inserted.

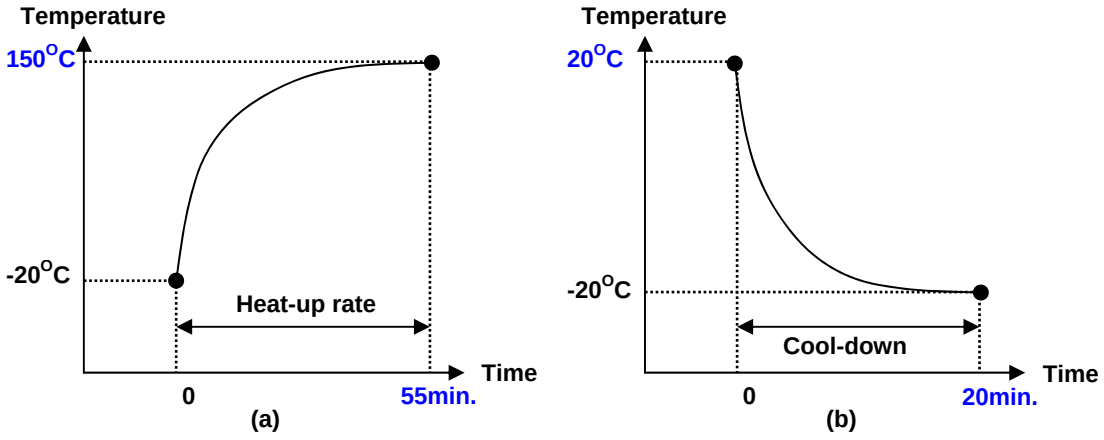

Figure 4-7 (a) Heat-up rate in the temperature chamber. (b) Cool-down rate in the temperature chamber.

Figure 4-7 shows schematics of the heat-up rate and cool-down rate in the temperature chamber. The specifications of the temperature/humidity chamber are: temperature, ±0.3^{o}C; humidity constancy, ±3% RH; temperature uniformity, ±0.5^{o}C; humidity uniformity, ±3% RH; temperature heat-up rate is within 55 minutes from -20 to +150^{o}C, and temperature cool-down rate is within 20 minute from +20^{o}C to -20^{o}C. The K-type thermocouple used to measure cell temperature has a 1/16" diameter, 0.062" sheath diameter, 4" length, and 0.28 seconds response time. The standard error is ±2.2^{o}C based on calibration using chromel as positive and alumel as a negative conductor.

4.6 Water Balance Module

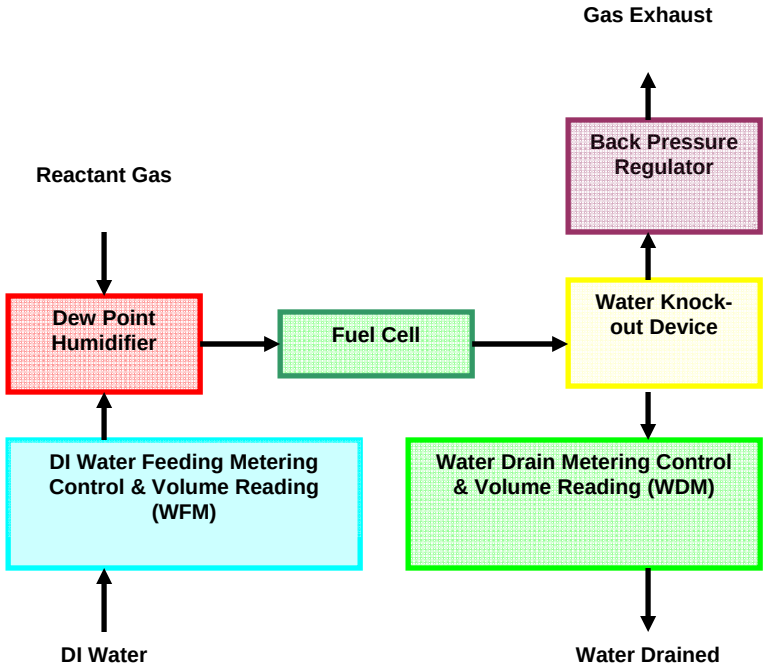

Figure 4-8 Schematic of the water balance module.

Figure 4-8 shows the schematic of one side of the water balance module (anode or cathode) used in this research. The whole water balance module includes four piston pumps to measure how much water is supplied and drained out.

Monitoring the amount of water added and drained (as “waste” from the humidification process and fuel cell reaction) could be achieved with some sort of metering system in place to enhance performance of PEM fuel cell stack. By taking into consideration the humidity and temperature of the exhaust gas/vapor mixture, the amount of water produced from the fuel cell reaction will be estimated and fuel cell efficiency will be calculated.

4.7 Stack Preparation and Experiment Setup

Figure 4-9 (a) shows one of the PEM fuel cell stacks which was used in this research, which has 100 cm^2 of active area with an 8 cell series. Integrated current collective plates are designed to replace the terminal fixing plate and current collective plate, which have high chemical resistance and low contact resistance. Compression pressure was applied to seal MEAs and polar plates so as to lead to good contact between them and good performance of MEAs. A synthetic graphite material was used for the bipolar plate, which had high electric conductivity and high temperature resistance. Figure 4-9 (b) shows the front and back of the anode and cathode graphite plate, which has flow fields for each gas (hydrogen, air) at front and coolant at the back. These graphite plates included the standard serpentine flow channels. After making a series stack, a cooling chamber was put between each anode and cathode flow field, which provided good heat

transfer from reactants to coolant. Figure 4-9 (c) shows the general experimental setup, which included a stack of 8 series PEM fuel cell, pressure sensors to measure pressure variation, thermocouples to measure the temperature of the graphite plates, and auxiliary voltage connections to measure each cell voltage.

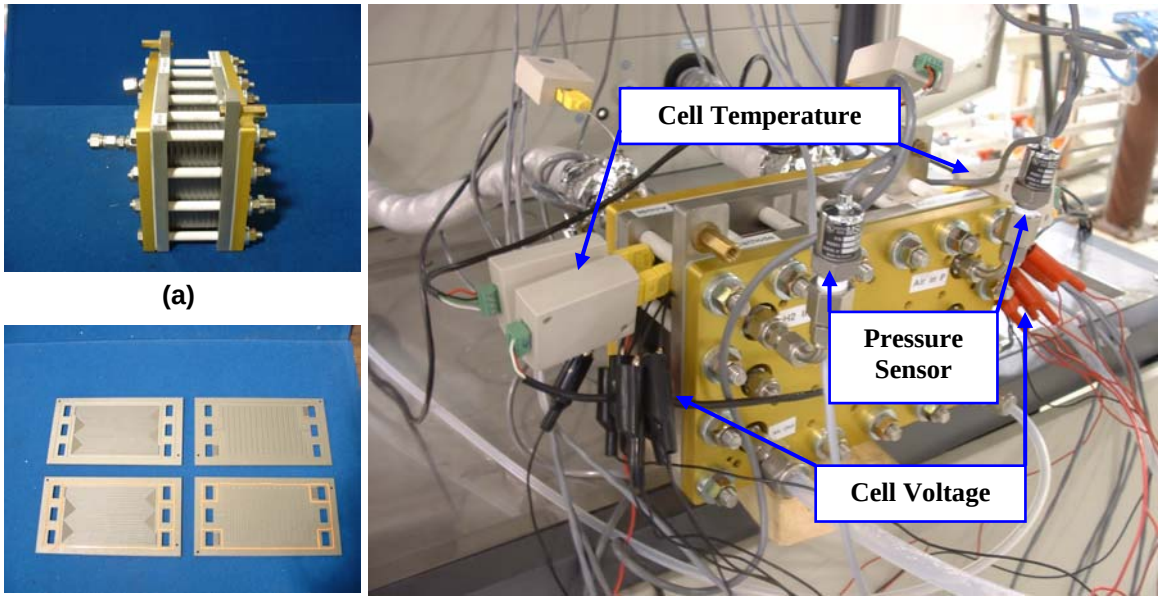

Figure 4-9 (a) PEM fuel cell stack used in this study, (b) anode and cathode graphite plates, and (c) testing setup of PEM fuel cell stack .

In the next section, using the above apparatus, the operation and water transport of a PEM fuel cell will be studied experimentally.

5. RESULTS AND DISCUSSION FOR OPTIMIZING OPERATING CONDITIONS OF A PEM FUEL CELL

5.1 A Study of Relative Humidity and Water Transport in a PEM Fuel Cell

Results are presented in five sections: (1) dry reactant gases, (2) humidified anode gas supply with dry gas at the cathode, (3) the humidified cathode gas supply with dry gas at the anode, (4) both sides humidified, and (5) pressure effects.

5.1.1 Testing Conditions

Table 5-1 Table of the operating conditions for a study of relative humidify effect.

Cases	Temperature (^{O}C)	RH (%) of Inlet H_2	RH (%) of Inlet Air	H_2 Flow Rate	Air Flow Rate	I_0 (amps)
A	70	Dry	Dry	St.=2.5	St.=5	20
B		50				
C		60				
D		70				
E		80				
F		90				
G		100				
H		Dry	50			
I			60			
J			70			
K			80			
L			90			
M			100			
N		80	50			
O		80	80			
P	60	50	50			
Q		80	50			
R		50	80			
S		80	80			
T		100	100			

Table 5-1 shows the operating conditions: temperature, relative humidity at the anode and cathode, flow rate of inlet gases, and starting current of the stoichiometric

flow rate control. First, experiments were conducted for the case of no humidification of the inlet gases (case A). The inlet gas temperature was 70^{o}C, the flow rate of air (St=5) and hydrogen (St=2.5), and started stoichiometric control at I_0=20 amps. After reaching the desired temperature and flow rate values, open circuit voltage was measured for one minute, and the current was discharged at a rate of 0.1 amps/second. When the voltage reached 0.2 volts, the current went back to zero to prevent irreversible damage to the MEA. The current remained at zero for 10 seconds, and then again was discharged at a rate of 0.1 amps/second. The cycle was repeated until either the fuel cell did not produce any useable energy or the back pressure remained constant.

5.1.2 Humidification Effects

Figure 5-1 (a) shows the current density and power density for case A (no humidification) as functions of the test time. For this experiment, residual humidification exists in the fuel cell, and therefore, some number of operating cycles must be completed to purge the residual humidity. For the first cycle, the maximum current density and power density obtained was over 1000 mA/cm^2 and 250 mW/cm^2, respectively. Since the electro-osmotic drag moves H^+ ion from anode to cathode with the water molecules, residual humidification produced this power. The performance of the fuel cell, however, decreased as time increased. After running more than one hour (~3600 seconds; see arrow in Figure 5-1 (a)), the fuel cell using dry hydrogen and air gas couldn't produce any more usable power due to inadequate water balance as shown in Figure 5-1 (a).

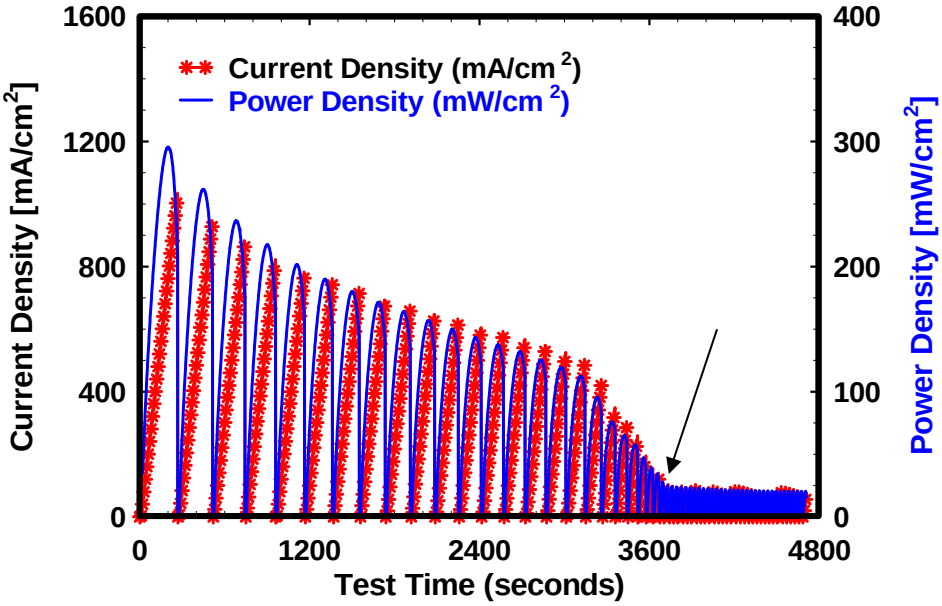

(a)

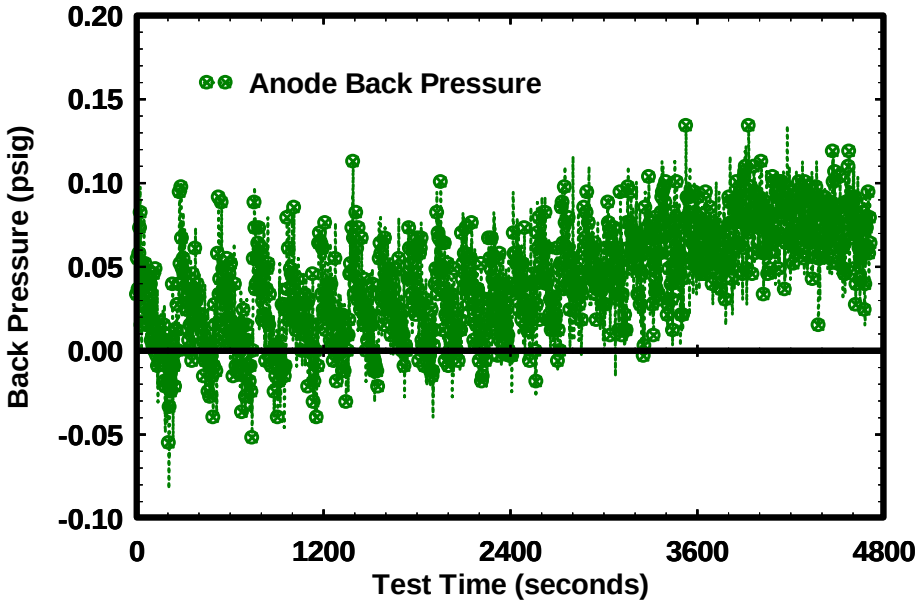

(b)

Figure 5-1 No humidification effect of inlet gases. Inlet gases temperature was set to 70°C. Figure (a) shows the current density (dotted line), power density (solid line) as a function of the testing time. Figure (b) shows the back pressure at the anode. Testing condition: case A.

Since this test was based on dry reactant gases, water molecules couldn't be dragged by protons from anode to cathode. This illustrates that when using dry gases/self-humidifying, one polarization cycle is not sufficient to prove the performance either using dry-reactant gases or self-humidifying.

Figure 5-1 (b) shows the back pressure of the anode side as a function of the test time. For each individual cycle, while the current was discharged 0.1 amps every second, the protons moved cross the membrane from anode to cathode, and the back pressure slightly decreased when current was drawn. During this experiment, the average back pressure continued to increase due to the back diffusion coming from the water concentration gradient between the anode and cathode. Even though no humidification was added to the inlet gases, the generated water at the cathode side lead to water diffusion which resulted in the increase of back pressure at the anode side as shown in Figure 5-1 (b). This action causes degradation of the performance of the MEA. Cases of self-humidification or low humidification inlet gases should be carefully investigated using long test times to insure steady state has been obtained. Steady state condition can not be obtained after just one cycle of the polarization curve, but rather, more than at least a couple of hours is needed to ascertain the performance of the fuel cell. Examples of the degrading performance of the fuel cell are decreasing discharged current at fixed voltage, and decreasing current density and power density as the cycle repeats.

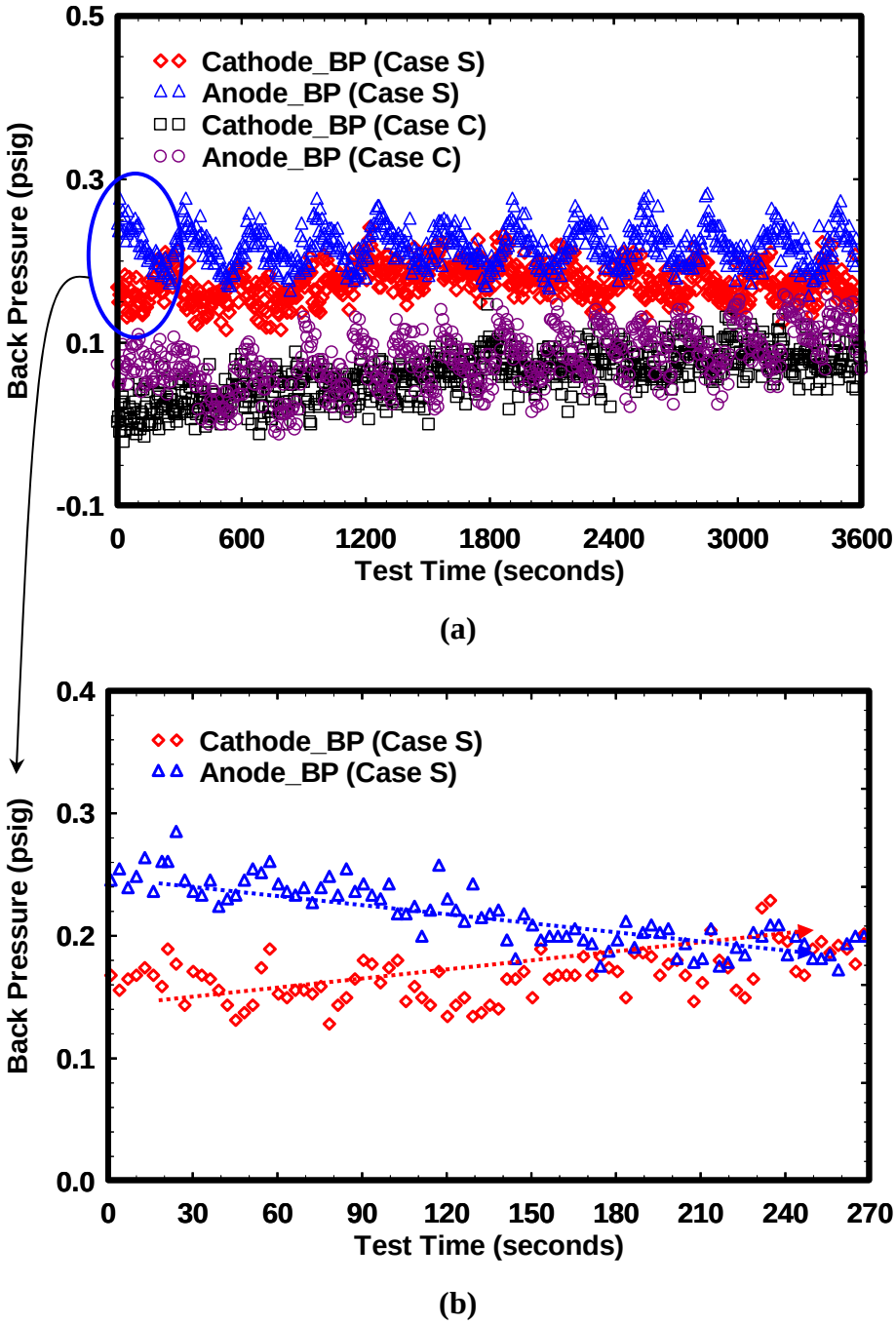

Figure 5-2 Pressure measured at the exhaust. Test conditions: Case S (◊, Δ) and Case C (□, O). Figure (a) shows the measured back pressure for one hour, and figure (b) shows the back pressure value for the first cycle (shown in circle at figure 5-2(a)).

Figure 5-2 (a), which is for the same test condition (case A) as Figure 5-1, shows that the measured back pressure in the exhaust module may be an indicator of how much water content is in the membrane and flow fields during the reaction in the cell. This is possible since the some of the generated water at the cathode and the water content at the anode from back diffusion tend to accumulate. For the case with 60% relative humidity of hydrogen gas at the anode and dry air at the cathode, the back pressure in the exhaust module increased with time. Humidified inlet gas enabled the electro osmotic flow and protons to flow through the membrane. For the case with a relative humidity of 80% for the inlet gases (H_2, Air), the back pressure didn't change much as time increased, which indicates that the membrane was able to maintain a constant water level. In other words, the produced water is removed by the supplying gas. These results indicate that for the 80% humidity case, no flooding occurred since the back pressure was constant. Figure 5-2 (b) shows the measured back pressure in the exhaust module for about the first cycle (~270 seconds). The back pressure at the anode decreased as time passed by, while the back pressure at the cathode increased. This explains that the protons move from the anode to the cathode during the reaction. This trend is repeated every cycle as shown in Figure 5-1 (b) and Figure 5-2 (b).

Figure 5-3 (a) and (b) show the cathode humidification effect with dry gases at the anode. Experiments were conducted to observe the response of fuel cell for humidity oscillation. To obtain the response of the humidification effect, the test ran 2 hours with the desired oscillation of humidity level.

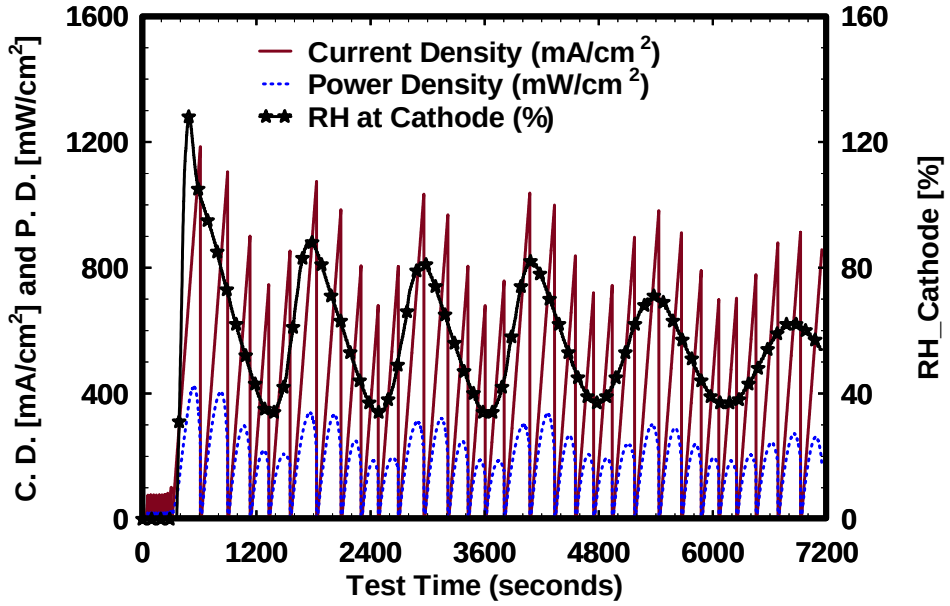

(a)

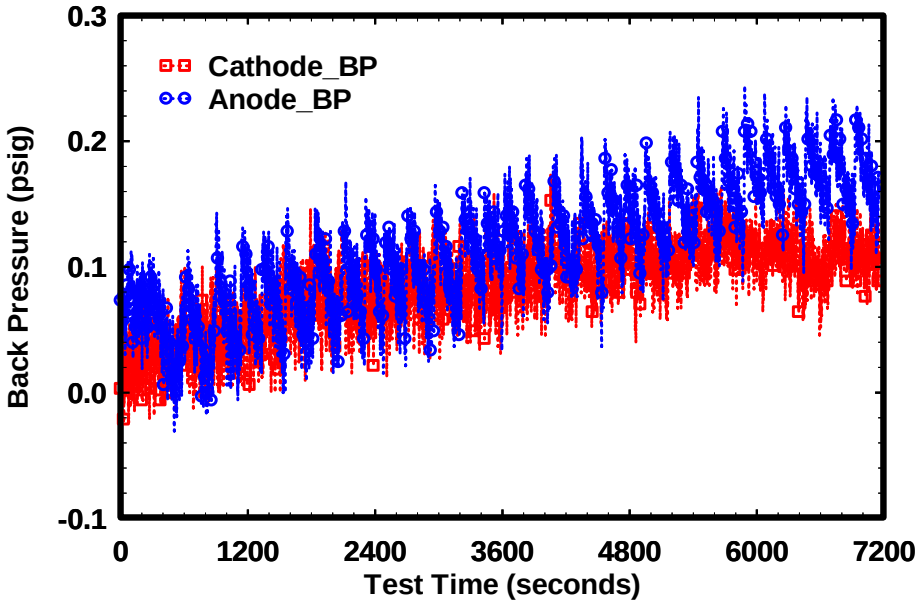

(b)

Figure 5-3 Cathode humidification effect with dry gas at the anode. Inlet gases temperature was set to 70^{o}C. Figure (a) shows the current density (solid line) , power density (dotted line) as a function of the test time. Figure (b) shows the back pressure at the anode (dashed line), cathode (solid line) side. Air (St:5), H_2 (St:2.5), starting stoichiometric control at I_0=20 amps.

The inlet humidity level was set between 35% and 85% for most cases, the inlet gas temperature was set to 70^{o}C, the flow rates of air (St=5) and hydrogen (St=2.5) were set with starting stoichiometric control with I_0=20 amp. The current drop was set at 0.1 amps/second. When the voltage reached 0.2 volts, it went back to open circuit voltage (OCV) and remained for 10 seconds, then was repeated (dI/dt=-0.1 amp/seconds). Figure 5-3 (a) shows the current density and power density with desired oscillation of cathode humidification. At the same humidity level, the current density and power density kept decreasing as the test continued, because of the lack of humidification at the anode which minimized the electro-osmotic drag. Since the humidified gas was supplied to only the cathode side and water was produced at the cathode from the reaction, water concentration at the cathode was much higher than at the anode. This resulted in water back diffusion from the cathode to the anode. As show in Figure 5-3 (b), the back pressure between anode and cathode was the same at the beginning of test. After one and half hours, the back pressure at the cathode remained constant, but the back pressure at the anode was still increasing owing to water diffusion. Figure 5-4 (a) shows the results for the case of anode humidification and dry gas at the cathode (except for two cases, test conditions: N and O), while Figure 5-4 (b) shows the results for the cathode humidification and dry gas at the anode.

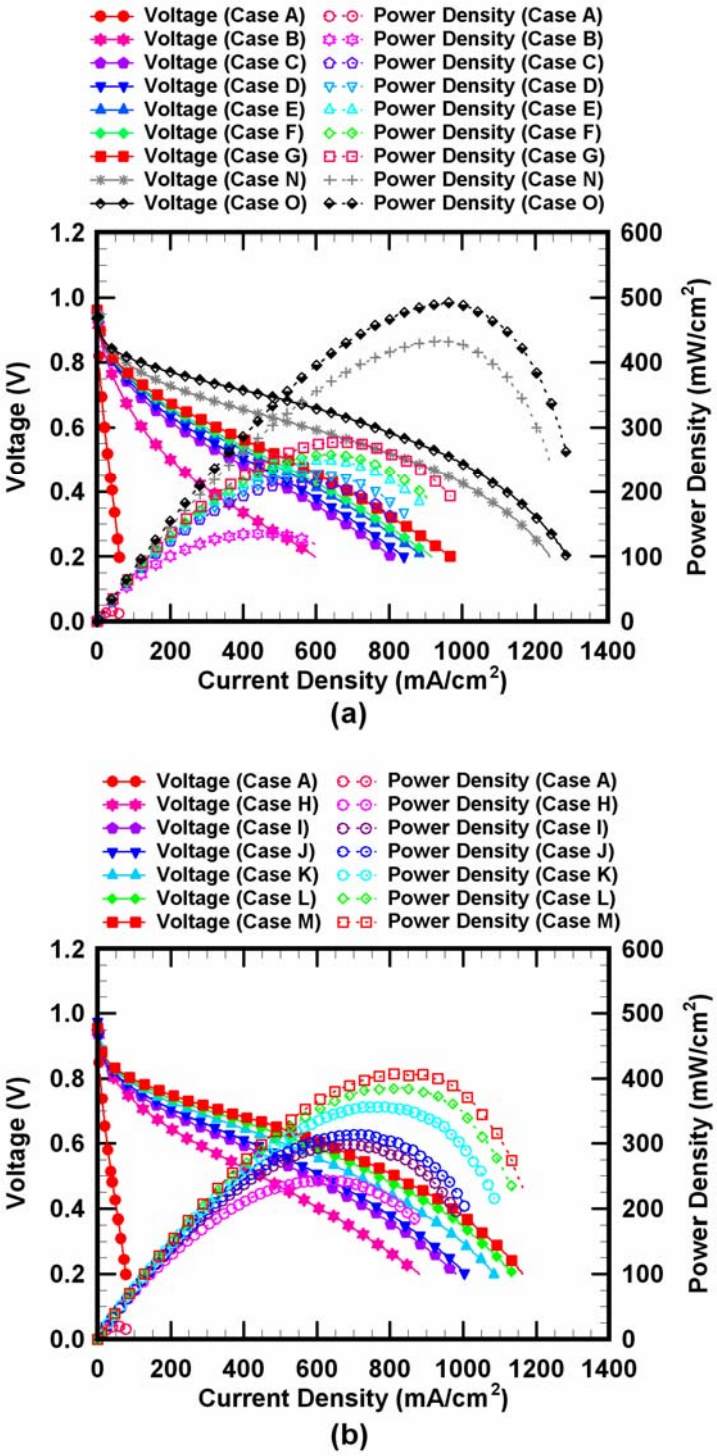

Figure 5-4 Partial humidification effect. Figure (a) shows the cases with only anode humidification [Test conditions: A, B, C, D, E, F, and G], and the both side humidification [Test conditions: N, O]. Figure (b) shows the cases with only cathode humidification [Test conditions: A, H, I, J, K, L, and M].

Relative humidity levels for these tests were no humidification, 50, 60, 70, 80, 90, and 100%, and the inlet gas temperature was 70^{o}C. The no humidification case was obtained after one hour of operation, and the other cases were obtained after running at least a half hour for stabilized performance. For the case of one side humidification, 100% relative humidity lead to the best performance. Because only one side humidification was used, no flooding was detected. Compared to the case of only cathode humidification, the polarization curve for the anode humidification case resulted in lower performance for the low current density region, where little water was produced by the cathode reaction. For the case of only cathode humidification, even for the low current density region, the polarization (I-V) curve represents better performance since water back-diffusion from cathode to anode may compensate a little for the electro-osmotic drag. However, those tests were done with only one side humidification, and one side suffered from drying out. Increasing the relative humidity ratio of the anode inlet gas from 50% to 100% resulted in the cell voltage increasing from 0.336 to 0.563 volts at a current density of 400 mA/cm^2.

Two cases (test conditions: N and O), included in Figure 5-4 (a), represent humidification for both the cathode and anode locations. The measurements were performed at a cell temperature of 70^{o}C. Even though these two cases had lower values of open circuit voltages compared to the case of only 100% relative humidity at the anode and dry gas at the cathode, the voltage obtained at the same current density started to increase even for the very low current density of 10 mA/cm^2. Adding the 80% relative

humidity at the cathode to the case of 80% relative humidity at the anode and dry air at the cathode increased the current density from 880 to 1290 mA/cm^2 at fixed 0.2 volts.

Increasing the relative humidity of the inlet gases at the cathode as shown in Figure 5-4 (b) improved the current density from 840 to 1175 mA/cm^2 at fixed 0.2 volts. Whereas when only humidified gas is supplied to the anode, the current densities (Figure 5-4 (a)) were obtained from 800 to 975 mA/cm^2 at fixed 0.2 volts. This result is because the membrane resistance was reduced since the air flow rate (St=5) was much higher than the hydrogen flow rate (St=2.5) in those tests. As shown in Figure 5-4 (a), both of these humidification cases obtained 50% better performance in I-V curve compared to only anode humidification case. For the cases with humidification at both sides at the low current density, the region for the activation loss transferred to ohmic loss region in a shorter time. The produced water at the cathode during the reaction and supplied humidified inlet gases lead to the sufficient water content in the membrane, and helped the membrane to keep hydrated. The maximum power density of 492 mW/cm^2 at 0.51 volts was obtained with both 80% relative humidity inlet gases.

Figure 5-5 (a) shows the voltage and power density as function of the current density for anode humidification of 50, 80, 100%, and cathode humidification of 50, 80, 100%. The case with anode and cathode 50% relative humidity has the lowest performance among these tests, which implies that there was insufficient humidification. Figure 5-5 (b) shows the voltage as function of the current density between 0 and 10 mA/cm^2. Increasing the relative humidity ratio for the inlet gases, the open circuit voltage (OCV) increased at low current density. The activation loss and ohmic resistance were increased

for the lower humidity level due to a lower ionic conductivity of the membrane because the conductivity of ionomer in the membrane has a strong relationship with the relative humidity.

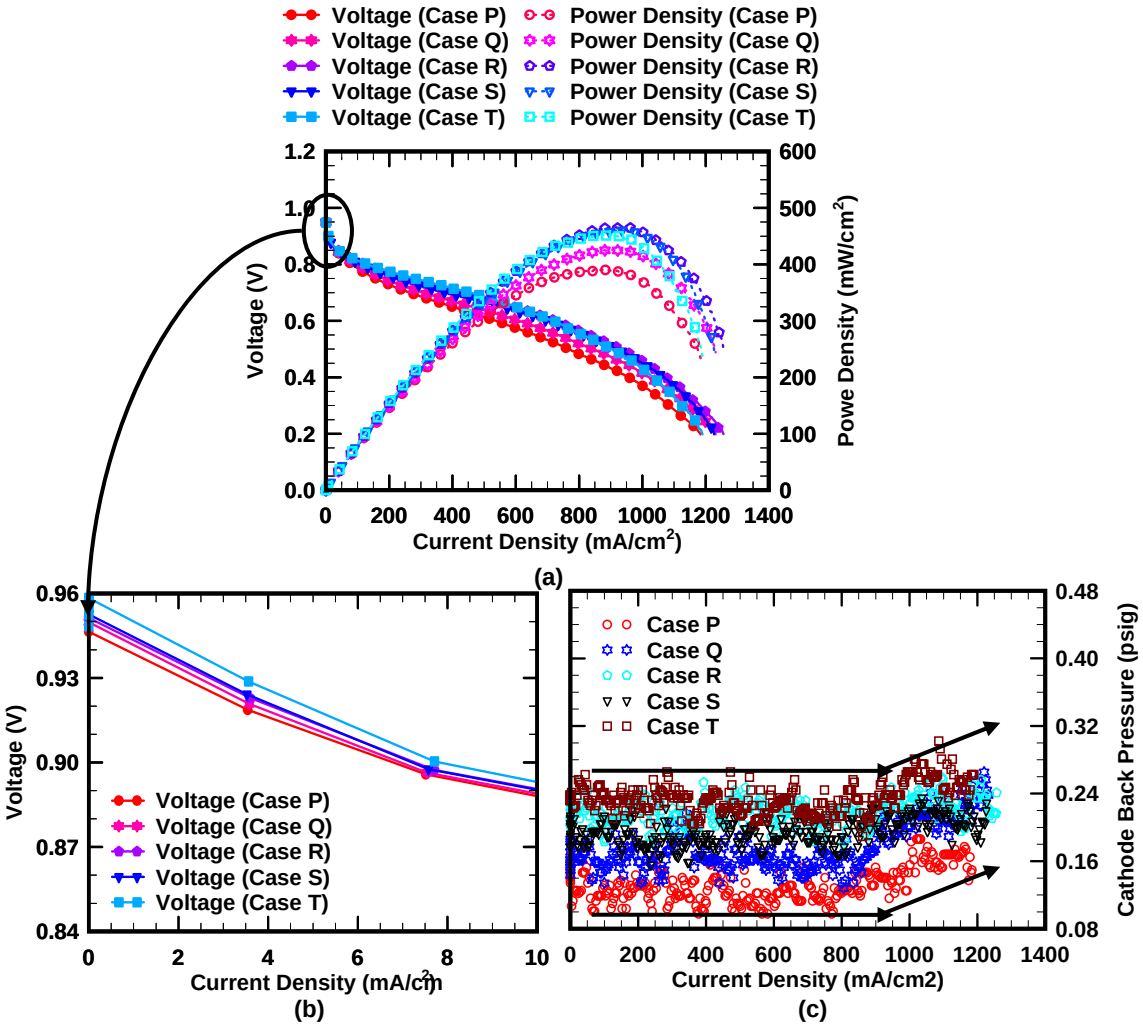

Figure 5-5 Humidification effect. Inlet gases temperature was set to 60^{O}C. Air (St:5), H_2 (St:2.5), starting stoichiometric control at I_0=20 amp. Test conditions: P, Q, R, S, and T. V stands for voltage, and P.D. stands for power density.

Another property that affects the performance of the fuel cell is the gas permeability through the membrane. This property depends on the temperature, relative humid-

ity, pressure, and membrane thickness. Compared to the case of the dry gas supply, the case supplying humidified inlet gases increases the permeability of the H_2, O_2 gases through the membrane.

The case with anode and cathode 100% relative humidity didn't produce the best performance due to water flooding at the high current density and gas permeability. The power density of this case was obtained to around 450 mW/cm^2 when the current density reached around 800 mW/cm^2. The voltage decreased faster than for the other cases for a current density greater than 800 mA/cm^2. The case with anode 50% and cathode 80% relative humidity ratio showed the best performance among these cases.

Figure 5-5 (c) shows the cathode back pressure as a function of the current density. Before reaching the high current density, the back pressure at the cathode seems to remain constant. But, the back pressure increased as the current density increased at the high current density (~800 mW/cm^2). This may indicate that the best region for long term fuel cell operation should be right before reaching the highest point of the power density when the performance of the fuel cell is given as a function of current density. Water management should be easier to control for this region since the flow field has less water production compared to the high current density region.

5.1.3 Pressure Effects

The fuel cell pressure in this work is referred to as the back pressure. This is the pressure against which the fuel or the air is flowing. Back diffusion in the MEA is the movement of the water molecules from the cathode to the anode due to the difference of the water concentration gradient. Therefore, pressure is one of the parameters to influ-

ence fuel cell performance. As investigated in previous research (Nieman, 2004, Larminie and Dick, 2000, Barbir, 2005), increasing back pressure results in a significant improvement in performance since there is reduction in the cathode activation over-voltage.

Table 5-2 Test conditions for investigating pressure and flow rate effect.

Cases	H_2 (sccm)	Air (sccm)	Back Pressure	T(^{O}C)
i	418.2	997.29	34.37 kPa (5psi)	60
ii			0	
iii	348.5	831.08	34.37 kPa (5psi)	
iv			0	
v	209.1	498.65	34.37 kPa (5psi)	
vi			0	

Table 5-2 shows the test conditions for investigating the pressure, and flow rate effect used for this study. Figure 5-6 (a) shows the voltage and power density as function of the current density for different flow rates and pressures. Figure 5-6 (b) enlarged the Figure 5-6 (a) between 0 and 200 mA/cm^2. It shows that the open circuit voltage increased when the pressure increased.

Operating at higher pressures could expel flooding water out, in case of flooding in the fuel cell flow field. A higher pressure at the cathode helps water diffusion to the anode, and it is beneficial to water management in the MEA. Due to losses and irreversibilities, the operating voltage in a test was less than the theoretical voltage. In this research, three different flow ranges with 0 and 34.37 kPa (5 psi) back pressure were selected at 60^{o}C temperature.

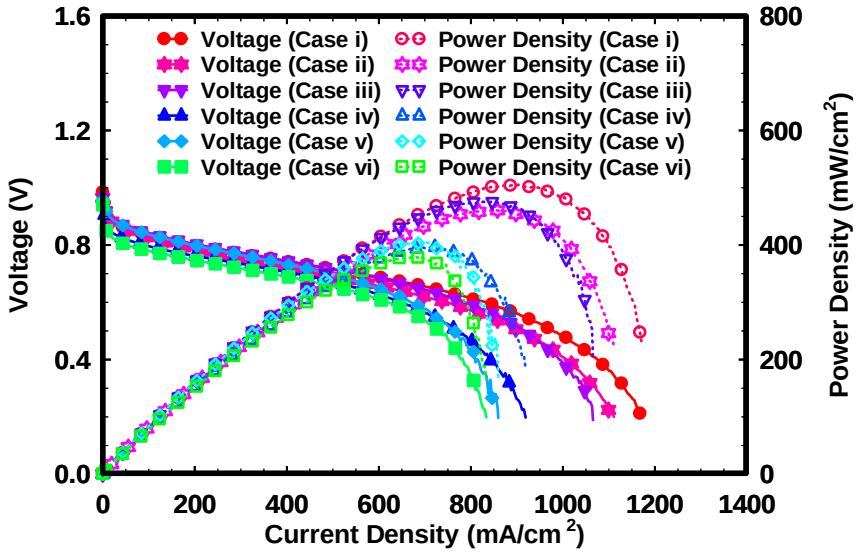

(a)

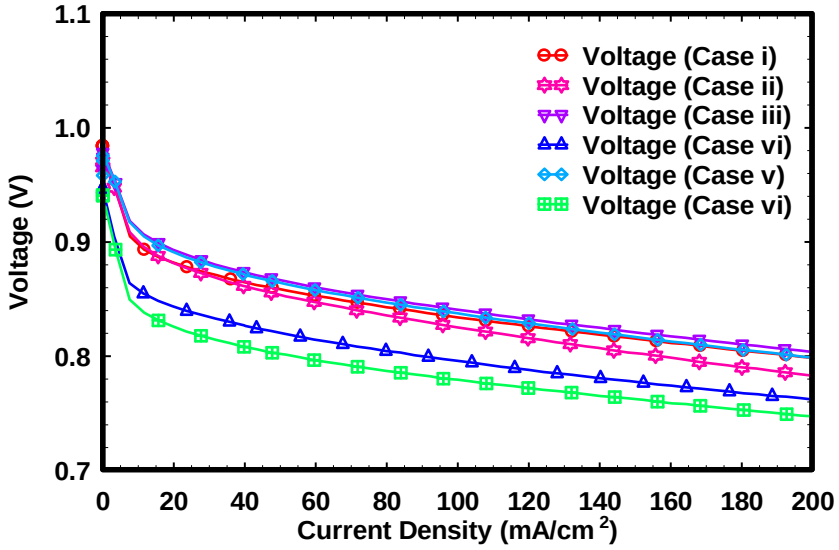

(b)

Figure 5-6 Pressure effect. Inlet gases temperature was set to 60^{o}C. Air (St:5), H_2 (St:2.5), starting stoichiometric control at I_0=20 amps. V. stands for voltage, and P.D. stands for power density.

For case #3 in Table 5-2, the power density was over 400 mW/cm^2 with between 575 mA/cm^2 and 1110 mA/cm^2 of current density with a 34.37 kPa (5 psi) back pres-

sure; but for case #2, the current density was between 570 mA/cm^2 and 1010 mA/cm^2 for the same power density region. As shown in Figure 5-6 (b), when the flow rate and pressure increased, open circuit voltage (OCV) increased and lead to reduce activation loss.

5.2 Effects of Temperature and Stoichiometric Ratio

The stoichiometric flow rate coefficient is thermodynamically a mass flow rate of a gas for generating 1 amp current by one cell, which should be known according to Faraday's Law. Thus, the stoichiometric flow rate coefficient of hydrogen (Fogler, 1999) is calculated by

$$K_{H_2} = \frac{1}{nF}[mol/s \cdot A] \times 22.4[STDl/mol] \times 60[s/\min] = 6.9647 \times 10^{-3}[slmp/A] \quad (5.1)$$

where n is number of electrons in an elementary electrochemical reaction and F is Faraday constant, 96,485 C/mol. For oxygen, the stoichiometric flow rate coefficient is

$$K_{O_2} = 0.5 \times 6.964788532 \times 10^{-3}[slmp/A] = 3.4823 \times 10^{-3}[slmp/A] \quad (5.2)$$

However, the reactants flow rate for a fuel cell reaction must be equal to or higher than the stoichiometric flow rate (Barbir, 2005). Since there is hydrogen crossover though MEA, hydrogen flow rate should be slightly higher than the stoichiometric flow rate (Barbir, 2005). To extend the ohmic loss region and reduce the mass concentration loss, the reactants flow rate needs to be supplied according to the current discharged in the fuel cell. The equations for the stoichiometric flow rate control are as follows:

$$\text{Flow Rate} = St * K * N * (I - I_0) + C, \quad \text{if } I > I_0 \quad (5.3)$$

$$\text{Flow Rate} = C, \text{ if } I \leq I_0 \tag{5.4}$$

$$\text{where } C = St * K * N * I_0 \tag{5.5}$$

where K is the stoichiometric flow rate coefficient, I is the discharged current, St is the reagent stoichiometric ratio, N is the number of cell in a stack, and I_0 is the desired current for starting stoichiometric flow rate.

Table 5-3 Test conditions for stoichiometric flow rate. Relative humidity = 80%.

Cases	Reagent stoichiometric ratio (St.)	Starting current for stoichiometires (I_0)	Temperature (^oC)
A-1	1	2.5	70
A-2		5	
A-3		10	
A-4		15	
A-5		20	
A-6	1.5	2.5	
A-7		5	
A-8		10	
A-9		15	
A-10		20	
A-11	2	2.5	
A-12		5	
A-13		10	
A-14		15	
A-15		20	
A-16	2.5	2.5	
A-17		5	
A-18		10	
A-19		15	
A-20		20	
A-21	3	2.5	
A-22		5	
A-23		10	
A-24		15	
A-25		20	
A-26	3.5	2.5	
A-27		5	
A-28		10	
A-29		15	
A-30		20	
A-31	3	5	60
A-32	1.5	10	
A-33	1	15	
A-34	1.5	20	
A-35	2	15	
A-36	3	10	

5.2.1 Effect of the Stoichiometric Ratio

Table 5-3 shows the test conditions for examining the effects of stoichiometric flow rate. The reagent stoichiometric ratios examined were 1, 1.5, 2, 2.5, 3, and 3.5. The discharged currents to start the stoichiometric flow were set to 2.5, 5, 10, 15, and 20 amps. Parts (A), (B), and (C) in Figure 5-7 show the flow rates corresponding to stoichiometric ratios of 1, 2 and 3, respectively. After reaching the stabilized desired temperature and flow rate values, the open circuit voltage was measured for one minute, and then the current was discharged 0.1 amps every one second. When the voltage reached 0.2 volts, the current went back to zero to prevent irreversible damage to MEA, which was open circuit voltage.

As shown in Figure 5-7 (A), for the case of St=1 (except the cases of stoichiometric flow rate control starting I_0=2.5 and I_0=5 amps), the fuel cell couldn't draw current to follow the stoichiometric flow rate. Even in the other two cases (stoichiometric flow rate control starting I_0=2.5 and I_0=5 amps), cell voltage reached 0.2 volts (I-V polarization ending condition in this test) as soon as starting stoichiometric flow rate control. This indicates some losses in the fuel cell reaction and in the connections between the fixture and the electronic load: crossover permeation or an internal current (Barbir, 2005). This means that excess reactant supply is necessary for the fuel cell to generate useful power. When the stoichiometric ratio was changed from 1 to 2, the flow rate was proportional to the discharged current obtained around 930 mA/cm^2. Increasing the stoichiometric ratio up to 3, the current density achieved up to around 1100 mA/cm^2.

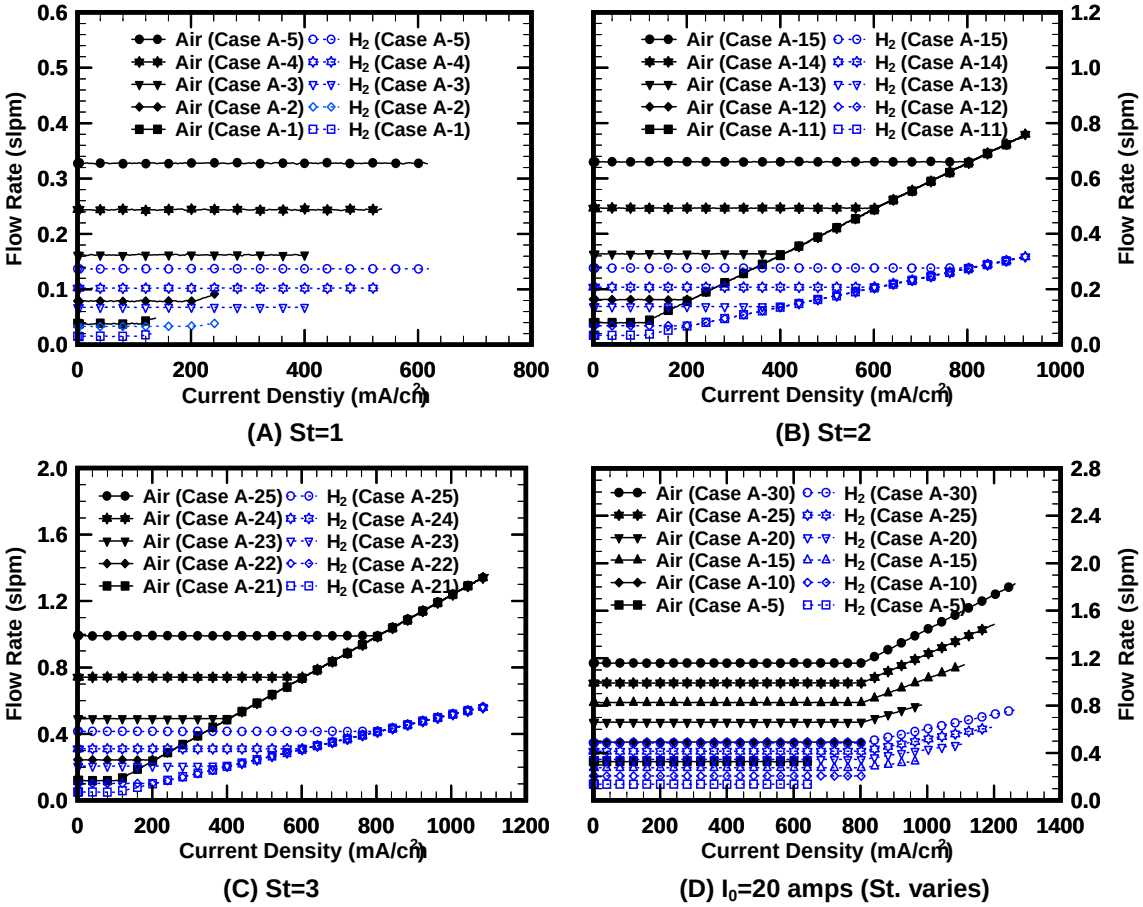

Figure 5-7 Flow rates (hydrogen, air) according to the stoichiometric ratio during tests.

Part (D) in Figure 5-7 shows the flow rate for different stoichiometric ratios when the desired current (I_0) to start the stoichiometric flow was set to 20 amps. The cases having stoichiometric ratios of 1 and 1.5 didn't start stoichiometric flow mode at I_0=20 amps. As the results from the flow rate response, the reagent stoichiometric ratio needs to be greater than about 2 for these conditions.

Figure 5-8 shows the polarization curves corresponding to the various stoichiometric ratios: figures (A), (B), (C), (D), (E), and (F) represent the stoichiometric ratios of 1, 1.5, 2, 2.5, 3, and 3.5, respectively. The discharged current was 0.1 amps per sec-

ond using the current ramp operation as the test condition for the polarization. Air was supplied to the cathode side for all experiments, instead of pure oxygen gas.

The voltage fluctuation shown (Figure 5-8 (A)) illustrates the influence of flooding or starvation of gases at the anode and cathode flow fields (Liu et al., 2006). In the polarization (I-V) curves, when the discharged current increased, the voltage fluctuation is one of the phenomena showing that the inlet gases are insufficient not to generate power fully from the fuel cell. In other words, the voltage was not generated proportionally according to current control.

When the stoichiometric ratio was set as St=1.0, the ohmic loss region was modest, and the mass concentration region was obtained suddenly as shown in Figure 5-8 (A). This behavior was reported (Liu et al., 2006) as due to cathode starvation. There was no such hump in the polarization curve, where it had been observed at the anode starvation (Liu et al., 2006). Since the activation loss is not significantly related to the flow rate, the open circuit voltage (OCV) and activation loss region seem to occupy some portions similarly at the polarization curves, regardless of flow rate shown in Figure 5-8. For the case of St=1.5 (Figure 5-8 (B)), the polarization curve improved compared to the case of St=1.0. The maximum power density reached approximately 350 mA/cm^2, but still there was much mass concentration loss after around a current density 600 mA/cm^2. When the stoichiometric ratio was 2.0 (Figure 5-8 (C)), the ohmic loss region extended up to around 750 mA/cm^2 of current density. When the stoichiometric ratio was 3.5, the maximum power density obtained was almost 500 mW/cm^2.

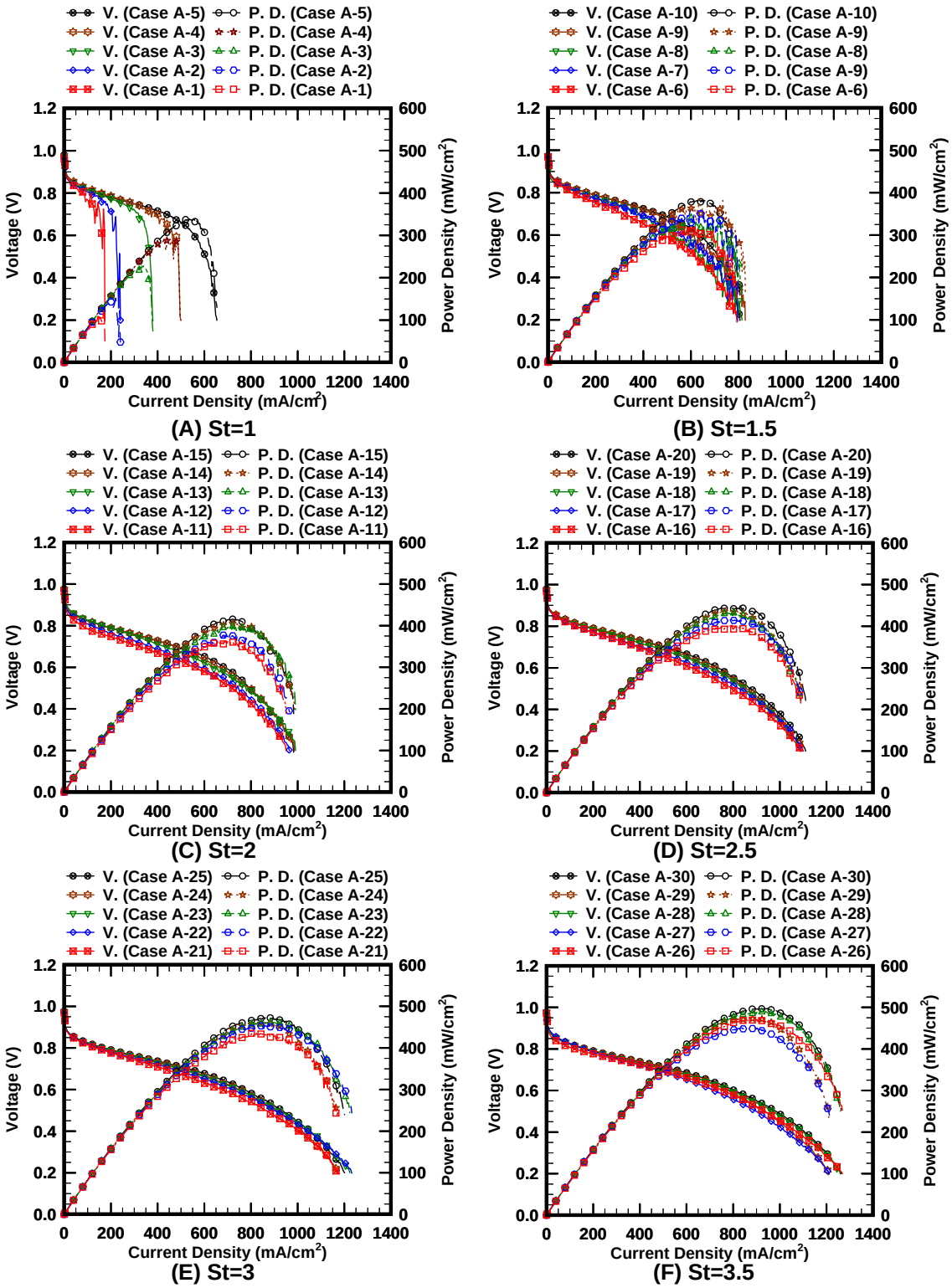

Figure 5-8 Polarization curves (I-V) and power density curves corresponding to the stoichiometric ratios.

As shown in Figure 5-8 (B)-(E), the cases of I_0=2.5 amps had the lowest power performance among the cases of I_0=2.5, 5, 10, 15 and 20 due to the smallest fuel/air supplied. However, for the case of St=3.5, the performance of the fuel cell between I_0=2.5 and I_0=10 amps as shown in Figure 5-8 (F) is roughly the same. The higher the stoichiometric ratio, the less is the fuel utilization obtained. An important factor to determine is the appropriate stoichiometric flow coefficient region. From the above results, the stoichiometric ratio for the PEM fuel cell for the conditions studied is around 3 in terms of maximizing fuel efficiency.

Figure 5-9 shows the polarization curves corresponding to the desired current to start the stoichiometric flow rate. Figures (A), (B), (C), and (D) represent the desired current to start the stoichiometric ratio, I_0=2.5, 5, 15, and 20 amps, respectively.

When the stoichiometric flow rate started at I_0=2.5 amps, for the case having St=1 (Case A-1), the voltage dropped sharply at even low current density (200 mA/cm^2) due to the lack of the concentration of fuel. Considering the two highest stoichiometric ratio cases (St=3.5 and St=3), the highest stoichiometric ratio case (St=3.5) has the same performance at low current density (0 ~ 600 mA/cm^2), has better performance at medium current density (between 600 ~ 1100 mA/cm^2), but has less performance at high current density over 1100 mA/cm^2.

As shown in Figure 5-8 and Figure 5-9, the higher stoichiometric ratio does not guarantee better performance all the time since more excess inlet gases leads to more water generation preventing reaction at high current density. Compared to the cases of

I_0=5 and I_0=15 amps, the case of I_0=2.5 amps seems to have a deficiency of inlet gases since the maximum power density didn't reach 500 mW/cm^2.

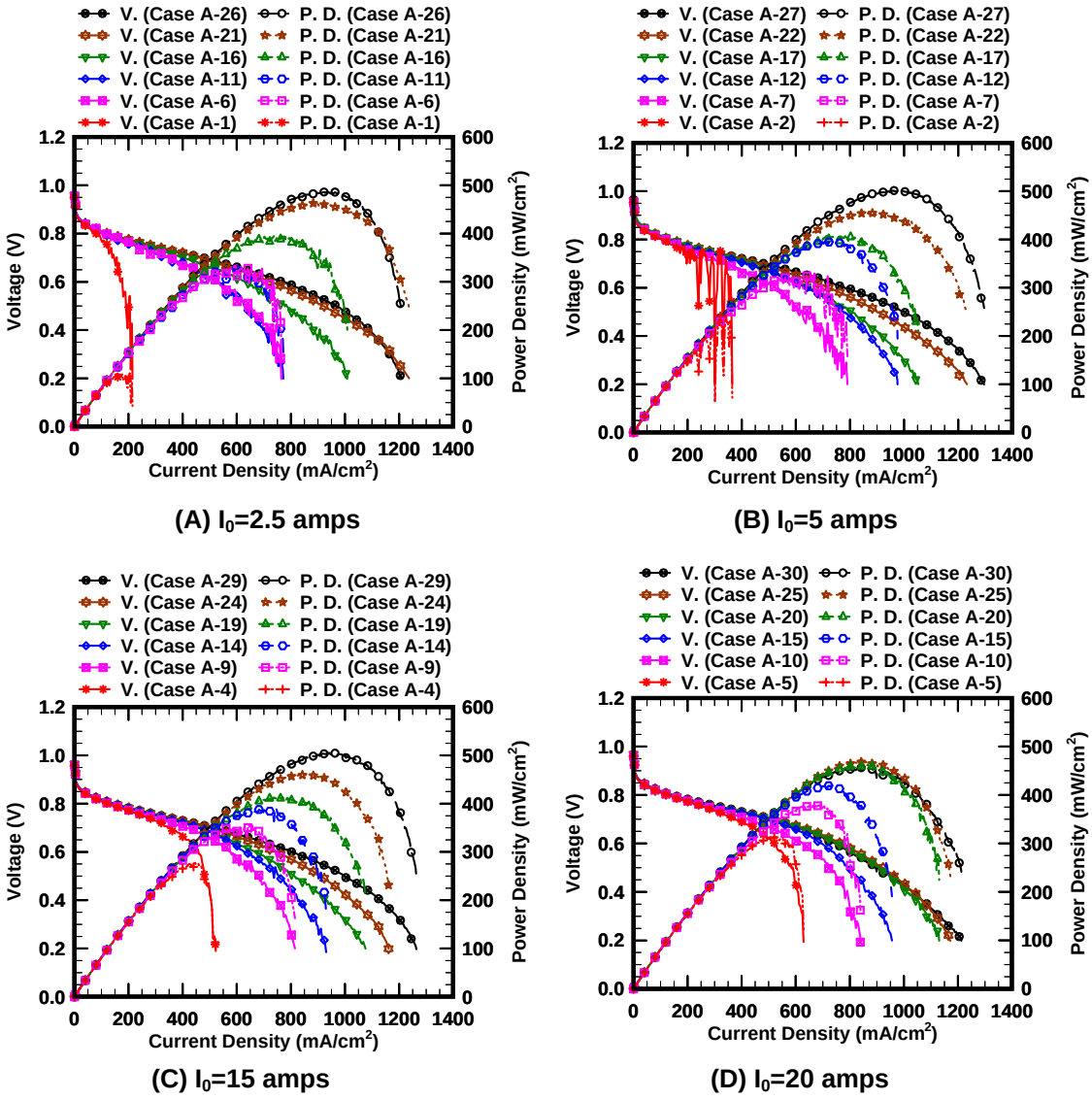

Figure 5-9 Polarization curves (I-V) corresponding to the desired current to start the stoichiometric flow rate control. (See **Table 5-3** for details of each case).

Table 5-4 Test conditions for temperature effects and constant flow rates. I_0=20 amps, RH = 80%.

Cases	Cell, Inlet gases temperature (^{O}C)	H_2 (St.)	Air (St.)
B-1	50	0.5	0.5
B-2		1	1
B-3		1.5	1.5
B-4		2.5	2.5
B-5		4	4
B-6		5	5
B-7		6	6
B-8	60	0.5	0.5
B-9		1	1
B-10		1.5	1.5
B-11		2.5	2.5
B-12		4	4
B-13		5	5
B-14		6	6
B-15	70	0.5	0.5
B-16		1	1
B-17		1.5	1.5
B-18		2.5	2.5
B-19		4	4
B-20		5	5
B-21		6	6
B-22	80	0.5	0.5
B-23		1	1
B-24		1.5	1.5
B-25		2.5	2.5
B-26		4	4
B-27		5	5
B-28		6	6

When the I_0 was set to 5 amps shown in Figure 5-9 (B), the cases for the two lower stoichiometric ratios (St=1 and 1.5) shows a voltage fluctuation, which means a shortage of supplying inlet gases. For the cases of I_0=20 amps in Figure 5-9 (D), stoichiometric flow control started for the cases with St=2 to 3.5. The performance for the cases of stoichiometric ratios from 2.5 to 3.5 was similar.

Considering fuel utilization, the inlet gases should reach the stoichiometric flow rate as early as possible after considering all the losses. For the single cell using 25 cm^2 of active area and using humidified air for cathode inlet gas, when the stoichiometric flow control start at I_0=5 ~ 15 amps with the stoichiometric ratio of 3.5, the best performance was obtained.

5.2.2 Effects of the Fuel Cell Operating Temperature

Table 5-4 is a list of the cases examined in this section with the values for the flow rates of hydrogen and air, and the operating temperature. Figure 5-10 (A, B, C, and D) shows the polarization curves corresponding to the different operating temperatures; 50, 60, 70, and 80^oC are shown in (A), (B), (C), and (D), respectively. The test conditions were the same as for Figure 5-7. The power density and the measured voltage are shown as functions of current density, which is the value of current divided by active area.

When the temperature of the inlet gases and cell was 50^oC, the maximum power density obtained was almost 435 mW/cm^2 for case (B-7) shown in Figure 5-10 (A). Increasing the temperature from 50^oC to 60^oC to 70^oC, the performance increased accordingly. This result agrees with previous temperature effect results (Natarajan and Nguyen, 2003, Qi and Kaufman, 2002b).

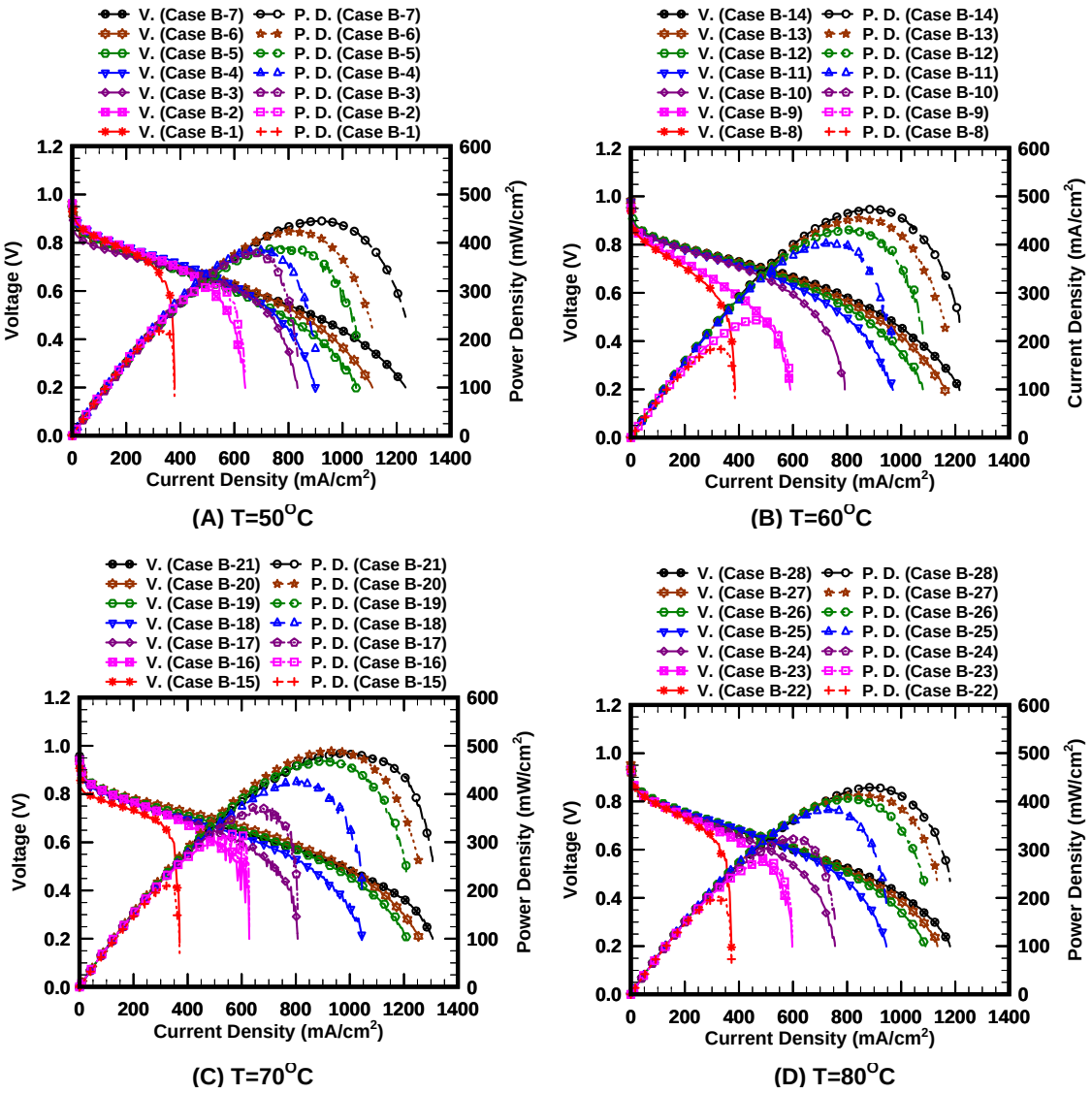

Figure 5-10 Temperature effect according to the flow rate. Relative humidity set 80% and flow rate of each condition illustrated in **Table 5-4**.

Increasing cell and humidification temperature from 35°C to 75°C results in increases of the kinetics of both the oxygen reduction reaction and the hydrogen oxidation reaction (Qi and Kaufman, 2002b). Among tests done in this study, part (C) with a temperature of 70°C, has the highest power density of about 500 mW/cm^2. When the tem-

perature was 80°C, the performance decreased around 10% for the same conditions. This decreasing of the cell performance for the higher temperatures is due to several reasons. Since there are the ohmic resistance losses of the membrane and increased ionic resistance inside the electrode catalyst layer because of the dehydration of the membrane, catalyst utilization was decreased and the oxygen solubility in the electrode ionmer was reduced (Jiang et al., 2006). Each MEA has a specific operating temperature for the maximum performance which depends on the catalyst loading, structure of membrane, and operating conditions. Higher temperature MEA and the right system configuration is necessary to commercialize a PEM fuel cell. But, in this test, too much of the hydrogen was used, and increasing the stoichiometric ratio at the anode was not able to increase the cell performance.

Table 5-5 Table for the effects of air stoichiometric ratio at St_H_2=2. I_0=20 amps, RH=80%.

Cases	H_2	Air	Cell, Inlet gases temperature (°C)
C-1	St=2	St=2	50
C-2		St=3	
C-3		St=4	
C-4		St=5	
C-5		St=6	
C-6		St=2	60
C-7		St=3	
C-8		St=4	
C-9		St=5	
C-10		St=6	
C-11		St=2	70
C-12		St=3	
C-13		St=4	
C-14		St=5	
C-15		St=6	
C-16		St=2	80
C-17		St=3	
C-18		St=4	
C-19		St=5	
C-20		St=6	

Table 5-5 is a list of the cases examined in this section for the various air flow rates; stoichiometric ratios of 2, 3, 4, 5, and 6 with constant hydrogen flow rate (St.=2). These tests were designed to determine the effect of air flow rate at the cathode flow fields for various cell temperatures.

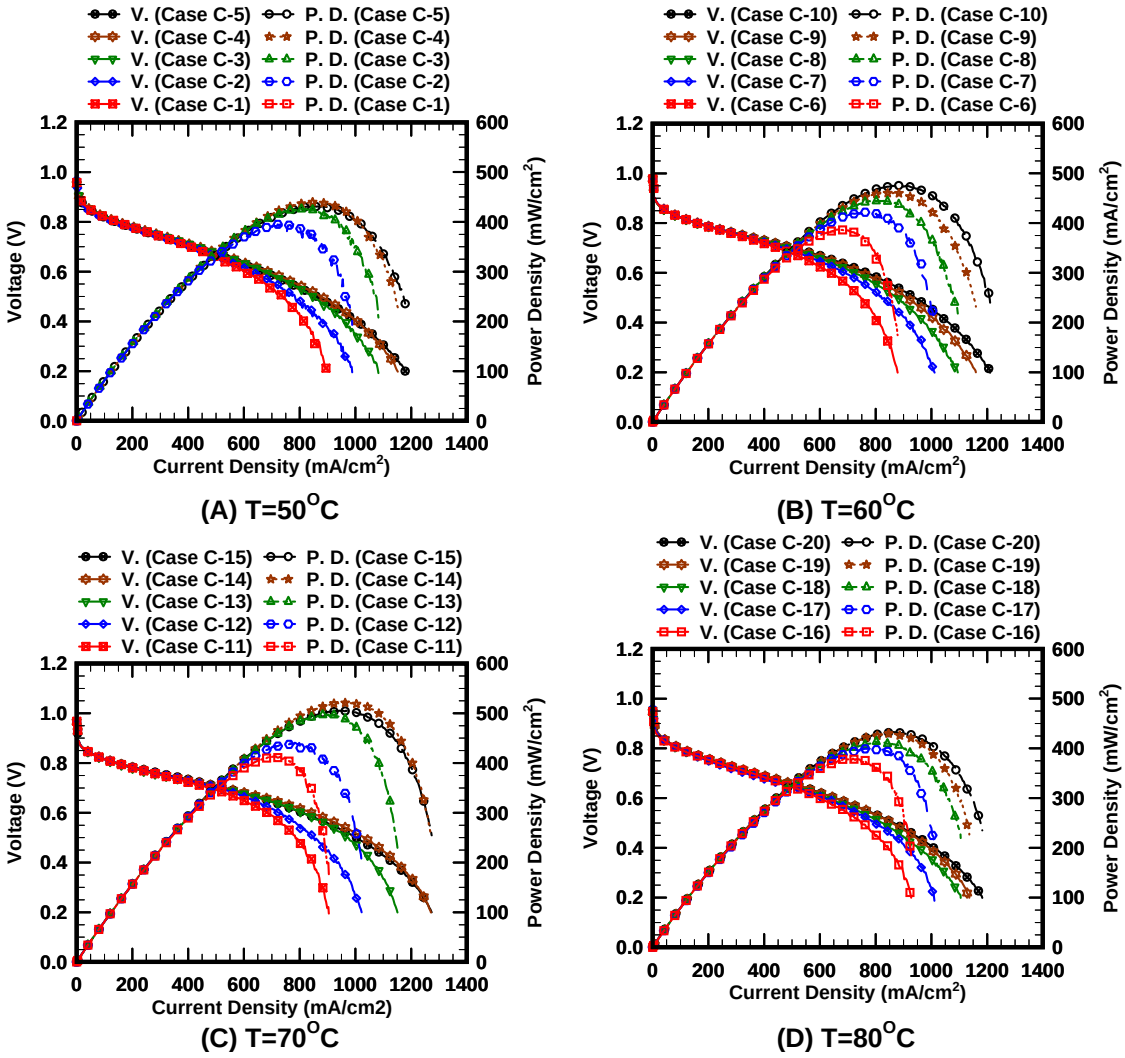

Figure 5-11 Temperature effect according to the flow rate. Hydrogen flow rate set to generate 40 amps theoretically, relative humidity set 80%, and flow rate as listed in **Table 5-5.**

Figure 5-11 shows the polarization curves for the different temperatures (50, 60, 70, and 80^{o}C) at one fixed hydrogen flow rate with five different air flow rates. The performance of the fuel cell using the I-V polarization curve depends very much on the oxygen/air flow rate of the cathode inlet gas at the high current density (Song et al., 2000, Wahdame et al., 2006).

The test conditions were the same as the previous experiment (in Figure 5-7), and the only difference was the flow rate of hydrogen and air. Regardless of the temperature, the voltage was about 0.7 volts at 400 mW/cm^2 of current density. The voltage and power density started to have different values which were dependent on the air flow rate at the cathode around 600 mW/cm^2 of current density. This is the area that the fuel cell started oxidant shortage because the supplied hydrogen flow rate was fixed at St.=2 shown in Table 5-5. The place where the maximum power density gained was much related with the operating temperature and flow rate of air at the cathode as well.

The case of 70^{o}C temperature has the highest power density, 515 mW/cm^2 at 980 mA/cm^2 of the current density, among the temperatures selected for this study. At a temperature of 70^{o}C shown in Figure 5-11 (C), case C-14 (St.=5) has a higher power density than case C-15 (St.=6); which suggests that there must be an over supply of air for the cathode at the fixed hydrogen supply. From this result, when the stoichiometric ratio of the hydrogen flow rate was set to 2 at 70^{o}C, the optimum stoichiometric ratio of the air was 5. Higher air supply cases leads to better performance, but not much for stoichiometric ratios greater than 5.

This result agrees well with previous results. High stoichiometry rates are needed for good fuel cell performance, and air flow contributes to the discharge of the produced water at the cathode (Song et al., 2000, Wahdame et al., 2006). The current density regions when the voltage reaches 0.2 volts has the narrowest area between 910 and 1180 mA/cm^2 for a temperature of 80^{o}C shown in Figure 5-11 (D). For cases with a temperature of 70^{o}C and 0.2 volts, current densities are between 910 and 1280 mA/cm^2.

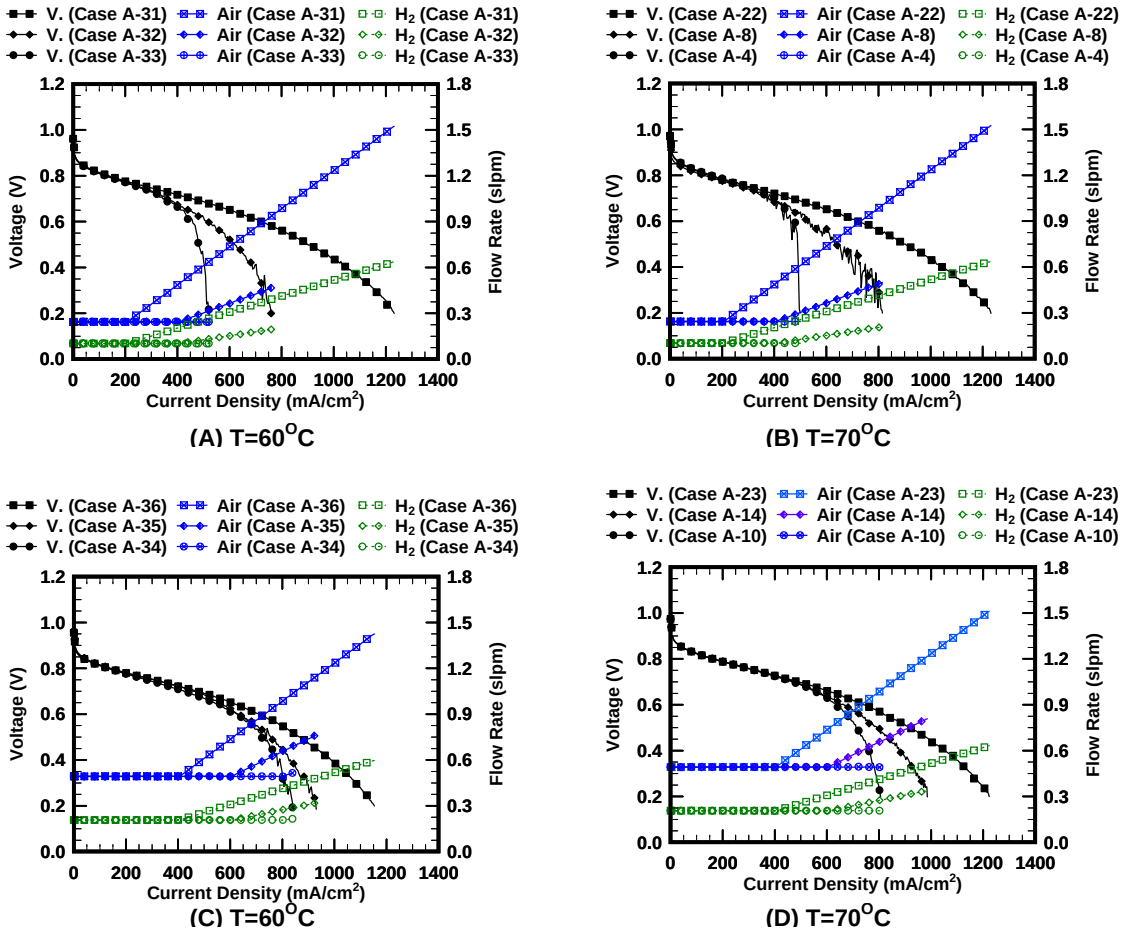

Figure 5-12 Stoichiometric ratio effect. Initial flow rates were same before starting the stoichiometric flow.

Figure 5-12 shows the polarization curves for two different temperatures (60 and 70^{o}C) at the same initial flow rates before starting the stoichiometric flow rate. In Figure 5-12, air was constant up to 200, 400, 600, 800 mA/cm^2 of the current density, respectively and the flow rate of air and hydrogen followed the stoichiometric control with the discharged current. When the stoichiometric ratios were 3 (cases A-31, A-22, A-36, and A-23) as shown in Figure 5-12 (A), (B), (C), and (D), smaller inlet constant amount (case A-31, A-22) of flow rates of air (249.3 sccm) and hydrogen (104.55 sccm) supplied than cases (A-36, A-23). The cases (case A-31, A-22) of starting stoichiometric flow rate at 200 mA/cm^2 generated more current compared to the cases (A-36, A-23) of starting stoichiometric flow rate at 400 mA/cm^2, with higher inlet constant flow rate of air (498.6 sccm) and hydrogen (209.1 sccm). From this result, just supplying more flow rate did not help to increase the performance of fuel cell all the time. The appropriate timing to start stoichiometric flow rate improve the fuel cell performance.

5.3 Effects of the Environmental Conditions and the Channel Depth for an Air-Breathing PEM Fuel Cell

Air-breathing (passive air supply) fuel cell technology for portable electric power applications would operate without forced air supply and humidification systems, and would rely only on natural convection due to concentration gradients (Barbir, 2005). The cathode graphite plate is unnecessary and the conduction plate has some area exposed to the atmosphere directly. The air-breathing fuel cell stacks using a metal hydride cylinder

can last at least three times as long as conventional batteries (Kenyon et al., 2002). These advantages are reasons to further study the air-breathing fuel cell.

Results are presented in two sections: (1) investigation of the environmental conditions for the air-breathing PEM fuel cell, which includes OCV with variation of temperature and relative humidity, temperature effects, relative humidity effects, and activation time, (2) investigation of the channel depths effects.

5.3.1 Environmental Effect

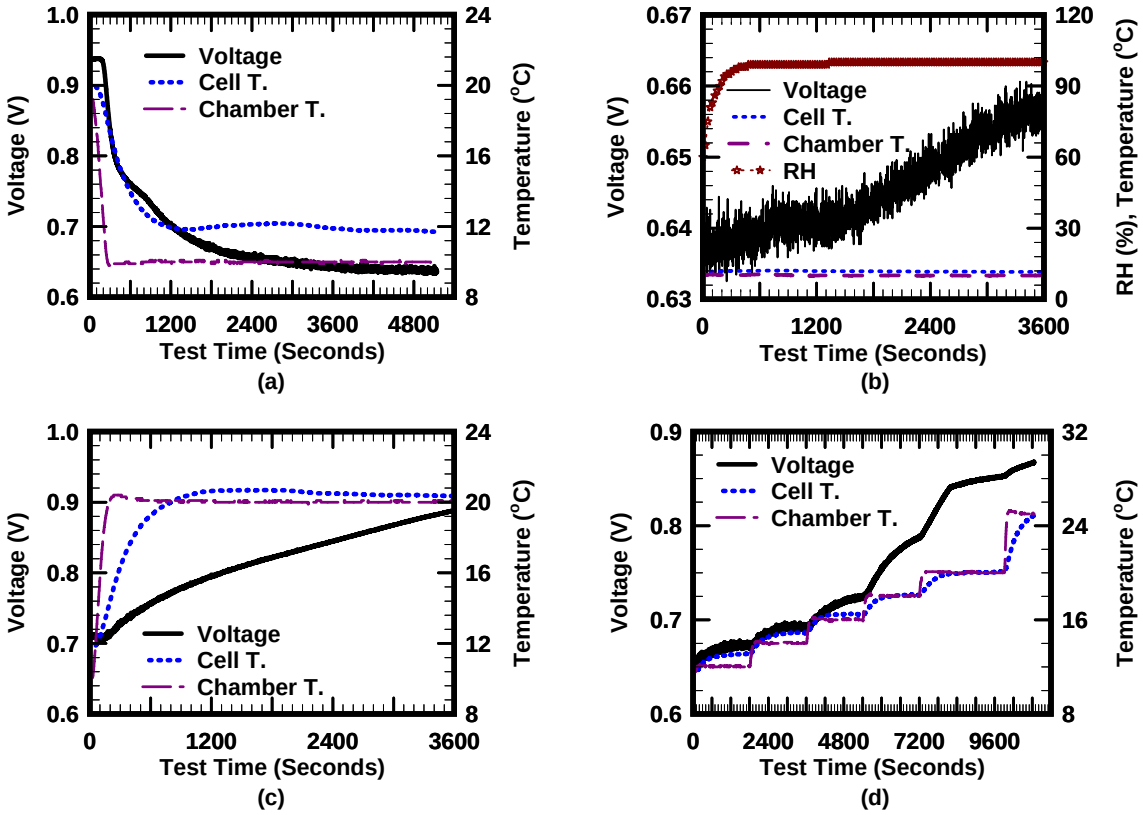

Figure 5-13 Open circuit voltage with different temperature and the relative humidity for the air-breathing PEM fuel cell. Flow field type (I-type).

Figure 5-13 shows the open circuit voltage with different temperatures and relative humidity for the air breathing PEM fuel cell. As a test condition for Figure 5-13 (a), the initial temperature of the fuel cell and temperature chamber was set to 20^{o}C and the relative humidity was set to 60%.

After starting the test, the fuel cell and chamber temperature was dropped to 10^{o}C. In the meantime, the relative humidity level was maintained at 60%. The open circuit voltage decreased sharply from 0.94 to 0.64 volts in 40 minutes according to the drop of the cell and chamber temperature. When the fuel cell temperature measured by the thermocouple inserted into the anode graphite plate was decreased, the open circuit voltage decreased accordingly.

The testing condition for Figure 5-13 (b) was that the temperature remained at 10^{o}C and the relative humidity was increased from 60% to 100%. The open circuit voltage increased from 0.635 to 0.655 volts. For the constant temperature of 10^{o}C, the open circuit voltage increased about 20 mV with increase of the relative humidity. Compared with Figure 5-13 (a) and (d), the widths of voltage line, which is related to the voltage fluctuation, were thin when the open circuit voltage was over 0.7 volts. When the open circuit voltage was less than 0.7 volts, more voltage fluctuation was observed. Voltage fluctuation was shown clearly in Figure 5-13 (b) when the operating temperature was set to 10^{o}C. This result shows how cathode over-potential is related to operating temperature and relative humidity at the open circuit voltage for air-breathing PEM fuel cell.

In Figure 5-13 (c), the temperature of the fuel cell and chamber was increased from 10^{o}C to 20^{o}C for a constant relative humidity of 60%. Compared to the case of the

temperature drop shown in Figure 5-13 (a) (from 20^{o}C to 10^{o}C), when the temperature was increased from 10^{o}C to 20^{o}C shown in Figure 5-13 (c), it took more than 1 hour to reach more than 0.9 volts (OCV). The response of the open circuit voltage when the temperature was increased was slower than that when the temperature was decreased.

To investigate the lowest temperature to operate the air-breathing fuel cell without big potential loss at the open circuit voltage, the temperature of the fuel cell and chamber was increased 2^{o}C (starting at 10^{o}C) on each step every 30 minutes shown in Figure 5-13 (d) and relative humidity maintained at 60%. When the temperature was increased from 10 to 12^{o}C, the OCV was increased from 0.665 to 0.68 volts, which was a 15mV increase. When it was increased from 12 to 14^{o}C, the OCV was increased from 0.68 to 0.695 volts, which was a 15mV increase. It was the same trend from 14^{o}C to 16^{o}C, when the OCV increased from 0.695 to 0.72 volts. The OCV started to increase sharply at a temperature after 18^{o}C. For these conditions, this fuel cell could operate as low as 20^{o}C without having much activation loss.

The proton conductivity is a strong function of water content (relative humidity) and temperature. From these results, temperature provided the largest effect on the proton conductivity compared to water content at low temperature (below 20^{o}C).

Figure 5-14 shows the polarization and power density curve as functions of the current density for the different temperatures and relative humidity. Parts (a), (b), (c), and (d) shown in Figure 5-14 represent the results for 20, 30, 40, and 50^{o}C, respectively. For the case of Figure 5-14 (a) at 20^{o}C temperature, polarization and power density curves with variation of the relative humidity didn't show much difference, which means

that water content in the MEA didn't lead to the performance increase much at 20°C. When the temperature was increased to 30°C (as shown in Figure 5-14 (b)), the current density reached about 140 mA/cm^2 for the case of 100% relative humidity. Whereas other cases, except the case of the 100% relative humidity, the current density reached between 115 and 120 mA/cm^2.

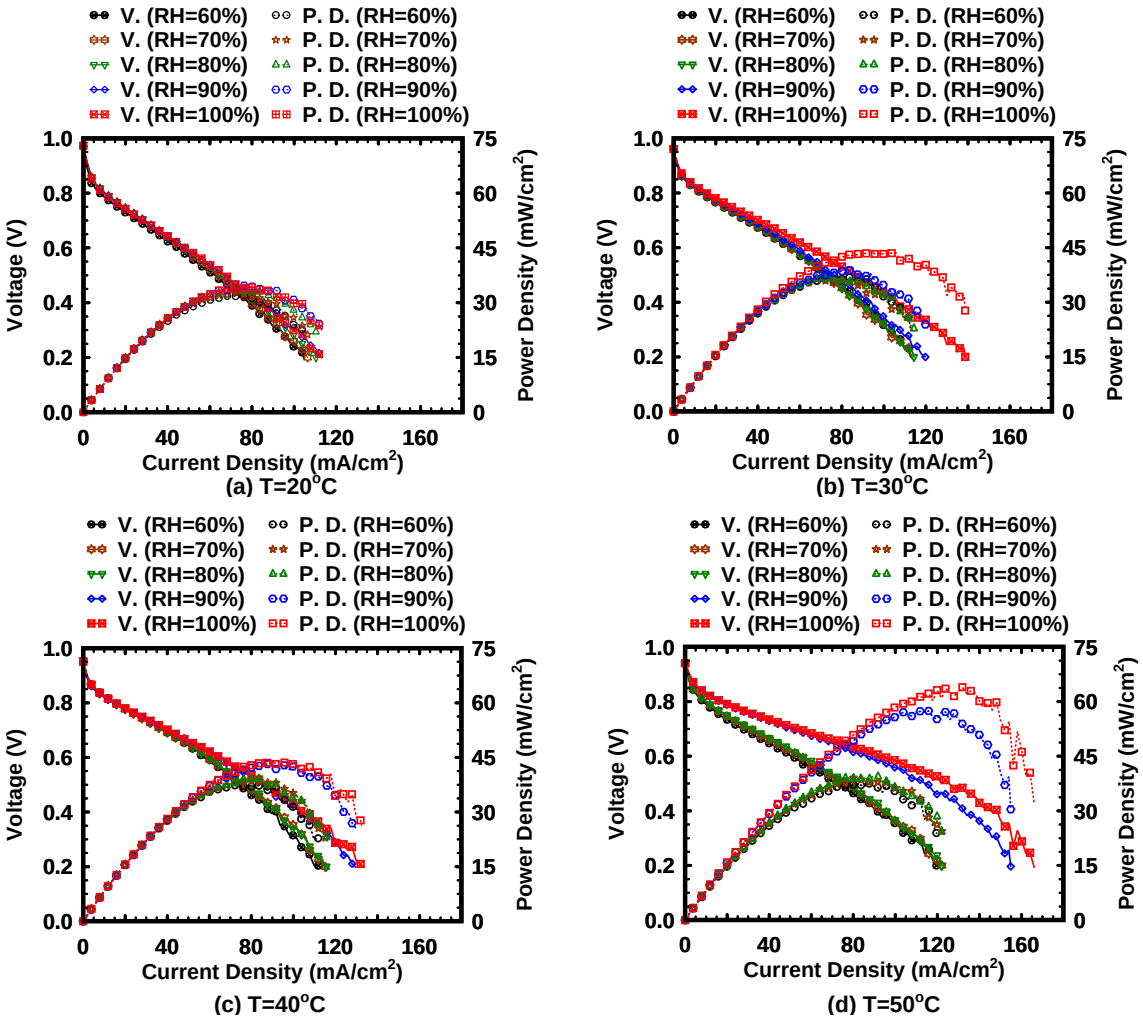

Figure 5-14 Polarization curves and power density curve as function of the current density with different temperature and relative humidity. Flow field type (I-type).

For the temperature of 40°C, the case of 90% relative humidity shows the same performance increase compared to the case of 100% relative humidity. When the chamber temperature was maintained at 50°C, the current density reached around 120 mA/cm^2 for the cases with relative humidity between 60% and 80%. For the higher relative humidity cases, the current density obtained was around 155 mA/cm^2 for 90% relative humidity of, 165 mA/cm^2 for 100% relative humidity.

In summary, when the temperature is low (such as 20°C), the relative humidity does not play a big role on increase of performance. For higher temperature, however, the higher relative humidity helps the proton to move from the anode to the cathode and improve performance.

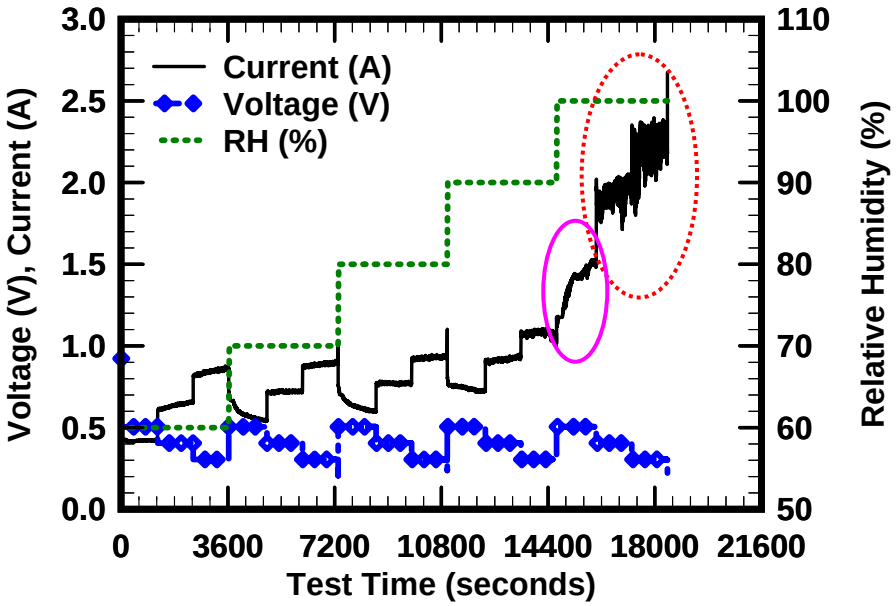

Figure 5-15 Current and voltage corresponding to the variation of relative humidity at the temperature chamber (40°C). Flow field type (II-type).

Figure 5-15 shows the current with different relative humidity levels and three different steps of voltage. The test procedure was to increase the relative humidity by 10% increments on every cycle starting from 60% relative humidity, and ending at 100% relative humidity. When the relative humidity reached the set value, the voltage dropped from OCV to 0.5 volts and was maintained for 20 minutes. After 20 minutes, the voltage dropped to 0.4 volts and 0.3 volts, which was maintained for 20 minutes on each step. These voltage steps repeated cycles with various relative humidity levels. At the initial state, the open circuit voltage was measured around 0.92 volts. Between 60% and 80% relative humidity, the discharged current slightly increased as the relative humidity increased. When the relative humidity was set to 100%, the current fluctuation became larger (dotted circle shown in Figure 5-15). Increasing the relative humidity leads to an increase of the current at the same voltage level, but the voltage fluctuation at 0.4 and 0.3 volts shows the concentration over-potential for the case of 100% relative humidity shown in Figure 5-15. At 0.5 volts for the case of 100% relative humidity, the discharge current increased from 1.0 amp to 1.5 amps (solid circle shown in Figure 5-15).

From these results, performance improved with conditions of 90% relative humidity or higher at low temperature (30 ~ 40^{o}C) for an air-breathing PEM fuel cell.

Figure 5-16 shows the polarization and power density curve as a function of the current density for different temperatures and relative humidity. Parts (a), (b), (c), and (d) shown in Figure 5-16 represent the results for a relative humidity of 60, 70, 80, 90, and 100%, respectively. Between case 70% (Figure 5-16 (a)) and 80% relative humidity (Figure 5-16 (b)), the polarization and power density curves with variation of the tem-

perature didn't show much difference. Higher temperatures lead to better performance due to less resistance to the ions, but not significantly. When the relative humidity increased to 90% shown in Figure 5-16 (c), the current density reached around 155 mA/cm^2 for the case with a temperature of 50^{o}C. Whereas other cases, except the case of the 50^{o}C temperature, the current density reached between 115 and 125 mA/cm^2. For the case of 100% relative humidity, the current density was to around 170 mA/cm^2 at 50^{o}C.

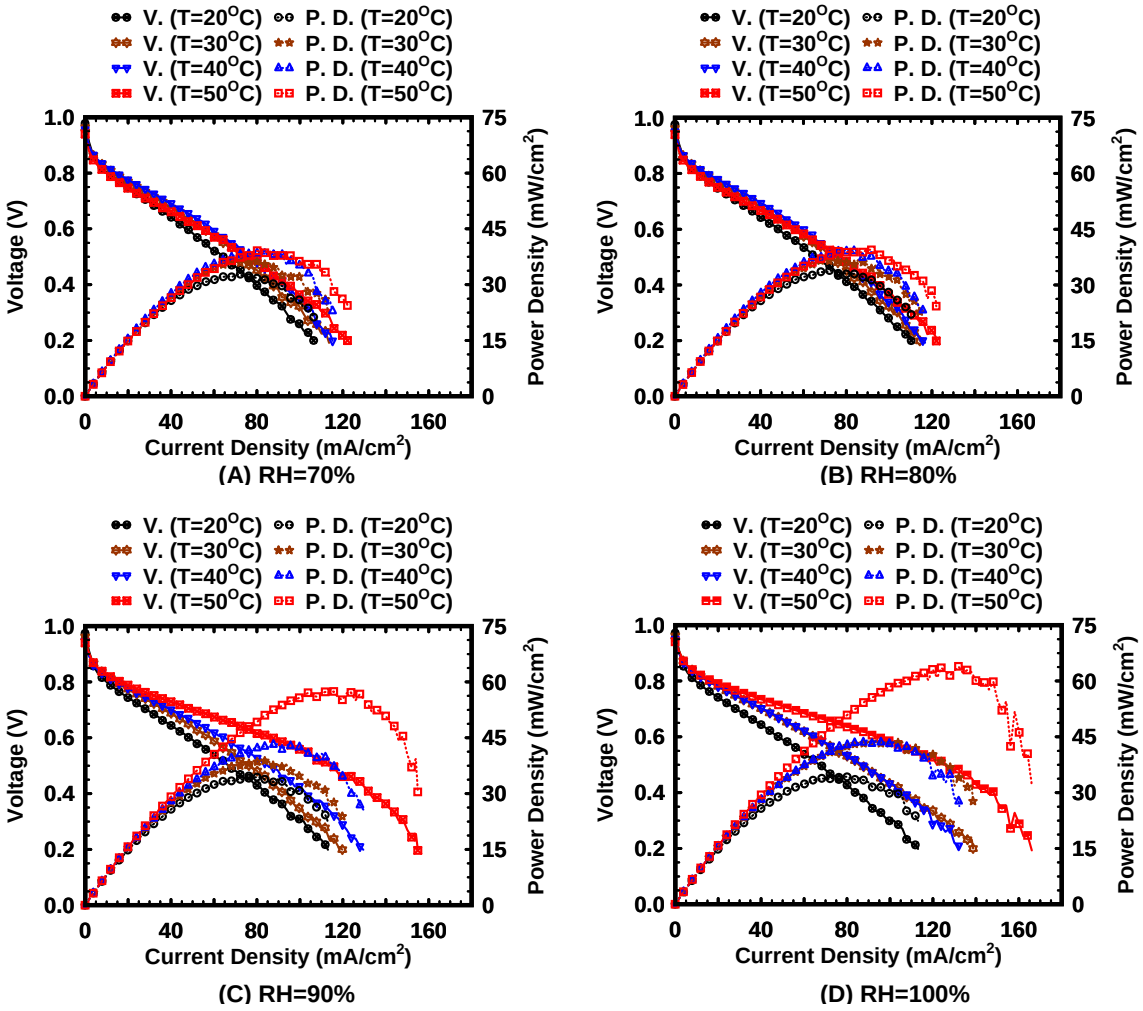

Figure 5-16 Polarization curves and power density curves as function of the current density with different temperature and relative humidity. Flow field type (I-type).

Figure 5-17 shows the current density and power density as functions of the test time. Two relative humidity (90% and 100%) and two temperatures (20°C and 50°C) were selected for comparison. After reaching the desired temperature and flow rate, open circuit voltage was measured for 30 seconds, and the current was discharged at a rate of 0.1 amps/second. When the voltage reached 0.2 volts, the current went back to zero to prevent irreversible damage to the MEA. The current remained at zero for 30 seconds, and then again was discharged at a rate of 0.1 amps/second. The cycle was repeated to investigate the rate of activation and long time operating stability.

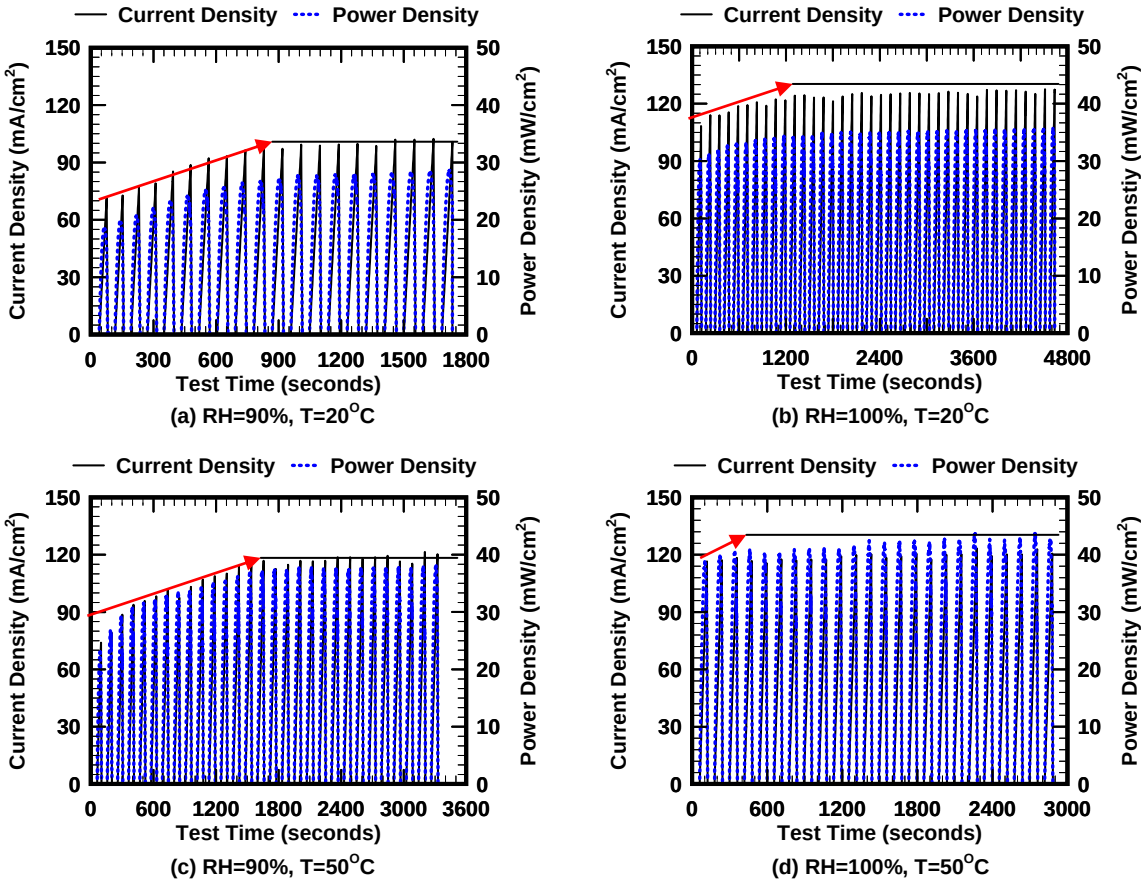

Figure 5-17 Current density and power density with testing time. Flow field type (II-type).

For the case of Figure 5-17 (a) (temperature 20^{o}C, RH=90%), the current density and power density increased with test time for the first 15 minutes, which was 10 cycles, and maintained around 100 mA/cm^2, 28 mW/cm^2, respectively. When the relative humidity was set to 100%, the current density and power density increased with test time for the first 10 cycles, which was 20 minutes, and maintained at 130 mA/cm^2 and 36 mW/cm^2, respectively. When the temperature was shifted to 50^{o}C, the current density and power density were increased for the first 15 cycles (around 27 minutes), and maintained. As shown in Figure 5-17 (d), the activation process didn't take too long. After a couple of cycles, the current density and power density obtained were 135 mA/cm^2, 45 mW/cm^2, respectively. The activation process is related to both the relative humidity and temperature.

5.3.2 Channel Depth Effect

Wong et al. (2006) conducted an experiment to determine the effect of flow channel depth on the performance using a direct methanol fuel cell. From their results, the performance increased rapidly when channel depth was reduced from 1.0 mm to 0.5 mm and 0.3 mm, but a further reduction from 0.3 mm to 0.2 mm and to 0.1 mm did not lead to better performance (Wong et al., 2006). Three different channel depths (0.5 mm, 1.0 mm, and 1.5 mm) using a numerical analysis model were examined by Inoue et al. (2006a). The cell voltage of a shallow channel (0.5 mm) was the highest at high current density among them since the differential pressure between adjoining channels increased in the case of the shallow channel (Inoue et al., 2006a). When the gas diffusion layer ef-

fective porosity was reduced, the effect of the channel depth was increased (Inoue et al., 2006b). When the channel was shallow, the gas flow rate through the gas diffusion layer increased, and the amount of water transfer from the cathode by back-diffusion was larger than that of vapor by gas flow (Inoue et al., 2006c). Whereas, in the case of deep flow type (II-type), the anode gas becomes dry compared to case of the shallow flow field (I-type). Even though the deep flow type was effective in uniform humidity distribution because the gas flow rate through the gas diffusion layers was reduced, which found using numerical study (Inoue et al., 2006c), air-breathing fuel cell, shallow flow type leads to better performance.

The current study examined the relative performance of the fuel cell as a function of channel depth. Figure 5-18 shows the polarization and power density curves as function of the current density with different temperature and relative humidity. Two different flow depths (0.5 mm depth and 1.3 mm depth) were selected for this study. For the case of I-type flow field, when the voltage reached 0.2 volts, the current density was almost 120 mA/cm^2 for the cases with 60% to 80% relative humidity as shown in Figure 5-18 (a) & (b). When the II-type flow field was used, the current density was only about 60 mA/cm^2 as shown in fig. Figure 5-18 (c) & (d), which was nearly half of the performance compared to the I-type flow field. When the relative humidity at the chamber was set to 90%, the current density reached 100 mA/cm^2 (II-type) and 130 ~ 140 mA/cm^2 (I-type). However, for the case of 100% relative humidity, the current density increased to about 130 mA/cm^2 (II-type) and 140 mA/cm^2 (I-type).

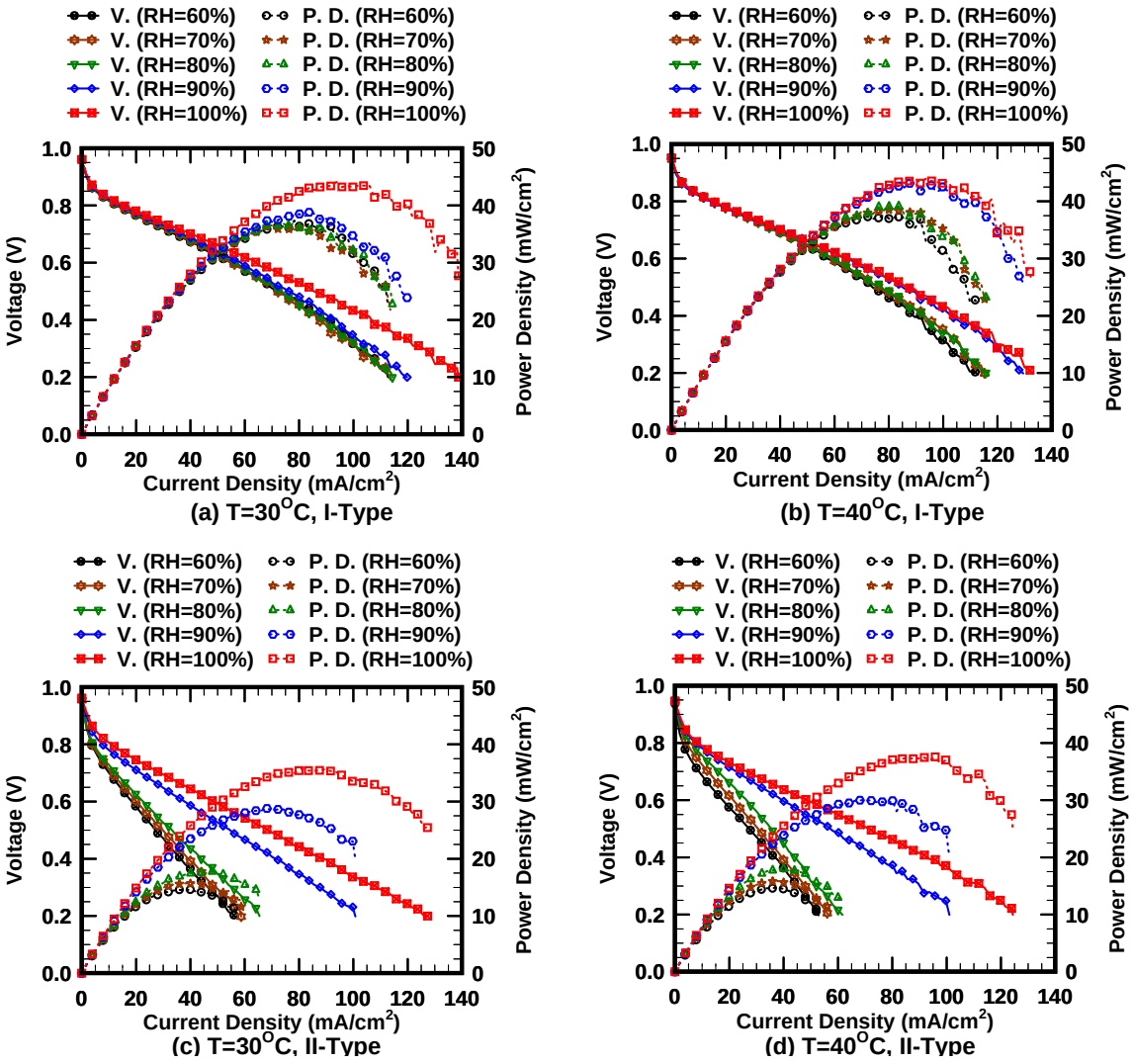

Figure 5-18 Polarization curves and power density curves as function of the current density with different temperature and relative humidity. Flow field type (I-type, II-type).

When the relative humidity is higher (90% or more), there is still a positive effect of the flow field depth, but the amount of increase of performance was less. The shallow flow field design plays a big role when the relative humidity is low at the environment condition since the gas flow rate through the gas diffusion layer increases. Using the

shallow flow field influences similarly effect of increasing of back pressure to the performance of fuel cell.

In summary, the shallow flow field deign improves dramatically the performance of the air-breathing fuel cell at low relative humidity, and slightly at thigh relative humidity.

5.4 Humidification Effect for a PEM Fuel Cell Stack

In this section (5.4), the effects of the inlet gases' relative humidity in a PEM fuel cell stack will be studied. The level of the inlet gases' relative humidity plays a role in water transport in the membrane and is related to thermal management in the fuel cell stack.

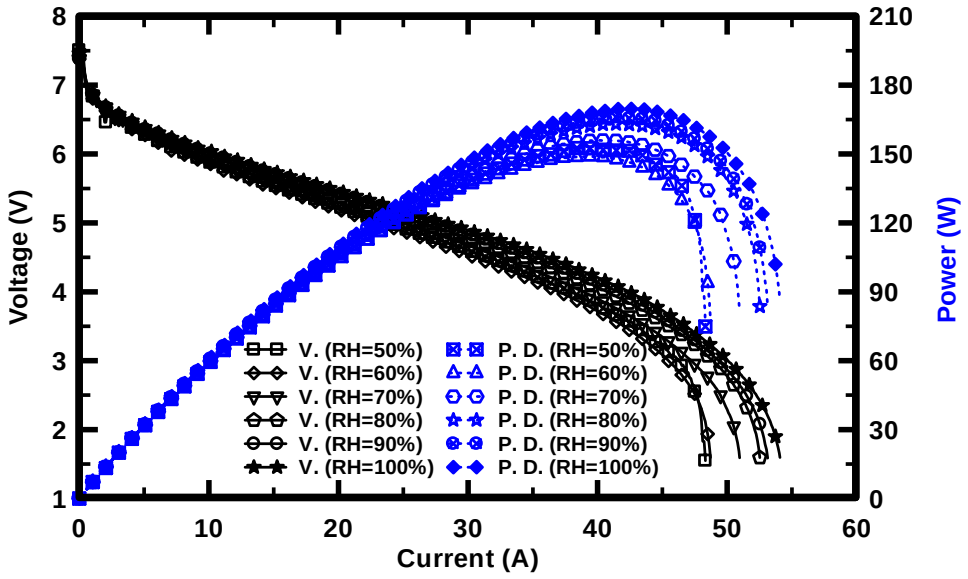

Figure 5-19 Polarization curves with different relative humidities at 70°C with fan cooling. St_H_2=1.2 and St_Air=3.

Figure 5-19 shows the voltage and power as a function of current with different relative humidity of the inlet gases. Since this stack had 8 cells in series, the open circuit voltage obtained around 7.5 volts. The maximum power obtained varied from 150 watts to 170 watts when the relative humidities of the inlet gases were varied from 50% to 100%, respectively.

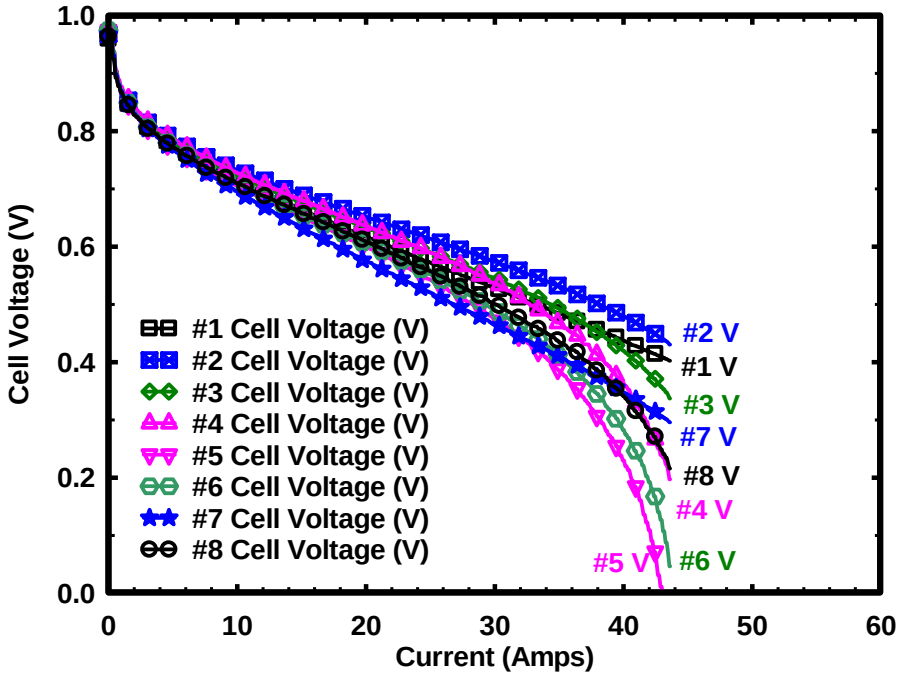

Figure 5-20 Cell voltages as a function of the discharged current. The temperature of the inlet gases were 70°C and the relative humidity was 80% with fan cooling. St_H_2=1.2 and St_Air=3.

Figure 5-20 shows the cell voltages as a function of the discharged current when the temperature of the inlet gases were 70°C and the relative humidity was 80% with fan cooling. The cells located around the center of the fuel cell stack (4th, 5th, and 6th cell) had a voltage drop after 30 amps, which resulted from the drying and overheating since no cooling media was supplied to the stack.

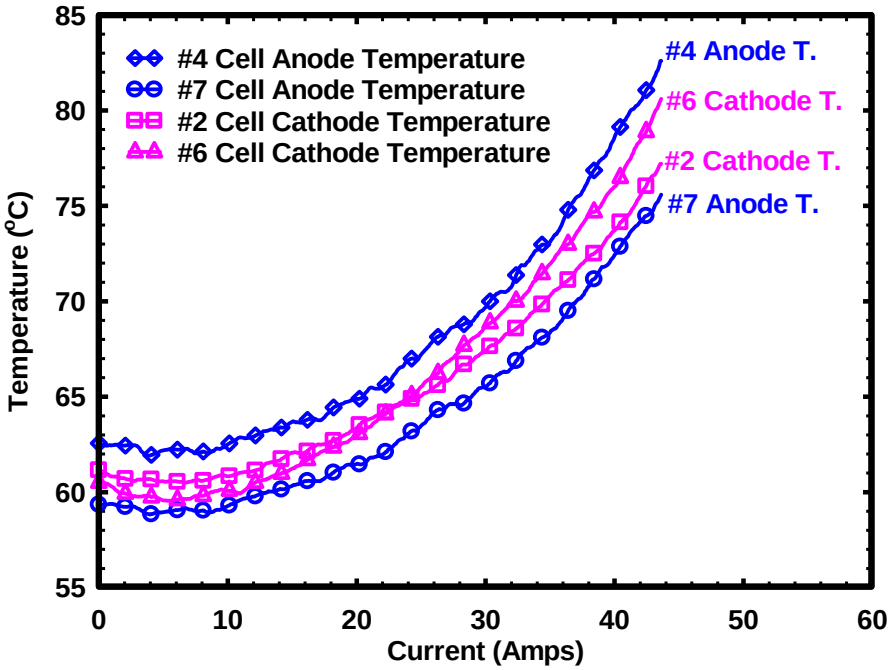

Figure 5-21 Cell temperature as a function of the discharged current. The temperature of the inlet gases were 70^{O}C and the relative humidity was 80% with fan cooling. St_H_2=1.2 and St_Air=3.

Figure 5-21 shows cell temperatures as a function of the discharged current. These temperatures were recorded at the same time as the polarization cycles for cases in Figure 5-20. At low current density, the cell temperature didn't increased a lot and remained steady. At high current density, the cell temperature increased sharply which led to the cell performance decreases.

Figure 5-22 shows the cell voltages as a function of the discharged current when the temperature of the inlet gases were 70^{o}C and the relative humidity was 90% with fan cooling.

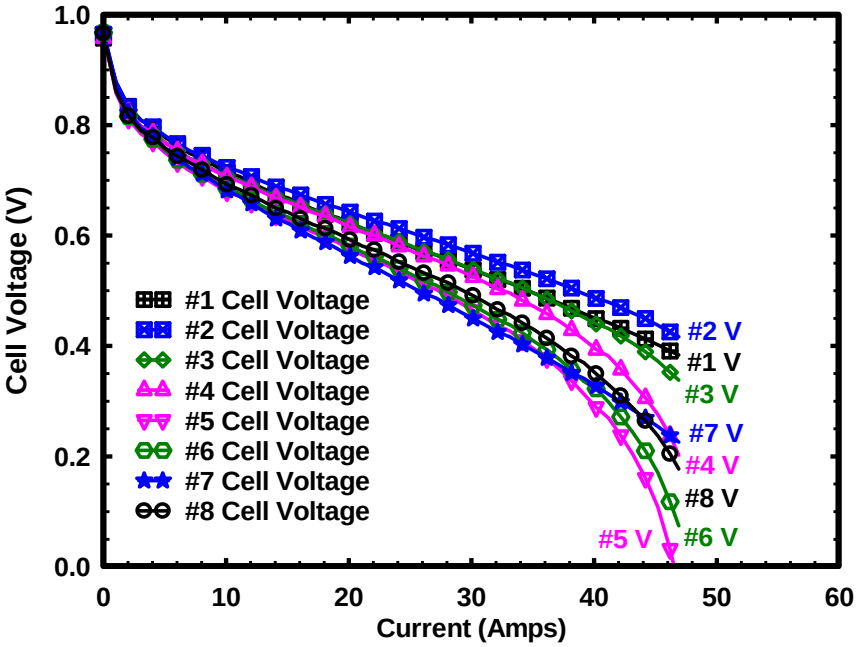

Figure 5-22 Cell voltages as a function of the discharged current. The temperature of the inlet gases were 70°C and the relative humidity was 90% with fan cooling. St_H_2=1.2 and St_Air=3.

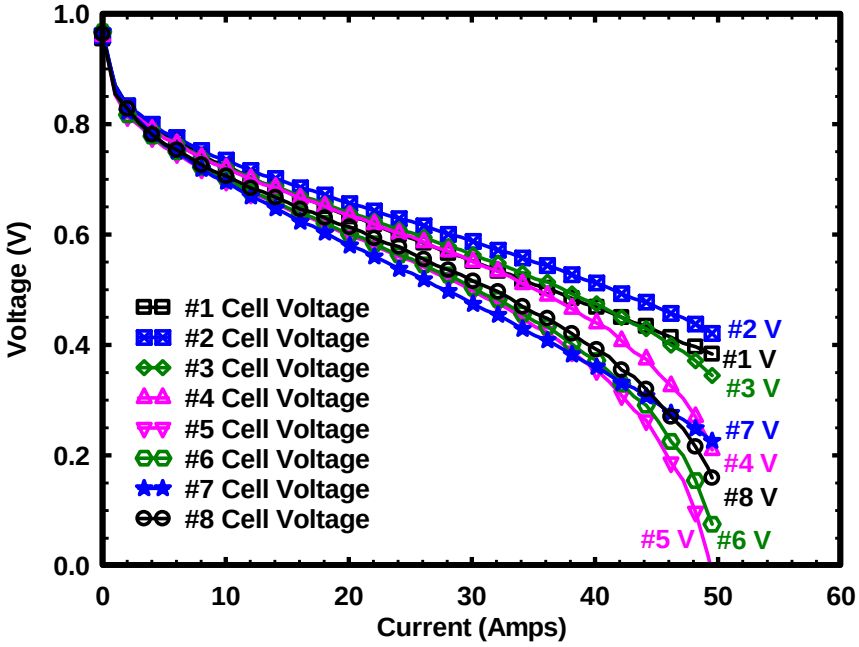

Figure 5-23 Cell voltages as a function of the discharged current. The temperature of the inlet gases were 70°C and the relative humidity was 100% with fan cooling. St_H_2=1.2 and St_Air=3.

Figure 5-23 shows cell voltages as a function of the discharged current when the temperature of the inlet gases were 70°C and the relative humidity was 100% with fan cooling. As seen in both figures (Figure 5-22 and Figure 5-23), cell voltages located at #1, #2, and #3 obtained much higher values than other cell's voltages, especially for the high currents. Since the inlet gases are supplied to one inlet, the hydrogen and air seemed to suffer from unequal distribution. If cell voltages had suffered from overheating, the cell voltages at the other side (#7 and #8) should have had higher voltages. Cell voltages located at cells #7 and #8 lacked sufficient inlet gases, voltage drop at cells #4, #5, and #6 resulted from the overheating. Equal distribution of the inlet gases for the fuel cell stack is left for future work.

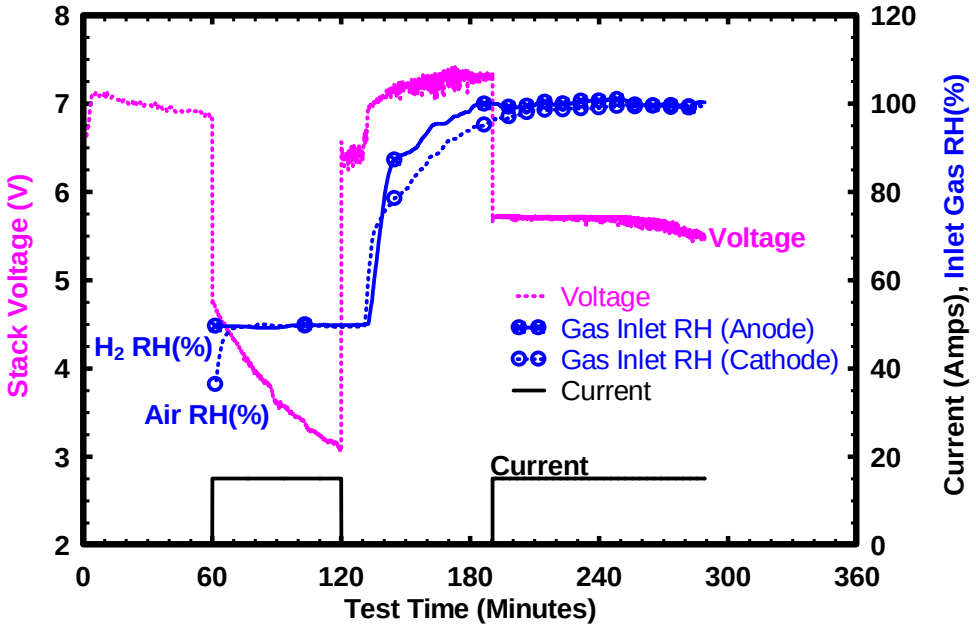

Figure 5-24 Stack voltage as a function of current with different inlet gases' relative humidity (50% and 100%). T=70°C, St_H_2=1.2 and St_Air=3.

Figure 5-24 shows the stack voltage corresponding to discharged current (15 amps). As an operation schedule, the open circuit voltage was measured for one hour to stabilize the relative humidity of the inlet gases, which was set to 50%. After one hour, fuel cell stack discharged 15 amps while the relative humidity of the inlet gases was maintained at 50% for one hour. After that, the relative humidity of the inlet gases was increased from 50% to 100%. Then, the fuel cell stack discharged 15 amps for 1 hour and 40 minutes. Air was supplied to the coolant channel and a fan was used to cool down the stack temperature. With the same operation conditions except for the relative humidity of the inlet gases, the obtained stack voltages were much different. For the case with 50% relative humidity, the stack voltage dropped from 4.7 to 3 volts for one hour. For the case with 100% relative humidity, however, the stack voltage maintained 5.7 volts for one hour and decreased a little after that.

The voltage drop shown in Figure 5-24 is related to drying operating conditions. To check whether the stack suffered from drying, cell temperatures at #2 cathode, #4 anode, #6 cathode, and #7 anode were measured (Figure 5-25). When the current discharged 15 amps, the cell temperatures increased around from 60 to 80^{o}C. For the region when the 100% relative humidity gases supplied, however, the cell temperatures maintained around 65^{o}C for one hour and then increased a little up to 70^{o}C.

As illustrated by these results, supplying fully hydrated inlet gases enabled protons to transport from the anode to the cathode easily and also helped the fuel cell stack to maintain operating temperature.

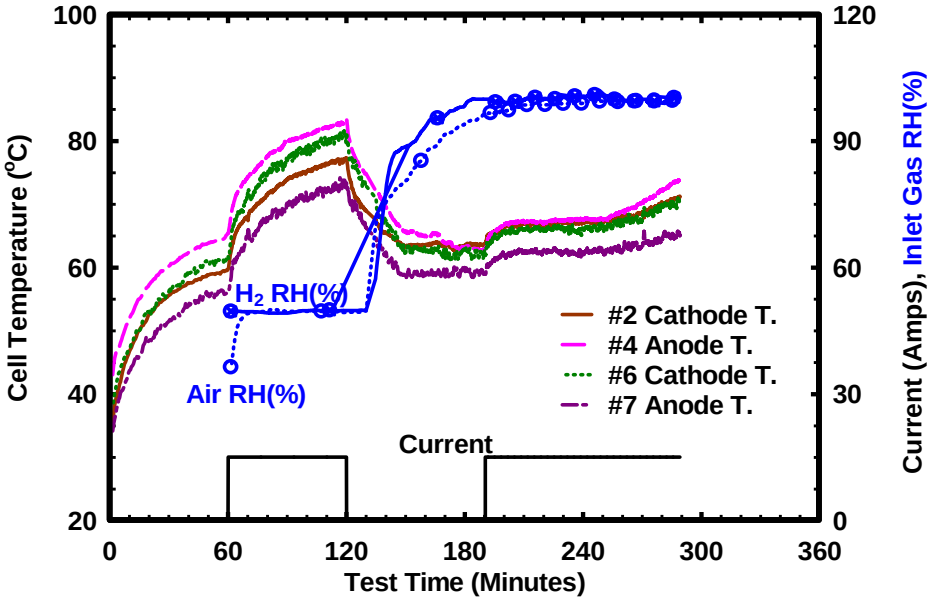

Figure 5-25 Cell temperatures variation with different inlet gases' relative humidity (50% and 100%). T=70°C, St_H_2=1.2 and St_Air=3.

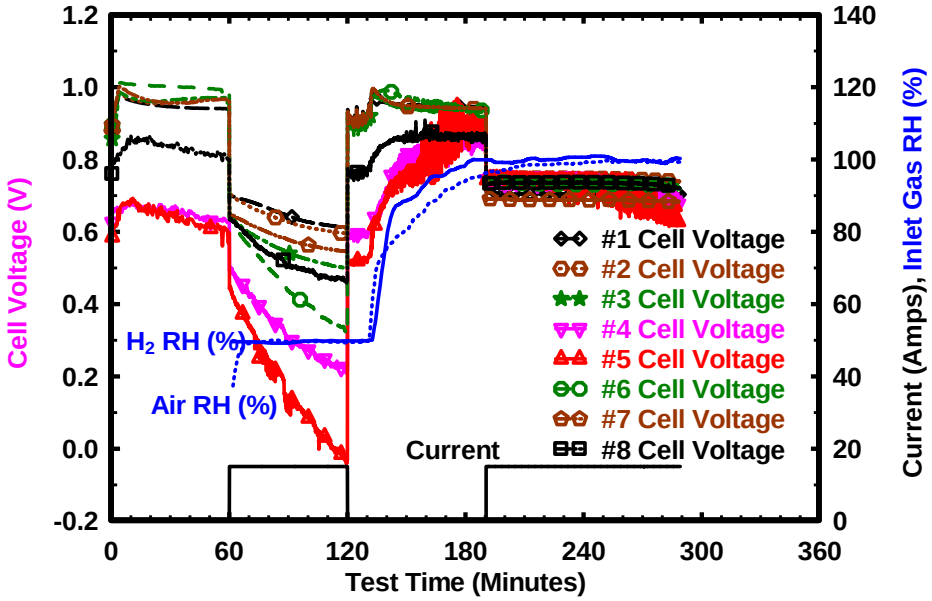

Figure 5-26 Cell voltages as a function of current with different inlet gases' relative humidity (50% and 100%). T=70°C, St_H_2=1.2 and St_Air=3.

Figure 5-26 shows the cell voltages corresponding to discharged current (15 amps). The cells located around the center: 4th, 5th, and 6th cells, had sharp drop of voltage during the first 15 amps discharged current when the 50% relative humidity gases was supplied, compared to the cases where the cells located at the sides: 1st, 2nd, 3rd, 7th, and 8th cells. When the relative humidity of the inlet gases increased to 100%, each cell obtained around 0.7 volts, regardless of where the cell was located. Increasing the relative humidity of the inlet gases from 50% to 100% provided the conditions for easy proton transport and maintained stack temperatures, as well.

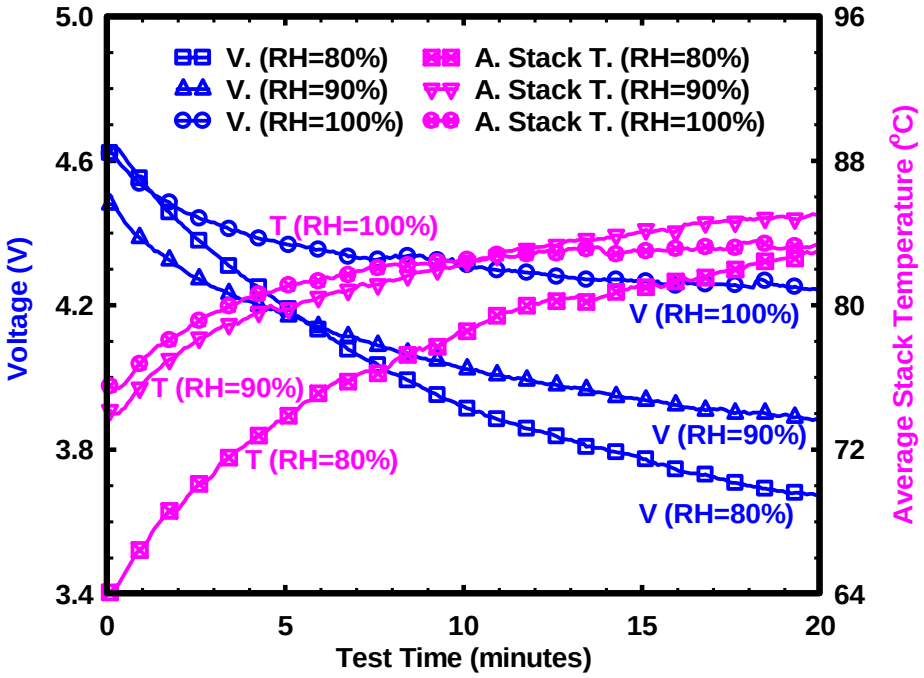

Figure 5-27 Voltage at constant current 25 amps with fan cooling. T=70°C, St_H_2=1.2 and St_Air=3.

Figure 5-27 shows the voltage and the average stack temperature as a function of the inlet gases' relative humidity at constant 25 amps. When the relative humidity of the inlet gases varied 80%, 90%, and 100%, the stack voltage dropped for 20 minutes

around from 4.6 volts to 3.7 volts, from 4.5 volts to 4.0 volts, and from 4.6 volts to 4.2 volts, respectively. In the meantime, the average stack temperatures increase from 64^{o}C to 83^{o}C, from 74^{o}C to 83^{o}C, and from 75 to 85^{o}C, respectively. From this result, it's known that the inlet gases play a role to maintain the stack temperature and each cell voltage.

5.5 Summary of This Section

Monitoring back pressure at the cathode provided information on whether the flow field suffered from flooding or not. When the fuel cell generated water and blocked some portions of the flow field, the back pressure increased. Supplying inlet gases enabled to push out the generated water until 0.8 A/cm^2 current density, after that point, generated water was not fully removed with the inlet gases. For the high current density conditions, additional water management techniques are needed to maintain the fuel cell performance.

Since water was generated during the electrochemical reaction, the case supplying 100% relative humidified gases did not lead to the best performance among tested conditions. For the case with 100% relative humidity, the voltage decreased faster than other cases at high current density.

Depending on the level of inlet gases' relative humidity, the fuel cell performance varied according to the water level of the inlet gases. To generate power from the fuel cell, the electrical circuit should be complete. When the hydrogen is supplied to the anode, the hydrogen oxidation reaction (HOR) will occur first, and then the generated

proton needs to transport from the anode to the cathode to make the electrical circuit. Water in a fuel cell plays an important role to achieve power during this process. The studies of water transport are described in the next section.

For this study, air was used for the oxidation process at the cathode. The amount of air to the cathode is related to the oxygen reduction reaction (ORR). For a fixed flow rate of hydrogen at the anode, more air leads to an increase of fuel cell performance, but when the air stoichiometric ratio was greater than 5, performance did not improve.

An air-breathing PEM fuel cell was studied to determine the effects of the flow depth and environmental conditions. When the temperature was low (such as 20^{o}C), the relative humidity does not play a big role on increasing the open circuit voltage. The shallow flow field design influenced dramatically the performance of the air-breathing fuel cell at low relative humidity, and slightly at high relative humidity. When the shallow flow field design is used, it increased the number of available reaction sites per unit area which lead that hydrogen transfer rate to electrode was increased by the gas flow through the gas diffusion layer.

Having fully hydrated inlet gases plays a good role both the water transport when the proton transports from the anode to the cathode and maintain fuel cell stack temperature to prevent the stack drying. Topics for future work include improving the distribution of the inlet gases to each cell, and thermal management related to overheated cells located at the center of the fuel cell.

6. EXPERIMENTAL INVESTIGATION OF THE WATER TRANSPORT IN A PEM FUEL CELL

In this section, the water transport in a PEM fuel cell will be studied experimentally. Through a water balance experiment, the electro-osmotic drag coefficient and the amount of water resulting from back diffusion will be found at given conditions.

6.1 Water Production Rate

As seen in equation (1.2), water is produced on the cathode side as a result of the electrochemical reaction, which is the rate of one mole for every two electrons. The rate of water production is defined as follows:

$$j_{H_2O\_prod} = \frac{i}{2F} \ [\frac{mol}{s*cm^2}] \tag{6-1}$$

where j is the molar flux of water, i is the current density [A/cm2], and F is the Faraday's constant (96,485 coulombs/electro-mol). When a proton moves from the anode to the cathode, water is "dragged". This is a called electro-osmotic-drag and the flux of dragged water is represented as follows:

$$j_{H_2O\_drag} = \xi(\lambda)\frac{i}{F} \ [\frac{mol}{s*cm^2}] \tag{6-2}$$

where ξ is the electro-osmotic drag coefficient defined as number of water molecules per proton and λ [$N(H_2O)/N(SO_3H)$] is the water content in the Nafion. After substituting the Faraday's constant and the molar mass of water (18.02 g/mol) into the equation (6.1), water production becomes

$$m_{H_2O\_prod} = 9.34 \times 10^{-5} \times i \tag{6-3}$$

Since water is generated at the cathode, there must be a concentration gradient between the anode and the cathode. When the concentration at the cathode is greater than the anode's, back diffusion occurs from the cathode and anode. The water back-diffusion flux can be determined by

$$j_{H_2O,back\_diffusion} = -\frac{\rho_{dry}}{M_m} D_\lambda \frac{d\lambda}{dz} \tag{6-4}$$

where ρ_{dry} is the dry density (kg/m^3) of the Nafion, M_m is the Nafion equivalent weight (kg/mol), D_λ is the water diffusivity in the Nafion, and z is the direction through the membrane thickness. The total water flux in the Nafion is the sum of the electro-osmotic drag and back diffusion as follows:

$$j_{H_2O} = \xi(\lambda)\frac{j}{F} - \frac{\rho_{dry}}{M_m} D_\lambda \frac{d\lambda}{dz} \tag{6-5}$$

6.2 Ionic Transport in Nafion

Figure 6-1 shows the chemical structure of Nafion. Nafion has a backbone structure and includes sulfonic acid ($SO_3^- H^+$) functional groups, which provide the site for transferring protons. The function, to transfer protons from the anode to the cathode, of the sulfonic acid depends on the presence of water since the protons form hydronium complexes (H_3O^+) and detach from the sulfonic acid side chains, which allows protons to move easily from the anode to the cathode. Zawodzinski et al. (1993) found a poly-

nomial equation to obtain a relationship between the water activity (a_w) on the faces of the membrane and the water content (λ) as follows:

$$a_w = \frac{p_w}{p_{sat}} \tag{6-6}$$

$$\lambda = 0.043 + 17.81 a_w - 39.85 a_w^2 + 36 a_w^3 \tag{6-7}$$

$$\lambda = 14 + 1.4(a_w - 1) \tag{6-8}$$

where p_w is the actual partial pressure of water vapor in the system and p_{sat} is the saturation water vapor pressure for the system at the temperature of operation.

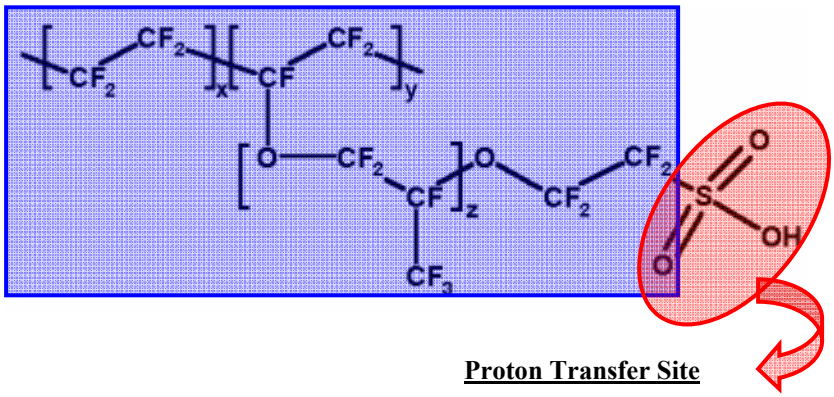

Figure 6-1 Chemical structure of Nafion.

The water content in the Nafion can be estimated using equations (6.6), (6.7), and (6.8) when the humidity conditions of the fuel cell are known. Figure 6-2 shows an example of this relation.

Another important term is the Nafion conductivity found by other researchers (Springer et al., 1991, Zawodzinski et al., 1993), which is strongly related to the water content and temperature.

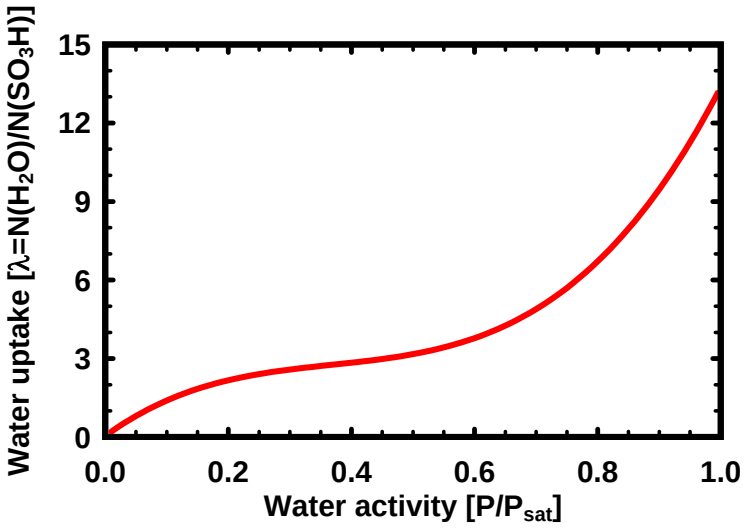

Figure 6-2 Water content versus water activity for Nafion 117.

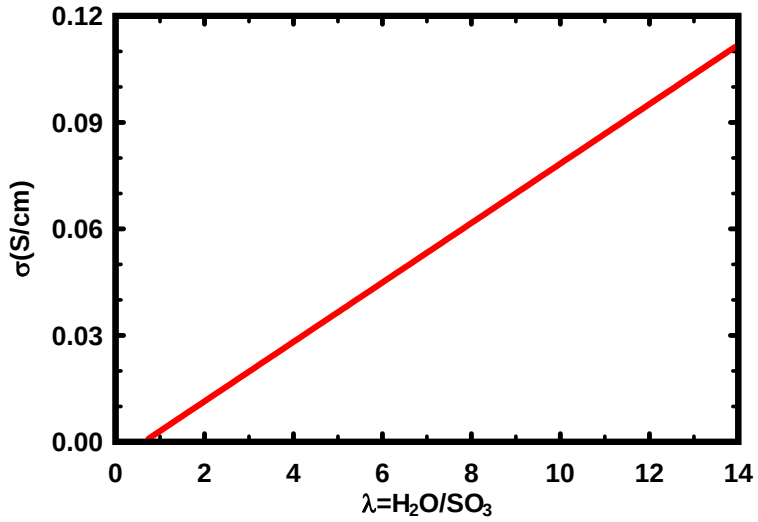

Figure 6-3 Ionic conductivity of Nafion versus water content λ at 70°C.

Based on experiments, correlation of the ionic conductivity (in S cm^{-1}) with water content (λ) and temperature (T) was found by Springer et al. (1991) as follows;

$$\sigma(T,\lambda) = (0.005139\lambda - 0.00326)\exp[1268(\frac{1}{303} - \frac{1}{T})] \qquad (6\text{-}9)$$

The proton conductivity increases linearly with increasing water content and exponentially with increasing temperature. For the case of 70°C temperature, the proton conductivity is plotted in Figure 6-3.

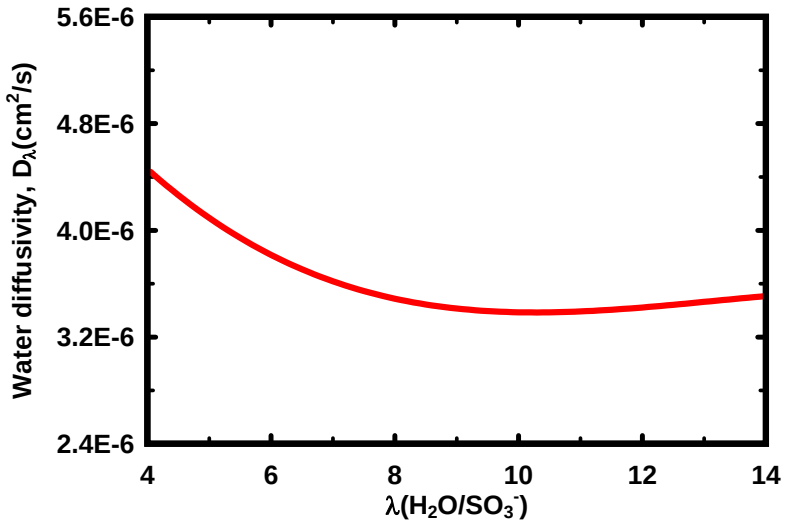

Figure 6-4 Water diffusivity D_λ in Nafion versus water content λ at 70°C.

The water diffusivity in Nafion is a term needed to understand water transport fully. Springer et al. (1991) found that the water diffusivity is a function of the water content and temperature and suggested following correlation based on their experiments.

$$D(\lambda) = \exp[2416(\frac{1}{303} - \frac{1}{T})] \times \frac{(2.563 - 0.33\lambda + 0.0264\lambda^2 - 0.000671\lambda^3)}{10^6}$$

for $\lambda > 4$ (6-10)

Figure 6-4 shows the water diffusivity (D_λ) in Nafion versus water content (λ) at 70°C. Motupally et al. (2000) suggested the following relationships from their own experiments by comparing the variation in literature values of water diffusivity.

$$D(\lambda) = 3.1\times10^{-3}\lambda(e^{0.28\lambda} - 1)\exp(\frac{-2436}{T}) \quad \text{for } 0 < \lambda < 3 \tag{6-11}$$

$$D(\lambda) = 4.17\times10^{-4}\lambda(161e^{-\lambda} + 1)\exp(\frac{-2436}{T}) \quad \text{for } 3 < \lambda < 17 \tag{6-12}$$

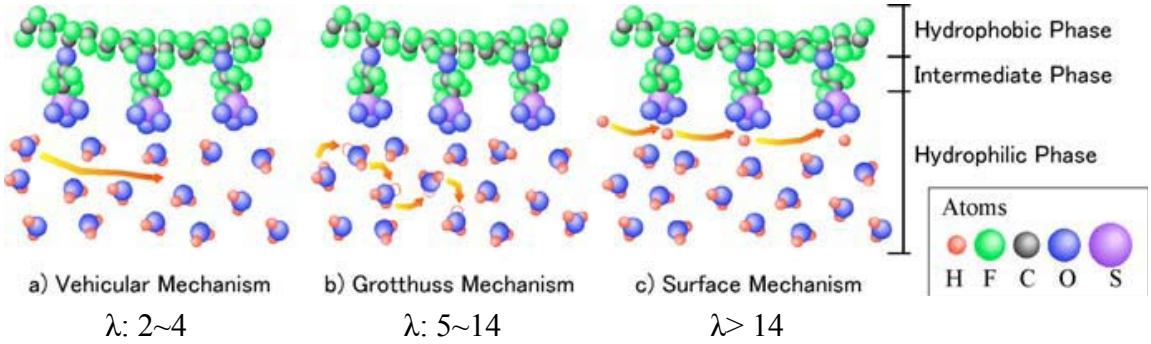

Figure 6-5[*] Proton conducting mechanism in Perfluorinated Sulfonic Acid membranes (Tsushima et al., 2006)

The proton conducting mechanism is illustrated at Figure 6-5. When the water content is very low (λ<4), there is a "vehicular mechanism" that hydronium ions (H_3O^+) move directly. As water content increases, protons "hop" from one water molecule to another by the formation and breakage of hydrogen bonds (5<λ<14). When they are fully hydrated (λ>14), protons are conducted along the array of Sulfonic acid groups easily and drag the water molecules. When the Nafion is fully hydrated with liquid water, Nafion maintains high proton conductivity comparable to that of a liquid electrolyte.

The amount of water supplied to the humidifier and the water drained out of the exhaust from a fuel cell was recorded by the water balance module. To capture all vapor from a fuel cell, chiller water (6^{o}C) was circulated through the exhaust to cool down the temperature of gases from a fuel cell.

[*] Reprinted with permission from "Experimental elucidation of proton conducting mechanism in a polymer electrolyte membrane of fuel cell by nuclei labeling MRI. 210 ECS Meeting – Cancun, Mexico, October 29 ~ November. Copyright 2006 by ECS.

Table 6-1 Test conditions for the water balance experiments. (A, C, RH stand for anode, cathode, and relative humidity of inlet gas)

Case	Current (Amps)	Current Density (A/cm^2)	A_RH (%)	C_RH (%)	T (^{O}C)
D-1	20	0.4	100	Dry	70
D-2	30	0.6			
D-3	40	0.8			
D-4	50	1.0			
D-5	60	1.2			
D-6	30	0.6	70	Dry	70
D-7	30	0.6	80		
D-8	30	0.6	90		
D-9	30	0.6	100		
D-10	20	0.4	50	50	70
D-11	30	0.6			
D-12	40	0.8			
D-13	50	1.0			
D-14	20	0.4	100	100	70
D-15	30	0.6			
D-16	40	0.8			
D-17	50	1.0			

Table 6-1 shows the test conditions for the study of the electro-osmotic drag and back diffusion in a PEM fuel cell. The temperature is set at 70^{o}C, and the relative humidity of the inlet gases varied from dry, 50 and 100%. The amount of water supplied to the humidifier was measured with different temperatures, relative humidities, and flow rates (Appendix A contains more details).

6.3 Net Electro-Osmotic Drag and Back Diffusion

6.3.1 Cases with 100% Relative Humidified Hydrogen and Dry Air at 70°C

Figure 6-6 shows the amount of water supplied to the anode's humidifier in proportion to the test time when the temperature was 70°C and relative humidity of 100%. As test conditions, the current was maintained at 10, 20, 30, 40, 50, and 60 amps, which corresponded to 0.2, 0.4, 0.6, 0.8, 1.0, and 1.2 A/cm^2, respectively. The active area of the fuel cell of 50 cm^2 was used for the water balance experiments. Each test ran about 8 hours (480 minutes) to get enough results. The amount of water supplied to the humidifier for the cases D-1, 2, 3, 4, and 5 was a linear relationship, which had the form of y=0.6739x, where y is the amount of water as "ccm" and x is the time in minutes. The correlation coefficient of the linear line as shown in Figure 6-6 was 0.9995. The amount of water supplied to the humidifier depends on the size of humidifier and the capacity of heater used in the humidifier.

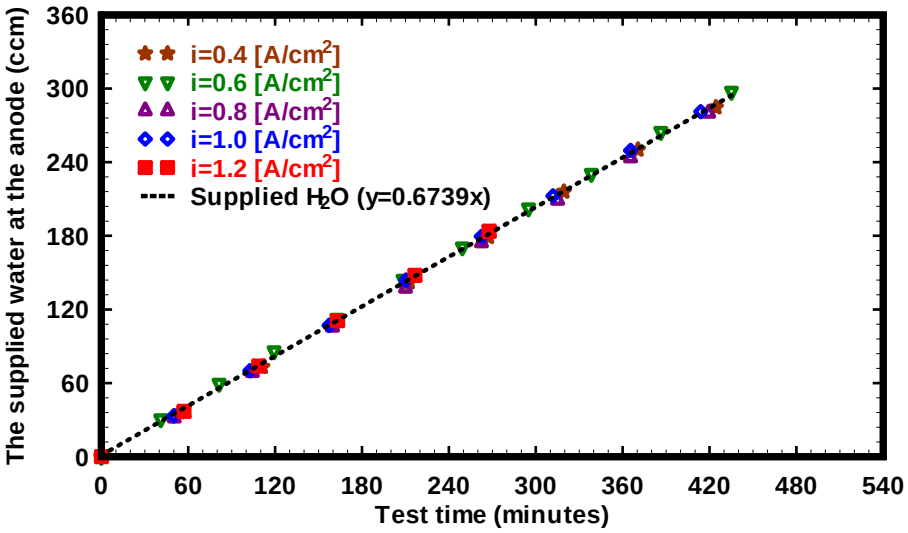

Figure 6-6 The amount of water supplied to the anode humidifier for cases D-1, 2, 3, 4, and 5. Linear curve fitting is plotted for all cases.

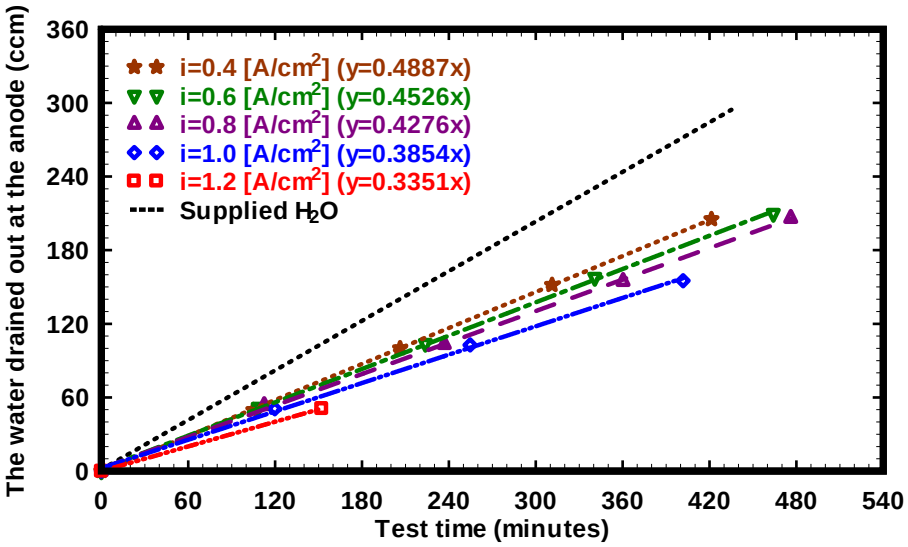

Figure 6-7 The amount of the water drained out to the anode exhaust for cases D-1, 2, 3, 4, and 5. Each linear line is the curve fitting for each result.

Figure 6-7 shows the amount of water drained out at the anode exhaust for the cases D-1, 2, 3, 4, and 5. When the current density increased, the amount of water drained out at the anode exhaust decreased. The linear trend-lines were obtained from the experimental results as shown in Figure 6-7. When the current densities were 0.4, 0.6, 0.8, 1.0, and 1.2 A/cm^2, the gradient of each linear line was decreased 0.4887, 0.4526, 0.4276, 0.3854, and 0.3351, respectively. The decreased amount of water at the anode exhaust explains that water was “dragged” from the anode to the cathode due to the movement of the protons.

As an internal consistency check, the balance of the input and output water was examined. It is expected that some portions of the water would have remained in the line of the system and leave as vapor with the exhausted gas.

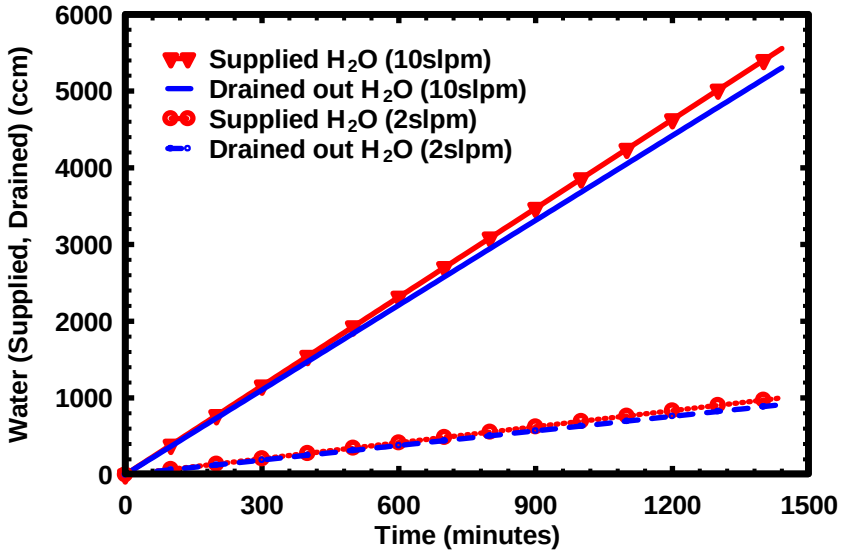

Figure 6-8 The amount of water supplied to the humidifier and drained out to the exhaust without discharging current.

Figure 6-8 shows the amount of water supplied to the humidifier and drained out to the exhaust without discharging a current of a fuel cell. The relative humidity of the inlet gases were 100% and the temperature was set to 70^{o}C. Supplied hydrogen and air were fixed at 2 slpm and 10 slpm for all cases, respectively. The 4.51% of cathode's input water and 8.87% of anode's input water were the amounts that water balance module could not detect in the system. This resulted from the water uptake in membrane, residual water in the system, and the water vapor that left with the exhausted gases. When the relative humidity of the inlet gases decreased, this amount not detected decreased. So, the above percentages (4.51% for cathode water input and 8.87% for anode water input) would be the maximum amounts not accounted for in this experiment.

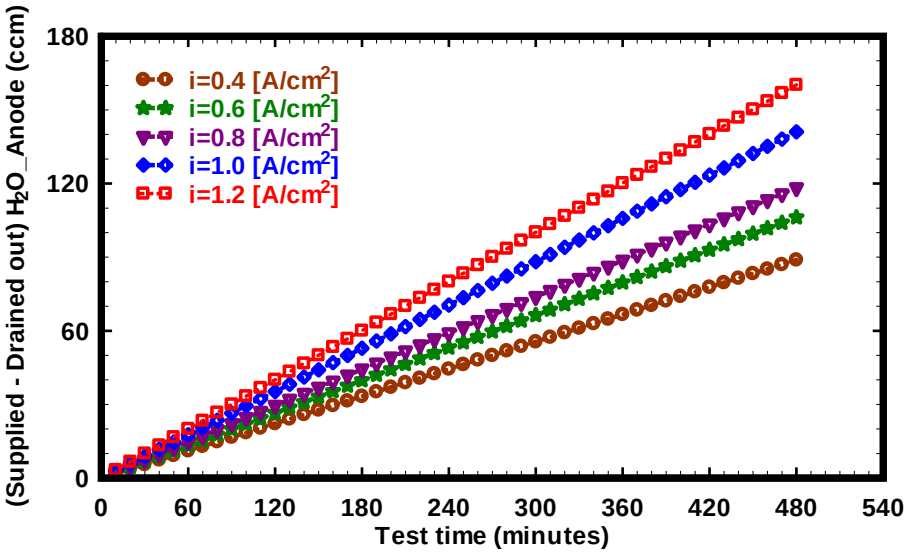

Figure 6-9 The amount of water deducting the drained out water from the supplied water at the anode of cases D-1, 2, 3, 4, and 5.

Figure 6-9 shows the difference between the amount of water supplied and drained at the anode exhaust for the cases D-1, 2, 3, 4, and 5. This amount of water was transported from the anode to the cathode during the reaction when the protons moved from the anode to the cathode with time.

The electro-osmotic drag coefficients for the cases D-1, 2, 3, and 4 were calculated and plotted in Figure 6-10 using equation (6.2) and data obtained from Figure 6-9. Detailed values including uncertainty for calculating the electro-osmotic drag coefficient were illustrated in Appendix B. When the current density increased, the electro-osmotic drag coefficient decreased. From these results, two main scenarios could be drawn. First, as the current density increased, more water was generated at the cathode catalyst layer by the oxygen reduction reaction (ORR). More generated water lead to the back diffusion, which resulted in the decrease of the net drag coefficient. Second, as the current

density increased, the flow of protons was increased. However, the protons' movement shared and dragged some of the water molecules together. These two scenarios probably occurred at the same time to explain these results.

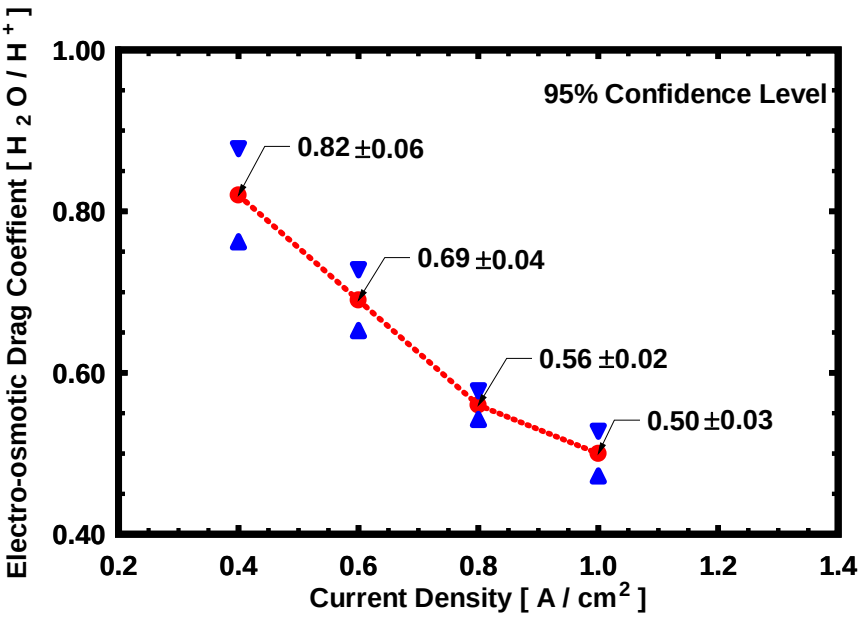

Figure 6-10 The electro-osmotic drag coefficients calculated from the water balance experiments at the anode for cases D-1, 2, 3, and 4.

From Figure 6-6 to Figure 6-10, the amount of water supplied to the humidifier, the amount of water drained out at the exhaust, the amount of water transported from the anode to the cathode, and the net drag coefficient were examined.

The amount of water drained out to the cathode exhaust was plotted in Figure 6-11. Since no water was added to the inlet air flow, the amount of water drained out to the cathode exhaust included the amount of water transported from the anode to the cathode because of the electro-osmotic flow and the generated water during the electrochemical reaction.

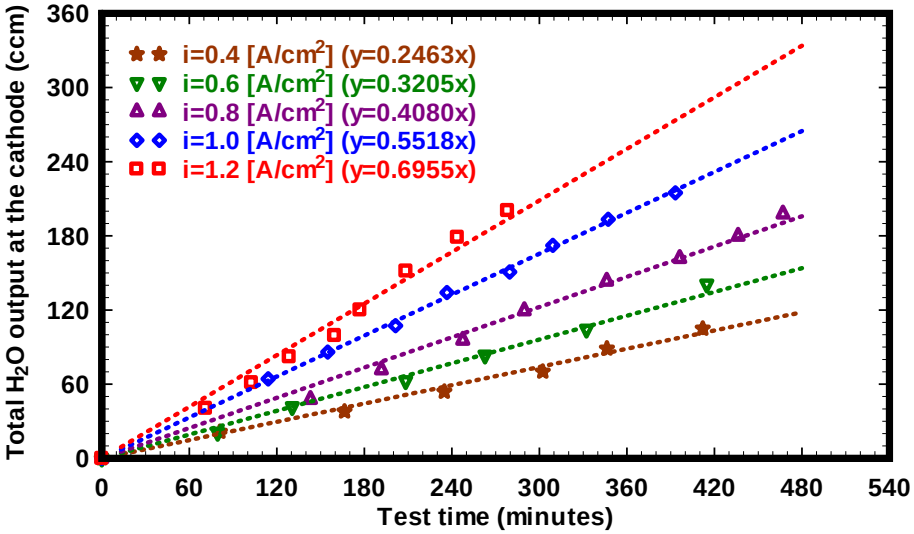

Figure 6-11 The amount of the drained out water to the cathode exhaust for cases D-1, 2, 3, 4, and 5. Each linear fitting is the curve fitting for each result.

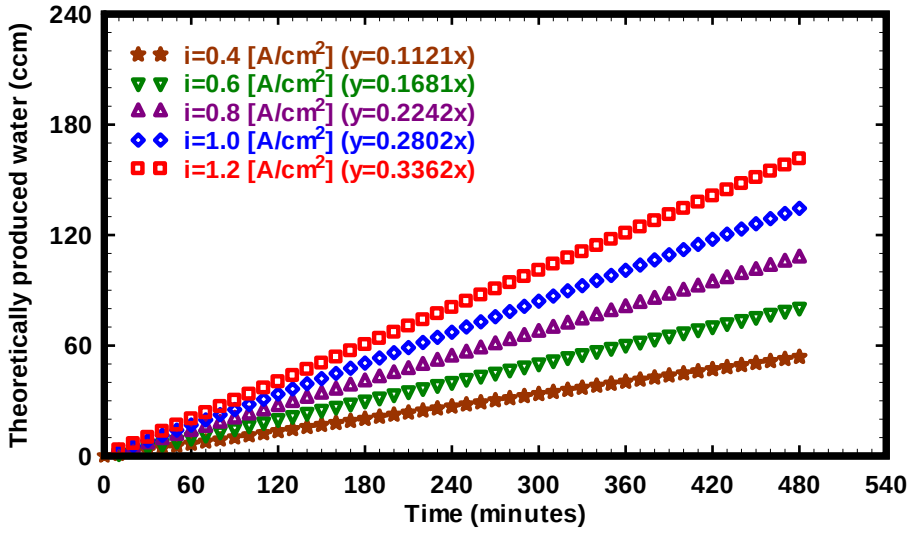

Figure 6-12 Theoretically produced water at the cathode according to the current density [A/cm^2].

Using equations (6.1) and (6.3), the theoretically produced amount of water owing to the electrochemical reaction was calculated and plotted in Figure 6-12. This amount of water using the equation (6.1) is not related with the level of relative humidity

of the inlet gases, only the product from the electrochemical reaction. To compare the experimental data for this research, the generated amount of water was represented with test time.

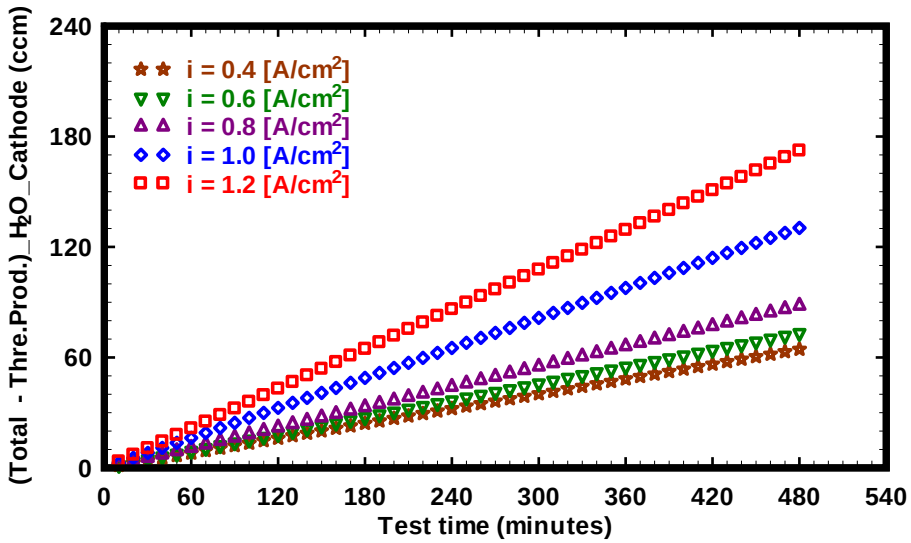

Figure 6-13 The amount of water deducting the theoretically produced water from the total water output at the cathode for cases D-1, 2, 3, 4, and 5.

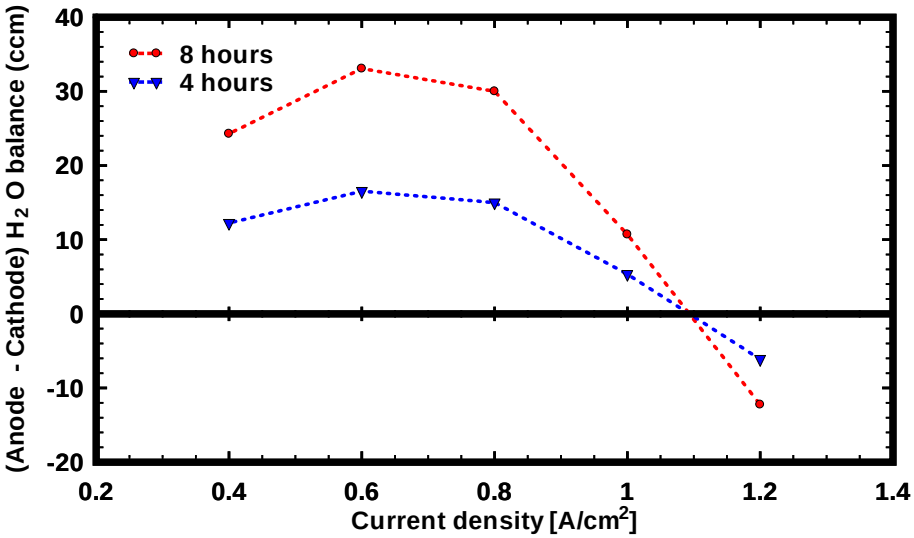

Figure 6-14 The difference between transported water from the anode to the cathode and the amount of water captured at the cathode for cases D-1, 2, 3, 4, and 5.

Figure 6-13 shows the difference between the theoretically produced water and the total water output at the cathode exhaust for cases D-1, 2, 3, 4, and 5. If the water balanced between the anode and the cathode, the amount of water shown both Figure 6-9 and Figure 6-13 should have been equal.

The amount of the water difference between Figure 6-9 and Figure 6-13 was plotted for two cases (4 hours and 8 hours) in Figure 6-14. The water balance (Total supplied – Total drained out) at the anode is higher than the water balance (Total drained out – Theoretically produced water) at the cathode for all cases D-1, 2, 3, and 4, except the case D-5. The water balance difference mainly resulted from the water uptake in the membrane, not captured water in the testing system line, and some residual vapor not collected between the anode/cathode outlets to the anode/cathode exhausts. As seen in Figure 6-14, the starting point when the water concentration gradient at the cathode was higher than anode's between the current density 1.0 and 1.2 A/cm^2. This is a point when the back diffusion occurred since the water concentration at the cathode was higher than the anode's. Even though there was no water added to inlet air at the cathode, as comparing both Figure 6-6 and Figure 6-11, the total water output at the cathode for the case D-5 was higher than the total input water at the anode. Comparing the two results in Figure 6-14, back diffusion occurred when the cathode's water concentration gradient was higher than the anode's.

Figure 6-15 (a) shows voltage and power density as a function of the current density, which was obtained after finishing test runs D-1, 2, 3, 4, and 5. Operating a fuel cell after passing by the maximum power density does not make sense since it consumes

more fuel. Also, it is hard to maintain the voltage because of mass transport loss and more generated water compared to the lower current density cases.

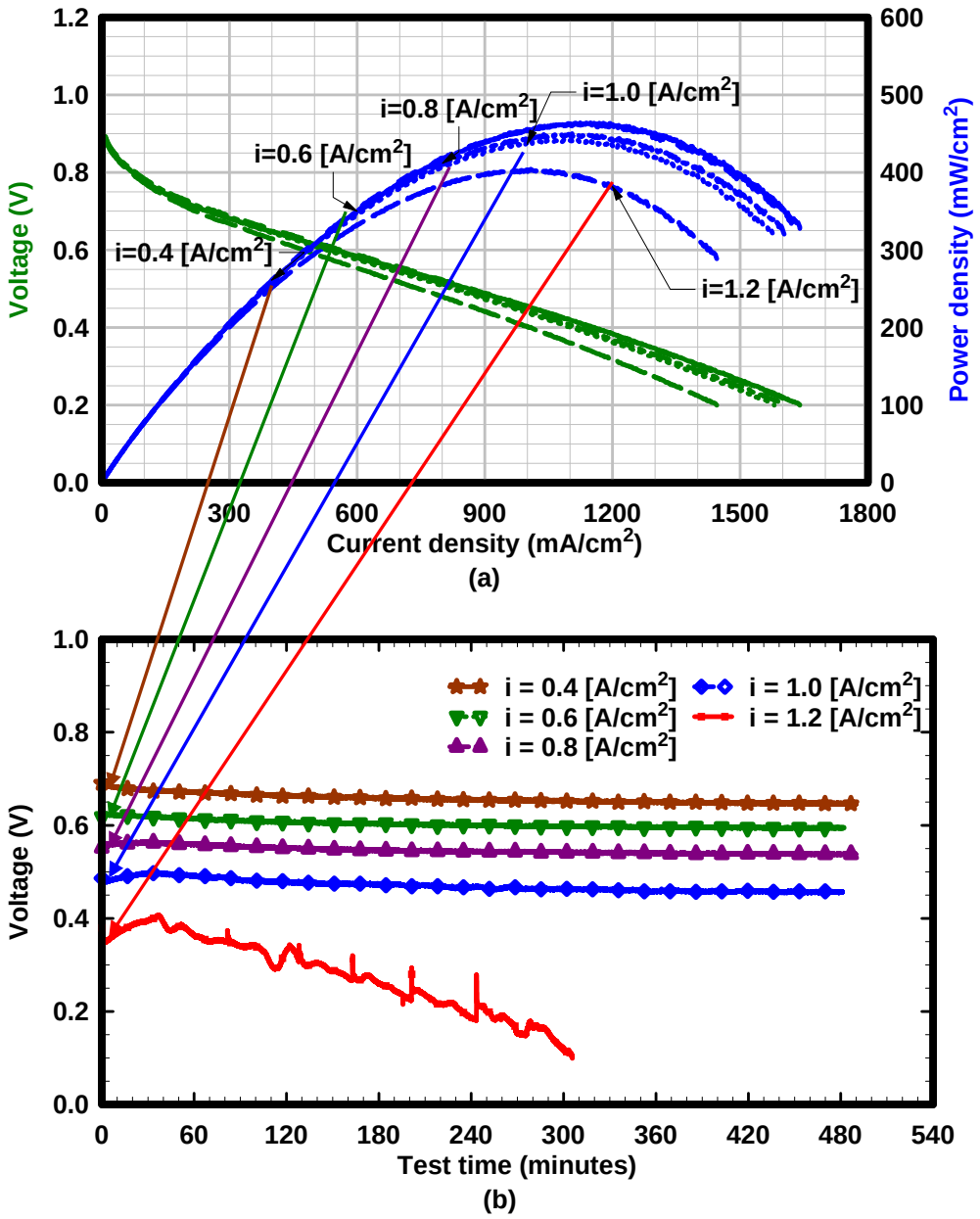

Figure 6-15 (a) Voltage and power density as a function of current density for the cases D-1, 2, 3, 4, and 5. (b) Voltage with test time at a constant current density for cases D-1, 2, 3, 4, and 5.

Figure 6-15 (b) shows the voltage responses during the constant current density, which were 0.4, 0.6, 0.8, 1.0, and 1.2 A/cm^2. As shown in Figure 6-15 (b), the voltage maintained during testing times, except the case D-5. For the case D-5, the voltage started 0.35 volts and dropped to the 0.1 volts after running 6 hours. This unstable performance mainly resulted from the mass transport block because of generated water and concentration over-voltage. For case D-1, 2, 3, 4, and 5, there was no water added to the inlet air. However, for the case D-5, the total water out at the cathode was higher than the water supplied to the anode. There must be a back diffusion only for the case D-5. That's the reason for the minus water balance for the case D-5, when compared with Figure 6-6 and Figure 6-11.

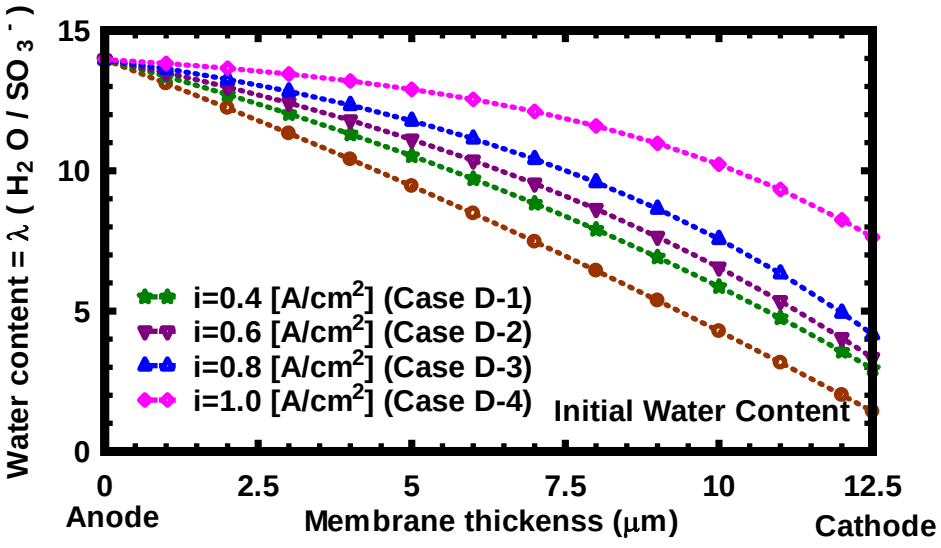

Figure 6-16 Calculated water content profile across Nafion membrane after discharging each current density for the cases D-1, 2, 3, 4, and 5.

Water content profiles across the Nafion membrane were calculated and plotted in Figure 6-16 using equations (6.1) to (6.12), results in Figure 6-6 and Figure 6-11, and

the boundary conditions. The initial boundary conditions were that the water activity (a_w) at the anode and cathode were 1 and 0.1, respectively, which were the inlet conditions of inlet gases. From the water activity values, the water content at the initial operation was obtained. The first assumption for calculating the water content profile was that the value of the water diffusivity in the Nafion was chosen with the average value between both sides of boundary. The second assumption for calculating the water content profile was that the final values of the water activity were obtained comparing the amount of inlet water to the anode to the sum of both the amount of water dragged from the anode to the cathode and the amount of water generated at the cathode. As seen in Figure 6-16, the water content of the layer contacting the cathode in the Nafion membrane was initially 1.428. After discharging constant currents (0.4, 0.6, 0.8, and 1.0 A/cm^2) continuously, protons dragged the water molecules and the water content in the Nafion membrane increased from 1.428 to 2.948, 3.334, 4.169, and 7.633 for the cases D-1, 2, 3, and 4, respectively.

The local conductivity across the Nafion membrane after discharging current was calculated and plotted in Figure 6-17 using equations (6.6) to (6.9) and the results in Figure 6-6 and Figure 6-11. Since the local conductivity is a function of water content and temperature, the shape of the local conductivity profile is as same as water content in Figure 6-16.

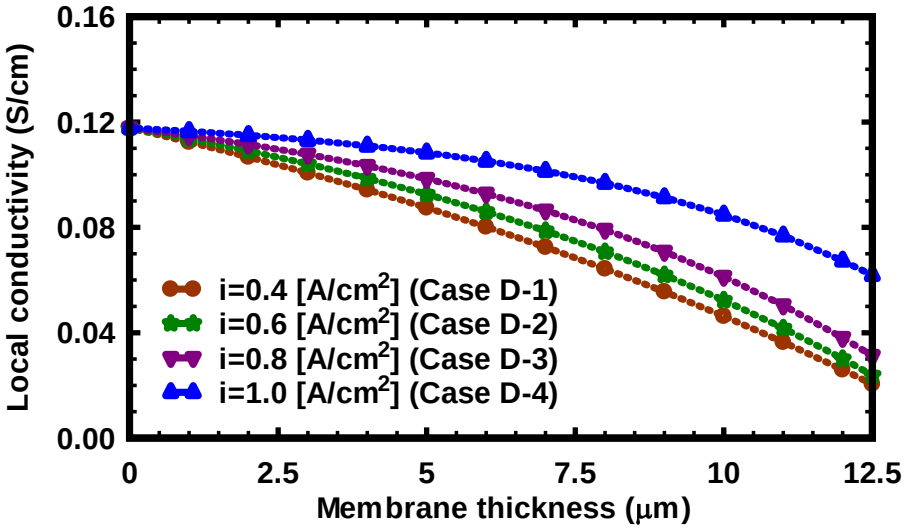

Figure 6-17 Calculated local conductivity across Nafion membrane after discharging each current density for the cases D-1, 2, 3, and 4.

6.3.2 Cases with 70, 80, 90, and 100% Relative Humidified Hydrogen and Dry Air at 70°C

In section 6.3.1, the water transport, the electro-osmotic drag, and back diffusion with cases having 100% relative humidity of hydrogen and dry air at 70°C temperature were studied. In this section (6.3.2), those items were studied with different relative humidities (70, 80, 90, and 100%) of the inlet hydrogen when the temperature set 70°C and current density was maintained at 0.6 A/cm^2.

Figure 6-18 shows the amount of the water supplied to the anode humidifier for cases D-6, 7, 8, and 9. The amount of water drained out at the anode exhaust for cased D-6, 7, 8, and 9 are shown in Figure 6-19. Experimental data points were plotted with test time as the x-axis and the amount of water as the y-axis. Linear curve fittings (trend line) were added to each case for the water balance calculation.

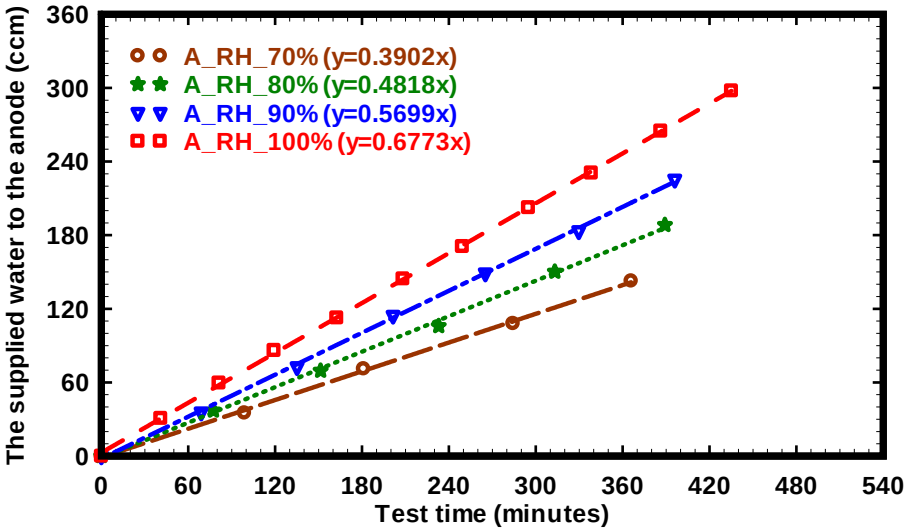

Figure 6-18 The amount of water supplied to the anode humidifier for the cases D-6, 7, 8, and 9.

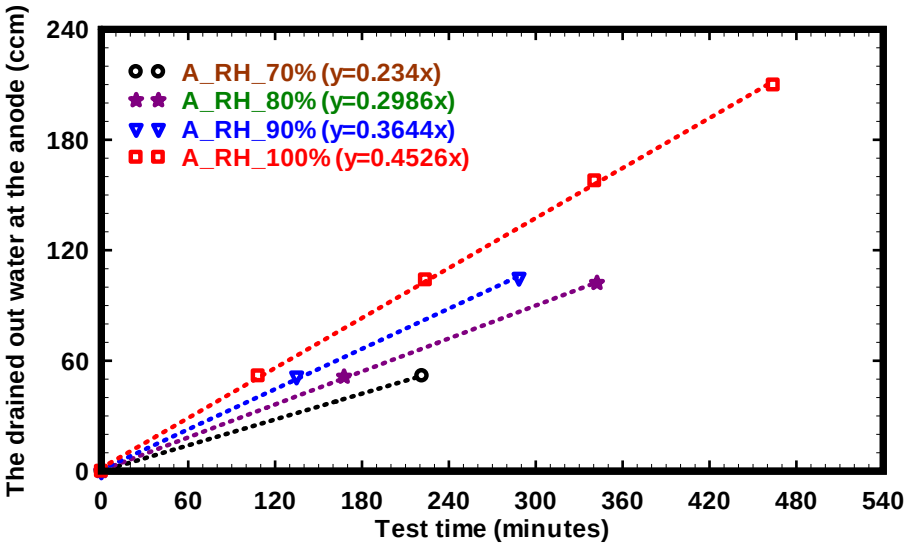

Figure 6-19 The amount of water drained out at the anode exhaust for the cases D-6, 7, 8, and 9.

After determining how much of the water supplied to the anode humidifier and how much of the water drained out to the anode exhaust, the amount of water dragged from the anode to the cathode for case D-6, 7, 8, and 9 was plotted in Figure 6-20. The electro-osmotic drag coefficients for the cases D-6, 7, 8, and 9 were calculated and plot-

ted in Figure 6-21 using equation 6.2 and the data obtained from Figure 6-20. Detailed values including uncertainty for calculating the electro-osmotic drag coefficients for cases D-6, 7, 8, and 9 were illustrated in Appendix B.

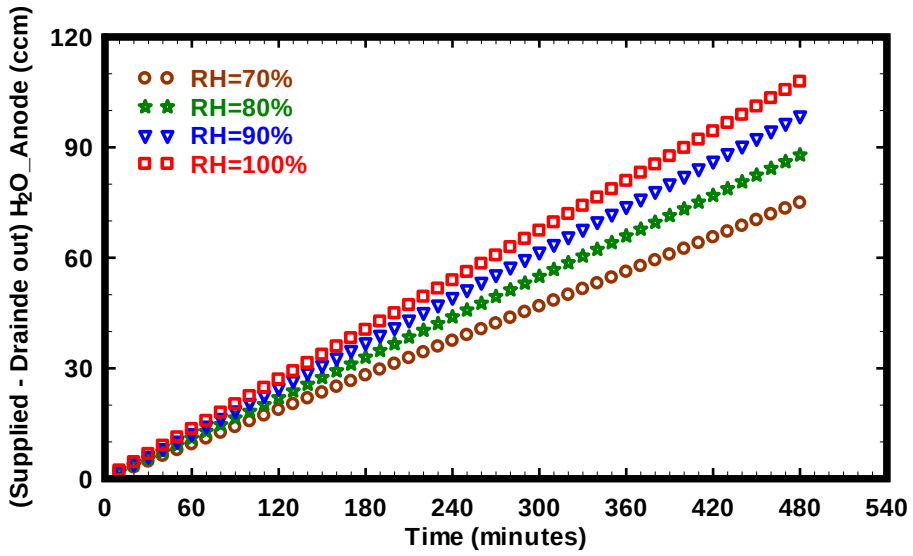

Figure 6-20 The amount of water deducting the drained out water from the supplied water at the anode for cases D-6, 7, 8, and 9.

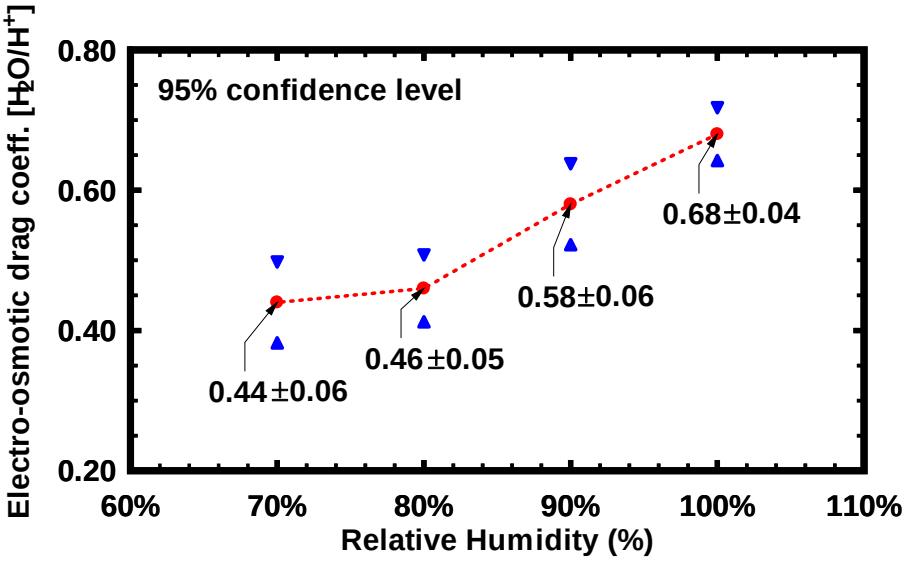

Figure 6-21 The electro-osmotic drag coefficients calculated from water balance at the anode for cases D-6, 7, 8, and 9.

When the relative humidity of the inlet hydrogen gas increased, the net drag coefficient increased. As the water content in the membrane increased, the numbers of water molecules dragged by protons increased at the constant current density. The case D-2 and D-9 in Table 6-1 were the same conditions. The case D-2 was run for the section 6.3.1 and the case D-9 was run for the section 6.3.2. The same condition was done twice. From running the same test running twice, the electro-osmotic drag coefficient was obtained 0.658 and 0.668, which was almost same result.

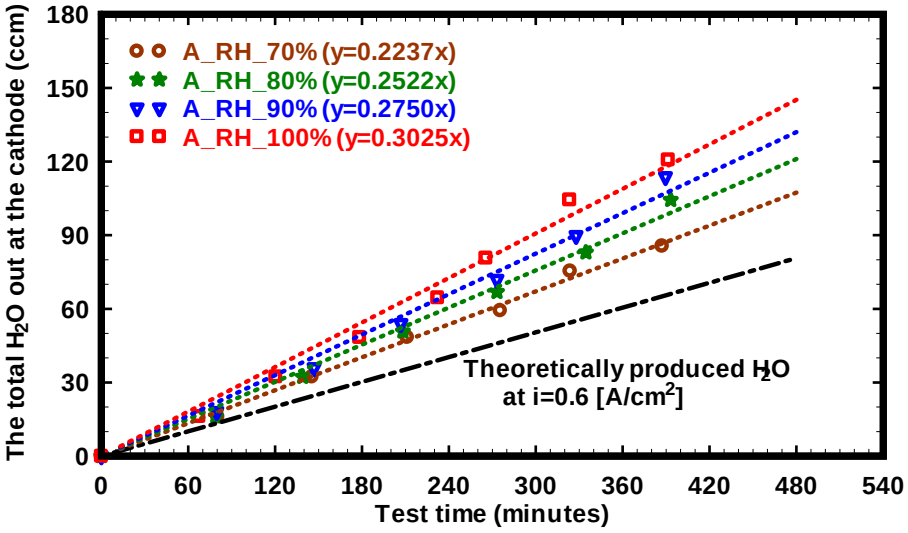

Figure 6-22 The amount of water at the cathode outlet for cases D-6, 7, 8, and 9. Linear fitting is the curve fitting for each result.

Figure 6-22 shows the amount of water drained out at the cathode exhaust for cases D-6, 7, 8, and 9. Each data are shown with symbol and linear trend lines were plotted for each case. Theoretically produced water at 0.6 A/cm^2 of current density was plotted for comparing how much of the water was transported from the anode to the cathode by electro-osmotic drag. The gap between each plotted lines and theoretically produced

water are the amount of water transported from the anode to the cathode with protons. The amount of water deducting the theoretically produced water at the current density 0.6 A/cm^2 from the total water output at the cathode exhaust for cases D-6, 7, 8, and 9 was shown in Figure 6-23. Since the total amount of water at the cathode exhaust was less than the supplied amount of water for all cases D-6, 7, 8, and 9, there was no chance to occur the back diffusion.

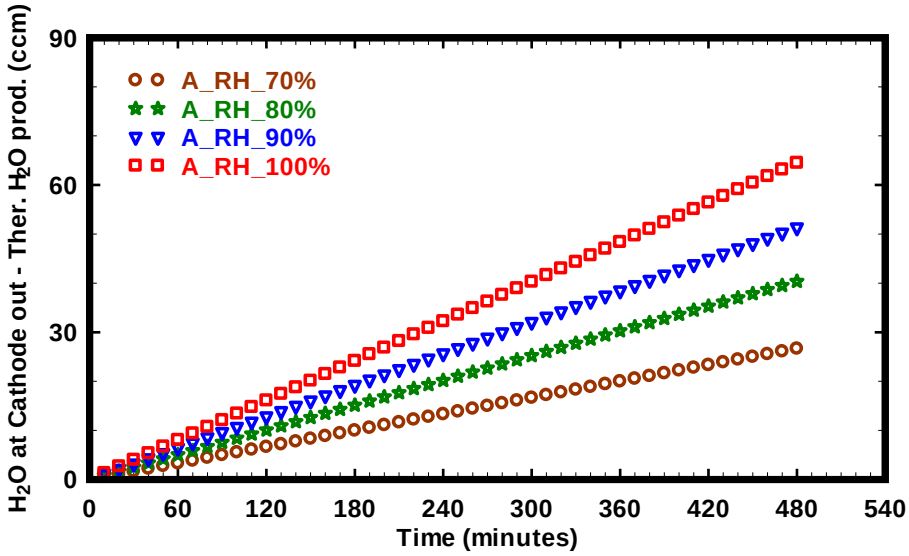

Figure 6-23 The amount of water deducting the theoretically produced water from the total water output at the cathode for the cases D-6, 7, 8, and 9.

Figure 6-24 shows the water balance between the anode and the cathode for the two times (4 hours and 8 hours). This difference resulted from the water uptake in the membrane, the residual water not captured in both the line between the anode/cathode inlet and the anode/cathode exhaust, and vapor leaving with the vented gases.

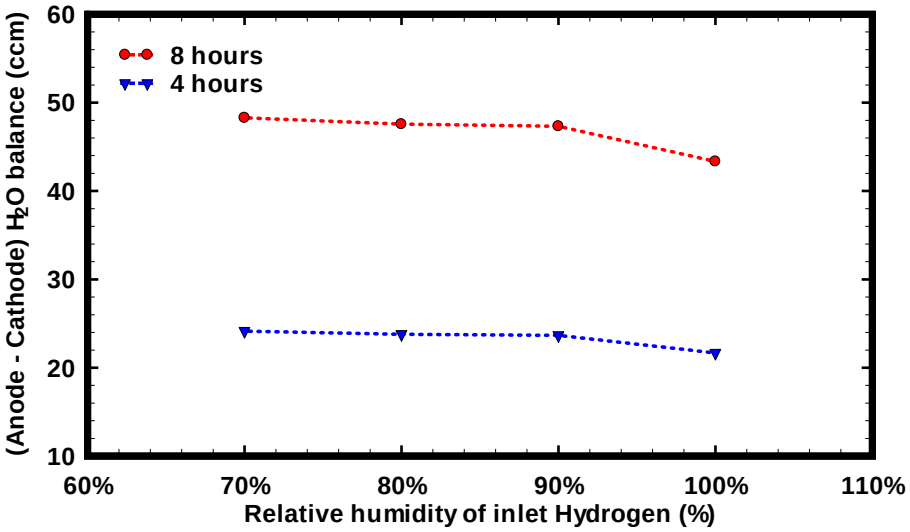

Figure 6-24 The difference between transported water from the anode to the cathode and the amount of water captured at the cathode for the cases D-6, 7, 8, and 9.

As seen in Figure 6-21, when the relative humidity of the inlet hydrogen gas was increased, the electro-osmotic drag coefficient was increased. The water balance between anode and cathode decreased when the relative humidity of the inlet hydrogen gas increased, which resulted from more water molecules transported from the anode to the cathode at high water content. Another reason is, for the cases (D-6, 7, and 8) with lower relative humidity, the gas diffusion layer and the electrode membrane holds more water compared to the cases of D-9. For the case D-9, since fully hydrated water vapor supplied to the anode, the water uptake ability already reached a maximum, which lead more water to move from the anode to the cathode. As a result of this, the water balance difference for the case D-9 shown in Figure 6-24 was less than the case of D-6, 7, and 8.

Calculated water content profiles across the Nafion membrane for initial stage and after discharging constant current density 0.6 A/cm^2 for the case D-6, 7, 8, and 9

were obtained and plotted in Figure 6-25 and Figure 6-26. Initial boundary conditions for the cases D-6, 7, 8, and 9 were that water activity of the anode varied 0.7, 0.8, 0.9, and 1 whereas the water activity of the supplied air was 0.1. The way that the water activity was obtained at the cathode after discharging current density of 0.6 A/cm^2 was the same as done for Figure 6-16. Since no water vapor was added to the cathode, only generated water from the electrochemical reaction and water transported from the anode to the cathode lead to increase the water content at the cathode layer. Because constant discharged current density was not high, the level of water content at the cathode was far from the fully hydrated stage.

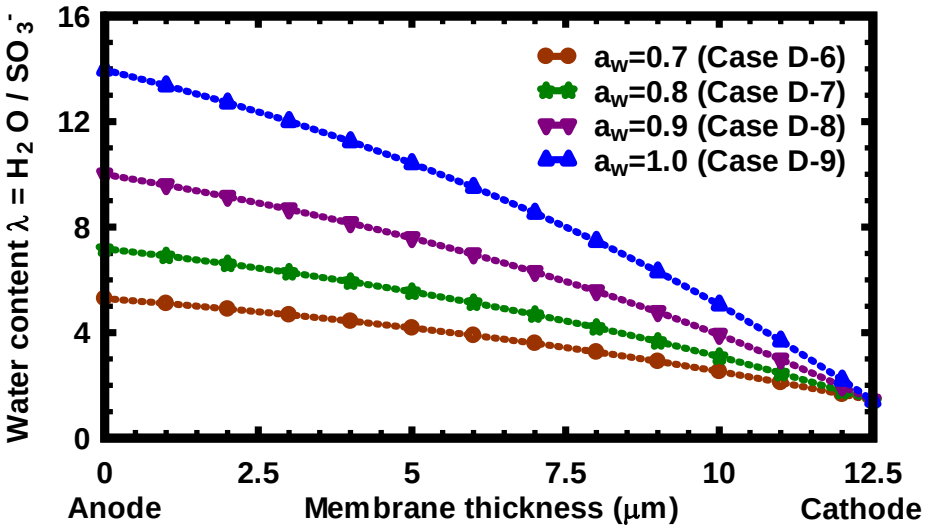

Figure 6-25 Calculated initial water content profile across Nafion membrane for the case D-6, 7, 8, and 9.

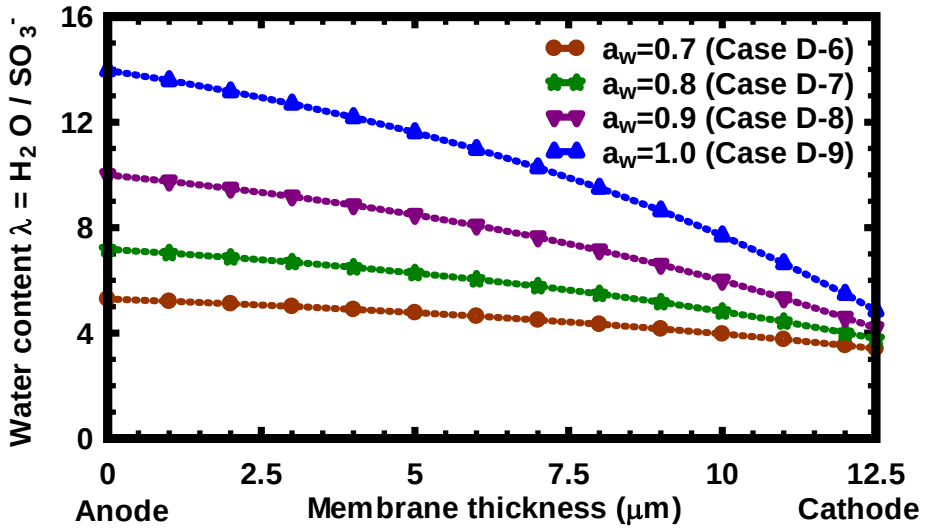

Figure 6-26 Calculated water content profile across Nafion membrane after discharging constant current density 0.6 A/cm^2 for the case D-6, 7, 8, and 9.

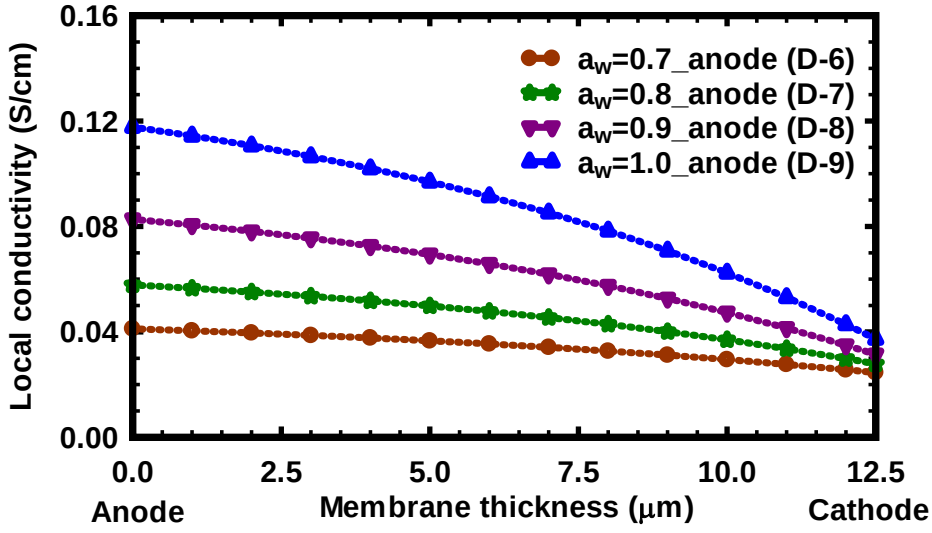

Figure 6-27 Calculated local conductivity profile across Nafion membrane for the cases D-6, 7, 8, and 9.

The local conductivity across the Nafion membrane for the cases D-6, 7, 8, and 9 was calculated as in section 6.3.1 and plotted in Figure 6-27. Since the water activity at the anode catalyst layer was varied with 0.7, 0.8, 0.9, and 1 and the water activity at the

cathode catalyst layer was 0.1, the local conductivity decreased from around 0.040, 0.058, 0.081, and 0.120 to around 0.042.

6.3.3 Cases with 50% Relative Humidified Hydrogen and Air at 70°C

Sections 6.3.1 and 6.3.2 reported on the water transport (the electro-osmotic drag and back diffusion) for cases having different relative humidity of hydrogen and dry air at 70°C temperature, and different current densities. In this section (6.3.3), the cases with 50% relative humidity hydrogen and air at 70°C were studied concerning the water transport. Since the inlet relative humidity of the hydrogen was 50% and the flow rate of hydrogen was small, the quantity of water supplied to the humidifier and of the water drained out to the anode exhaust were below the measurement capabilities.

Figure 6-28 shows the amount of water supplied to the cathode humidifier for cases D-10, 11, 12, and 13. All cases had the same linear relation.

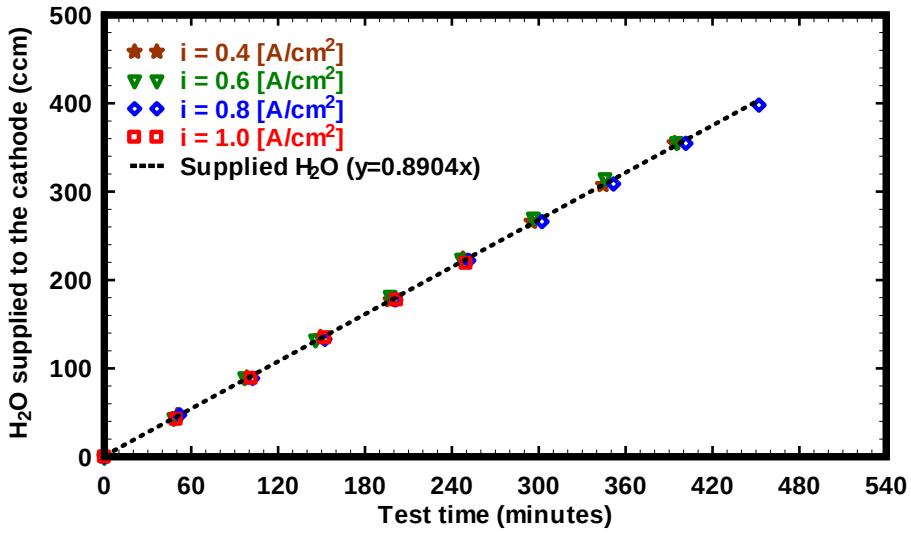

Figure 6-28 The amount of water supplied to the anode humidifier for cases D-10, 11, 12, and 13. Linear curve fitting is plotted for all cases.

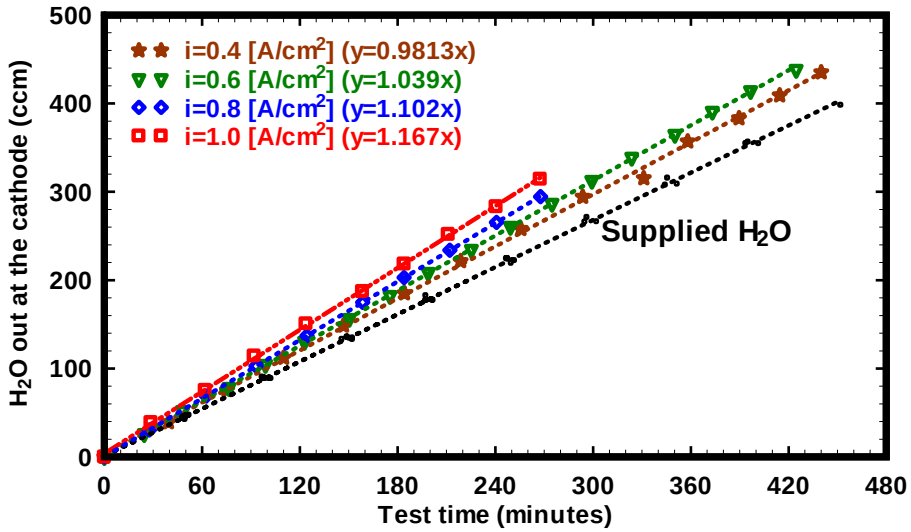

Figure 6-29 The amount of water drained out to the anode exhaust for cases D-10, 11, 12, and 13. Each linear line is the curve fitting for each result.

The amount of water drained out to the cathode exhaust for cases D-10, 11, 12, and 13 and the amount of water supplied to the cathode humidifier were plotted together in Figure 6-29. As the current density was increased, the amount of water drained out to the cathode exhaust increased. This total amount of water drained out to the cathode exhaust included the amount of water supplied to the cathode humidifier, the generated water at the cathode because of electrochemical reaction, and the water dragged from the anode to the cathode because of the electro-osmotic drag.

Figure 6-30 shows the amount of water deducting the inlet water from the total water output to the cathode exhaust with time for cases D-10, 11, 12, and 14, which were the sum of produced water from the reaction and dragged water from the anode with electro-osmotic drag.

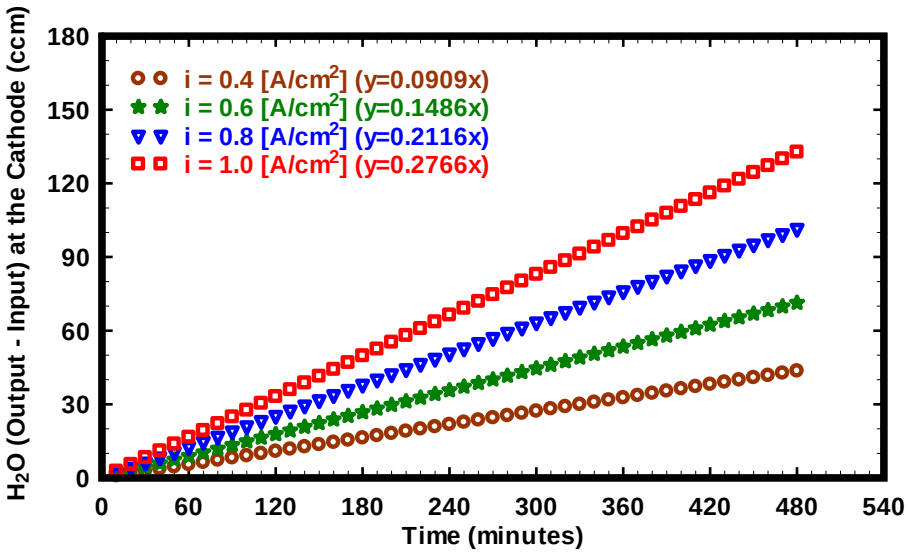

Figure 6-30 The amount of water deducting inlet water from the total water output to the cathode exhaust for cases D-10, 11, 12, and 13.

Figure 6-31 shows the amount of water deducting theoretically produced water and supplied water from the total water output at the cathode exhaust. All cases show the minus water value, which explains that the water molecules transported from the cathode to the anode because the water concentration at the cathode must be higher than the anode's. As the current density increased, even though more water was generated, in the meantime, more water molecules were dragged from the anode to the cathode along with proton's transport, the amount of water transported from the cathode to the anode because of back diffusion seemed to be decreased. At first, this was not thought to be reasonable. There must be one main reason why the back diffusion was small at the high current density. The main reason is related to the inlet condition of the supplied gases. The inlet condition of the hydrogen gas was maintained at 50% relative humidity, which suffered from the drying at the membrane. At the high current density, the water trans-

ported from the back diffusion dragged again from the anode to the cathode, which explains why the water was lower in Figure 6-31.

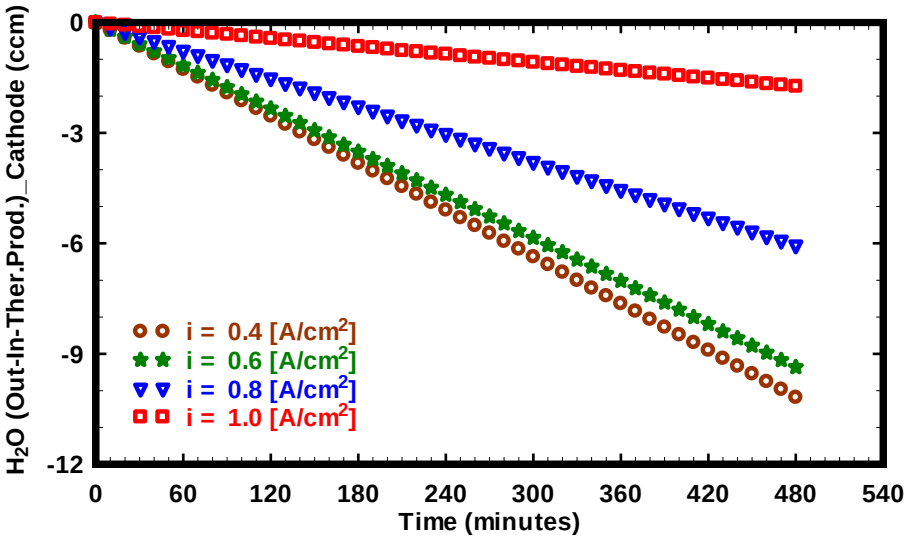

Figure 6-31 The amount of water deducting the amount of theoretically produced water from the **Figure 6-30** for cases D-10, 11, 12, and 13.

One finding from this section 6.3.3 was that when the anode suffered from dehydration condition, the water transported from the cathode to the anode because of the back diffusion which resulted from the water concentration gradient difference would transport again from the anode to the cathode with the protons' movement.

The calculated water content profile across the Nafion membrane for the cases D-10, 11, 12, and 13 is plotted in Figure 6-32. Since the anode's water balance was not available, and the amount of water from the cathode to the anode because of the back diffusion was very small, the water activity at the anode was assumed as fixed at the initial inlet condition of the hydrogen gas. Even though the inlet air with 50% relative humidity constantly supplied to the cathode, the water content across the membrane in-

creased when membrane thickness and the discharged current density increased. Since the water was generated at the catalyst layer because of oxygen reduction reaction (ORR), the water content across the membrane sharply increased close to the cathode catalyst side.

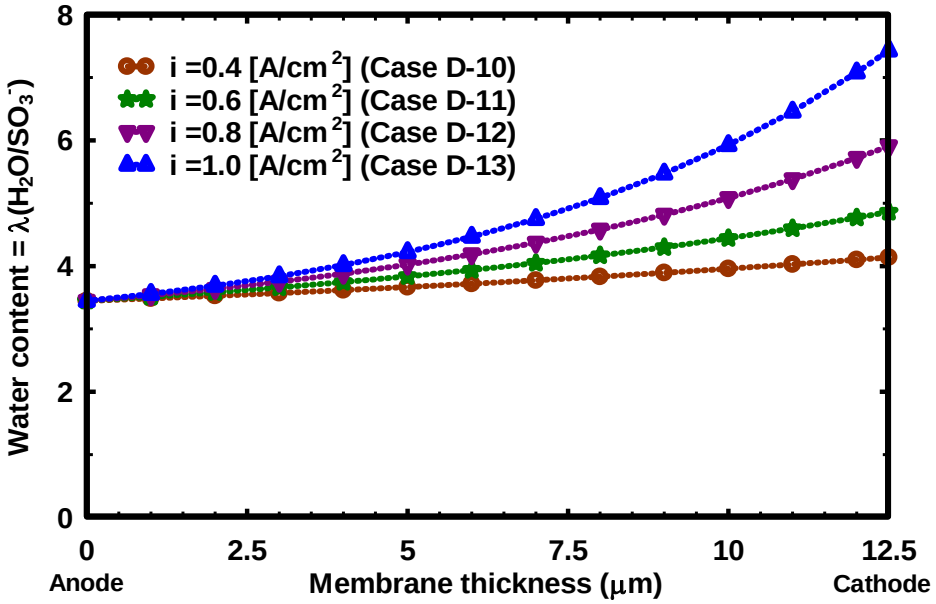

Figure 6-32 Calculated water content profile across Nafion membrane for the cases D-10, 11, 12, and 13.

Using equation 6.9 and the calculated water content shown in Figure 6-32, the conductivity profile of the membrane was calculated and plotted in Figure 6-33. When the current density increased, more water was generated which lead that conduction of protons in the membrane was like in an aqueous electrolyte. The local conductivity increased exponentially with increasing water content at the cathode catalyst side.

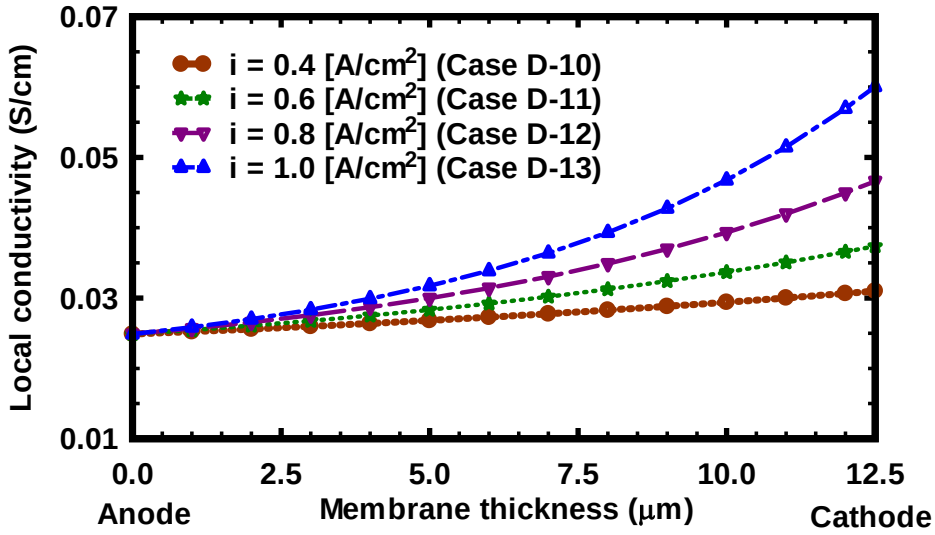

Figure 6-33 Calculated local conductivity profile across Nafion membrane for the cases D-10, 11, 12, and 13.

6.3.4 Cases with 100% Relative Humidified Hydrogen and Air at 70°C

In section 6.3.3, from the results for the cases D-10, 11, 12, and 13, the back diffusion (the water transferred from the cathode to the anode because of the water concentration gradient) was studied. Because the amount of water supplied to the anode humidifier and drained out to the anode exhaust were not obtainable for the cases D-10, 11, 12, and 13, only limited results are presented.

In section 6.3.4, 100% relative humidified hydrogen and air supplied to the fuel cell at 70°C will be studied. Figure 6-34 shows the amount of water supplied to the anode humidifier and the water drained out to the anode exhaust as a function of the test time for the cases D-14, 15, 16, and 17. There was not much difference among these cases. The results in Figure 6-7 and Figure 6-34 may be compared. For these two cases, the inlet condition at the anode was the same, but the water level at the cathode was dif-

ferent. Dry air was supplied to the cathode for Figure 6-7, 100% relative humidified air was supplied to the cathode for Figure 6-34.

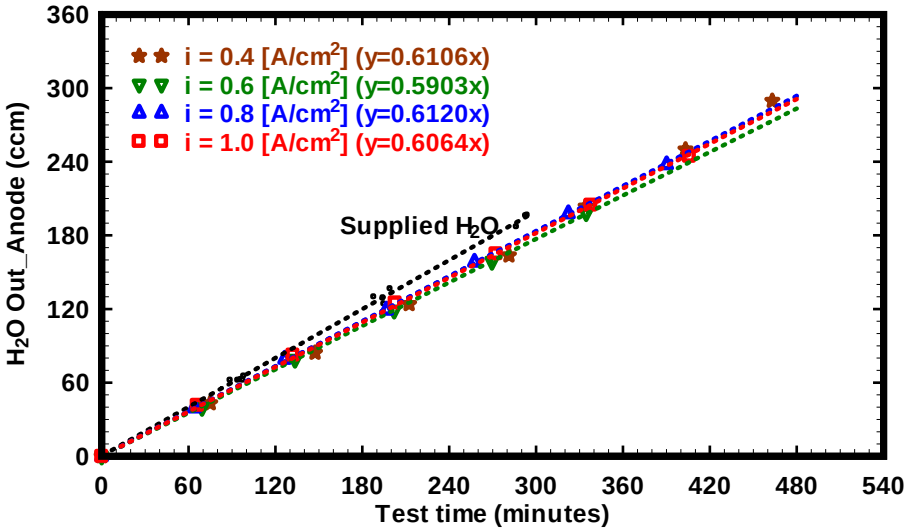

Figure 6-34 The amount of water supplied to the anode humidifier and water drained out to the anode exhaust for cases D-14, 15, 16, and 17.

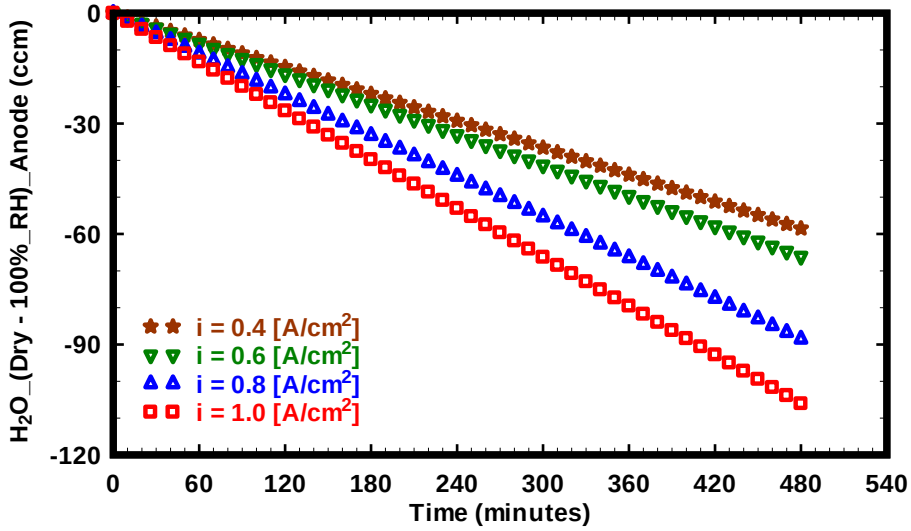

Figure 6-35 The amount of water because of the back diffusion with time comparing the cases D-1, 2, 3, and 4 to the cases D-14, 15, 16, and 17.

To know how much of water was transported from the cathode to the anode because of the back diffusion, the results of the cases D-1, 2, 3, and 4 and the cases D-14, 15, 16, and 17 were compared, calculated, and plotted in Figure 6-35. Inlet conditions for the anode and discharge current densities were same both section 6.3.1 and section 6.3.4. Only difference was the humidity level of inlet air. For the section 6.3.1, dry air was supplied, whereas, 100% relative humidified air supplied for the section 6.3.4. Increasing the current density from 0.4 to 1.0 A/cm^2, the amount of water because of the back diffusion was changed around 58 to 106 ccm after 8 hours. Depending on the water level at the cathode, the back diffusion was significantly changed. When the membrane suffered from the de-hydration for the cases D-10, 11, 12, and 13, the detected water (because of the back diffusion) decreased with increasing current density. However, when the membrane was fully hydrated at both the anode and cathode of the cases D-14, 15, 16, and 17, the back diffusion was increased with increasing the current density.

The amount of water drained out to the cathode exhaust for cases D-14, 15, 16, and 17 and the amount of water supplied to the cathode humidifier were plotted together in Figure 6-36. As the current density was increased, the amount of water drained out to the cathode exhaust increased accordingly, except the case of the highest current density (1.0 A/cm^2). This total amount of water drained out to the cathode exhaust included the amount of water supplied to the cathode humidifier, the generated water at the cathode because of reaction, and the water dragged from the anode to the cathode because of the electro-osmotic drag.

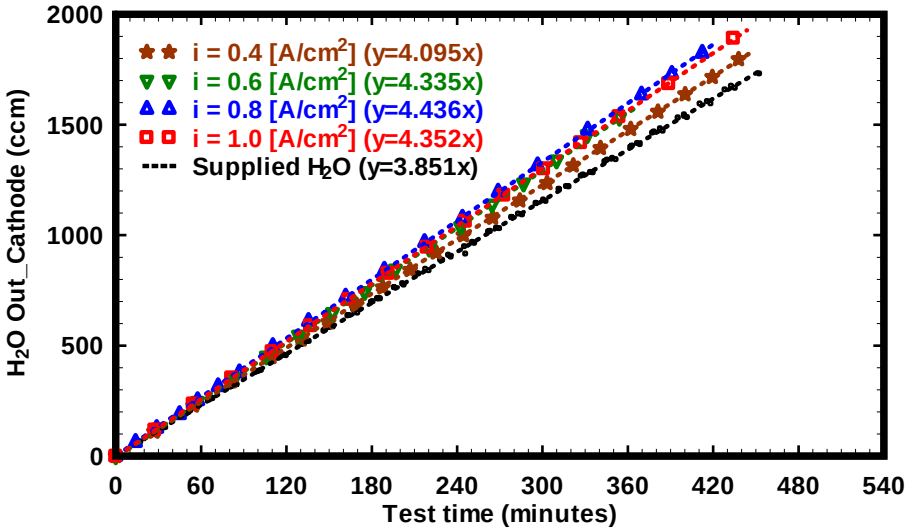

Figure 6-36 The amount of the drained out water to the cathode exhaust and supplied water to the cathode humidifier for cases D-14, 15, 16, and 17. Linear curve fitting for each result is supplied.

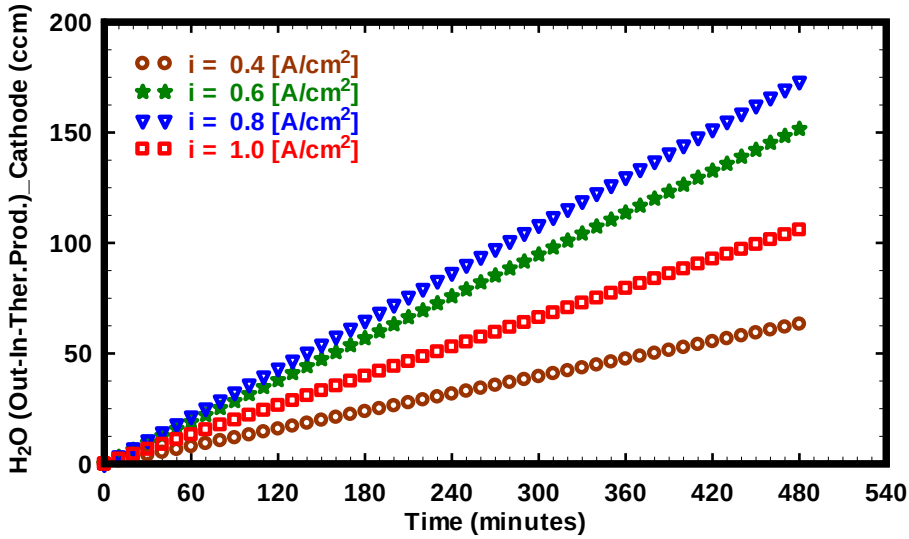

Figure 6-37 The amount of water subtracting the amount of theoretically produced water and water input to the cathode humidifier from the total water output for cases D-14, 15, 16, and 17.

Figure 6-37 shows the total amount of water output minus the amount of theoretically produced water and water input to the cathode humidifier for cases D-14, 15, 16, and 17. The amount of water from the cathode to the anode because of the back diffusion

was shown in Figure 6-35. Figure 6-37 shows the amount of water because of the electro-osmotic drag with times for cases D-14, 15, 16, and 17.

In summary, through the water balance experiments, water transport (electro-osmotic drag and back diffusion) were studied experimentally. When the current density was increased, the electro-osmotic drag coefficient decreased. When the anode side experienced a drying out condition, the water transported from the back diffusion from the cathode to the anode would move back to the cathode again.

6.4 Summary of This Section

Through the use of water balance experiment, the electro-drag coefficients of Nafion 115 were obtained at several conditions (discharged current density and relative humidity of the inlet gases). The phenomenon of the back diffusion in the membrane, also, was found experimentally. When the fuel cell was not fully hydrated, transported water from the anode to the cathode with proton was decreased. When the fuel cell suffered from flooding, the net drag coefficient was decreased, as well. Increasing the water content at the membrane leads to increase the electro-osmotic drag coefficient.

7. SUMMARY AND CONCLUSIONS

The PEM fuel cell used in this work included a membrane and electrode assembly (MEA) which possessed active areas of 25 cm^2, 50 cm^2, and 100 cm^2 with Nafion® 117 and 115 membranes. As operating parameters, temperatures of 50, 60, 70 and 80^oC, back pressures of 0 and 34.47 kPa (5 psi) were selected. The relative humidity was dry, 50, 60, 70, 80, 90, and 100% for this research. To investigate the channel depth effect, triple serpentine designs for the flow fields with two different flow depths (0.5 mm and 1.3 mm) were used in this research.

7.1 Summary Discussion

The tests using only one side humidification (either at the anode or cathode) were helpful to understand the necessity of the water back diffusion and electro-osmotic drag in the fuel cell reaction. But one side suffered from drying out, and this demonstrates the importance of proper water management. Inlet gases with no humidification, for long time operation, lead to higher ionic resistance and low proton conductivity, which are detrimental to the MEA, since water molecules could not be dragged fully by protons from the anode to the cathode. Self-humidification/low humidification methods should be carefully studied using long time operation (~hours), because this action causes a continuous degrading of the performance of the MEA. Adding cathode side humidification to the case with only anode side humidification decreased the cathode activation loss. Open circuit voltage was increased when the pressure, flow rate of the inlet gases

and the relative humidity ratio of the inlet gases were increased. The case with anode and cathode 100% relative humidity didn't produce the highest performance due to water flooding at the high current density. The voltage decreased faster than the other cases for current density greater than 800 mA/cm^2.

The high flow rate of inlet gases exerts influence on the fuel cell performance, expels off the overflowing water in the flow field, and decreases the mass transportation loss region at high current density. Air-breathing PEM fuel cell was studied for the effects of the flow depth and environmental conditions.

Through the water balance experiments, the water transport (electro-osmotic drag and back diffusion) was studied experimentally. When the current density was increased, the electro-osmotic drag coefficient decreased. Even if there was no humidified air supplied to the cathode (for the 100% relative humidity hydrogen supplied case), water concentration at the cathode was higher than at the anode at high current density 1.2 A/cm^2. This was attributed to back diffusion.

7.2 Major Findings

Major findings of this work fall into 4 categories: (1) finding the role/effect of the relative humidity of the inlet gases for a PEM fuel cell, (2) finding the appropriate stoichiometric flow coefficient, (3) investigating the effects of the channel depth and environmental conditions for the air-breathing PEM fuel cell, and (4) obtaining the electro-osmotic drag coefficient for the Nafion 115 membrane. Each category has listings of the major findings as follows:

1) The role/effects of the relative humidity of the inlet gases for a PEM fuel cell was studied and found. The following findings were drawn from this investigation:
    - Increasing the relative humidity of the inlet gases at the cathode improved the current density from 840 to 1175 mA/cm^2 at fixed 0.2 volts. Whereas, when only humidified gas is supplied to the anode, the current densities were obtained from 800 to 975 mA/cm^2 at fixed 0.2 volts.
    - Among different inlet temperatures, when the inlet and cell temperature was set as 70^oC, the best performance occurred. Increasing temperature increases water generation and also helps water removal in water flooding. For temperatures above 70^oC, however, the water generation rate exceeds the water removal rate, which resulted in water flooding in the flow field.
    - Measured back pressure at the exhaust is an indication of how much water content is in the membrane during the reaction in the fuel cell. When humidified inlet gases are supplied to the fuel cell, maintaining back pressure at the exhaust is an indication not only of how much water exists at the flow field inside of a cell, but also is an indication that the produced water is removed properly by the supplying gas.

2) To operate a fuel cell efficiently and increase the performance, the amount of the inlet gases should be supplied properly. The following findings for the flow rate were drawn from this investigation.

- To run the stoichiometric flow rate control, at least a value of two for the reagent stoichiometric ratio is necessary at the cathode inlet.
- The desired current to start the stoichiometric flow rate should be decided corresponding to the stoichiometric flow rate. The desired current to start the stoichiometric flow rate should be between the 0.25 and 0.6 A/cm^2 of the current density to have best performance.

3) The air-breathing PEM fuel cell was studied for the effects of the environmental conditions and the channel depth. The following findings for the air-breathing PEM fuel cell were drawn from this investigation.
   - The shallow flow field design influenced dramatically the performance of the air-breathing fuel cell at low relative humidity, and slightly at high relative humidity. When the shallow flow field design is used, it increased the number of available reaction sites per unit area. The hydrogen transfer rate to the electrode was increased by the gas flow through the gas diffusion layer.
   - When the temperature is low (such as 20^oC), the relative humidity does not play a big role in increasing the performance of the air-breathing PEM fuel cell. The higher relative humidity at higher temperatures, however, helps the protons move from the anode to the cathode.

4) Through a water balance experiment, the electro-osmotic drag coefficients of the Nafion 115 were found. The following findings for the electro-osmotic drag were drawn from this investigation:

    - For the cases where the anode was fully hydrated and the cathode suffered from the drying when dry air supplied, the electro-osmotic drag coefficients varied from 0.82 (±0.06) to 0.50 (±0.03) H_2O/H^+ when the current density varied from 0.4 to 1.0 A/cm^2 (95% confidence level). When the current density increased, the electro-osmotic drag coefficient decreased.
    - When the inlet hydrogen gas's relative humidity varied from 70% to 100% and the fuel cell discharged the constant current density at 0.6 A/cm^2, the electro-osmotic drag coefficient increased from 0.44 (±0.06) to 0.68 (±0.06) H_2O/H^+ (95% confidence level).
    - Higher relative humidity gas leads to higher electro osmotic drag coefficient at constant current density.
    - When the fuel cell suffered from drying, the water transported from the back diffusion from the cathode to the anode would move back to the cathode again.

7.3 Summary of Conclusions

The following conclusions were drawn from the experiments presented in this work:

- Monitoring back pressure at the exhaust is an effective method for checking whether a PEM fuel cell suffers from flooding during the electro-chemical reaction.
- Depending on the water content at the membrane, even at the same discharged current, the heat generated at the fuel cell stack varied. When the protons transport from the anode to the cathode at low water content, heat is generated more because of the low conductivity and high resistance of the drying.
- The cathode's relative humidity plays a more important role for having higher power density since the cathode activation loss is larger than the anode's
- Higher air supply leads to have better performance at the constant stoichiometric ratio at the anode, but not much increase after the stoichiometric ratio of 5.
- A water balance experiment is an effective means of investigating both how much of water transported from the anode to the cathode and when the back diffusion occurred during the electro-chemical reaction.

8. RECOMMENDATIONS

The following recommendations are for future research concerning the PEM fuel cell.

1. Improve the flow distribution of the inlet gases of the PEM fuel cell stack.
    - Uneven flow distribution causes reactant starvation in unit cell.

2. Improve the flow structure and design of the stack not only to increase performance of the fuel cell, but also to prevent local overheating in a PEM fuel cell.
    - Currently, most of the PEM fuel cell stacks use the air cooling or coolant to maintain the stack temperature. Depend on the location of each cell, the temperatures of each cell vary. Some cells undergo overheating, others has low temperature compared to the optimum operating temperature, which lead to the degradation of the catalyst.

3. Investigate a durability related with water management for a PEM fuel cell.
    - The minimum operating hours (lifespan) for a PEM fuel cell vehicle should be more than 5000 hours. For stationary applications, more than 40,000 hours of reliable operation is required.

NOMENCLATURE

A	Current (Amp) or Anode
a	Water activity
a_{fuel}	Fuel availability
AFC	Alkaline Fuel Cell
An	Anode
b	Tafel slope (mV per decade)
C	Cathode
C_p	Constant-pressure heat capacity (J kg^{-1} K^{-1})
Ca	Cathode
CCM	Catalyst Coated Membrane
ccm	Cubic centimeter (cm^3)
D_λ	Water content diffusivity (mol m^{-1} s^{-1})
DMFC	Direct Methanol Fuel Cell
DPH	Dew point humidifier
dp	Dew point temperature (^oC)
e^-	Electron
E	Reversible open circuit voltage or Exergy
E_{cell}	Cell operation potential (V)
E_0 (v)	Open circuit voltage (V)

e_{ph}	Physical exergy
e_{Ch}	Chemical exergy
F	Faraday constant (96,487 C mol^{-1})
FR	Flow rate
g	Gas
g_f	Gibbs free energy
H	Enthalpy
h_0	Enthalpy
H_2	Hydrogen
H^+	Proton
H_f^o	Enthalpies of formation
H_2O	Water
I	Current (Amp) or Cell operating current density (A/m^2)
I_0	Current to start the stoichiometric flow mode (Amp)
i	Cell operating current density (A/m^2)
K	Stoichiometric flow rate coefficient
l	Liquid
MCFC	Molten Carbonate Fuel Cell
MEA	Membrane electrode assembly
MW	Molecular weight
N	Number of cells in a stack

O_2	Oxygen
PAFC	Phosphoric Acid Fuel Cell
PEM	Polymer Electrolyte Membrane
P	Pressure (Pa)
ⓟ	Purge
P_{sat}	Saturation pressure (Pa)
P_e	Electrical output power (Watt)
R	Ohmic resistance ($\Omega\ cm^2$)
RH	Relative humidity (%)
$R_{H_2O\_\mathrm{Pr}od}$	Rate of water production
R_{u}	Universal gas constant (J mol^{-1} K^{-1})
S	Entropy
s_0	Entropy
slpm	Standard liters per minute
St	Reagent stoichiometric ratio
t	time (s)
T	Temperature (K or ^{o}C)
T_b	Stack temperature (^{o}C)
T_c	Cell temperature
T_{cell}	Cell temperature
T_{dp}	Dew point temperature

V_c	Mean voltage of each cell (V)
V_3	#3 Cell voltage in the stack
V_5	#5 Cell voltage in the stack
V^T	Theoretical air consumption
V^A	Actual air consumption
W	Power (Watt)
x_n	Mole fraction of the n specie
x_{an}	Anode fuel utilization
x_{ca}	Cathode oxidant utilization

Greek letters

η	Over-potential (V) or Efficiency
κ	Proton conductivity (S m^{-1})
λ	Water content
λ	Stoichiometric ratio
λ_{H_2}	Hydrogen stoichiometric ratio
λ_{O_2}	Oxygen stoichiometric ratio
υ_{FC}	Fuel cell stack voltage (V)

Superscripts

A	Actual

l	Liquid phase
sat	Saturation value
T	Theoretical
v	Vapor phase

Subscripts

act	Activation
air	Air
an	Anode
c	Mean value
ca	Cathode
Ch	Chemical
FC	Fuel cell
fuel	Fuel
g	Gaseous phase
H_2	Hydrogen
i	Species
l	Liquid
O_2	Oxygen
ohmic	Ohmic
Ph	Physical
sat	Saturation value

w	Water vapor
Tot	Total

REFERENCES

Ahn, S., Lee, Y., Ha, H., Hong, S., Oh, I. (2004). Effect of the ionomers in the electrode on the performance of PEMFC under non-humidifying conditions. *Electrochimica Acta* 50:673-676.

Ahn, S., Shin, S., Ha, H., Hong, S., Lee, Y., Lim, T., Oh, I. (2002). Performance and lifetime analysis of the kW-class PEMFC stack. *J. Power Sources* 106:295-303.

Andresen, J. (2003). Carbon materials for high temperature proton exchange membrane fuel cells. Workshop at Penn Sate University, December 11, University Park, PA.

Arbin Instruments. (2006). MITS Pro-FCTS 5.0 – FCTS User Manual, College Station, TX, pp 1-58. (Cited July, 12, 2007)
http://www.fuelcelltestingsystem.com/Download/products/MITSPro_FCT.pdf

Barbir, F. (2005). Chapter 3. Fuel cell electrochemistry. *PEM Fuel Cells,* Burlington, MA, Elsevier Academic Press.

Bejan, A. (1996). *Entropy Generation Minimization*, Boca Raton, FL, CRC Press.

Bonville, L., Kunz, H., Song, Y., Mientek, A., Williams, M., Ching, A., Fenton, J. (2005). Development and demonstration of a higher temperature PEM fuel cell stack. *J. Power Sources* 144:107-112.

Buchi, F. N., Scherer, G. G. (2000). Investigation of the transversal water profile in Nafion membranes in polymer electrolyte fuel cells. *J. Electrochemical Society* 148:A181-A188.

Cho, E., Jeon, U., Hong, S., Oh, I., Kang, S. (2005). Performance of 1 kW-class PEMFC stack using TiN-coated 316 stainless steel bipolar plates. *J. Power Sources* 142:177-183.

Choi, K., Park, D., Rho, Y., Kho, Y., Lee, T. (1998). A study of the internal humidification of an integrated PEMFC stack. *J. Power Sources* 74:146-150.

Chu, D., Jiang, R. (1999a). Performance of polymer electrolyte membrane fuel cell (PEMFC) stacks: Part I. Evaluation and simulation of an air-breathing PEMFC stack. *J. Power Sources* 83:128-133.

Chu, D., Jiang, R. (1999b). Comparative studies of polymer electrolyte membrane fuel cell stack and single cell. *J. Power Sources* 80:226-234.

Coppo, M., Siegel, N., Spakovsky, M. (2006). On the influence of temperature on PEM fuel cell operation. *J. Power Sources* 159:560-569.

Dhathathreyan, K., Sridhar, P., Sasujynar, G., Ghosh, K., Velayutham, G., Rajalakshmi, N., Subramaniam, C., Raja, M., Ramya, K. (1999). Development of polymer electrode membrane fuel cell stack. *Int. J. Hydrogen Energy* 24:1107-1115.

Eckl, R., Zehtner, W., Leu, C., Wagner, U. (2004). Experimental analysis of water management in a self-humidifying polymer fuel cell stack. *J. Power Sources* 138:137-144.

Fabian, T., Posner, J., O'Hayre, R., Cha, S., Eaton, J., Prinz, F., Santiago, J. (2006). The role of ambient conditions on the performance of a planar air-breathing hydrogen PEM fuel cell. *J. Power Sources* 161:168-182.

Fogler, S. (1999). *Elements of chemical reaction engineering*, 3rd Edition. Upper Saddle River: Prentice Hall.

Ghadamian, H., Saboohi, Y. (2004). Quantitative analysis of irreversibility causes voltage fuel cell (simulation & modeling). *Electrochimica Acta* 50:699-704.

Gibbs, J.W. (1873). A method of geometrical representation of thermodynamic properties of substances by means of surfaces: reprinted in Gibbs, *Collected Works*, ed. W. R. Longley and R. G. Van Name (New York: Longmans, Green, 1931). *Transactions of the Connecticut Academy of Arts and Sciences* 2:382–404.

Giddey, S., Ciacchi, F., Badwal, S. (2004). Design, assembly and operation of polymer electrolyte membrane fuel cell stacks to 1 kW_e capacity. *J.Power Sources* 125:155-165.

Görgün. H., Arcak, M., Barbir, F. (2006). An algorithm for estimation of membrane water content in PEM fuel cells. *J. Power Sources* 157:389-394.

Hogarth, W., Benziger, J. (2006) Operation of polymer electrolyte membrane fuel cells with dry feeds: Design and operating strategies. *J. Power Sources* 159:968-978.

Hu, M., Sui, S., Zhu, X., Yu, Q., Cao, G., Hong, X., Tu, H. (2006). A 10 kW class PEM fuel cell stack based on the catalyst-coated membrane (CCM) method. *Int. J. Hydrogen Energy* 31:1010-1018.

Hwang, J., Hwang, H. (2002). Parametric studies of a double-cell stack of PEMFC using grafoil™ flow-field plates. *J. Power Sources* 104:24-32.

Jaouen, F., Hassl, S., Van Der Wijngaart, W., Lundblad, A., Lindbergh, G., Stemme, G., (2005). Adhesive copper films for an air-breathing polymer electrolyte fuel cell. *J. Power Sources* 144:113-121.

Jeong, S., Cho, E., Kim, H., Lin, T., Oh, I., Kim, S. (2006a). Effects of cathode open area and relative humidity on the performance of air-breathing polymer electrolyte membrane fuel cells. *J. Power Sources* 158:348-353.

Jeong, S., Cho, E., Kim, H., Lin, T., Oh, I., Kim, S. (2006b). A study on cathode structure and water transport in air-breathing PEM fuel cells. *J. Power Sources* 159:1089-1094.

Jiang, R., Chu, D. (2001a). Voltage-time behavior of a polymer electrolyte membrane fuel cell stack at constant current discharge. *J. Power Sources* 92:193-198.

Jiang, R., Chu, D. (2001b). Stack design and performance of polymer electrolyte membrane fuel cells. *J. Power Sources* 93:25-31.

Jiang, R., Kunz, R., Fenton, J. (2006). Influence of temperature and relative humidity on performance and CO tolerance of PEM fuel cells with Nafion-Teflon-$Zr(HPO_4)_2$ higher temperature composite membranes. *Electrochimica Acta* 51:5596-5605.

Kazemini, M. (2001). 1kW PEM stack design. Proc. the First Iranian Fuel Cell Conference, Oct. 3-4, Sharif University, Tehran, Iran.

Kenyon, K, Doeppers, M., Ibrahim, S. (2002). Passive air breathing fuel cells. US patent No. 5,514,486.

Knobbe, M.W., He, W., Chong, P.Y., Nguyen, T.V. (2004). Active gas management for PEM fuel cell stacks. *J. Power Sources* 138:94-100.

Larminie, J., Dicks, A. (2000). *Fuel cell systems explained*. New York: John Willey and Sons. 92-97.

Lau, S.C. (2002) MEEN 464 Heat Transfer Laboratory Instruction Manual, Texas A&M University. College Station, TX.

Lee, J., Lalk, T. (1998). Modeling fuel cell stack systems. *J. Power Sources* 73:229-241.

Lee, W., Zee, L., Shimpalee, S., Dutta, S. (1999). Effect of humidity on PEM fuel cell performance part I: experiments. *Proc. ASME, Heat Transfer Division* 5:359-366.

Li, P., Zhang, T., Wang, Q., Schaefer, L., Chyu, M. (2003). The performance of PEM fuel cells fed with oxygen through the free-convection mode. *J. Power Sources* 114:63-69.

Mennola, T. (2004). Mass transport in polymer electrolyte membrane fuel cells using natural convection for air supply. Dissertation, Helsinki Univ. of Technology, Espoo, Finland.

Liu, Z., Yang, L., Mao, Z., Zhuge, W., Zhang, Y., Wang, L. (2006). Behavior of PEMFC in starvation. *J. Power Sources* 157:166-176.

Min, K., Tanaka, S., Esashi, M. (2006). Fabrication of novel MEMS-based polymer electrolyte fuel cell architectures with catalytic electrodes supported on porous SiO2. *J. Micromechanics and Microengineering* 16:505-511.

Moore, J., Lakeman, J., Mepsted, G. (2002). Development of a PEM fuel cell powered portable field generator for the dismounted soldier. *J. Power Sources* 106:16-20.

More, K. (2004). Microstructual characterization of PEM fuel cell membrane electrode assemblies. DOE Hydrogen Program, FY 2004 Progress Report.

Motupally, S., Becker, A., Weidner, J. (2000). Diffusion of water in Nafion 115 membranes. *J. Electrochemical Society* 147:3171-3177.

Murphy, O., Cisar, A., Clarke, E. (1998). Low-cost light weight high power density PEM fuel cell stack. *Electrochimica Acta* 43:3829-3840.

Natarajan, D., Nguyen, T. (2003). Three-dimensional effects of liquid water flooding in the cathode of a PEM fuel cell. *J. Power Sources* 115:66-80.

Nguyen, V. T., Knobbe, M. W. (2003). A liquid water management strategy for PEM fuel cell stacks. *J. Power Sources* 114:70-79.

Natarajan, D., Nguyen, T. (2003). Three-dimensional effects of liquid water flooding in the cathode of a PEM fuel cell. *J. Power Sources* 115:66-80.

Nieman, J., (2004). Unraveling Fuel Cell Electrical Measurements. The Magazine of Fuel Cell Business and Technology, April/May:32-35.

O'Hayre, R., Cha, S., Colella, W., Prinz, F. (2005). *Fuel Cell Fundamentals*, Hoboken: Wiley.

Philipps, F., Simons, G., Schiefer, K. (2006). Dynamic investigation of PEFC stacks in interaction with the air supply system. *J. Power Sources* 154:412-419.

Qi, Z., Kaufman, A. (2002a). PEM fuel Cell stacks operated under dry-reactant conditions. *J. Power Sources* 109:469-476.

Qi, Z.,Kaufman, A. (2002b). Activation of low temperature PEM fell cells. *J.Power Sources* 111:181-184.

Rajalakshmi, N., Jayanth, T., Thangamuthu, R., Sasikumar, G., Sridhar, P. (2004). Water transport characteristics of polymer electrolyte membrane fuel cell**.** *Int. J. Hydrogen Energy* 29:1009-1014.

Rodatz, P., Buchi, F., Onder, C., Guzzella, L. (2004). Operational aspects of a large PEFC stack under practical conditions. *J. Power Sources* 128:208-217.

Santarelli, M., Torchio, M., Cali, M., Giaretto, V. (2007). Experimental analysis of cathode flow stoichiometry on the electrical performance of a PEMFC stack. *Int. J. Hydrogen Energy* 32:710-716.

Savinell, R., Payer, J. (2001). Engineering fundamentals of low temperature (PEM) fuel cells. National science foundation workshop, Nov., 14-15, Arlington, VA.

Scholta, J., Berg, N., Wilde, P., Jorissen, L., Garche, J. (2004). Development and performance of a 10 kW PEMFC stack. *J. Power Sources* 127:206-212.

Scholta, J., Haussler, F., Zhang, W., Kuppers, L., Jorissen, L., Lehnert, W. (2006). Development of a stack having an optimized flow field structure with low cross transport effects. *J. Power Sources* 155:60-65.

Sena, D., Ticianelli, E., Paganin, V., Gonzalez, E. (1999). Effect of water transport in a PEFC at low temperatures operating with dry hydrogen. *J. Electro. Chem.* 477: 164-170.

Shan, Y., Choe, S. (2005). A high dynamic PEM fuel cell model with temperature effects. *J. Power Sources* 145:30-39.

Song, R., Kim, C., Shin, D. (2000). Effects of flow rate and starvation of reactant gases on the performance of phosphoric acid fuel cells. *J. Power Sources* 86:289-293.

Springer, T., Zawodzinski, T., Gottesfeld, S. (1991). Polymer electrolyte fuel cell model. *J. Electrochemical Society* 138:2334-2342.

Tafel, J. (1905) Über die Polarisation bei kathodischer Wasserstoff-entwicklung. *Z. Phys. Chem. A* 50:641-712.

Tsushima, S., Teranishi, K., Hirai, S. (2006). Experimental elucidation of proton conducting mechanism in a polymer electrolyte membrane of fuel cell by nuclei labeling MRI. 210 ECS Meeting – Cancun, Mexico, October 29 ~ November 03.

Torchio, M., Santarelli, M, Nicali, A. (2005). Experimental analysis of the CHP performance of a PEMFC stack by a 2^4 factorial design. *J. Power Sources* 149:33-43.

Turns, S.R. (1996). *An Introduction to Combustion*, New York: McGraw Hills.

Wahdame, B., Candusso, D., Kauffmann, J. (2006). Study of gas pressure and flow rate influences on a 500W PEM fuel cell, thanks to the experimental design methodology. *J. Power Sources* 156:92-99.

Williams, M., Kunz, H., Fenton, J., (2004). Operation of Nafion®-based PEM fuel cells with no external humidification: Influence of operating conditions and gas diffusion layers. *J. Power Sources* 135:124-134.

Wong, C., Zhao, T., Ye, Q., Liu, J. (2006). Experimental investigations of the anode flow field of a micro direct methanol fuel cell. *J. Power Sources* 155:291-296.

Yan, Q., Toghiani, H., Wu, J. (2005). Investigation of water transport through membrane in a PEM fuel cell by water balance experiments. *J. Power Sources* 158:316-325.

Yan, Q., Toghiani, H., Causey, H. (2006). Steady state and dynamic performance of proton exchange membrane fuel cells (PEMFCs) under various operating conditions and load changes. *J. Power Source* 161:492-502.

Yan, X., Hou, M., Zhang, H., Jing, F., Ming, P., Yi, B. (2006). Performance of PEMFC stack using expanded graphite bipolar plates. *J. Power Sources* 160:252-257.

Yang, B., Fu, Y., Manthiram, A. (2005). Operation of thin Nafion-based self-humidifying membranes in proton exchange membrane fuel cells with dry H_2 and O_2. *J. Power Sources* 139:170-175.

Ying, W., Sohn, Y., Lee, W., Ke, J., Kim, C. (2005). Three-dimensional modeling and experimental investigation for an air-breathing polymer electrolyte membrane fuel cell (PEMFC). *J. Power Sources* 145:563-571.

Ying, W., Sohn, Y., Lee, W., Ke, J., Kim, C. (2005). Three-dimensional analysis for effect of channel configuration on the performance of a small air-breathing proton exchange membrane fuel cell (PEMFC). *J. Power Sources* 145:572-581.

Yoshioka, S., Yoshimura, A., Fukumoto, H., Hiroi, O., Yoshiyasu, H. (2005). Development of a PEFC under low humidified conditions. *J. Power Sources* 144:146-151.

Zawodzinski, Jr. T. A., Deroiun, C., Radzinski, S., Sherman, R., Springer, T., Gottesfeld, S. (1993a). Water uptake by and transport through Nafion 117 membranes. *J. Electrochemical Society* 140:1041-1047.

Zawodzinski, Jr. T. A., Lopez, C., Jestel, R., Valerio, J., Gottesfeld, S. (1993b). A comparative study of water uptake by and transport through ionomeric fuel cell membranes. *J. Electrochemical Society*.140:1981-1985.

Zhang, J. (2005). Dew Point Humidifier (DPH) and Related Gas Temperature Control. U.S Patent 6,863,268.

A. APPENDIX A

B. RELATIONSHIP BETWEEN THE AMOUNT OF WATER SUPPLIED TO THE DEW POINT HUMIDIFIER (DPH) AND THE RELATIVE HUMIDITY OF THE INLET GAS WITH VARIOUS CONDITIONS

Table A-1 Table for the cases of 10 slpm with different temperatures and relative humidity.

Figure	Flow Rate (slpm)	Temperature (^{o}C)	Relative Humidity (%)
A-1	10	50	50
			60
			70
			80
			90
			100
A-2		60	50
			60
			70
			80
			90
			100
A-3		70	50
			60
			70
			80
			90
			100
A-4		80	50
			60
			70
			80
			90
			100

To study water transports in a fuel cell, a water balance module was used. The amount of water supplied to the humidifier varied with the flow rates, the temperatures,

and the relative humidities. To determine how much water was supplied to the humidifier, two water pumps (one for the anode, another for the cathode) recorded the amount of water supplied to the humidifier with time. After finishing calibration of all four water pumps, the amounts of water supplied to the humidifier were recorded for different conditions. Table A-1 shows the test conditions for the cases with 10 slpm flow rate where the temperatures varied 50, 60, 70, and 80^{o}C, and the relative humidity varied 50, 60, 70, 80, 90, and 100%. Figures A-1, 2, 3, and 4 show the accumulated water inputs with different temperatures and flow rates.

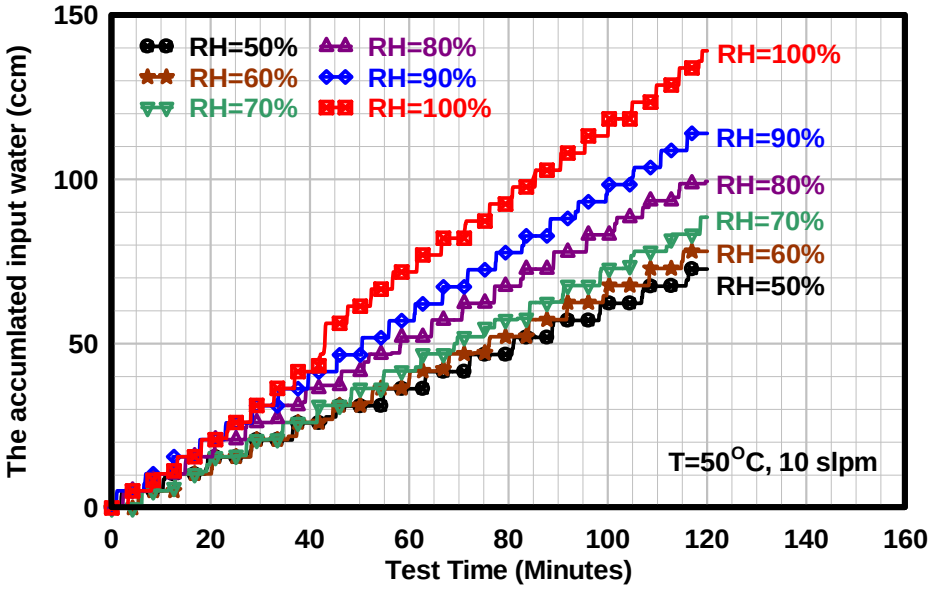

Figure A-1 The accumulated input water corresponding to the relative humidity at 50^{o}C, 10 slpm.

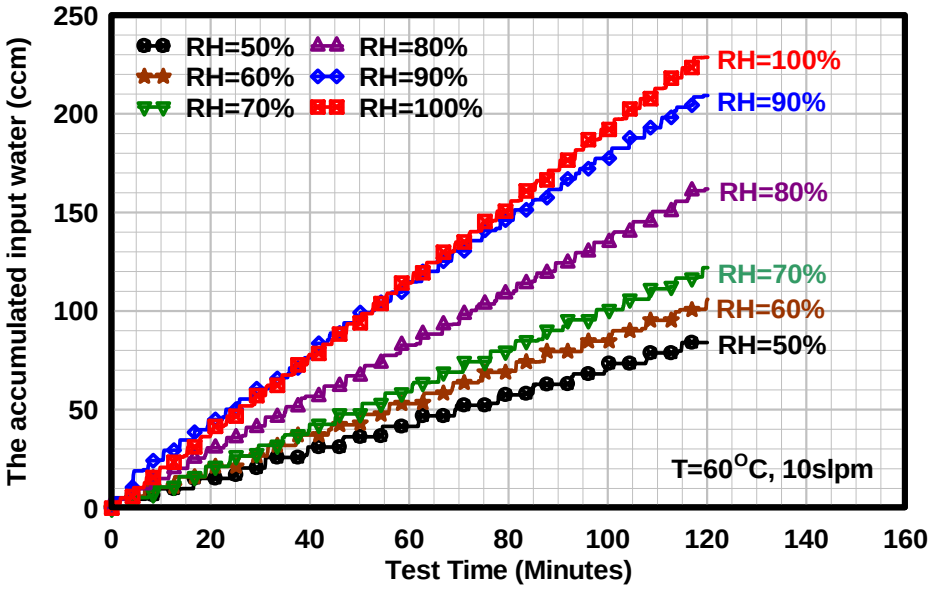

Figure A-2 The accumulated input water corresponding to the relative humidity at 60°C, 10 slpm.

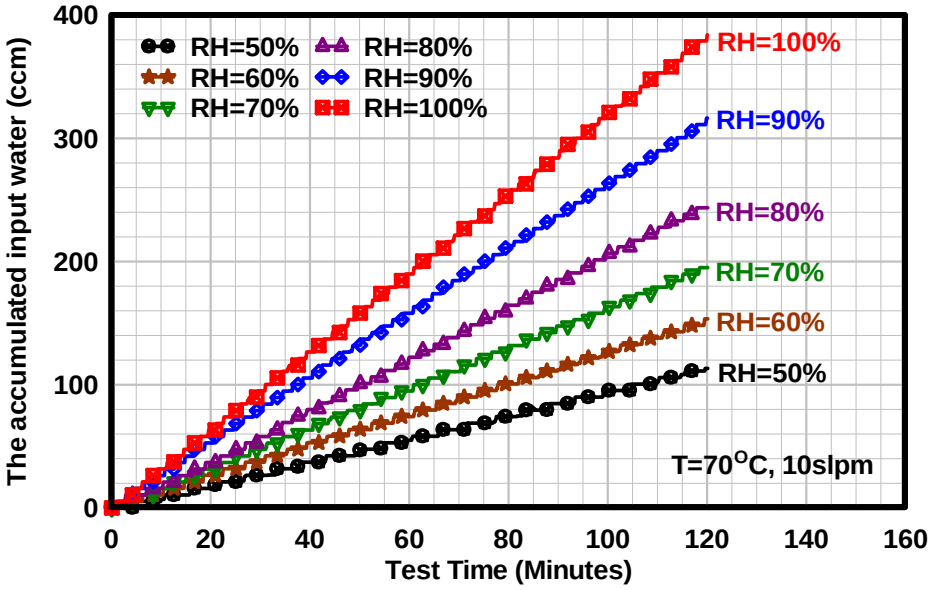

Figure A-3 The accumulated input water corresponding to the relative humidity at 70°C, 10 slpm.

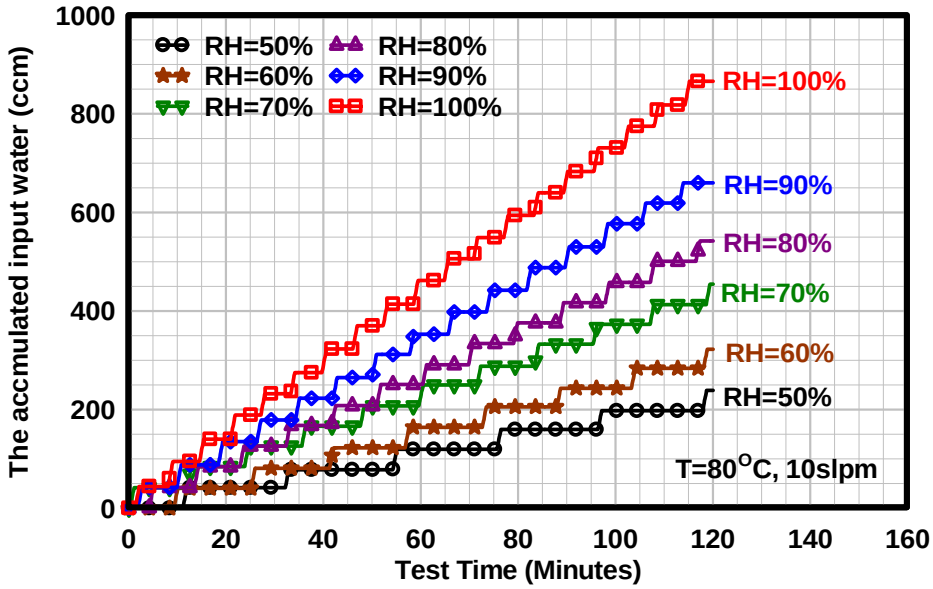

Figure A-4 The accumulated input water corresponding to the relative humidity at 80°C, 10 slpm.

Table A-2 Table for the cases of 100% relative humidity with different temperatures and flow rates.

Figure	Flow Rate (slpm)	Temperature (°C)	Relative Humidity (%)
A-5	5	60	100
	10		
	20		
	30		
	40		
	50		
A-6	5	80	
	10		
	20		
	30		
	40		
	50		
A-7	5	70	
	10		
	20		
	30		
	40		
	50		

Table A-2 shows the test conditions for the cases with 100% relative humidity where the temperatures varied 50, 60, 70, and 80^{o}C, and the flow rates varied 5, 10, 20, 30, 40, and 50 slpm. Figures A-5, 6, and 7 show the accumulated water inputs with different temperatures and flow rates at 100% relative humidity cases.

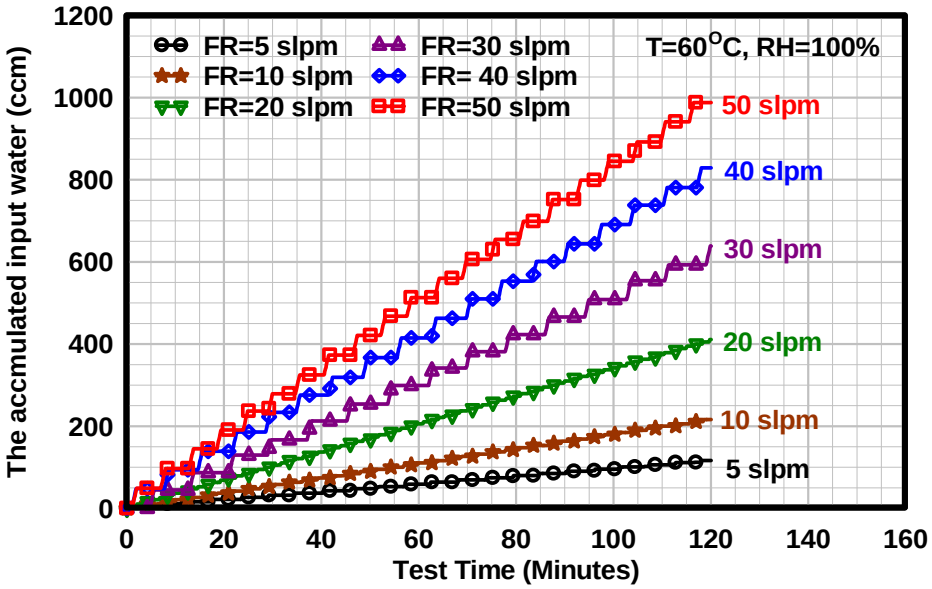

Figure A-5 The accumulated input water corresponding to the flow rate at 60^{o}C, 100%.

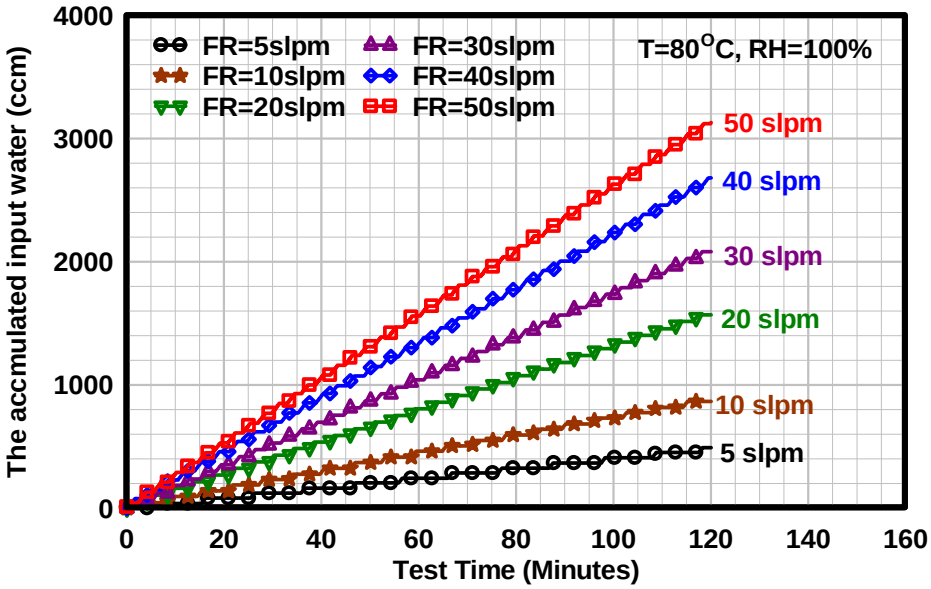

Figure A-6 The accumulated input water corresponding to the flow rate at 80°C, 100%.

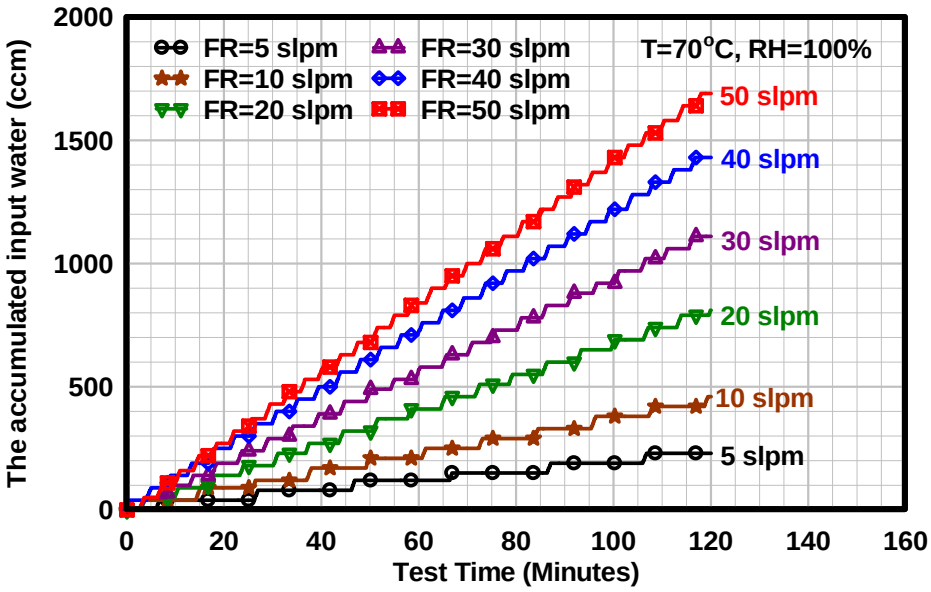

Figure A-7 The accumulated input water corresponding to the flow rate at 70°C, 100%.

Table A-3 Table for the cases of 70°C with different flow rates and relative humidities.

Figure	Flow Rate (slpm)	Temperature (°C)	Relative Humidity (%)
A-7	5	70	100
	10		
	20		
	30		
	40		
	50		
A-8	5		90
	10		
	20		
	30		
	40		
	50		
A-9	5		80
	10		
	20		
	30		
	40		
	50		
A-10	5		70
	10		
	20		
	30		
	40		
	50		
A-11	5		60
	10		
	20		
	30		
	40		
	50		
A-12	5		50
	10		
	20		
	30		
	40		
	50		

Table A-3 shows the test conditions for the cases with 70°C temperature where the relative humidity varied 50, 60, 70, 80, 90, and 100% and the flow rates varied 5, 10,

20, 30, 40, and 50 slpm. Figures A-8, 9, 10, 11, and 12 show the accumulated water inputs with different relative humidity and flow rates at 70°C temperature.

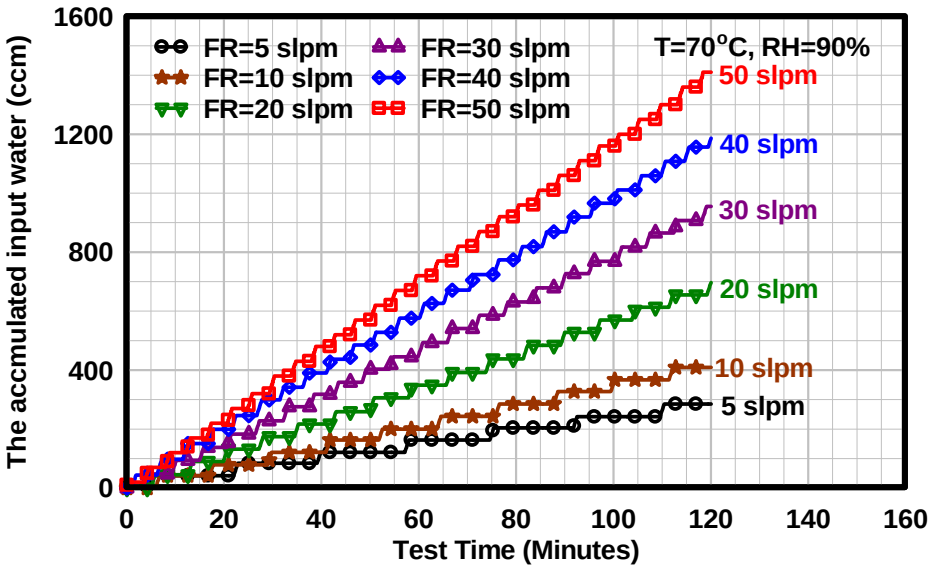

Figure A-8 The accumulated input water corresponding to the flow rate at 70°C, 90%.

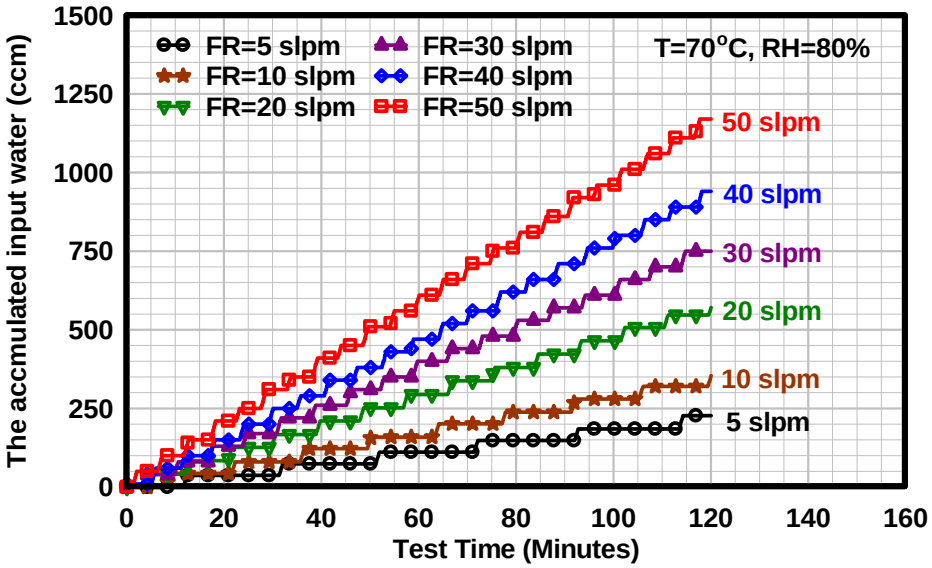

Figure A-9 The accumulated input water corresponding to the flow rate at 70°C, 80%.

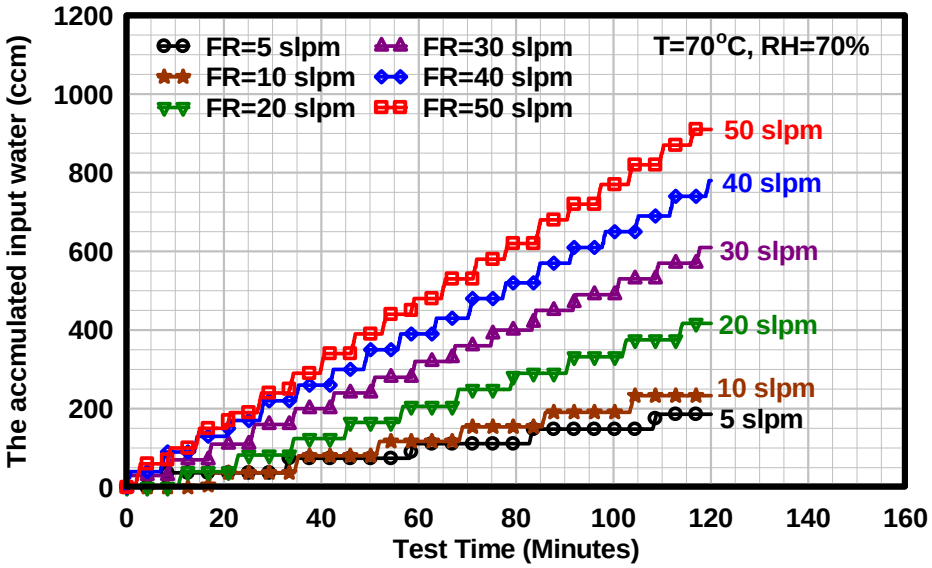

Figure A-10 The accumulated input water corresponding to the flow rate at 70°C, 70%.

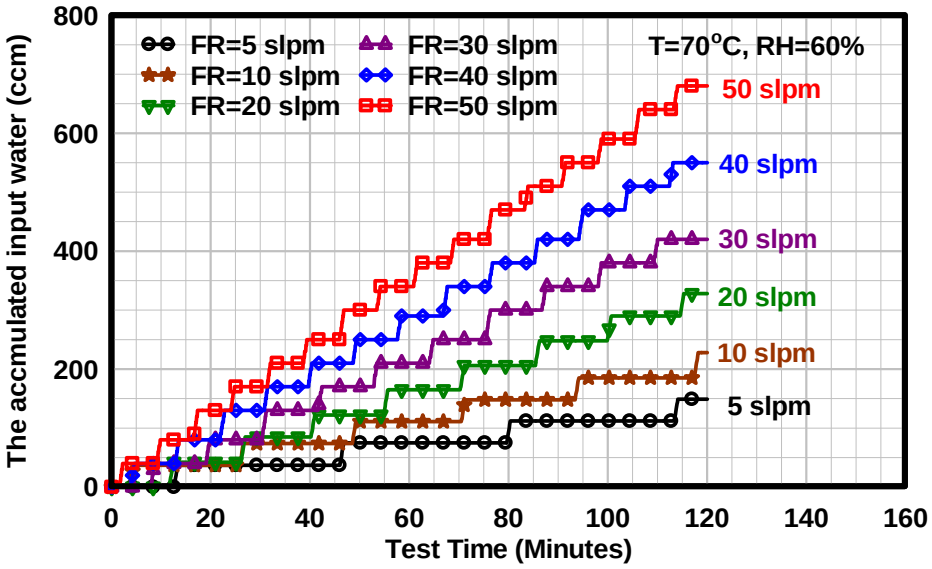

Figure A-11 The accumulated input water corresponding to the flow rate at 70°C, 60%.

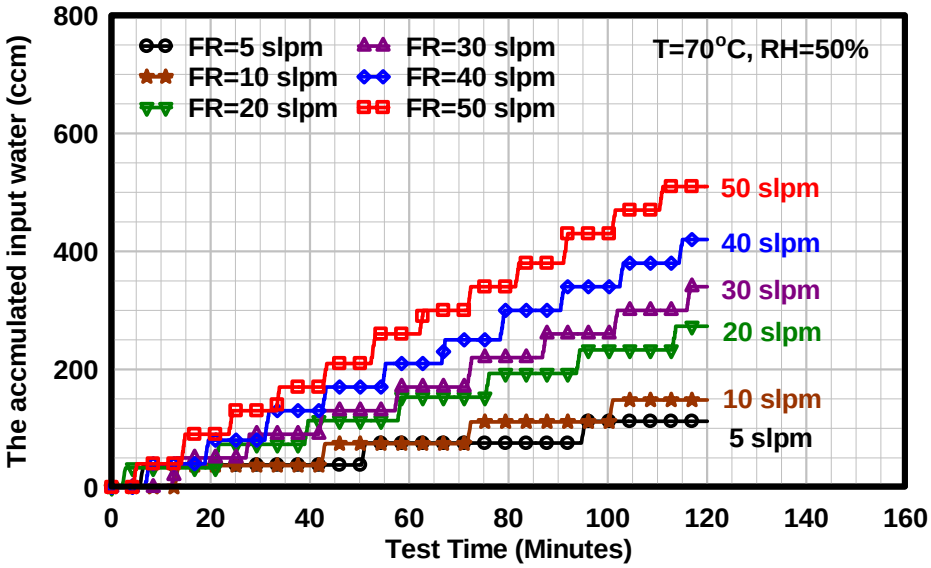

Figure A-12 The accumulated input water corresponding to the flow rate at 70°C, 50%.

APPENDIX B

UNCERTAINTY ANALYSIS OF THE ELECTRO-OSMOTIC DRAG COEFFICIENT

To find out the uncertainty of the electro-osmotic drag coefficients (cases D-1, 2, 3, 4, 6, 7, 8, and 9), data found from experiments were listed for each case from Table B-1 to B-10.

The precision index of a sample population is defined as

$$S_X = [\frac{1}{N-1}\sum_{i=1}^{N}(X_i - \overline{X})^2]^{\frac{1}{2}} \quad \text{(B-1)}$$

where the mean of X_i is $\overline{X} = \frac{1}{N}\sum_{i=1}^{N} X_i$. The precision limit of the sample population is the limit of the random error, and is related to the precision index as follows:

$$P_X = t \times S_X \quad \text{(B-2)}$$

where $t=t\ (N,\ C)$ is dependent on the number of sample readings of X_i and the confidence level. The overall uncertainty is then calculated as:

$$U_X = \sqrt{(B^2 + P_X{}^2)} \quad \text{(B-3)}$$

where B= bias limit. The standard deviation for a Gaussian distribution is

$$\sigma = \lim_{N\to\infty}[\frac{1}{N}\sum_{i=1}^{N}(X_i - \mu)^2]^{\frac{1}{2}} \quad \text{(B-4)}$$

where the mean of X_i is

$$\mu = \lim_{N\to\infty} \frac{1}{N} \sum_{i=1}^{N} X_i \qquad \text{(B-5)}$$

With a confidence level of 95%, the mean of the distribution should fall within ±1.96σ of a single reading X_i is, that is, 95% of the population of X_i should lie within ±1.96σ of the mean, μ. Table B-1 shows values of t for a 95% confidence level. Bias limit in this uncertainty analysis considered only the calibration error, which was assumed as 0.01.

Table B-1 Value of t for a confidence level (95%), C, and number of degrees of freedom, $\nu=N-1$.

$\nu=N-1$	C (0.95)
1	12.70
2	4.30
3	3.18
4	2.78
5	2.57
6	2.45
7	2.36
8	2.31
9	2.26
10	2.23

Table B-1, 2, 3, and 4 shows the uncertainty analysis for the case D-1, 2, 3, 4, and 5. Table B-5, 6, 7, and 8 shows the uncertainty analysis for cases D-6, 7, 8, and 9.

Table B-2 Uncertainty analysis for the case D-1 (current density of 0.4 A/cm^2 and RH100% H_2 & dry air at 70^{o}C).

Current Density (A/cm^2)	Test Time (Minutes)	Supplied-Drained out (ccm)	Electro-osmotic Drag Coefficient
0.4	0.00	0.0	N/A
	53.83	10.8	0.90
	104.93	20.2	0.86
	161.48	31.4	0.87
	206.28	38.1	0.82
	267.35	45.1	0.75
	311.21	56.4	0.81
	370.60	61.9	0.75
	421.30	74.2	0.79
Average			**0.82**
Standard Deviation			0.05
Standard Error of the Mean (S)			0.02
Bias Limit	0.01	t_{95}	2.36
		Uncertainty	**0.06**

Table B-3 Uncertainty analysis for the case D-2 (current density of 0.6 A/cm^2 and RH100% H_2 & dry Air at 70^{o}C).

Current Density (A/cm^2)	Test Time (Minutes)	Supplied-Drained out (ccm)	Electro-osmotic Drag Coefficient
0.6	0.00	0.0	N/A
	41.03	10.2	0.74
	81.29	20.3	0.74
	108.31	26.8	0.74
	119.23	29.6	0.74
	162.58	36.7	0.67
	208.26	47.8	0.68
	223.72	56.5	0.75
	294.98	65.1	0.66
	338.33	72.1	0.63
	386.33	82.6	0.64
	435.11	91.8	0.63
Average			**0.69**
Standard Deviation			0.05
Standard Error of the Mean (S)			0.02
Bias Limit	0.01	t_{95}	2.23
		Uncertainty	**0.04**

Table B-4 Uncertainty analysis for the case D-3 (current density of 0.8 A/cm^2 and RH100% H_2 & dry air at 70^{o}C).

Current Density (A/cm^2)	Test Time (Minutes)	Supplied-Drained out (ccm)	Electro-osmotic Drag Coefficient
0.8	0.0	0.0	N/A
	159.6	40.8	0.57
	210.0	53.1	0.56
	262.5	64.2	0.55
	315.1	78.2	0.55
	236.9	60.1	0.57
	360.3	92.6	0.57
	476.0	114.8	0.54
Average			**0.56**
Standard Deviation			0.01
Standard Error of the Mean (S)			0.01
Bias Limit	0.0	t_{95}	2.45
		Uncertainty	**0.02**

Table B-5 Uncertainty analysis for the case D-4 (current density of 1.0 A/cm^2 and RH100% H_2 & dry air at 70^{o}C).

Current Density (A/cm^2)	Test Time (Minutes)	Supplied-Drained out (ccm)	Electro-osmotic Drag Coefficient
1.0	0.00	0.0	N/A
	119.79	30.6	0.46
	157.22	41.5	0.47
	210.32	58.2	0.49
	254.64	71.2	0.50
	262.37	74.6	0.51
	311.86	90.1	0.52
	365.46	108.6	0.53
	401.71	117.5	0.52
	413.92	123.9	0.53
Average			**0.50**
Standard Deviation			0.02
Standard Error of the Mean (S)			0.01
Bias Limit	0.01	t_{95}	2.31
		Uncertainty	**0.03**

Table B-6 Uncertainty analysis for the case D-5 (current density of 1.2 A/cm^2 and RH100% H_2 & dry air at 70^{o}C).

Current Density (A/cm^2)	Test Time (Minutes)	Supplied-Drained out (ccm)	Net Drag Coefficient
1.2	0.00	0.0	N/A
	57.13	19.1	0.50
	108.76	38.1	0.52
	152.20	52.6	0.51
	163.12	54.6	0.50
	216.58	69.5	0.48
	267.48	84.4	0.47
Average			**0.50**
Standard Deviation			0.02
Standard Error of the Mean (S)			0.01
Bias Limit	0.01	t_{95}	2.57
		Uncertainty	**0.03**

Table B-7 Uncertainty analysis for the case D-6 (current density of 0.6 A/cm^2 and RH70% H_2 & dry air at 70^{o}C).

Current Density (A/cm^2)	Test Time (Minutes)	Supplied-Drained out (ccm)	Electro-osmotic Drag Coefficient
0.6	0.00	0.0	N/A
	98.75	12.1	0.36
	181.05	28.8	0.47
	221.38	32.7	0.44
	284.29	41.6	0.44
	365.85	57.1	0.46
Average			**0.44**
Standard Deviation			0.04
Standard Error of the Mean (S)			0.02
Bias Limit	0.01	t_{95}	2.78
		Uncertainty	**0.06**

Table B-8 Uncertainty analysis for the case D-7 (current density of 0.6 A/cm^2 and RH80% H_2 & dry air at 70^{o}C).

Current Density (A/cm^2)	Test Time (Minutes)	Supplied-Drained out (ccm)	Electro-osmotic Drag Coefficient
0.6	0.00	0.0	N/A
	77.42	12.1	0.46
	151.38	20.6	0.40
	167.61	26.5	0.47
	313.14	49.0	0.47
	389.18	62.6	0.48
Average			**0.46**
Standard Deviation			0.03
Standard Error of the Mean (S)			0.01
Bias Limit	0.01	t_{95}	2.78
		Uncertainty	**0.05**

Table B-9 Uncertainty analysis for the case D-8 (current density of 0.6 A/cm^2 and RH90% H_2 & dry air at 70^{o}C).

Current Density (A/cm^2)	Test Time (Minutes)	Supplied-Drained out (ccm)	Electro-osmotic Drag Coefficient
0.6	0.00	0.0	N/A
	134.82	23.0	0.51
	201.46	38.4	0.57
	265.13	50.5	0.57
	288.39	63.0	0.65
	329.66	63.0	0.57
	395.93	83.4	0.63
Average			**0.58**
Standard Deviation			0.05
Standard Error of the Mean (S)			0.02
Bias Limit	0.01	t_{95}	2.57
		Uncertainty	**0.06**

Table B-10 Uncertainty analysis for the case D-9 (current density of 0.6 A/cm^2 and RH10% H_2 & dry air at 70^{o}C).

Current Density (A/cm^2)	**Test Time (Minutes)**	**Supplied-Drained out (ccm)**	**Electro-osmotic Drag Coefficient**
0.6	0.00	0.0	N/A
	41.03	10.2	0.74
	81.29	20.3	0.74
	119.23	29.6	0.74
	162.58	36.7	0.67
	208.26	47.8	0.68
	249.30	55.1	0.66
	294.98	65.1	0.66
	338.33	72.1	0.63
	386.33	82.6	0.64
	435.11	91.8	0.63
Average			**0.68**
Standard Deviation			0.05
Standard Error of the Mean (S)			0.01
Bias Limit	0.01	t_{95}	2.26
		Uncertainty	**0.04**

VITA

Yong Hun Park was born in Tae-Gu, Republic of Korea. He received his Bachelor of Science degree in mechanical engineering from the Kyungpook National University in 1999. He served in the military service from Jan. 1994 to Mar. 1996 in the Republic of Korea. He entered the graduate program at Texas A&M University in August 2000, and he received his Master of Science degree in May 2003 and his Ph.D. in December 2007.